RUPRECHT-KARLS-UNIVERSITÄT HEIDELBERG

Kambiz Mahboubi

ATLAS Level-1 Jet Trigger Rates and study of the ATLAS discovery potential of the neutral MSSM Higgs bosons in b-jet decay channels

Dissertation

HD-KIP-01-06

KIRCHHOFF-INSTITUT FÜR PHYSIK

INAUGURAL-DISSERTATION

zur

Erlangung der Doktorwürde

der

Naturwissenschaftlich–Mathematischen

Gesamtfakultät

der

Ruprecht–Karls–Universität
Heidelberg

vorgelegt von

Diplom–Ingenieur Kambiz Mahboubi
aus Tehran/Iran

Tag der mündlichen Prüfung: 25. 4. 2001

ATLAS Level-1 Jet Trigger Rates and study of the ATLAS discovery potential of the neutral MSSM Higgs bosons in b-jet decay channels

Kambiz Mahboubi

Gutachter: Prof. Dr. Klaus Tittel
Prof. Dr. Karl Jakobs

Dissertation
submitted to the
Joint Faculties for Natural Sciences and Mathematics
of the Ruperto Carola University of
Heidelberg, Germany,
for the degree of
Doctor of Natural Sciences

ATLAS Level-1 Jet Trigger Rates and study of the ATLAS discovery potential of the neutral MSSM Higgs bosons in b-jet decay channels

presented by

Diploma–Engineer: Kambiz Mahboubi
born in: Tehran / Iran

Heidelberg, March 12, 2001

Referees: Prof. Dr. Klaus Tittel
Prof. Dr. Karl Jakobs

"The good life is inspired by love and guided by knowledge."

Bertrand Russel
What I believe, 1925

ABSTRACT

The response of the ATLAS calorimeters to electrons, photons and hadrons, in terms of the longitudinal and lateral shower development, is parameterized using the GEANT package and a detailed detector description (DICE). The parameterizations are implemented in the ATLAS Level-1 (LVL1) Calorimeter Trigger fast simulation package which, based on an average detector geometry, simulates the complete chain of the LVL1 calorimeter trigger system. In addition, pile-up effects due to multiple primary interactions are implemented taking into account the shape and time history of the trigger signals. An interface to the fast physics simulation package (ATLFAST) is also developed in order to perform ATLAS physics analysis, including the LVL1 trigger effects, in a consistent way. The simulation tools, the details of the parameterization and the interface are described. The LVL1 jet trigger thresholds corresponding to the current trigger menus are determined within the framework of the fast simulation, and the LVL1 jet trigger rates are estimated. Further, the combination of $\mathrm{E_T^{miss}}$ signature with jet and τ triggers is also discussed.

A study of the discovery potential of the ATLAS experiment of the neutral MSSM Higgs bosons in the decay channels with multi b-jet final state topologies, namely $H \to h\,h \to bb\,bb$ and $bb\,A/H \to bb\,bb$, is performed. The signal acceptance of the ATLAS LVL1 jet trigger, based on the determined trigger thresholds, is evaluated. Given the dominating jet trigger rates from the QCD multi-jet processes, the b-tagging capability of the LVL2 trigger is essential for the Higgs discovery in these channels. Canonical ATLAS b-tag/mistag efficiencies are applied on reconstructed jets. Finally, 5σ discovery contours in the $(tan\beta, m_A)$ plane are derived.

ZUSAMMENFASSUNG

Das Ansprechverhalten der ATLAS Kalorimeter für Elektronen, Photonen und Hadronen wird bezüglich der longitudinalen und transversalen Schauerentwicklung parametrisiert. Als Ausgangsdaten dienen voll simulierte Ereignisse, die unter Verwendung des GEANT Programmpakets und einer detaillierten Detektorbeschreibung (DICE) erzeugt werden. Die Parametrisierungen werden in das Programm zur schnellen Simulation des ATLAS Level-1 (LVL1) Kalorimetertriggers integriert, das mit einer vereinfachten Detektorgeometrie die vollständige Kette dieses Triggers simuliert. Darüberhinaus werden auch die Effekte durch die zeitliche Überlagerung mehrer Ereignisse im Detekor unter Berücksichtingung der zeitlichen Form und Vorgeschichte der Triggersignale einbezogen. Außerdem wird eine Schnittstelle zum Programmpaket für die ATLAS Physikanlyse (ATLFAST) entwickelt, um Analysen einschließlich LVL1 Triggereffekten konsistent durchführen zu können. Die Simulationswerkzeuge, die Einzelheiten der Parametrisierung und die Schnittstelle werden beschrieben. Im Rahmen der 'schnellen Simulation' werden die LVL1 Jet-Triggerschwellen für die entsprechenden Triggermenüs bestimmt und die LVL1 Jet-Triggerraten abgeschätzt. Weiter wird die Kombination von $\mathrm{E_T^{miss}}$ -Signatur mit Jet und τ-Trigger diskutiert.

Eine Studie über das Entdeckungspotential des ATLAS Experiments für die neutrale MSSM Higgs Bosonen in Zerfallskanälen mit Multi-b-Jet Endzuständen, namentlich $H \to h\,h \to bb\,bb$ und $bb\,A/H \to bb\,bb$, wird durchgeführt. Die Nachweiswahrscheinlichkeit des ATLAS LVL1 Jet-Triggers mit den zuvor bestimmten Triggerschwellen wird untersucht. Angesichts der dominierenden Jet-Trigger-Raten aus QCD Multi-Jet Prozessen ist für die Entdeckung des Higgs in diesen Kanälen die b-tagging Fähigkeit des LVL2 Triggers unverzichtbar. Kanonische ATLAS b-tag Identifikations- und Missidentifikationswahrscheinlichkeiten werden auf rekonstruierte Jets angewendet. Schließlich werden 5σ Entdeckungskonturen in der $(tan\beta, m_A)$ Ebene ermittelt.

Contents

Introduction

The accumulated knowledge on the elementary particle physics during the last two decades is compiled in a theoretical framework called the Standard Model (SM). This theory is able to describe essentially all basic phenomena in the field of high energy physics with great accuracy. The SM parameters have been measured with great precision at various experimental facilities. One parameter is however essentially unknown, the mass of the scalar Higgs boson, which according to theory can explain the symmetry breaking in the electroweak sector through the so called Higgs mechanism and is responsible for masses of all of the other particles through its coupling to them. Direct and indirect searches at the LEP collider, till its closure, have only put limits on the allowed mass of this hypothetical particle.

The Standard Model, despite its success in describing the experimental observations to an amazing precision, has some short-comings which call for other more complete theories of nature. One of the most attractive of these theories, beyond the Standard Model, is the SUperSYmmetric extension to it, i.e. SUSY. The supersymmetric models have been discussed the recent years and guide us where to look for new physics beyond the Standard Model. Although the particle content of these models is quite rich and although they introduce yet more parameters into the theory, some restricted versions of SUSY, making it possible to perform searches and studies. One of these models is the Minimal Supersymmetric extension to the Standard Model (MSSM) with a rich Higgs sector with five Higgs bosons, three neutral and two charged, instead of the single neutral Higgs in the minimal version of the SM.

It is obvious that based on these arguments any future experiment should aim at the question of the symmetry breaking mechanism and at searching for the Higgs particle(s). Based on the latest results from LEP2 the next step in the particle physics should be a collider experiment penetrating the TeV energy range. Such a program is the future pp collider, LHC, planned at CERN, with related experiments, like ATLAS and CMS, and scheduled to start operation at the year 2005. Here many open questions within the SM will be explored. Optimizations of these future detectors rely strongly on the results obtained from Monte Carlo and simulation studies.

Given the fact that the ATLAS detector will be operating at the LHC with high jet activity from the QCD processes, and considering its ability to measure and identify electrons, photons, and muons, with high rejection against background jets, a critical point for the trigger system is signal extraction based on multi-jet final states. It is not the efficiency on triggering on jets, but the question of background rejection which degrades the acceptance of interesting signals with multi-jet final state topologies. The reason for this is that in order to be able to reduce the QCD jet rate to an acceptable level (a few percent of the overall trigger rate) the trigger thresholds should be put quite high, whereas an efficient signal extraction

would require low thresholds. In ATLAS the second trigger level is not able to reduce the jet rate for jets with a transverse energy in excess of about 50 GeV. Therefore the LVL1 jet trigger rate goes through the trigger system essentially untouched. The only exception would be if the jet under consideration happen to be a b-jet. In this case the special b-tag trigger of the ATLAS Inner Detector could be used in order to achieve a higher acceptance (and efficiency) on processes with multi b-jet topologies. In this case the jet trigger thresholds could in principle be reduced at LVL1 so that the b-tag capabilities at the next trigger level may be used to reduce the overall jet rate to an acceptable level. These issues are addressed in this work for the Higgs searches in the neutral components of the MSSM Higgs sector.

The study presented here is performed using a simulation framework containing details of the relevant subdetectors' effects, the complete LVL1 trigger chain and the pile-up contributions at low and high luminosities. In particular the implemented simulation tool contains detailed parameterizations of the detector response and the longitudinal shower development between the ECAL and the HCAL, as well as the lateral shower profile within each calorimeter type, extracted form full detector simulation. This is done both for the electromagnetic and for the hadronic particles. The effect of the Barrel/EndCap transition region on the response of the calorimeters to different types of particles are also implemented in the simulation tool. Furthermore, the pileup effect is simulated taking into account, apart from the average number of minimum-bias events per bunch crossing, the time history of the calorimeter signals. The offline analysis and the LVL1 trigger impact are performed in the same simulation framework, which ensures consistency of the obtained results with and without the trigger effects.

The central interest of this work is essentially the impact of the trigger system of ATLAS detector on the discovery potential of the neutral MSSM Higgs bosons through their decay channels with multi b-jet final states. The $H \to h\,h \to bb\,bb$ and the $bb\,A/H \to bb\,bb$ decay modes at small (1.5–3.0) and at large (30–50) $tan\,\beta$ values and at intermediate to high m_A (100 GeV–300 GeV) are studied in terms of the statistical significances with and without the LVL1/LVL2 trigger effects. These are important decay channels given the fact that, for the parameter sets considered here, the direct and associated production cross-sections are large, and the bb decay branching ratios are dominating, resulting consequently in high signal rates. The only serious background distorting this picture is the QCD jet events, making it a demanding task to extract the signal efficiently. For this reason, multi b-jet final states are in general difficult signals for the ATLAS trigger to extract effectively above the dominating, and the much higher rate, multi-jet QCD background processes. Further, thresholds for the level–1 jet triggers are determined and estimates on the expected level–1 jet trigger rates are obtained. The acceptance of the level–1 jet trigger of the signal processes is estimated and the impact of the level–2 special b-tag capability, of great importance for the decay channels, is illustrated.

Chapter 1

Theory and Phenomenology

The present understanding of the elementary particles and their interactions is described by a theoretical framework, known as the Standard Model (SM) [2, 3, 4, 5, 6]. This framework is an interplay between local gauge field theories, described by appropriate Lagrangian densities, and phenomenological symmetries observed in nature and experiments. Matter fields are associated to a number of point-like (spin 1/2) (anti)fermions, (anti)quarks and (anti)leptons, organized in three families (each with two flavours), whereas interactions are mediated by a series of (spin 1) vector gauge bosons, summarized in Table 1.1.

Table 1.1: *Matter fermions, lepton and quark multiplets, and force carriers, gauge bosons, of the electroweak and strong interactions in the Standard Model. The multiplet structure indicated in the table refers to the transformation properties of the left and right chiral fermion fields under electroweak gauge symmetry operations. The strong interactions, mediated by gluons, apply only to the quark fields. Each quark flavour appears as colour triplet in colour space. In this connection the single gluon in the table represents 8 different (doubly colour–charged) gluons.*

Leptons	**Quarks**	**Gauge bosons**
$\begin{pmatrix} \nu_e \\ e \end{pmatrix}_L \quad e_R$	$\begin{pmatrix} u^{r,g,b} \\ d^{r,g,b} \end{pmatrix}_L \quad u_R^{r,g,b} \ , \ d_R^{r,g,b}$	**electro-**
		γ
		weak ,
$\begin{pmatrix} \nu_\mu \\ \mu \end{pmatrix}_L \quad \mu_R$	$\begin{pmatrix} c^{r,g,b} \\ s^{r,g,b} \end{pmatrix}_L \quad s_R^{r,g,b} \ , \ c_R^{r,g,b}$	$W^\pm \ , \ Z^\circ$
		strong
$\begin{pmatrix} \nu_\tau \\ \tau \end{pmatrix}_L \quad \tau_R$	$\begin{pmatrix} t^{r,g,b} \\ b^{r,g,b} \end{pmatrix}_L \quad b_R^{r,g,b} \ , \ t_R^{r,g,b}$	g
		interactions

Field theories describing the elementary particle interactions [24] obey the so-called local gauge invariance principle [10], which could be described as follows: *If the theory, i.e. the La-*

*grangian density function for the physical system, is completely invariant under a set of local** *field transformations described by a Lie-group† with parameters* $\{\theta_i\}$*, then the theory is said to be gauge invariant.* Physical quantities, e.g. cross-section, are determined through perturbation theory [8], by calculating the amplitudes of the corresponding Feynman diagrams [9] to different orders. A simple perturbative interpretation of Feynman diagrams, containing loops, generates ultraviolet divergences, when integrating over momentae propagating inside the loops. Since the field theories describing the elementary particles and their interactions should be renormalizable [14], these divergent integrals must be removed. The infinities are absorbed into a redefinition of the physical parameters of the theory, e.g. couplings, through a combination of *regularization* and *renormalization* procedures. Regularization consists of rendering sense (or meaning) to the divergences by introducing a regularizing parameter. This is done by, for instance, introducing an ultraviolet momentum cutoff, Λ, or by evaluating the integrals over a fractional space-time dimension, $d = 4-2\epsilon$. This re-expression of the infinities in terms of the new parameter makes the divergent quantities finite and well–defined. The contribution from the regularized loop integrals could in principle be split into a divergent and a finite term. This splitting is not unique and a given choice of the finite term defines a particular scheme. Clearly the regularized quantities still have divergent limits, e.g. when letting $\Lambda \to \infty$ or $\epsilon \to 0$. They are though removed from the final physical results through the renormalization procedure. A consequence of the regularization/renormalization procedure is that the renormalized quantities, e.g. the couplings, will however depend on an arbitrary mass scale μ, introduced into the theory through the renormalization. The regularized infinities, after renormalization, are absorbed into so-called *bare* quantities, which are meaningless and could not be measured experimentally. The only thing which could be measured is the effective, i.e. μ dependent, quantities. The mass scale could for instance be the energy scale characterizing a given experiment, e.g. four-momentum transfer $\mu^2 = Q^2$. Several methods exist to perform the renormalization, and each introduces basically a (different) dimensional scale. Physical quantities on the other hand should be independent of the renormalization schemes. The invariance of the observable quantities under changes of the scale parameter μ is expressed by the so–called *Renormalization Group Equations*, RGEs.

1.1 The Standard Model

The Standard Model of the strong, weak and electromagnetic interactions is based on a local non-abelian gauge field theory, with the symmetry group $SU(3)_C \times SU(2)_L \times U(1)_Y$. Index C refers to the quantum number of the strong interaction, the *colour* charge, L indicates the chirality characteristic of the weak isospin group, and Y is the weak hyper charge.

The symmetry group of the strong interactions is the local non-abelian gauge group $SU(3)_C$ of the Quantum ChromoDynamics (QCD) [19]. Quarks form colour triplets, $q = (q^r, q^g, q^b)^T$, in colour space with respect to the strong interactions, and interact with an octet of coloured gluons. The QCD Lagrangian could be written as [1, 24, 25]:

$$\mathcal{L}_{QCD} = -\frac{1}{4} G_a^{\mu\nu} G^a_{\mu\nu} + \sum_q \bar{q}(i\gamma_\mu \mathcal{D}^\mu - m_q)q \ , \tag{1.1}$$

*Local transformations of the group elements are functions of the space–time coordinates of the fields.

†The members of a Lie–group are continuously differential functions of a set of parameters.

where a refers to colour states of the gluon, $a = 1, \ldots, 8$, and the sum runs over all quark flavours $q = u, d, s, c, b, t$. Quark masses, m_q, are arbitrary parameters of the theory, which have to be input from outside. The covariant derivative, $\mathcal{D}_\mu$, acting on the quark fields, q, and generating interactions, is given by:

$$\mathcal{D}^\mu = \partial^\mu + ig_s \frac{\lambda^a}{2} G_a^\mu,$$

where G_a^μ is the gluon field, g_s is the strong coupling and λ^a are 3×3 hermitian, traceless (Gell-Mann) matrices. The gluon field strength tensor, $G_a^{\mu\nu}$, is given by:

$$G_a^{\mu\nu} = \partial^\mu G_a^\nu - \partial^\nu G_a^\mu - g_s f_{abc} G_b^\mu G_c^\nu,$$

where f^{abc} are $SU(3)$ structure constants, defined by the commutation relations of the group generators: $[T^a, T^b] = if^{abc}T^c$, with $T^a = \lambda^a/2$. The QCD Lagrangian is invariant under simultaneous (infinitesimal) local gauge transformations of the quark, q, and gluon, G_a^μ fields. The blown-up, and more informative, version of $\mathcal{L}_{QCD}$ reads as follows:

$$\begin{aligned}
\mathcal{L}_{QCD} &= -\frac{1}{4}(\partial^\mu G_a^\nu - \partial^\nu G_a^\mu)(\partial_\mu G_\nu^a - \partial_\nu G_\mu^a) + \sum_q \bar{q}(i\gamma^\mu \partial_\mu - m_q)q \\
&\quad + g_s G_a^\mu \sum_q \bar{q}\gamma_\mu \frac{\lambda^a}{2} q \\
&\quad - \frac{g_s}{2} f^{abc}(\partial^\mu G_a^\nu - \partial^\nu G_a^\mu) G_\mu^b G_\nu^c \; - \; \frac{g_s^2}{4} f_{abc} f^{ade} G_b^\mu G_c^\nu G_\mu^d G_\nu^e \,.
\end{aligned}$$

In this equation the first two terms are the kinetic terms for gluon and quark fields respectively, giving rise to propagators. The third term, involving the group generators, represents the colour interaction between quarks and gluons. The last two terms are cubic and quartic gluon self-interactions. Theoretically, the self–interaction property of gluons is due to the fact that QCD is a non-abelian theory and hence the group generators do not commute.

The (running) coupling constant of the strong interaction is to next-to-leading order given by the formula [1, 24, 25]:

$$\begin{aligned}
\alpha_s(Q^2) &= \frac{4\pi}{\beta_0 \, ln(\frac{Q^2}{\Lambda^2})} \left[1 - \frac{2\beta_1 \, ln(ln(\frac{Q^2}{\Lambda^2}))}{\beta_0^2 \, ln(\frac{Q^2}{\Lambda^2})} + \mathcal{O}(\alpha_s^3) \right], \qquad (1.2) \\
\beta_0 &= \frac{1}{3}(11N_c - 2N_f), \\
\beta_1 &= \frac{1}{3}(17N_c^2 - 5N_c N_f - 3C_f N_f),
\end{aligned}$$

where $N_c = 3$ is the number of colour charges, $C_f = \frac{4}{3}$, N_f is the number of quark flavours with a mass less than the squared four momentum transfer Q^2 and Λ is the QCD scale parameter of the order of a few MeV. It is obvious from this formula that $\alpha_s(Q^2) \to \infty$ as $Q^2 \to \Lambda^2$, hence Λ, in a sense, is the scale at which the strong interaction becomes strong. This in turn means that the methods of perturbative QCD are not applicable at small Q^2.

The symmetry group of the (unified) electroweak interactions [13] is the $SU(2)_L \otimes U(1)_Y$ gauge group. The Lagrangian density is given by [24, 2]:

$$\mathcal{L} = -\frac{1}{4}\sum_{i=1}^{3} W_i^{\mu\nu} W_{i\mu\nu} - \frac{1}{4} B^{\mu\nu} B_{\mu\nu} + \bar{\psi}_L i\gamma^\mu \mathcal{D}_\mu \psi_L + \bar{\psi}_R i\gamma^\mu \mathcal{D}_\mu \psi_R \ ,$$

with field tensors $B_{\mu\nu}$ and $\boldsymbol{W}_{\mu\nu}$ given by:

$$\begin{aligned} B^{\mu\nu} &= \partial^\mu B^\nu - \partial^\nu B^\mu \,, \\ W_i^{\mu\nu} &= \partial^\mu W_i^\nu - \partial^\nu W_i^\mu + g\epsilon_{ijk} W_j^\mu W_k^\nu \,, \end{aligned}$$

where B_μ is the singlet gauge field associated with $U(1)$, and $\boldsymbol{W}_\mu$ is the isotriplet gauge field connected to $SU(2)$. The $SU(2)$ group structure constants are denoted by ϵ_{ijk}. Fermion fields, $\psi_{L,R}$, refer to left and right chirality fermion fields. Left and right handed fermions have different transformation properties under $SU(2)$. Left handed fermions form doublets under $SU(2)$ symmetry operations, which transform the components of a doublet into each other. Right handed fermions, on the other hand, transform trivially under $SU(2)$ and are singlets. Both right and left handed fermions transform non-trivially under $U(1)$ phase transformations. This multiplet structure of the electroweak interactions is indicated in Table 1.1. In the quark sector, the weak isospin quark eigenstates are not the same as their mass eigenstates. The quark isospin eigenstates are obtained from their mass eigenstates by a rotation in isospin space. The usual method is to rotate only the $I_3 = -1/2$ members of the quark families. Thus One considers the unitary transformation (change of basis from mass to weak isospin):

$$\begin{pmatrix} d' \\ s' \\ b' \end{pmatrix} \quad = \quad V \begin{pmatrix} d \\ s \\ b \end{pmatrix},$$

where V, the Cabibbo–Kobayashi–Maskawa (CKM) matrix [17] is given by the approximate Wolfenstein parameterization [18]:

$$V = \begin{pmatrix} V_{ud} & V_{us} & V_{ub} \\ V_{cd} & V_{cd} & V_{cd} \\ V_{td} & V_{td} & V_{td} \end{pmatrix} \simeq \begin{pmatrix} 1-\lambda^2/2 & \lambda & A\lambda^3(\rho - i\eta) \\ -\lambda & 1-\lambda^2/2 & A\lambda^2 \\ A\lambda^3(1-\rho-i\eta) & -A\lambda^2 & 1 \end{pmatrix} + \mathcal{O}(\lambda^4)\,,$$

where different parameters have the experimentally obtained values [1]: $\lambda = 0.2196 \pm 0.0023$, $A = 0.83 \pm 0.04$, $\eta = 0.3 \pm 0.1$ and $\sqrt{\rho^2+\eta^2} = 0.4 \pm 0.1$. The covariant derivative, generating the interactions, could be expressed as:

$$\mathcal{D}_\mu = \partial_\mu - ig'\frac{Y}{2} B_\mu + ig \sum_{i=1}^{3} \frac{\tau^i}{2} W_\mu^i \,,$$

where $\boldsymbol{\tau}$ are Pauli matrices, g' and g are $SU(2)$ and $U(1)$ couplings respectively. The weak isospin, $\boldsymbol{I} = \boldsymbol{\tau}/2 = (\tau_1/2, \tau_2/2, \tau_3/2)$, and the weak hypercharge, Y, are the generators of the $SU(2)_L$ and $U(1)_Y$ gauge groups respectively. The weak hypercharge is defined as $Q = Y/2 + I_3$, where Q is the electromagnetic charge and I_3 is the third component of the weak isospin. The physical charged vector bosons, $W^\pm$, are linear combinations of the first two components of the field $\boldsymbol{W} = (W_1, W_2, W_3) \to W^+, W^-, W^0$, defined as:

$$W_\mu^\pm = \frac{1}{\sqrt{2}} \left(W_{1\,\mu} \mp i\, W_{2\,\mu} \right) \ , \quad W_\mu^0 = W_{3\,\mu}$$

and the neural vector boson, Z^μ, and the photon, A^μ, are orthogonal and normalized linear combinations of W_3^μ and B^μ:

$$\begin{array}{rcrcl} A^\mu & = & cos(\theta_W)B^\mu & + & sin(\theta_W)W_3^\mu\,, \\ Z^\mu & = & -sin(\theta_W)B^\mu & + & cos(\theta_W)W_3^\mu\,, \end{array}$$

where θ_W is the weak mixing angle. Requiring the photon to couple equally to left and right handed fermions, with strength e, the electric charge, the following relations are obtained:

$$g\,sin(\theta_W) = g'\,cos(\theta_W) = e \qquad \Rightarrow \qquad tan(\theta_W) = g'/g\,.$$

Any mass term in this theory will break the Lagrangian invariance under the gauge transformations of the group. Therefore, as it stands, all fermions and gauge bosons are massless. This is contrary to the experimental results, where, for instance, all vector bosons of the electroweak sector, except the photon, are massive. The same holds for fermions (including perhaps the neutrinos). A method to generate mass for intermediate gauge bosons and the fermions, without destroying the gauge invariance of the theory, is the spontaneous symmetry breaking Higgs mechanism [12]. The usual method is to introduce new complex scalar fields, the Higgs fields, into the theory. The gauge bosons and the fermions acquire masses upon coupling to the Higgs field. The basic idea is to add extra symmetry-breaking terms, i.e. the Higgs Lagrangian, to the original Lagrangian. These extra terms should, like the symmetric part of the Lagrangian, be renormalizable. In the minimal symmetry-breaking scheme, the simplest and the most general Higgs Lagrangian, which fulfills these requirements, is [27, 28, 29]:

$$\mathcal{L}_{Higgs} = (\mathcal{D}_\mu\Phi)^\dagger(\mathcal{D}_\mu\Phi) - V(\Phi^\dagger\Phi) - \bar{\psi}_L G_f \psi_R \Phi - \bar{\psi}_R G_f^\dagger \psi_L \Phi^\dagger,$$

where Φ is the complex scalar isodoublet, containing the Higgs fields, with the quantum numbers $(I, Y) = (1/2, 1)$ with respect to the $SU(2)\otimes U(1)$:

$$\Phi = \begin{pmatrix} \phi^+ \\ \phi^0 \end{pmatrix} \;=\; \frac{1}{\sqrt{2}} \begin{pmatrix} \phi_1 + i\phi_2 \\ \phi_3 + i\phi_4 \end{pmatrix}$$

where ϕ_i, with $i = 1 \ldots 4$, are real scalar fields. The last two terms in the Higgs Lagrangian are the Yukawa couplings of the Φ field to fermions, giving them their masses. The fermionic Yukawa couplings to the Higgs field are represented by the quantity G_f (which depends on the fermion mass). The Higgs potential V is given by:

$$V(\Phi^\dagger\Phi) = \mu^2\Phi^\dagger\Phi + \lambda(\Phi^\dagger\Phi)^2,$$

where λ and μ^2 are real constants, with $\lambda > 0$. The second term in the Higgs potential is responsible for the cubic and quartic Higgs self-couplings, and the parameter λ is the Higgs (running) self-coupling. Taking $\mu^2 < 0$, the minimum of the Higgs potential lies on the circle $\Phi^\dagger\Phi = |\Phi|^2 = -\frac{1}{2}\mu^2/\lambda > 0$. Quantum mechanically, the lowest energy state of the system, the vacuum, gets a none zero expectation value (vev), i.e. it is not free of field. This vacuum state is completely symmetric and infinitely degenerate. Choosing a given minimum of the potential to be the vacuum, breaks the symmetry property of the vacuum state. This is referred to as spontaneous symmetry breaking, since the symmetry of the vacuum state is broken, whereas the Lagrangian itself is still symmetric. The common choice is to let only the neutral component of the Higgs field to develop a real none zero vev:

$$\Phi^0 \;\equiv\; \langle 0|\Phi|0\rangle \quad = \quad \frac{1}{\sqrt{2}} \begin{pmatrix} 0 \\ v \end{pmatrix} \;\equiv\; \frac{v}{\sqrt{2}}\,,$$

where $v = \sqrt{-\mu^2/\lambda}$, i.e. the vev, is a real non-zero free parameter. Introducing the vev into the Lagrangian mass terms of the fermions and the gauge bosons are obtained. The fact that only the neutral[‡] component of the Higgs doublet acquires a vacuum expectation value guarantees that the photon remains massless. This means that the electromagnetism is unbroken by the scalar vev. Hence the symmetry breaking scheme: $SU(2)_L \otimes U(1)_Y \longrightarrow U(1)_{EM}$. Masses of the $W^{\pm}$ and Z° weak gauge bosons are obtained from the kinetic term of the Higgs Lagrangian, by replacing Φ with it's vev, v:

$$M_W^2 = \frac{1}{4} g^2 v^2 \quad ; \qquad M_Z^2 = \frac{1}{4}(g^2 + g'^2)v^2 = \frac{g^2 v^2}{4cos^2(\theta_W)}.$$

Using the electroweak expressions for the masses of the gauge bosons one could determine the vacuum expectation value of the Higgs field: $v = (\sqrt{2}G_F)^{-1/2} \sim 246$ GeV, using $g^2/8M_W^2 = G_F/\sqrt{2}$, where G_F is the Fermi coupling constant. By introducing excitations, H, about the vev, through the replacement:

$$\Phi_H^0 = \frac{1}{\sqrt{2}} \begin{pmatrix} 0 \\ v + H \end{pmatrix},$$

a physical neutral scalar Higgs boson with a mass: $M_H^2 = -2\mu^2 = \lambda v^2$, enters the theory. It's couplings to the $W^{\pm}$ and Z° gauge bosons are also determined:

$$\mathcal{L}_{H,W,Z} = \frac{g^2 v}{2} W_\mu^+ W^{-\mu} H + \frac{g^2}{4} W_\mu^+ W^{-\mu} H^2 + \frac{g^2 v/2}{2cos^2(\theta_W)} Z_\mu Z^\mu H + \frac{g^2/4}{2cos^2(\theta_W)} Z_\mu Z^\mu H^2$$

The Yukawa couplings give masses to fermions, i.e. fermion couplings to the Higgs field are proportional to their masses: $m_f = G_f\, v/\sqrt{2}$, where the index f stands for fermion.

The existence of the Higgs particle is a necessary ingredient of the Standard Model. Apart from generating masses for the fermions and gauge bosons, it also cures some undesirable infinities of the theory. The electroweak radiative corrections would be infinite and longitudinal gauge boson scattering would grow without limit with energy, violating the unitarity at high energy scales. In the minimal version of the SM a scalar neutral Higgs boson could remedy these short-comings of the theory.

According to Grand Unified Theories (GUTs) [20, 24, 31], the Standard Model provides only an effective low energy description of a more fundamental theory. In these theories the group structure of the SM is unified into a larger and simpler grand unified gauge symmetry group, G, with for example only one coupling constant. This grand unification would occur at a large mass scale known as the GUT mass scale, M_{GUT} or $M_X \sim 10^{15}$ GeV. Above this mass scale the higher symmetry is unbroken, and leptons and quarks would belong to the same multiplets of G. This grand unification could be tested by evolving the coupling constants from their known values at the weak scale, $\mu \equiv M_{Z^\circ}$, to the GUT scale, $\mu \equiv M_X$, to see if they really meet (or unify). In the SM this is not the case. Although the couplings approach each other at about M_X, they do not unify. Evolving beyond the GUT scale, the hierarchy of the couplings is changed.

[‡]Probably this should be expressed the other way around: in order to ensure that the vacuum is electrically neutral, only the neutral component of the Higgs field is required to develop a vacuum expectation value (vev).

1.2 Beyond the Standard Model

The Standard Model, pictured above, with a single $SU(2)$ Higgs doublet, confronts with theoretical problems when radiative corrections to the Higgs mass are calculated. Higgs self coupling, at one loop, generates quadratically divergent contributions to the mass-squared [27, 28, 29]. Theoretically these mass terms could be canceled by introducing large mass counter-terms. In Quantum ElectroDynamics (QED) ultraviolet divergences, from radiative corrections to photon self–energy, do also exist but are canceled, in the perturbative theory, by a regularization/renormalization procedure. The renormalizability of the QED guarantees a massless photon at every order of perturbation. The quadratic divergences of the Higgs sector in the SM, on the other hand, could not be eliminated in this way. At each order of perturbation one should introduce large mass-counterterms, by hand, in order to renormalize the scalar Higgs boson mass and to keep it at ≤ 1 TeV. By introducing a cutoff Λ in these divergences, of the order of the largest mass scale in the theory, the corrections would be very large (of the order of GUT scale). The Higgs mass in the SM is not bounded from above, and approaches the largest mass scale in the theory. This is known as the Hierarchy problem. There exist bosons with masses at the weak scale and scalar bosons with a mass at the GUT scale, and nothing in between!

Several extensions to the Standard Model try to solve these problems. The most popular of these are the SUperSYmmetric theories [21, 30]. SUperSYmmetry (SUSY) tries to tackle the SM problems by introducing higher symmetry and new fields. It relates masses and couplings of particles with different spins. Each particle in the SM is related to a supersymmetric partner with a spin differing by 1/2. Fermions are related to scalar (spin 0) superpartners, vector bosons and scalar Higgs bosons to (Majorana) fermion (spin 1/2) superpartners. Particles and their superpartners (or sparticles) are combined into *superfields*. Supersymmetric operations change the spin of the particles by 1/2 but leave all other characteristics, i.e. mass and all the other quantum numbers, unchanged. Table 1.2 summarizes the particle content of the SUSY theory. In supersymmetry two complex scalar Higgs doublets are needed to break the electroweak symmetry and to generate masses for gauge bosons and fermions. Spartners of the Higgs bosons are spin 1/2 Higgsinos. Higgsinos mix with the superpartners of the electroweak gauge bosons to produce electrically charged and neutral particles, called *charginos* $\tilde{\chi}^{\pm}_{1,2}$ and *neutralinos* $\tilde{\chi}^{0}_{1,2,3,4}$ respectively. Local supersymmetry requires super partners of both the graviton[§] and the gauge bosons. In a global supersymmetric theory, on the other hand, the gravitino would not be present. In the unbroken SUSY theory, all superpartners have the same masses and couplings as the corresponding SM particles. The lack of any experimental evidence for such a degeneracy, implies that supersymmetry must be broken. In the broken SUSY, the superpartners of the SM particles could be heavy, possibly of the order of 1 TeV, based on *naturalness* or *hierarchy* arguments. The masses of the ordinary particles are generated at the lower weak scales. Couplings are not changed by the symmetry breaking.

A new discrete multiplicative quantum number $R = (-1)^{3(B-L)+2S}$, the R-parity, is assigned to each particle. In this relation, B is the baryon number, L is the lepton number and S is the spin. This means that SM particles have even R-parity, whereas their supersymmetric partners have odd R-parity. The mass of the SUSY partners of the SM particles are unknown and are among the free parameters of the theory.

[§] The spin 2 graviton, the quantum of the gravitational field, has the gravitino superpartner with spin 3/2.

Table 1.2: Particle content of the SUSY model.

Particle	Spin		Sparticle	Spin
quark $q_{L,R}$	1/2		squark $\tilde{q}_{L,R}$	0
lepton $\ell_{L,R}$	1/2		slepton $\tilde{\ell}_{L,R}$	0
photon γ	1	gauginos	photino $\tilde{\gamma}$	1/2
gluon g	1		gluino $\tilde{g}$	1/2
W	1		wino $\tilde{W}$	1/2
Z	1		zino $\tilde{Z}$	1/2
Higgses H	0	Higgsinos	$\tilde{H}$	1/2
Graviton G	2		Gravitino $\tilde{G}$	3/2

In the SUperSYmmetric GUT theories the couplings, as opposed to the SM case, do in fact meet at mass scales of the order of $\mathrm{M}_X \sim 10^{16}$ GeV. The Standard Model does not include the gravitational interactions, and hence could only be valid up to energies of the order of the Planck mass, $\mathrm{M}_{Planck} = 1/\sqrt{G_N} \sim 10^{19}$ GeV with G_N the gravitational constant, where gravitational effects become important. Superstring theories offer the most promising unification of the elementary particles and their interactions, including a quantum mechanical inclusion of gravity. Instead of starting from a point particle in space, in superstring theories, one starts from a one-dimensional string. As a consequence the trajectory of a point in space–time is a world–line, whereas that of a one-dimensional string is a world–sheet. A world–sheet depends on both the usual space–time coordinate and the string parameters defining the location of points along the string. Particles are assigned to vibrational modes of closed strings, i.e. strings with their ends closed to form a loop or a ring. The fundamental scale of string theory is the string tension with the dimension of mass squared.

1.2.1 Minimal Supersymmetric extension of the SM (MSSM)

In the Minimal Supersymmetric extension of the SM (MSSM) and with the assumption of R-parity conservation SUSY particles are always pair produced and (cascade) decay to the SM particles and the lightest SUSY particle (LSP). The LSP must be stable and weakly interacting. The MSSM respects the same gauge symmetries as the standard model, namely that of the $SU(3)_C \times SU(2)_L \times U(1)_Y$ gauge group. The MSSM is assumed to be a theory at the electroweak scale, i.e. an effective low energy theory. The supersymmetry, in this effective theory, is broken by adding *soft* mass terms to the Lagrangian. These terms do not

re-introduce quadratic divergences into the theory, hence the softness. The soft terms are mass terms, bi-linear mixing terms (B terms) and tri-linear scalar mixing terms (A terms). Over 100 free parameters, e.g. masses, exist in this theory.

In the Higgs sector of the MSSM, two complex scalar Higgs doublets [27, 28, 29, 30]:

$$H_1 = \begin{pmatrix} \phi_1^0 \\ \phi_1^- \end{pmatrix} \quad , \qquad H_2 = \begin{pmatrix} \phi_2^+ \\ \phi_2^0 \end{pmatrix},$$

with hypercharges -1 and $+1$ respectively, are introduced. The supersymmetric Higgs potential is given by [28, 29]:

$$V = |\mu|^2 \left(|H_1|^2 + |H_2|^2\right) + \frac{g^2 + g'^2}{8} \left(|H_1|^2 - |H_2|^2\right)^2 + \frac{g^2}{2}|H_1^\dagger \cdot H_2|^2,$$

where μ (< 0) is the Higgs mass parameter. The electroweak and SUSY symmetry breaking is now implemented by introducing the soft SUSY breaking terms. The modified Higgs potential then becomes:

$$\begin{aligned} V = \left(|\mu|^2 + m_1^2\right)|H_1|^2 + \left(|\mu|^2 + m_2^2\right)|H_2|^2 - \mu B \epsilon_{ij} \left(H_1^i \cdot H_2^j + \text{h.}c.\right) \\ + \frac{g^2 + g'^2}{8} \left(|H_1|^2 - |H_2|^2\right)^2 + \frac{g^2}{2}|H_1^* \cdot H_2|^2, \end{aligned}$$

where m_1, m_2 and B are new mass parameters. Apart from the third term, with the factor μB, all other terms in this expression are positive. Hence for $\mu B = 0$ one obtains the trivial vacuum, with zero vev, and no symmetry breaking is generated. To implement properly the electroweak symmetry breaking, the parameters of the Higgs potential should satisfy the relations:

$$\begin{aligned} (\mu B)^2 &> \left(|\mu|^2 + m_1^2\right)\left(|\mu|^2 + m_2^2\right) , \\ |\mu|^2 + \frac{m_1^2 + m_2^2}{2} &> |\mu B| , \end{aligned}$$

which contain the condition to guarantee the stability of the potential at large field values. With a similar prescription as in the SM, the electroweak symmetry breaking is implemented by letting only the neutral components of the Higgs fields to get non-zero vev's:

$$\langle H_1^0 \rangle = \begin{pmatrix} v_1 \\ 0 \end{pmatrix} \equiv v_1 \ , \quad \langle H_2^0 \rangle = \begin{pmatrix} 0 \\ v_2 \end{pmatrix} \equiv v_2 \ ,$$

where v_1 and v_2 are real and positive (like v in SM). The W and Z° gauge bosons acquire the masses:

$$M_W^2 = \frac{1}{2}(v_1^2 + v_2^2)g^2 \quad , \qquad M_Z^2 = \frac{1}{2}(g^2 + g'^2)(v_1^2 + v_2^2) .$$

Before the symmetry breaking the two complex scalar $SU(2)_L$ Higgs doublets had 8 degrees of freedom (i.e. 8 real massless fields). Three degrees of freedom, the so–called Goldstone bosons [11], have been absorbed by the $W^\pm$ and Z° gauge bosons giving them their longitudinal degrees of freedom or equivalently their masses. This leaves 5 physical degrees of freedom. The spectrum of the Higgs sector is then: a charged Higgs boson pair, $H^\pm$, a neutral CP–odd Higgs boson, A, and two neutral CP-even Higgs bosons, h and H, with $m_h < m_H$.

These physical mass eigenstates could not be derived in a straight forward manner, as in the SM case, by simply introducing field excitations about the vev's and identifying them as the physical states. The physical states are mass eigenstates, which are obtained by diagonalizing the corresponding mass matrices. The Higgs sector could now in principle be described by two parameters after using the known W mass to specify $v_1^2 + v_2^2$. These parameters are the mass of the pseudo-scalar Higgs boson, M_A, and the ratio of the two Higgs vev's:

$$tan\,\beta \;\equiv\; \frac{v_2}{v_1}\,, \qquad M_A^2 \;=\; \frac{2\,|\mu B|}{sin\,2\beta}\,,$$

where $v_1, v_2 > 0$ and therefore $0 < \beta < \pi/2$. The couplings of the (neutral) MSSM Higgs bosons to fermions and gauge bosons, at the tree level, differ from that of the SM Higgs scenario with α and β dependent factors. The correction factors of the MSSM neutral Higgs couplings to the massive fermions and gauge bosons, with respect to that of the SM Higgs, are given in Table 1.3. The coupling of the charged MSSM Higgs, $H^{\pm}$, which couples u–type to d–type massive fermions, at the tree level, is given by: $\frac{ig}{2\sqrt{2}m_W}\left[(m_d\,tan\,\beta + m_u\,cot\,\beta) \pm (m_d\,tan\,\beta + m_u\,cot\,\beta)\,\gamma_5\right]$ where u and d stand for (massive) down and up type fermions respectively. The CP–even neutral Higgs mixing angle, α, which enters into many couplings, is at the tree level, in terms of m_A and $tan\,\beta$, given by:

$$tan\,2\alpha = tan\,2\beta\left(\frac{m_A^2 + m_Z^2}{m_A^2 - m_Z^2}\right)\,, \qquad -\,\pi/2 < \alpha < 0\,.$$

Table 1.3: *SM Higgs boson couplings (vertex factors) and the corresponding correction factors, at tree level, of the neutral MSSM Higgs bosons to massive fermions and gauge bosons.*

	SM	MSSM (*correction factors*)		
	H	h	H	A
d–type fermions	$-ig\frac{m_f}{2m_W}$	$-\frac{sin\,\alpha}{cos\,\beta}$	$\frac{cos\,\alpha}{cos\,\beta}$	$-i\gamma_5\,tan\,\beta$
u–type fermions	$-ig\frac{m_f}{2m_W}$	$\frac{cos\,\alpha}{sin\,\beta}$	$\frac{sin\,\alpha}{sin\,\beta}$	$-i\gamma_5\,cot\,\beta$
$W\,W$	$igm_W\,g^{\mu\nu}$	$sin(\beta-\alpha)$	$cos(\beta-\alpha)$	0
$Z\,Z$	$\frac{igm_Z}{cos\,\theta_W}\,g^{\mu\nu}$	$sin(\beta-\alpha)$	$cos(\beta-\alpha)$	0

All masses and couplings in the MSSM Higgs sector, at the tree level, could be completely specified in terms of m_A and $tan\,\beta$ parameters. But with the inclusion of radiative corrections large effects are obtained, which depend on, for instance, top, scalar-top and scalar-quark masses and different mixing parameters. As an example, the upper bound on the mass of the lightest Higgs boson[¶] h gets corrections like $m_t^4\,log(m_{\tilde{t}}/m_t)$, where m_t ($m_{\tilde{t}}$) is the mass of the top (scalar–top) quark mass. An interesting feature is that, regardless of the inclusion of radiative corrections, for a very heavy A, i.e. $M_A \gg M_Z$ or $M_A \to \infty$, the mass of $H^{\pm}$, A and H become large and degenerate, and only the lightest neutral CP–even Higgs, h, has a mass

[¶]At the tree level the upper bound on the lightest Higgs boson mass is given by: $m_h^2 \leq cos\,2\beta\,M_Z^2 \leq M_Z^2$.

(of the order of the weak scale). In this limit $\alpha \to \beta - \pi/2$, which implies a decoupouling of the heavy Higgses, e.g. from gauge bosons. Whereas the h couplings become the same as that of a SM Higgs. Another interesting feature is that, due to radiative corrections, the mass of the lightest neutral CP–even Higgs boson, m_h, could be significantly larger than m_Z. At one–loop level m_h depends on the stop mixing parameter $X_t = A_t + \mu\, cot\beta$ in such a way that the upper limit of m_h shows a maximum at a nonzero value of X_t. This point is referred to as *maximal mixing*. At $X_t = 0$, on the other hand, the upper limit on m_h goes through a minimum. Hence the $X_t = 0$ point is referred to as the *minimal mixing*. An interesting point is that, regardless of the inclusion of radiative corrections to the masses, for a given set of parameter values, as $tan\,\beta$ and squark masses, the is always an upper bound on the lightest Higgs boson mass, m_h. The upper bound for large $tan\,\beta$ (> 10) and/or for heavy A ($M_A > 300$ GeV) saturates at values in the weak scale range ($m_h < 130$).

Incorporating SUSY models into GUT theories, the so-called SUSY GUTs, has resulted in interesting observations. Assuming a mass of the order of 1 TeV for the SUSY particles and running the couplings from their values at the weak scale to higher scales, it is observed that the couplings do actually meet at an enrgy scale of the order of 10^{16} GeV, which is compatible with the energy scale M_X in GUT theories. Therefore this is assumed that the couplings are unified at the high energy scale $M_X \sim 10^{16}$ GeV into a single coupling[‖] g_X. In the so–called super–gravity inspired MSSM one assumes also gaugino mass unification at the M_X scale, referred to as the common gaugino mass, $m_{1/2}$. A further assumption is likewise a common scalar mass, m_0, at the unification scale, M_X. And finally one assumes a common soft supersymmetry breaking trilinear couplings, i.e. $A_{t,b,...}$ parameters, denoted by A_0. These *ad hoc* assumptions make it possible to describe the SUSY model at the GUT scale, completely, by only 5 parameters:

$$m_0\ ,\quad m_{1/2}\ ,\quad A_0\ ,\quad tan\beta\ ,\quad sign(\mu),$$

where the last parameter is the sign of the Higgs mass parameter ($\mu \neq 0$). The corresponding quantities at the weak scale can then be calculated by evolving from M_X back to the weak scale.

[‖] Actually the normalization reads: $\sqrt{5/3}\, g(M_X) = g'(M_X) = g_s(M_X) = g_X$.

1.3 Proton-proton interactions

According to the parton model a proton may be considered as a cluster of confined partons (i.e. quarks, anti-quarks and gluons) [2, 7, 32]. Each virtual parton carries a fraction x of the longitudinal momentum of the proton[**]. To first approximation, in collider experiments, any intrinsic transverse momentum of the constituent partons could be neglected, assumed small compared to high beam energies. Hence proton-proton interactions in the parton model are described in terms of interactions between their constituent partons. At very small p-p impact parameters a large momentum–squared, Q^2, may be transferred between the interacting partons. This is referred to as the hard (i.e. high Q^2) process. But a large fraction of the p-p interaction cross-section is due to soft (i.e. low Q^2), non-perturbative subprocesses among their constituent partons. These soft processes can not be calculated from first principles, i.e. using QCD perturbation theory. They are for instance described by the exchange of *Regge trajectories* [22] containing $\pi^{\pm,0}$, $\rho^{\pm,0}$, etc., which involve quark-pair exchanges, and by *Pomeron* [23] exchanges composed of gluons (or something similar). The disturbed protons fragment into multi-particle final states. These soft interaction events are referred to collectively as minimum bias[††] events. Occasionally, depending on the kinematics, the underlying partons undergo hard scattering (i.e. high Q^2), which is predictable in the framework of perturbative QCD. At small distances, or equivalently at high momentum transfers, the strong coupling constant, $\alpha_s(Q^2)$, due to the principle of asymptotic freedom, becomes small for the perturbative QCD methods to be applicable on hard subprocesses. The cross section for the overall process could then in principle be calculated by summing over the cross sections of the underlying partonic subprocesses.

1.3.1 The parton distribution functions

The mere fact that the strong coupling $\alpha_s(Q^2)$ becomes large at low Q^2 and that the perturbative QCD is only applicable at small enough $\alpha_s(Q^2)$ (i.e. at large enough Q^2) makes it impossible to calculate parton distributions from first principles. It is, however, possible to predict the distributions at a higher Q^2 once they are given at a different smaller Q_0^2. The latter should then be extracted from experimental data. The distribution of partons in the proton has been obtained from lepton-proton and/or lepton-antiproton deep inelastic scattering experiments. The parton distribution functions for proton are normally parametrised as:

$$x \cdot f(x) = C \cdot x^{\alpha} \cdot (1 - x^{\beta})^{\gamma}, \tag{1.3}$$

where α, β and γ are positive parameters and C is a flavour specific normalisation constant, x is the (longitudinal) momentum fraction of the proton carried by the parton[‡‡]. The function

[**]Strictly speaking this is only valid in a frame where the proton's mass and transverse momentum could be neglected. This is called the infinite-momentum frame. At high energy p-p colliders the laboratory frame is to a good approximation identical to the infinite-momentum frame.

[††]The notion *minimum bias* has an experimental justification, originating from the fact that any trigger selection introduces bias to the experimental results: the trigger bias. No particular selection criteria need to be applied in order to trigger on (or select) the soft (p-p) events. Consequently a trigger *bias* which is *minimum* would be introduced. Hence the name minimum bias events.

[‡‡]More precisely x is the fraction of the proton's four-momentum carried by the parton, assuming no transverse three-momentum neither for the parton nor for the proton.

$f(x)$ is a density distribution, hence $f(x)dx$ gives the number of partons between x and $x + dx$. Since x is the (longitudinal) momentum fraction carried by the parton, $xf(x)dx$ is the momentum distribution of partons between x and $x+dx$. A schematic view of the parton distribution functions for gluons, valence quarks and sea quarks-antiquarks within the proton at a fixed Q^2 based on these parametrisations is shown on figure 1.1. At small x, for a fixed Q^2, the valence quark density behaves as $\sqrt{x}$, whereas that of sea quarks and antiquarks as $1/x$.

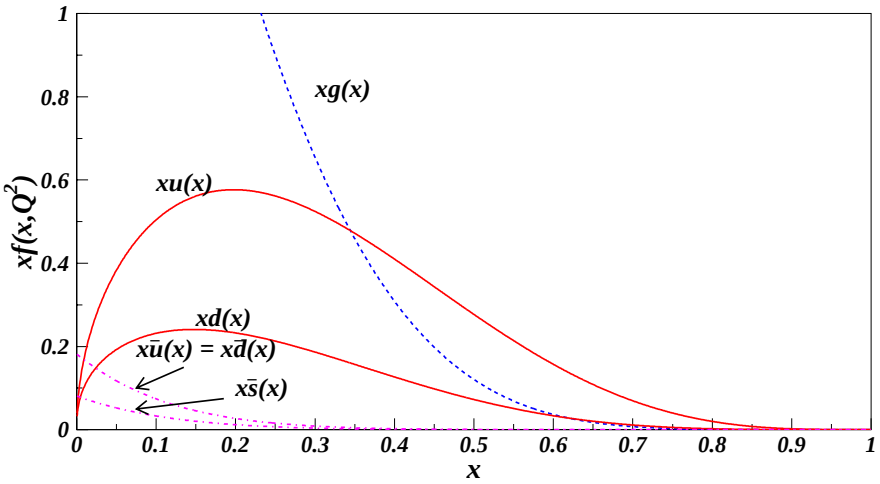

Figure 1.1: *Gluon, valence (sea) quark (quark-antiquark) parton distribution functions for the proton. Eichten et al. (EHLQ) parametrisations.*

Each parton can in principle radiate other partons via the so called splitting processes [26] depicted in figure 1.2. A quark, on account of these QCD splitting vertices, is itself surrounded

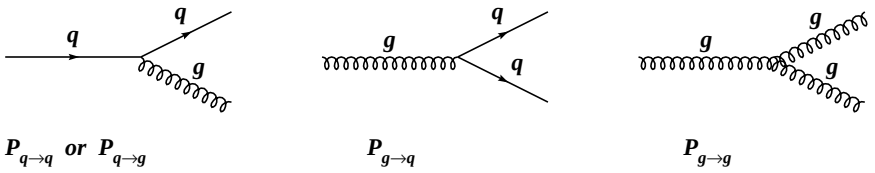

Figure 1.2: *Parton splitting diagrams. The corresponding probability functions represented by each diagram is also given beneath each process.*

by a cloud of gluons and a sea of quark-antiquark pairs. As a consequence the number of gluons, sea quark and antiquarks sharing the protons momentum increases with increasing Q^2. This in turn would mean a higher (lower) probability to find quarks with a small (large) x. A sketch of this Q^2 evolution of the quark distribution function is shown on figure 1.3.

The existence of gluons and sea quark-antiquark pairs within a proton is due to radiative processes. For this reason their number (at a fixed Q^2) increases (logarithmically) with decreasing x. An empirical observation is that quarks account approximately for only half of the momentum carried by a proton. The rest is then associated to gluons.

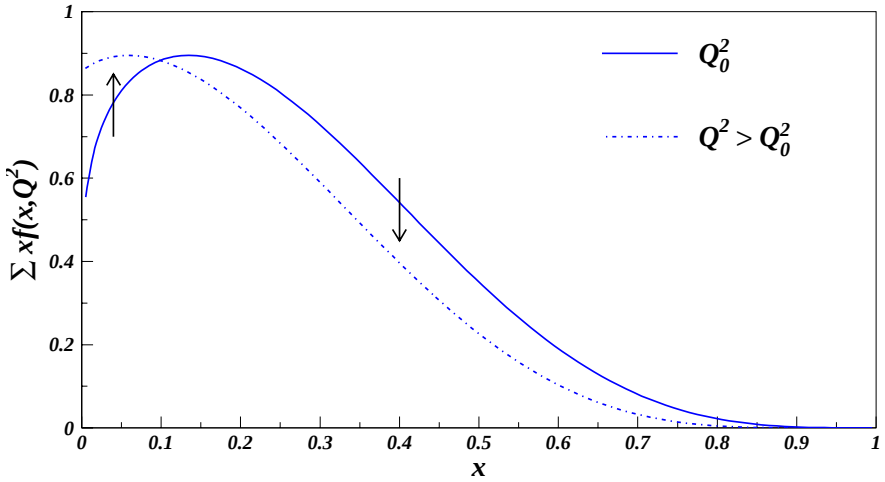

Figure 1.3: *Qualitative evolution of quark distribution in a proton. Plotted are snapshots of the distribution function at two different momentum transfer squared, i.e.* $Q^2 > Q_0^2$. *Sea* $q - \bar{q}$ *pairs contribute at very low* x *values, which increases with increasing* Q^2. *The arrows indicate the change in the shape of the distribution with increasing* Q^2 *of the hard scattering.*

1.3.2 The hard scattering subprocess

At high enough centre of mass energies, in a p-p collider, the constituent partons of the protons could scatter on each other with a small impact parameter. In such high energetic partonic interactions the outgoing partons will come out at a large angles to the beam axis. Given the high momentums involved in these scatterings, a large scattering angle, in turn, would mean a large transverse momentum of the scattered partons. The higher the centre of mass energy of the p-p system (and therefore of the partonic sub-system) the higher the probability of such so-called high $\boldsymbol{p}_T$ processes. In this respect proton-proton interactions could be subdivided in (two partially overlapping) low and high transverse momentum domains, referred to as soft and hard interaction regions respectively. In the parton model the hard scattering subprocess in a proton-proton collision can be described schematically as shown on figure 1.4. The kinematics of the hard partonic subprocess together with it's relation to the original p-p scattering is also shown on this figure.

The four-momenta of the beams are given by: $P_A = (E, \mathbf{P}), \quad P_B = (E, -\mathbf{P})$, where E is the beam energy, and the three-momentum $\mathbf{P} \| \hat{z}$. The probability of finding parton i carrying a (longitudinal) momentum fraction x_i in proton I is described by $f_I^i(x_i)$, where $(i, I) = (a, A), (b, B)$. The four-momenta of the partonic sub-system are given by: $\hat{p}_i = x_i P_I$. Specialising to the case of the p-p colliders, i.e. beams with equal energies and equal but oppositely directed momenta, the invariant centre of mass energy squared of the p-p system s and that of the hard scattering sub-system $\hat{s}$ is then calculated as (see figure 1.4):

$$s = (P_A + P_B)^2 = (2E, \mathbf{0})^2 = 4E^2, \tag{1.4}$$

$$\begin{aligned} \hat{s} &= (\hat{p}_a + \hat{p}_b)^2 = (x_a P_A + x_b P_b)^2 \\ &\sim 4 x_a x_b E^2 = x_a x_b s \equiv \tau s\,, \quad (\textit{neglecting all masses}) \end{aligned} \tag{1.5}$$

where $\hat{s} = x_a x_b s \equiv \tau s$ is the invariant mass of the parton sub-system. In general $x_a \neq x_b$.

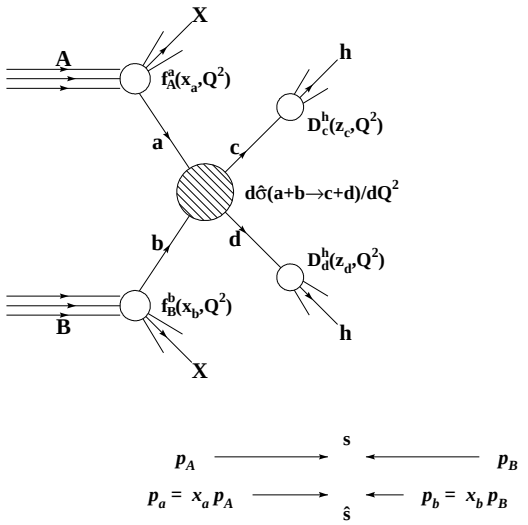

Figure 1.4: *kinematics of the partonic subprocess, and it's relation to that of the proton-proton system.*

Therefore the laboratory frame, while being the centre of mass frame for the original p-p collision, is not so for the partonic subprocess. Hence the partonic subsystem would in general have a boost in the longitudinal direction (relative to the beam axis). The amount of this longitudinal boost is given by the Feynman x, where $x = x_a - x_b$.

Since incident partons taking part in the hard scattering carry, on average, only a given small fraction of the four-momentum, the total c.m. energy is scaled down by a corresponding factor in going from proton to parton system. The total energy available for particle production at rest, in the hard scattering sub-process, would be the total energy in the centre of momentum frame of the partonic sub-system. Considering the case $x = x_a \sim x_b$, for simplicity, a particle created at rest in the laboratory frame of reference, will have a mass $m \sim 2\,x\sqrt{s} = 2\,xE \rightarrow x \sim m/2E$ (see equations 1.4 and 1.5).

The cross section for the hard process can be expressed in terms of the partonic subprocesses as:

$$\sigma_{(A+B\rightarrow X)} \sim \sum_{a,b} \int f_p^a(x_a, Q^2) dx_a f_p^b(x_b, Q^2) dx_b \times \hat{\sigma}_{(a+b\rightarrow c+d)}\,,$$

where $\hat{\sigma}$ is the cross–section of the underlying (hard) parton–parton interaction and X represents any kinematically allowed final state. In the high energies involved in the hard scatterings, the running coupling costant $\alpha_s(Q^2)$ is small, and the cross section of the hard process can be calculated perturbatively in expansion series of $\alpha_s(Q^2)$. Introducing $\hat{s} = x_a x_b s = \tau s$ and keeping x_a and τ then:

$$\frac{d\sigma}{d\tau} = \sum_{a,b} \int \frac{d\mathcal{L}_{ab}}{d\tau} \hat{\sigma}(\hat{s} = \tau s)\,,$$

with:

$$\frac{d\mathcal{L}_{ab}}{d\tau} = C_{ab} \sum_{a,b} \int_\tau^1 \frac{dx_a}{x_a} f_p^a(x_a, Q^2) f_p^b(x_b, Q^2) \times \hat{\sigma}(\hat{s} = \tau s)\,,$$

where C_{ab} is constant factor. $d\mathcal{L}_{ab}/d\tau$ is called *parton luminosity*, since $\hat{\sigma} \cdot d\mathcal{L}_{ab}/d\tau$ gives the particle cross section $d\sigma/d\tau$ in proton collisions.

1.3.3 The fragmentation

Quarks, antiquarks and gluons, being coloured, are bound in colourless hadrons, a consequence of the principle of QCD (colour) confinement. After the scattering, however, the colour force will confine the partons into colourless hadrons. This process, referred to as the hadronisation or the fragmentation, involves typically the creation of additional quark-antiquark pairs, e.g. in the colour field between a scattered quark and the spectator partons. A scattered parton (with a high p_T) manifests itself in a detector environment as a debris of (hadronic) fragments called jet.

The hadronisation involves soft processes which are not calculable by the methods of perturbative QCD. Therefore one should resort to parametrisations extracted from, and tuned to, experimental data. The fragmentation of light quarks is usually parametrised as:

$$z \cdot D(z) = C \cdot (1 - z)^{\alpha}, \tag{1.6}$$

where α is a constant, z is the fraction of the parton's momentum carried by the fragmented hadron and C is a normalisation factor. The function $D(z)$, usually denoted as D_a^h, is the so-called fragmentation function and gives the probability of finding hadron h with a momentum fraction z among the fragments of parton a.

Heavy quark fragmentation is parametrised as:

$$z \cdot D_Q^H(z) = C \cdot \left[1 - \frac{1}{z} - \frac{\epsilon_Q}{1 - z}\right], \tag{1.7}$$

where Q denotes a heavy quark, i.e. c, b or t, and H denotes a heavy hadron fragment of Q ($H(Q\bar{q})$ for instance). The parameter $\epsilon_Q = 0.40\ \mathrm{GeV}^2/m_Q^2$, with $m_c \sim 1.5$ GeV and $m_b \sim 5$ GeV. The top quark with a mass $m_t \sim 175$ GeV, is very short lived and decays before having time to hadronise. The normalisation constant is obtained by requiring $\int D(z) \cdot dz = 1$.

It is obvious from the so–called Peterson fragmentation formula, i.e. equation 1.7, that the heavier the quark the harder is the momentum distribution of its fragments. Kinematically heavy decay products carry a large fraction of the momentum of the decaying particle. Being coloured quarks will loose some fraction of their momentum to the surrounding colour field to materialise (mostly light) quark-antiquark pairs. In this process the heaviness of the quark plays also an important role. The heavier the quark the smaller the fraction of the momentum loss. If then the heavy quark combines with one or more of the (in general lighter) quarks and/or antiquarks, a heavy hadron (e.g. $H(Q\bar{q})$) would be produced. This heavy hadron will then carry most of the heavy quark's momentum. The result, as mentioned above, would be a hard momentum distribution of the hadrons within the debris of a heavy quark. This empirically confirmed behaviour is well described by the Peterson parametrisations.

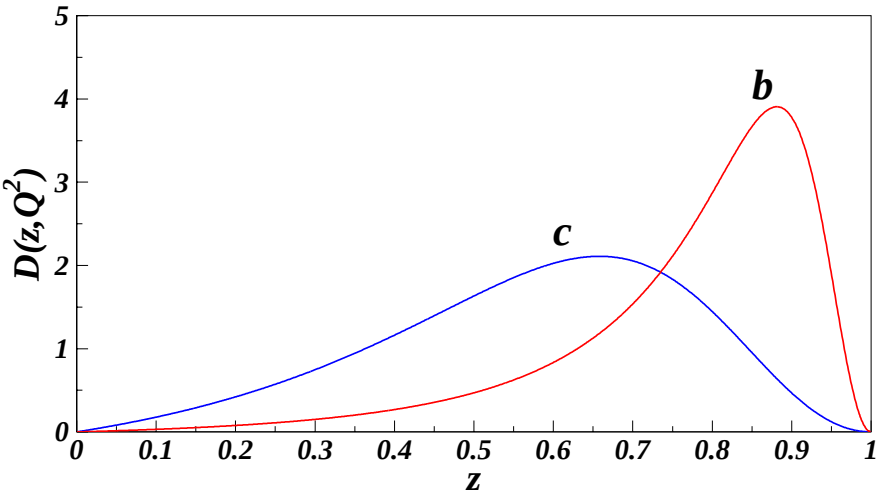

Figure 1.5: *Peterson parametrisation for the fragmentation of heavy quark $Q = c$ or b.*

1.3.4 Kinematics

The momentum vector of an outgoing jet (or particle), in the p-p frame, makes an angle θ with respect to the beam (z) axis. Hence the transverse and longitudinal momenta are given by:

$$p_z \equiv p_{||} = |\boldsymbol{p}| \cdot cos(\theta) \ , \quad p_T \equiv p_\perp = |\boldsymbol{p}| \cdot sin(\theta) \, .$$

It is customary, in collider experiments, to introduce *rapidity*, y, defined by:

$$y = -\frac{1}{2} \ell n \left(\frac{E + p_{||}}{E - p_{||}} \right) \, .$$

For massless particles, or at (relativistically) high momenta, of interest at the LHC for instance, one has in general the *pseudo-rapidity*, η, defined as:

$$y \Big|_{\frac{m}{p} \to 0} \longrightarrow -\ell n \left(tan \left(\frac{\theta}{2} \right) \right) \equiv \eta \, .$$

The *pseudo-rapidity*, η, is much easier to measure, as it does not require particle identification, and is what is normally used experimentally.

Chapter 2

Experimental facilities

Particle physicists believe that many of the fundamental questions left unanswered or even raised by high energy experiments so far could probably be answered at still higher energies. The new accelerator facility, CERN's next big machine, due to start operating in 2005, and it's related experiments are being designed to answer these questions and to look for theoretically predicted phenomena. However, they must also be prepared, as far as possible, for unforeseen phenomena. This task is a great challenge and requires great effort on the part of the physicists and engineers.

2.1 The Large Hadron Collider

The **L**arge **H**adron **C**ollider, **LHC** [33], is planned to be switched on in the year 2005. The collider ring is being installed in the existing **L**arge **E**lectron **P**ositron, **LEP**, collider tunnel at **CERN**[*]. A consequence of this cost-effective strategy is that the LHC layout is defined, and to some extent constrained, by the geometry of the LEP ring. The LEP tunnel is about 27 km round and is buried 100 meters below the ground.

The LHC will collide both protons (p-p) and heavy nuclei/ions (Pb-Pb) with a beam energy of 7.0 TeV per unit charge. This would mean a center-of-mass energy of 14 TeV for the p-p and of 1148 TeV for the Pb-Pb collisions[†]. The required beams would be produced in the **CERN**'s existing particle sources and pre-accelerators (Linac/Booster/PS/SPS). A schematic view of the CERN accelerator complex is shown in Figure 2.1, where the LEP/LHC ring is also shown.

The LHC machine will be built with a two-ring system with parallel rings, one ring per beam, with a two-in-one magnet structure operating in super-fluid helium (requiring complex cryogenic systems). A very advanced super-conducting magnet system and complex accelerator technologies have been employed. A cross-sectional view of the LHC dipole is shown in Figure 2.2. The two-in-one magnet structure and the beam pipes, surrounded by super-conducting coils, could be seen in this figure.

[*] European Organization for Nuclear Research, Geneva/Switzerland

[†] Our major interest here is the p-p operating mode and in the following everything refers to this option.

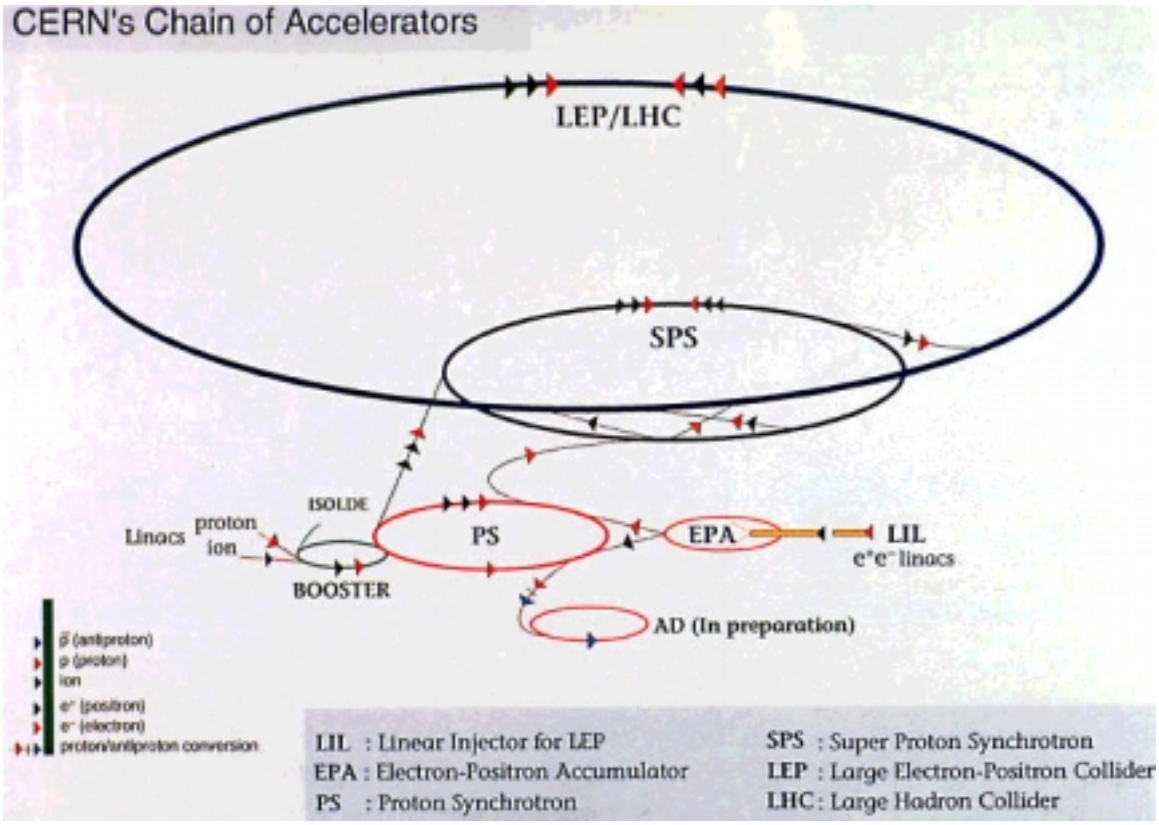

Figure 2.1: *The CERN accelerator complex (Linac/Booster/PS/SPS/LEP/LHC).*

The design luminosity at the LHC will have a peak value of 10^{34} $cm^{-2}s^{-1}$. The first three years of it's operation though, the LHC will run with a somewhat lower luminosity with a peak value of 10^{33} $cm^{-2}s^{-1}$. This will correspond to an accumulated luminosity of about 10 fb^{-1} (30 fb^{-1}) and 100 fb^{-1} (300 fb^{-1}) after one year (three years) operation at low and high luminosities respectively. Officially, after 5–7 years of operation an integrated luminosity of at least300 fb^{-1} should be collected. The very high luminosities are achieved by using two counter-rotating beams made up of closely spaced bunches. In the p-p operating mode the proton beams are comprised of 2835 bunches of 10^{11} protons each. The bunches have a longitudinal spread (rms) of about 7.7 cm and are spaced 7.5 m apart corresponding to 25 ns bunch separation. This corresponds to a bunch crossing rate of 40 MHz. A tabular representation of the main machine performance parameters in the p-p operating mode can be found in Table 2.1.

A simplified schematic view of the LHC layout is displayed in Figure 2.3. The two beams cross only in four intersections. The two general purpose experiments, i.e. **ATLAS** [35] and **CMS** [36], are located at the two diametrically-opposite high-luminosity insertions of the machine. Two other experimental utilities, i.e. **ALICE** [38] and **LHCb** [37], are located at two other insertion points as depicted in Figure 2.3. The beams cross from one ring to the other only at these four intersections, where the experimental utilities are installed.

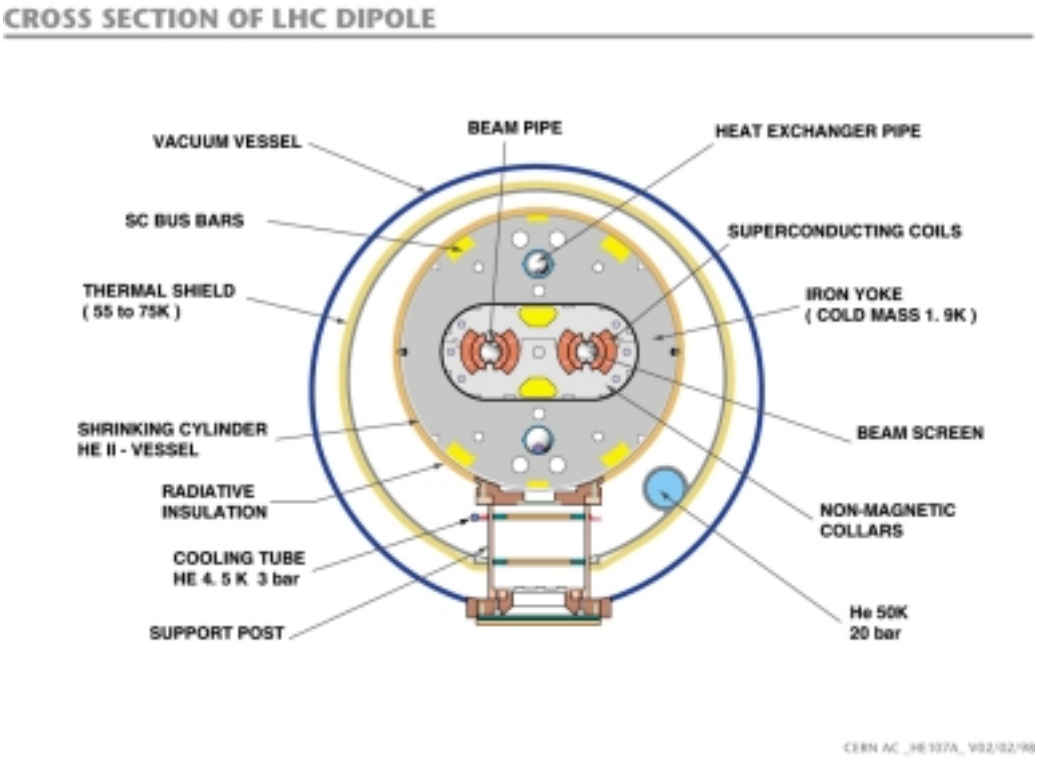

Figure 2.2: *The cross-section of the LHC guide dipoles, illustrating the two-in-one structure of their superconducting magnets.*

Table 2.1: *Some of the main LHC p-p performance parameters.*

Parameter	Value
Ring circumference	26.66 km
Dipole field	8.386 T
Proton (center-of-mass) energy	7.0 (14.0) TeV
Protons per bunch, design (initial)	1.05×10^{11} (0.17×10^{11})
Total number of bunches	3564
Number of filled bunches	2835
Bunch spacing (separation)	7.48 m (24.95 ns)
r.m.s x,y beam size	15.9 μm
r.m.s bunch length	7.7 cm (0.257 ns)
Design (initial) luminosity	10^{34} (10^{33}) $cm^{-2}s^{-1}$

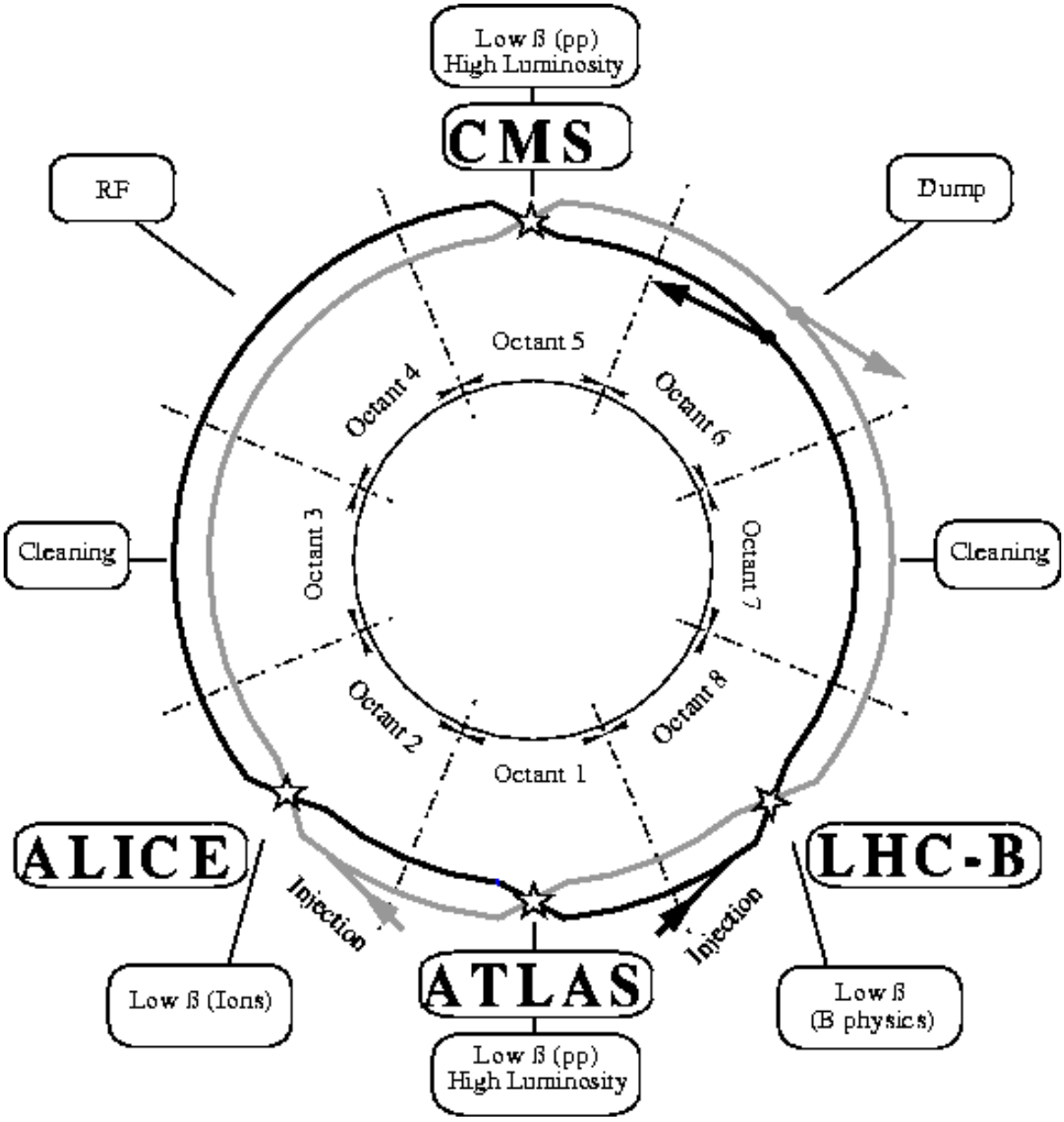

Figure 2.3: *Schematic view of the basic layout of the LHC.*

2.1.1 Physics goals

The physics motivation for LHC experiments is to search for the theoretically predicted Higgs particle (or particles!), essential for the mass generation and $SU(2)\times U(1)$ symmetry breaking mechanisms within the framework of the Standard Model (SM). Incidentally, alternative schemes for symmetry breaking and mass generating mechanisms should also be investigated if the Higgs boson(s) is not detected. In addition searches for new physics beyond the SM such as supersymmetry, and performing studies and measurements on predicted (and possibly unexpected) physics phenomena are also among the main topics of the program.

The combined results of direct and indirect searches for a SM Higgs boson at the four experiments at LEP, (ALEPH, L3, DELPHI and OPAL), is illustrated in Figure 2.4. Direct searches at LEP allow the exclusion of a SM Higgs with a mass below 113.7 GeV at 95% confidence level [49]. This is indicated in the figure by the grey region on the left. Direct searches are essentially based on the so-called Higgs-strahlung process by the Z° boson, with the Z° boson decaying into lepton or neutrino pairs and the Higgs boson decaying into a $\ell^+\ell^-$ or mainly into a $b\bar{b}$ pair. The result of the indirect searches at LEP [48, 49] are based on precision measurements of the minimal SM electroweak parameters as well as the strong coupling constant at the weak scale. A χ^2 fit of the theoretical models, including radiative corrections, to the data, with the Higgs mass as a free parameter, predicts at 95% confidence level a mass for the Higgs particle below approximately 165 GeV. The results of the global fit to electroweak data depend on the central value of the parameters involved. The running of the fine structure constant, α, due to quark loop contributions, has a significant effect on the fit results. This is also shown in this figure.

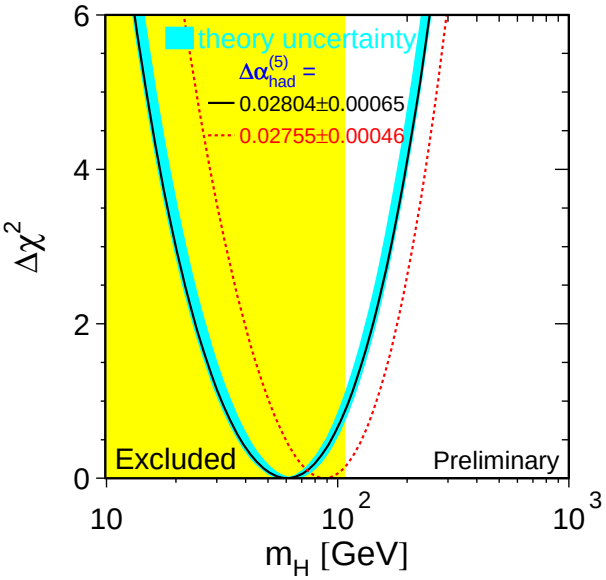

Figure 2.4: $\Delta\chi^2$ *distribution of the SM fit results, for indirect Higgs searches at LEP, as a function of the Higgs mass. The solid line, and the gray band about it, show the official fit results and the corresponding uncertainty. The dotted line illustrates the sensitivity of the predicted Higgs mass on the running of the fine structure (constant) due to hadronic loops.*

In the Minimal Supersymmetric extension of the Standard Model the obtained lower limit on the mass of a light neutral Higgs boson is about[‡] 88 GeV [48]. The Higgs boson, if it exists, would have a mass theoretically bounded at about 1 TeV. The LHC will explore the entire mass range up to this theoretical upper limit.

In the *p-p* collision operation mode, the LHC experimental program will be explored by the two major detectors ATLAS [35] and CMS [36]. These general p-p experiments are designed to cover the physics issues of interest in LHC in complementary approaches, i.e. with overlapping physics program but with essentially different sensitivity to different final

[‡]All the stated limits are 95% confidence level bounds.

state signatures and topologies. They should investigate the question of compositeness of the fundamental particles (i.e. quarks and leptons), the existence of further families (heavy leptons, L, and heavy quarks, Q), heavy gauge bosons (W', Z'), leptoquarks ($D \rightarrow l\,q$) and to some extent the CP-violation in the B-sector. Most important of all though they should detect the Higgs boson(s) if they exist, and supersymmetric partners of particles. In addition, the quite abundant B hadron production at the LHC will be explored with the LHCb [37] dedicated experiment.

SUSY searches are one of the essential programs of the LHC experiments. The assumption is usually made that the R-parity is a conserved quantum number, implying that SUSY particles are produced in pairs and that the Lightest SUSY particle, the LSP, is stable (and doubly produced). Quite complicated final states with many leptons and/or jets and a large transverse momentum imbalance in form of $\mathrm{E}_{\mathrm{T}}^{miss}$ signal are, in this case possible, through cascade decay of the SUSY particles into two LSP's and SM particles. As an example the production cross-section of the squarks and gluinos are quite large, which decay into neutralinos and charginos plus SM particles. Depending on their masses, relative to each other, the production cross-section of the one or the other dominates. Because of the much smaller parameter space of the (minimal) SUGRA models specific points have been investigated for LHC SUSY discovery potential in detail. Apart from this models relaxing the conservation of the R-parity are also being investigated for the discovery potential of the LHC.

The heavy ion program of the LHC, i.e. the Pb-Pb operation mode, will explore the quark-gluon matter with a dedicated experiment, ALICE [38], to investigate different stages of quark-gluon plasma production and the formation of the normal hadronic matter, the so-called phase transition.

2.2 The ATLAS Experiment

The omni purpose p-p experiment **ATLAS**, **A** **T**oroidal **L**HC **A**pparatu**S**, will start exploiting the full discovery potential of the LHC from the startup of the machine. A major focus in the design and optimization of the ATLAS detector has been put on the discovery potential of the mass generating Higgs boson(s). In addition, many expected physics processes and also a large variety of physics phenomena beyond the Standard Model, like SUperSYmmetry searches, have played an important role in the detector optimization. The primary goal is a detector with the ability to cope with a broad range of important physics processes. This is a great challenge considering the high interaction rate at the LHC conditions. Given the total inelastic non-diffractive proton-proton cross-section of about 70 mb and the high design luminosity at the LHC ($\mathcal{L} \sim 10^{34}\ cm^{-2}s^{-1} \equiv 10^{7}\ mb^{-1}s^{-1}$) an interaction rate of about $10^{9}\ Hz$ is expected. Many cross-sections of interesting physics processes at the LHC are many orders of magnitudes smaller. The proton-proton cross-sections and their corresponding rates at the standard high luminosity are shown in Figure 2.5.

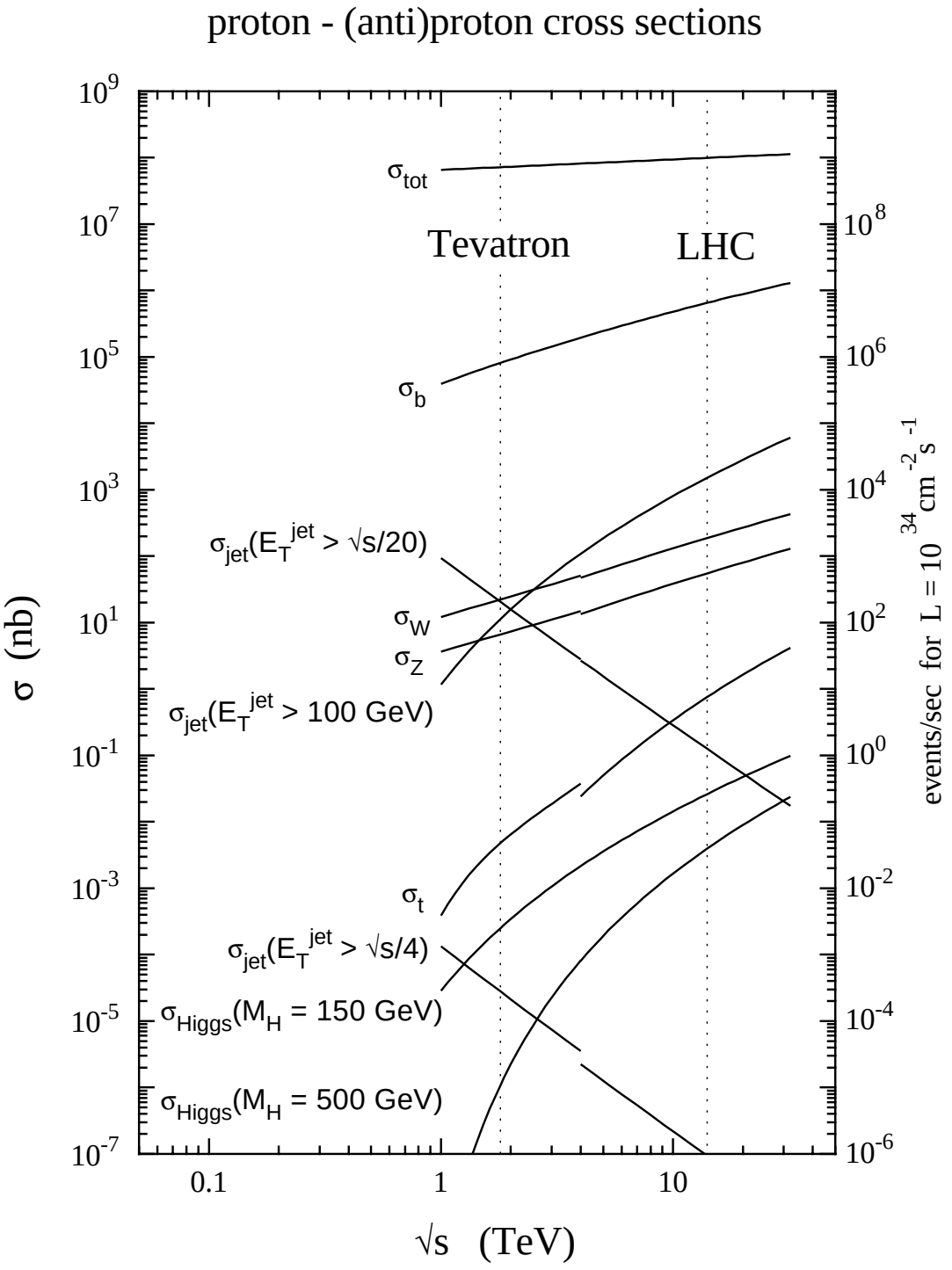

Figure 2.5: *Some characteristic proton-proton cross-sections and their corresponding rates in the high luminosity environment of the LHC. Taken from [39].*

2.2.1 General detector description and basic design issues

A general purpose detector should be able to access the complex final state topologies expected in the LHC environment. It should be capable of providing many signatures using electron, photon, muon, jet and missing transverse energy (E_T^{miss}) measurements. Searches for the Standard Model Higgs has been used as the primary benchmark for the detector optimization. Searches for particles of the Minimal Supersymmetric extension of the Standard Model (MSSM) have played the role of a secondary benchmark resulting for instance in final state signatures like E_T^{miss} from the undetected lightest stable SUSY particle (LSP). Based on such studies some basic design principles and requirements for the ATLAS detector goes as follows: a very good electromagnetic calorimetry in terms of energy/angular resolution and efficient particle ($e/\gamma/\pi^\circ$) identification capabilities; hermetic calorimetry for jet and missing E_T measurements; efficient tracking and lepton momentum measurements; efficient τ and heavy flavour tagging and vertexing capabilities; precision measurements for muons; measurements of particles at low momenta; large acceptance in η coverage. See [34, 35, 39].

The detector and the associated (read-out) electronics have to be fast and radiation resistant due to the huge neutron and charged particle fluxes in proton-proton interactions over several (at least 10) years operation at high luminosity especially in forward regions.

The ATLAS detector is segmented in a barrel and two endcap regions with $\sim 42\ m$ total lenght and with $\sim 22\ m$ total height. The overall weight of the ATLAS detector is about 7000 *tons*. The detector is composed of three main components: the inner detector, the calorimetry and the muon spectrometer. A three dimensional view of the overall layout of the ATLAS detector is shown in Figure 2.6. In the following a short description of different sub-detectors will be given. A complete and detailed discussion of these and the related issues can be found in [35, 40, 41, 42, 44, 45].

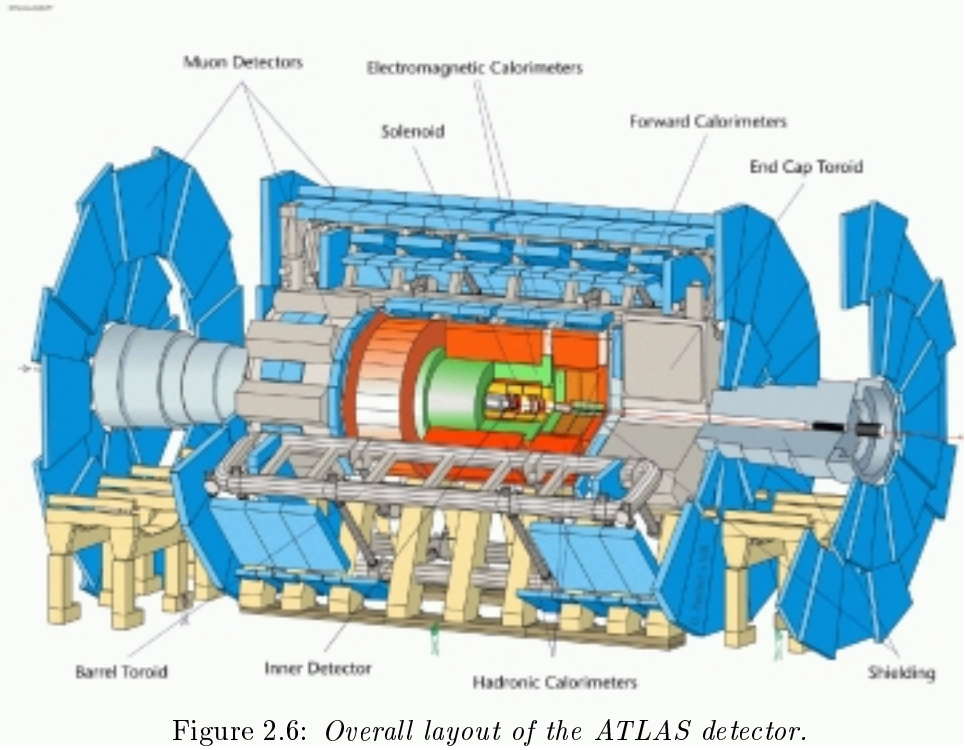

Figure 2.6: *Overall layout of the ATLAS detector.*

2.2.1.1 Magnet system

The magnet system of ATLAS is a 2 T super-conducting solenoid surrounding the inner detector in front of the barrel electromagnetic calorimeter and a super conducting air-core toroid in the barrel and in the end-cap regions. The solenoid is installed in the same cryostat as the barrel calorimeter, whereas the toroid magnets reside in their own cryostat with their own cryogenic system. The air-core toroid system, with a long barrel and two inserted end-cap magnets, generates a large field volume and strong bending power with a light and open structure [35].

2.2.1.2 Inner Detector

Reconstruction of tracks and (secondary) vertices are the tasks of the inner detector [40]. Given the very large track density expected at LHC, high precision measurements on momentum and vertex resolution require fine-granularity detectors. The Inner Detector, ID, is contained within a cylinder parallel to the beam axis, centered at the interaction point. It covers the range $|\eta| < 2.5$, in accord with the other precision measurement systems in ATLAS. The outer radius of the tracker cavity, constrained by the barrel calorimeter cryostat, is 115 cm. The ID is mechanically divided in a barrel and two identical forward units. A transition from barrel, layer geometry (parallel to the beam axis) to forward (also called end-cap), disk geometry (perpendicular to the beam axis), is made starting at $|\eta| < 1$ in order to minimize the amount of material traversed by particles.

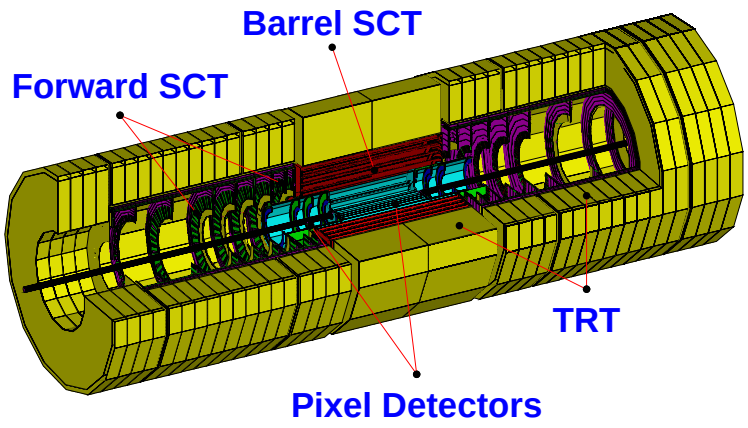

Figure 2.7: *A 3D cut-away view of the ATLAS Inner Detector.*

The ID combines high-resolution detectors at inner radii followed by continuous tracking elements at outer radii. The high precision tracking detector layers are in the barrel arranged on concentric cylinders around the beam axis, and in the forward directions mounted on disks perpendicular to the beam axis. In the vicinity of the beam pipe (from 4 to 22 cm in radius) high precision, silicon substrate, **Pixel detectors** are used to achieve highest granularity (3 space points per track). The innermost silicon layer of the pixel detector located at about 4 cm from the Interaction Point (IP), known as the B-layer, improves secondary vertex measurements considerably, and is designed to be replaceable. Moving radially outward, up to a radius of 56 cm, are Si-strip detectors, the **Semi-Conductor Tracker (SCT)**,

which provide 4 space points per track. Enclosing these is a straw tube **Transition Radiation Tracker (TRT)** to improve momentum reconstruction, pattern recognition and electron identification (36 points per track). The electron identification capability is added by employing Xe gas to detect transition radiation photons created in a radiator between the straws. The electronic channels of the TRT provide a drift-time measurement and two independent thresholds. The detector can discriminate between tracking hits, passing the lower threshold, and transition-radiation hits, passing the higher.

2.2.1.3 Calorimeters

Calorimeters will play an important role in detectors at the LHC. The ATLAS calorimetry is required to measure the energy and direction of electrons, photons, jets and isolated hadron (hadronic τ decays), as well as missing and total transverse energies. It covers the range $|\eta| < 4.9$ using different techniques best suited to the requirements. A three dimensional view of the ATLAS calorimetry is shown in Figure 2.8.

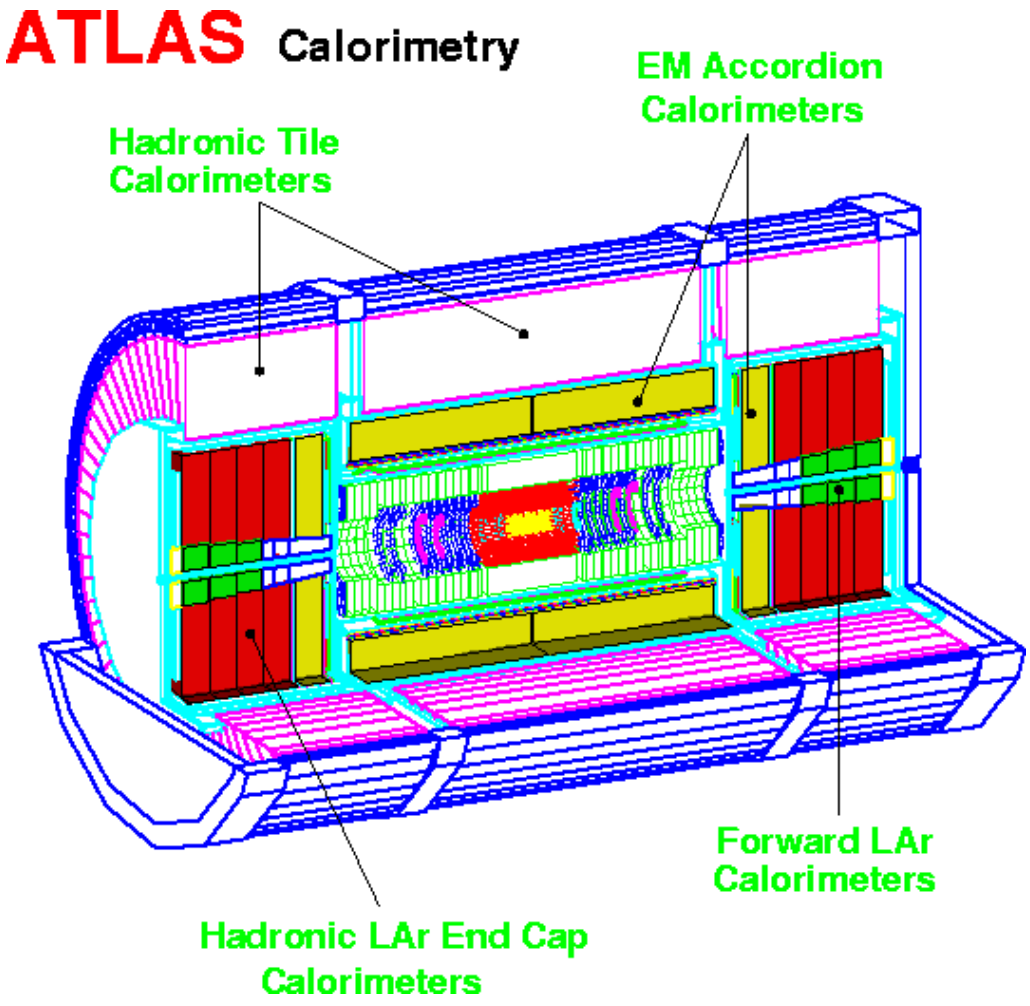

Figure 2.8: *The ATLAS Calorimetry.*

The **Electromagnetic calorimeter**, ECAL [41, 42], system uses a sampling technique with liquid argon as active medium and lead plates, bent in accordion shape, as passive material. Signal readout is performed by three-layered copper-polyimide flexible printed circuit boards placed between the absorber plates and held in place using honeycomb spacers. The necessary drift field is provided by applying high voltage to the outer layers of the readout electrodes.

The *barrel calorimeter* covers the range $0 < |\eta| < 1.4$, and is located inside the barrel cryostat, right behind the super-conducting solenoid. It covers the radial distance from $1.5\,m$ to $2\,m$ from the beam axis and is mechanically divided in two half-barrels, each subdivided in 16 modules. The bending axis of the absorber plates runs parallel to the beam axis. A uniform sampling fraction in the radial direction is achieved by decreasing the folding angle and by increasing the fold length between bends as moving outwards. A uniform sampling fraction in ϕ can be achieved with sharp angles on the absorber folds if the ϕ amplitude of folds were 4 times the absorber spacing. With the chosen absorber type, though, sharp bendings are not possible, leading to ϕ modulation of the response. This effect is minimized by making the ϕ amplitude of the folds 4.067 times of the absorber spacing. The decrease in sampling frequency with η is compensated by increasing the sampling fraction. This is done by using two different absorber thicknesses, with a transition from thick to thin plates at $|\eta| < 0.8$.

The *end-cap calorimeter* covers the range $1.375 < |\eta| < 3.2$ and is located inside the end-cap cryostat. It covers in longitudinal direction, along the beam axis, from $3.6\,m$ to $4.2\,m$ from the interaction point. The accordion geometry is implemented by arranging the absorber plates as the spokes of a wheel, with the bending axis of the folds running perpendicular to the beam axis. A consequence of this geometry is that the folding angle and the wave height must vary with the distance from the beam axis. Due to mechanical limitations each end-cap calorimeter is divided into two coaxial wheels in order to cover the whole pseudo-rapidity range. An inner wheel covers the range $|\eta| < 2.5$ and an outer wheel the range $|\eta| > 2.5$. Each endcap is mechanically divided in eight wedge shaped modules. A constant lead thickness together with a varying liquid argon gap could result in a strong variation of the calorimeter response with η. By feeding different regions of η with different values of the high voltage a moderate compensation of the response can be obtained. Any residual non-uniformity should be corrected by software after careful calibration in test beam.

To be able to measure the energy associated to the low momentum particles produced in the interaction of electro-magnetic particles (e/γ) with the (dead) material ($1.4X_\circ - 3X_\circ$ depending on η) in front of the calorimeters, a *pre-sampler detector* is installed in front of the barrel calorimeter. In the end-cap, since for a given E_T the average energy is larger than in the barrel, the pre-sampler is less important. Only in the region $1.5 < |\eta| < 1.8$, where the amount of the dead material is more than $3X_\circ$, a pre-sampler is put in front of the end-cap calorimeter.

The total thickness of the *ECAL* is $\sim 25X_\circ$ in the barrel and $\sim 26X_\circ$ in the end-caps. The $|\eta| < 2.5$ region of the *ECAL*, devoted to precision measurements, is segmented in three longitudinal samplings. The high-granularity readout of the *ECAL* in this region, shown in Figure 2.9, provides, apart from the traditional energy measurement, a powerful γ/π° identification and background jet rejection. The readout cells are, in the η direction, projective to the interaction region. A unique feature of this calorimeter is the narrow strips in the first sampling. They allow π° rejection, which is crucial for the $H \to \gamma\gamma$ channel discussed before.

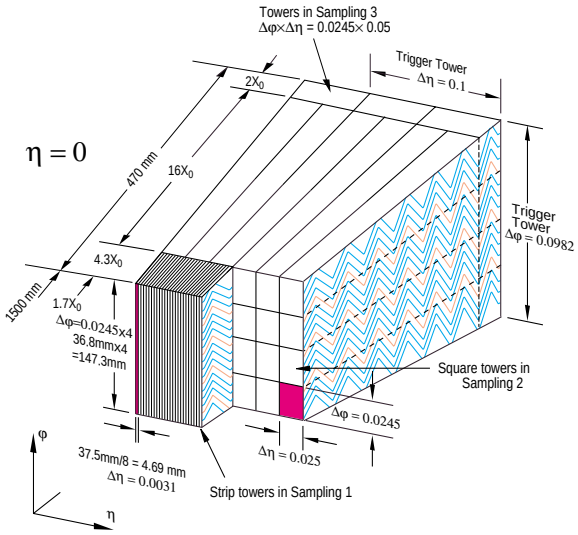

Figure 2.9: *Illustration of the longitudinal and lateral segmentation, along with the trigger tower definition, in the Barrel ECAL at $\eta \sim 0$. For details see text.*

The **Hadronic Calorimeter**, HCAL, system covers the range $|\eta| < 4.9$ and uses different techniques best suited for the different requirements. An important design parameter is the thickness of the calorimeter to provide good containment for the hadronic showers and reduce punch through for the muon system.

The *Tile Hadronic Calorimeter* [44] covers the range $|\eta| < 1.6$ and utilizes a sampling technique with plastic scintillator tiles, as active material, embedded in iron absorbers. It is composed of one barrel and two extended barrels, subdivided azimuthally in 64 modules, and is segmented in three layers. The pseudo-projective readout cells in η are built by grouping wavelength-shifting fibers to a photo-multiplier. The calorimeter is placed behind the *ECAL* ($\sim 1.2\lambda$ at $\eta = 0$), and is $\sim 7.2\lambda$ thick at $\eta = 0$.

In the end-cap regions, i.e. $1.5 < |\eta| < 3.2$, the *Liquid Argon Hadronic Calorimetry* [41, 41] takes over. Each hadronic end-cap calorimeter consists of two, equal diameter, independent wheels. Copper plates are used as absorber material. The absorber plates in the second wheel are twice as thick as those in the inner wheel ($25\,mm$ vs. $50\,mm$ respectively). The wheels are divided in two longitudinal readout segments. The readout cells are fully pointing in ϕ and only pseudo-pointing in η. The calorimeter is placed behind the *ECAL* inside the same cryostat housing, and the thickness of it's active part is $\sim 12\lambda$.

The high density **Forward Calorimeter**, FCAL, covers the range $3.1 < |\eta| < 4.9$, and is integrated in the end-cap cryostat. It's front face is at about $5\,m$ from the interaction point. It consists of three longitudinal sections: the first one is in copper, while the other two are tungsten. In each of them the calorimeter consists of a metal matrix with regularly spaced longitudinal channels filled with rods. The sensitive medium is Liquid Argon, which fills the gap between the rod and the metal matrix. The *FCAL* accommodates $\sim 9\lambda$ of active detector in a rather short longitudinal space.

2.2.1.4 Muon Spectrometer

The **muon spectrometer** [45] is surrounding the calorimeters and defines the overall dimensions of the ATLAS detector. A schematic view of the muon detector system is shown in Figure 2.10.

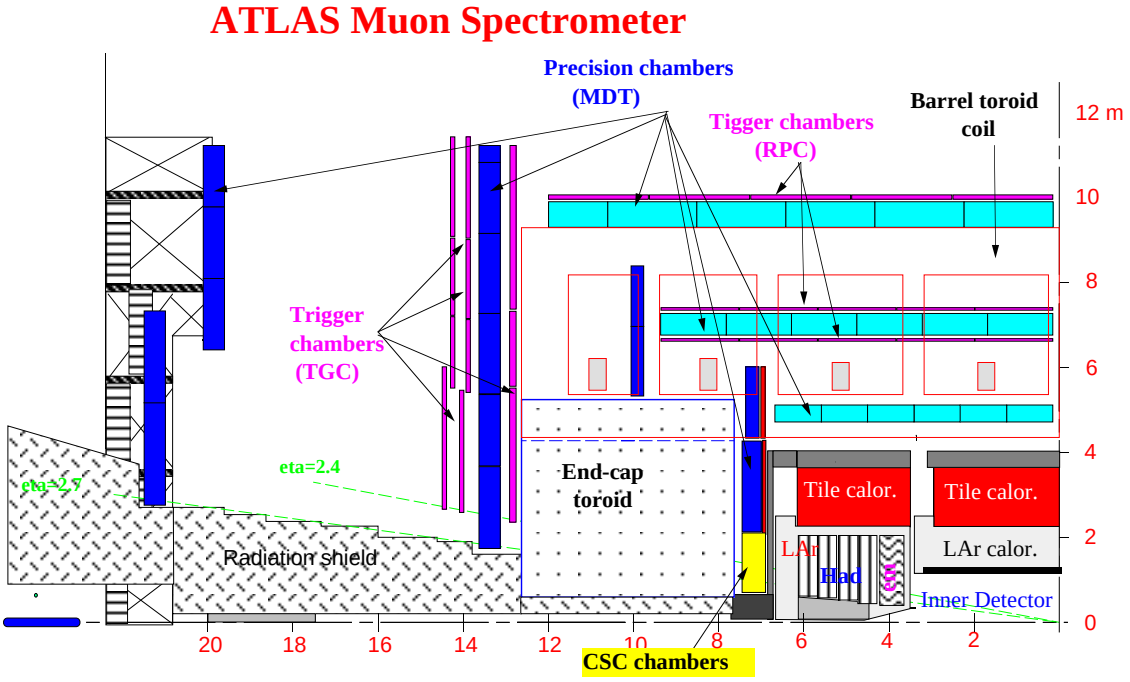

Figure 2.10: *The ATLAS Muon Spectrometer.*

The performance of the muon spectrometer is optimized based on high-momentum final-state muons, which are among the most promising physics signatures at the LHC environment. Low transverse momentum muons are of major interest for b-physics and CP-violation studies. The main components of the muon spectrometer are a system of three large super-conducting air-core toroid magnets (one barrel and two end-caps), precision tracking detectors with high intrinsic resolution, and a powerful dedicated (stand-alone) trigger system. Emphasis is given to high-resolution performance over a p_{T} range from $5\,GeV$ to $1\,TeV$ or more. In the range $|\eta| < 1$, magnetic bending is provided by a large barrel magnet consisting of eight coils surrounding the hadron calorimeter. In the range $1.4 < |\eta| < 2.7$, muon tracks are bent in two smaller end-cap magnets inserted into the ends of the barrel toroid. The magnetic deflection in the transition region, i.e. $1 < |\eta| < 1.4$, is provided by a combination of barrel and end-cap fields. An excellent muon momentum measurement is achieved with three stations of high-precision tracking chambers. The resolution is limited by energy loss fluctuations at low momenta and by detector resolution at high momenta.

Precision measurements, over most of the pseudo-rapidity range, is provided by the **Monitored Drift Tubes** (**MDT**s). The basic detection elements are round aluminium tubes with central wires. The tubes operate with a non-flammable gas mixture at 3–5 bar absolute pressure. To provide finer granularity, in order to cope with high rates, **Cathode Strip Chambers** (**CSC**s) are used in the range $|\eta| > 2$. The CSCs are multi-wire proportional chambers with cathode strip readout and with a symmetric cell in which the anode-cathode spacing is equal to the anode wire pitch. The precision coordinate is obtained by measuring the charge on the segmented cathode by the avalanche formed on the anode wire.

Two different types of detectors are employed for the muon **Trigger Chamber** system: **Resistive Plate Chambers** (**RPC**s) in the barrel ($|eta| < 1.4$) and **Thin Gap Chambers** (**TGC**s) in the end-cap region. The RPC is a gaseous detector with a narrow gas gap formed by two parallel resistive plates separated by insulating spacers. The TGC is designed similar to multi-wire proportional chambers, with the difference that the anode wire pitch is larger than the cathode-anode distance.

2.2.2 Physics prospects

It is impossible to exploit the manifold of physics program of ATLAS and its performance issues in this thesis. An exhaustive account of the physics performance of ATLAS is given in reference[§] [46]. The physics aspects of the ATLAS experiment covers essentially those of the LHC *p-p* run mode program explained at the beginning of this chapter. For easier reference here is a recapitulation of the main program items in a compact form:

- searches for the Higgs boson(s) within the SM and the MSSM framework and alternative symmetry breaking schemes,
- searches for SUSY and determination of its parameters, like the masses of the super-symmetric particles,
- searches for the alternative extensions, such as compositeness, technicolor, heavy quarks and leptons (forth generation) and heavy vector bosons (W$'$, Z'),
- measurements of the SM parameters, e.g. the mass of the W vector boson and the top quark and the gauge couplings,
- measurements of CP-violation in B-decays ($B_d^\circ \to J/\psi\, K_s^\circ$).

In the following the searches in the Higgs sector of the SM and the MSSM will be explained in some detail and the discovery potential of ATLAS will be addressed.

2.2.2.1 SM Higgs searches

The phenomenology of a scalar Higgs boson in the minimal Standard Model has been explained in the first chapter. A summarized version of the Higgs properties including it's couplings to bosons and fermions is reproduced in the table on the right. The mass of the Higgs particle is a free parameter of the theory. Based on theoretical arguments the SM Higgs mass is less than about 1 TeV.

quantum numbers	$Q = 0$ $J^{PC} = 0^{++}$
v.e.v : v	$(\sqrt{2}\,G_F)^{1/2} \simeq 246\,GeV$
coupling to vector bosons	$2\,M_V^2\,/\,v$
coupling to fermions	$\sqrt{2}\,m_f\,/\,v$
self–coupling	$\lambda = 2\,M_H^2\,/\,v^2$

The production mechanisms of a scalar Higgs boson depend on its mass. In hadronic interactions the most important production channel of a scalar Higgs boson is the gluon fusion, proceeding through a heavy quark triangle. The next important production mechanism in a hadron collider is the vector boson fusion, where the vector bosons are radiated from the incoming quarks. The associated production mechanisms, the so-called Higgs radiation or strahlung processes, play a less important role. These production processes along with the corresponding cross-sections are shown in Figure 2.11. It must be noted that the plotted cross-xections correspond to calculations to leading order in the strong coupling constant and any corrections due to higher order diagrams in the perturbation theory, although calculable and known, are neglected. The reason for neglecting the K-factors (the ratio of the higher order corrections to leading order calculations) is that the corresponding higher order corrections for the QCD background are not known (or calculated) for all of the processes.

[§]For a compact and summarized version of the ATLAS physics potential see for instance [72].

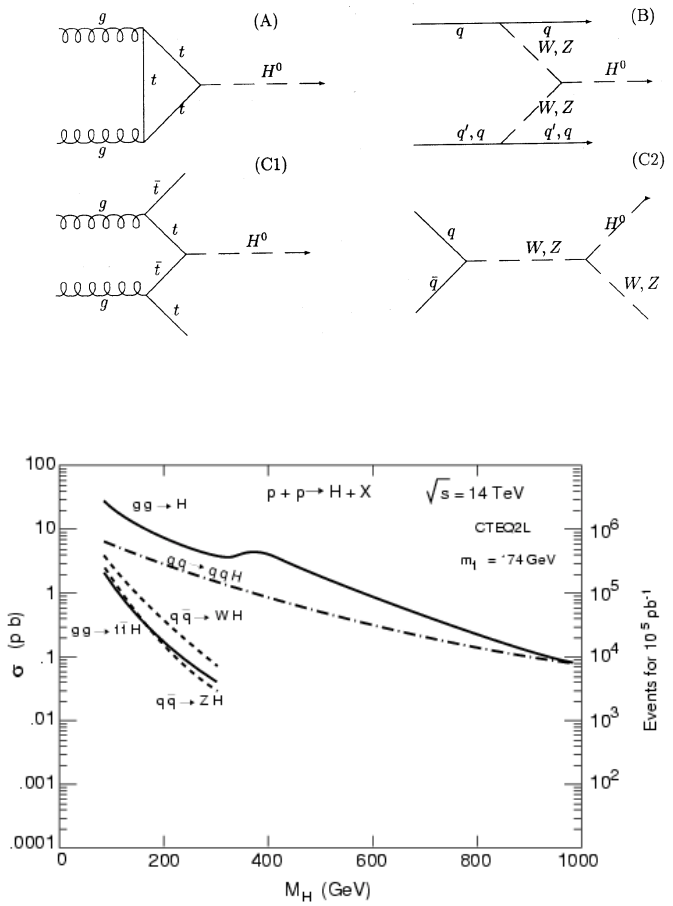

Figure 2.11: *SM Higgs production cross-sections (y-axis on the left) for the different production mechanisms as a function of the Higgs boson mass. The corresponding number of events for an integrated luminosity of* 100 fb^{-1} *is also indicated (y-axis on the right). Taken from [73].*

As seen in Figure 2.11 the gluon fusion through a top-quark loop is the dominating production process over the entire mass range in the LHC environment. The hypothetical Higgs particle, when produced, will decay into fermionic and/or bosonic final states immediately after its production. The total decay width of the Higgs boson in the SM is shown in Figure 2.12 as a function of its mass. Since the Higgs boson couples to the mass, the dominant decay mode is always to the kinematically allowed heaviest particles. Figure 2.13 summarizes the branching ratios to accessible final states depending on the mass of the Higgs boson. The rise in the total decay width at $M_H \sim 160$ GeV is due to the turn-on of the W^+W^- decay mode. At Higgs masses below this threshold the dominant decay channel is the $b\bar{b}$ final state. Decay branching ratios to other fermionic final states are at least 1 order of magnitude smaller in this mass range. The branching ratio of the $\gamma\gamma$ rare decay mode shows a slow rise with the Higgs mass up to around 130 GeV, where it reaches its maximum, and drops rather rapidly beyond that. The branching ratio to $\gamma\gamma$ in this region is about 3 orders of magnitude smaller than that of the $b\bar{b}$ channel. A SM Higgs with a mass in the intermediate range decays predominantly into a pair of massive weak bosons. Above the $t\bar{t}$ threshold, decays into top quarks become also important.

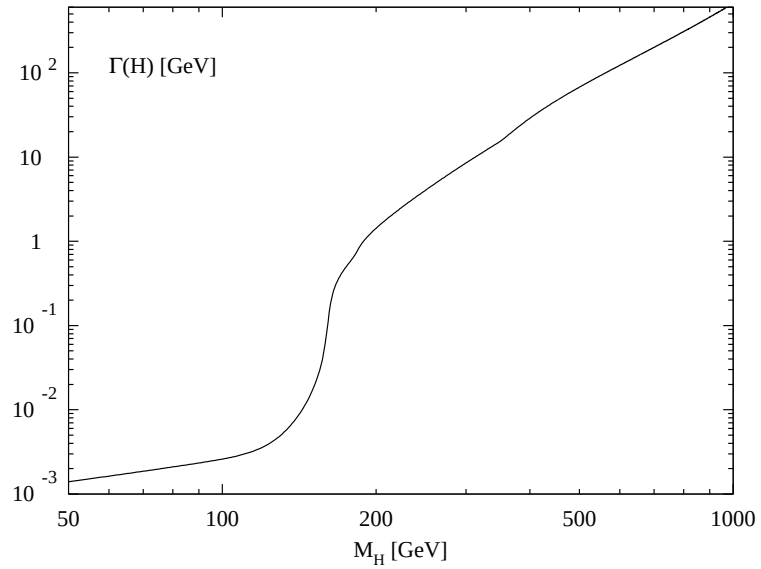

Figure 2.12: *Branching ratios for Higgs decays, as obtained from the HDECAY program [58].*

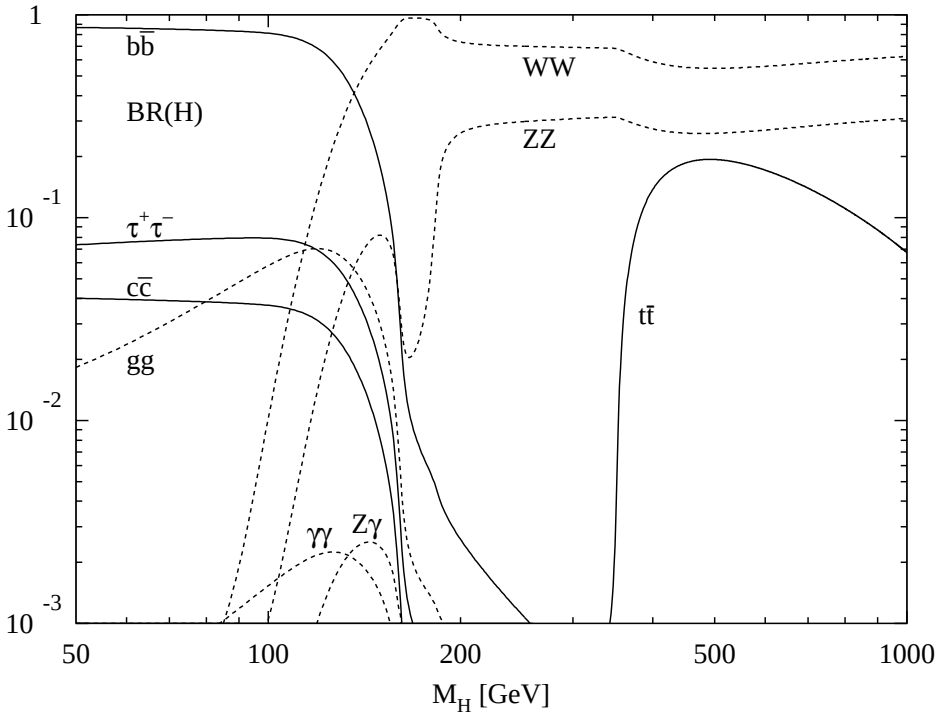

Figure 2.13: *SM Higgs total decay width, as obtained from the HDECAY program [58].*

In order to observe a possible signal from a Standard Model neutral Higgs boson, the expected mass range, from about 110 GeV (LEP lower limit) to about 1000 GeV (theoretical upper limit), is divided in several mass windows. In each window one or the other of the possible final state signals, corresponding to different decay channels of the SM Higgs, could be extracted efficiently above the background with reasonable significance. The choices in the specified mass windows are based on intensive Monte Carlo simulation and analyzes on the signal rates and signal-to-background ratios. The search strategy adopted by ATLAS for a SM Higgs is compiled in Table 2.2, where the observable decay channels together with the corresponding mass ranges are displayed. These benchmark processes put very severe requirements on the overall detector performance and specially on the electromagnetic calorimetry. Detector performance is absolutely crucial, specially for channels available for a relatively light Higgs boson.

Table 2.2: Reliable decay channels for a discovery of the SM Higgs boson, depending on its mass. The most important background for each case is also indicated. For details see text.

Mass range (GeV)	Signal	important backgrounds
80 – 130	$gg \to H \to \gamma\gamma$	$q\bar{q},\ gg \to \gamma\gamma$ $qg \to q\gamma \to q\gamma\gamma$
	$gg,\ q\bar{q} \to t\bar{t}H \to \ell\nu b\,\bar{t}\,b\bar{b}$	$t\bar{t}Z\ ,\ \ t\bar{t}b\bar{b}$
120 – 180	$gg \to H \to ZZ^{(*)} \to 4\ell$ $gg \to H \to WW^{(*)} \to \ell\nu\,\ell\nu$	$ZZ^*,\ Z\gamma^* \to 4\ell$
180 – 600	$gg \to H \to ZZ \to \ell\ell\nu\nu$	$ZZ \to \ell\ell\,\nu\nu$
400 – 900	$gg \to H \to ZZ \to \ell\ell\nu\nu$ $gg \to H \to WW \to \ell\nu\,jj$ $gg \to H \to ZZ \to \ell\ell\,jj$	$ZZ \to \ell\ell\,\nu\nu$ $ZZ \to \ell\ell\,\nu\nu$ $ZZ \to \ell\ell\,jj$
> 600	$gg \to H \to WW \to \ell\nu\,jj$	$ZZ \to \ell\ell\,\nu\nu$

As seen in Figure 2.13 a light standard model Higgs, with a mass between about 80 GeV to about 150 GeV, decays predominantly via the $b\bar{b}$ channel, which is completely swamped by the QCD, $pp \rightarrow jet + jet + X$, background processes. The most reliable channel in this mass range is the $H \rightarrow \gamma\gamma$ with a pair of photons in the final state, which suffers from two different backgrounds: the large irreducible $pp \rightarrow \gamma\gamma + X$ processes and the reducible $pp \rightarrow j\,j/j\,\gamma$ processes, where jets fake photons. The former requires a very good energy and angular resolution for photon pairs, and the latter demands an excellent γ/jet separation. For masses of the SM Higgs boson up to $2\,m_Z$ the H $\rightarrow ZZ^{(*)}\,/\,Z^{(*)}Z^{(*)}$ decays with both of the Z bosons, either off-shell or on-shell, decaying into muon pairs are also accessible. In this case no mass constraint on the parent Z boson could be applied. Above the $2\,m_Z$ mass the H $\rightarrow ZZ \rightarrow \ell\ell\,\nu\nu\,/\,\ell\ell\ell\ell$ and the H $\rightarrow WW \rightarrow \ell\nu\,jj$ decay channels, with $\ell = e/\mu$, become important.

The expected sensitivity to different decay channels as a function of the Higgs mass, for an integrated luminosity of 30 fb^{-1} and of 100 fb^{-1}, is displayed in Figure 2.14. The H $\rightarrow ZZ^{(*)} \rightarrow 4\ell$ channel, with four charged leptons in the final state, is the so-called gold-plated channel because of the clean and almost background-free final state signal. This channel is accessible at intermediate to high mass range and is way above 5σ discovery limit already during the initial low luminosity run period.

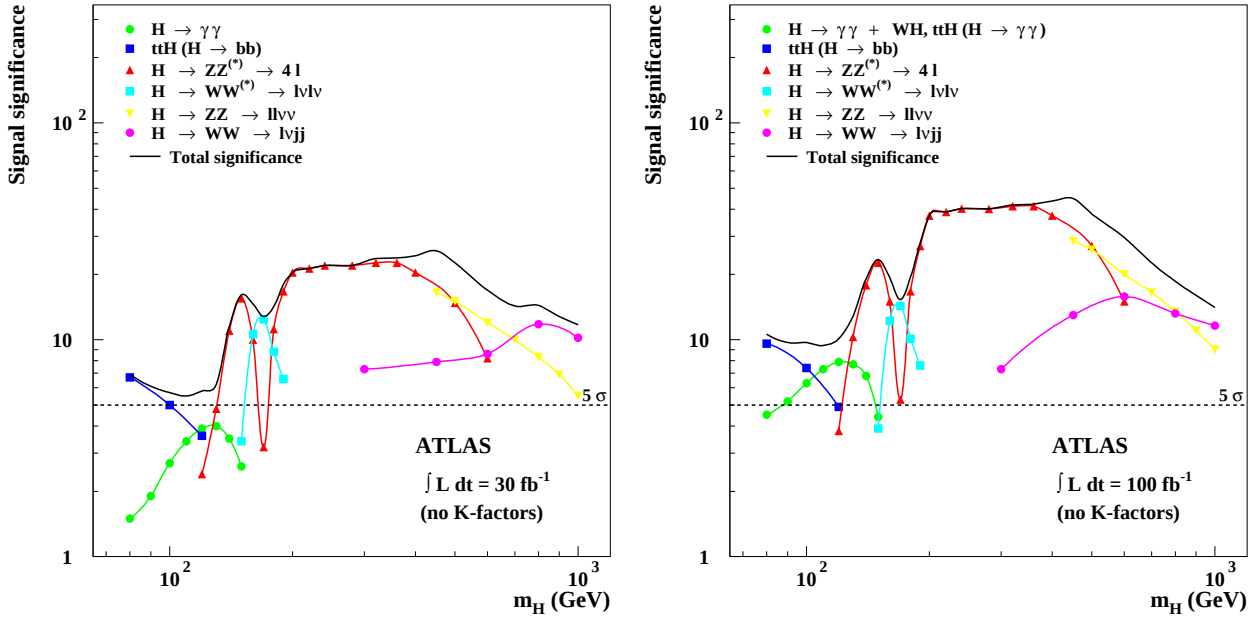

Figure 2.14: Expected observability of the Standard Model Higgs boson in ATLAS, in terms of the statistical significances for various decay channels, as a function of the Higgs mass and for an integrated luminosity of 30 fb^{-1} (left) and of 100 fb^{-1} (right). The statistical significance for the combination of all the decay channels are also superimposed on both plots. Taken from [46].

2.2.2.2 MSSM Higgs searches

Searches in the Higgs sector of the Minimal Supersymmetric extension of the Standard Model (MSSM) should be possible given the large discovery potential of the ATLAS experiment for physics beyond the standard model. Couplings of the neutral Higgs boson in the MSSM, depending on m_A and $tan\,\beta$, are in general different from those of the SM Higgs. As a consequence the production rates and the branching ratios of the MSSM Higgses are different from the SM Higgs. The production rate of the neutral CP–even Higgs bosons at certain regions of the $(tan\,\beta, m_A)$ parameter space may be lower/higher than in the SM case. Moreover, their branching ratios to the important bosonic final states may also be lower. For this reason experimentally more demanding leptonic decay modes of, for instance, the $\tau^+\tau^-$ and the $b\bar{b}$ final states must be utilized. As an example an excess of τ leptons, in comparison to e/μ, in the final state could signal a charged Higgs, with a much higher $\tau^+\tau^-$ branching ratio than the ee or the $\mu\mu$, which is not the case for a charged vector boson (with equal $\ell\ell$, with $\ell = e/\tau/\mu$, branching ratios). Several intensive studies have been performed to analyze the discovery reach of ATLAS in the MSSM Higgs sector. Contour curves representing the 5-σ discovery of the MSSM Higgs bosons, drawn on the conventional ($tan\,\beta$, m_A) plane, is shown in Figure 2.15. The exclusion contours deduced from LEP2 results for different center-of-mass energies and luminosities are also superimposed on the same plots.

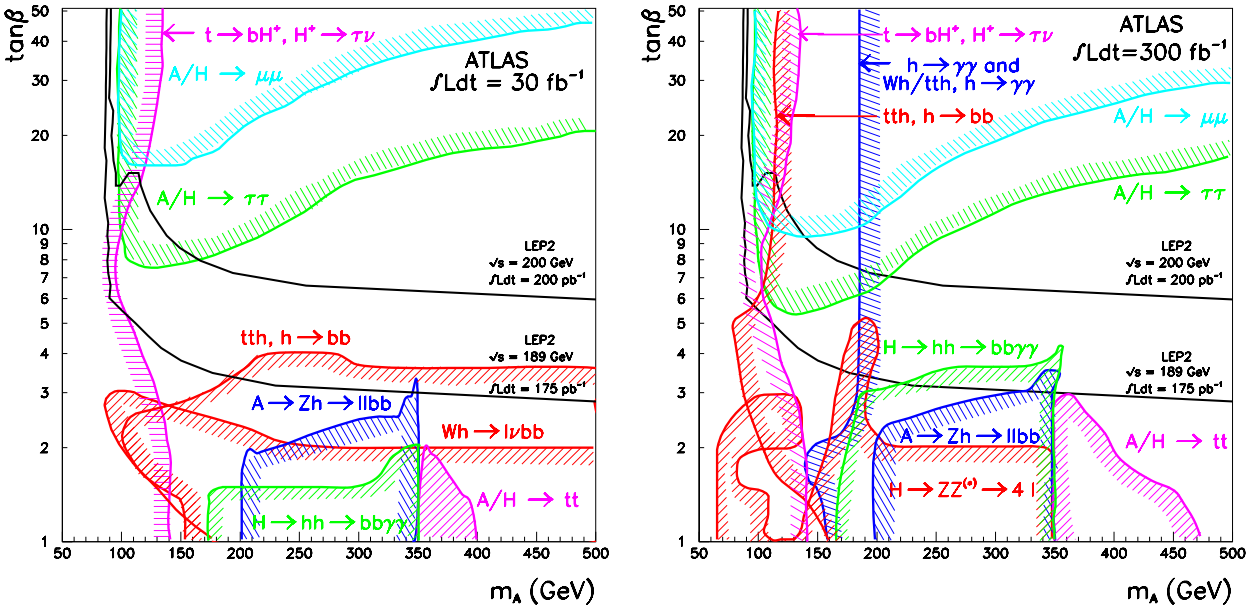

Figure 2.15: *The discovery potential of the ATLAS experiment in the Higgs sector of the MSSM, in terms of the* 5σ *discovery contours for different decay modes, in the usual* $(tan\,\beta, m_A)$ *parameter space for an integrated luminosity of* 30 fb^{-1} *(left) and of* 300 fb^{-1} *(right). The LEP2 limits corresponding to* 175 pb^{-1} *and* 200 pb^{-1} *integrated luminosities per experiment are also included. Taken from [46].*

It can be seen from the discovery contours that the neutral Higgs bosons, $A/H/h$, are detectable in a large fraction of the ($tan\,\beta$, m_A) plane in complementary decay channels. The $tt\,h \to tt\,bb$ and the $W/tt\,h$, $h \to \gamma\gamma$ decay channels cover the moderate to high m_A re-

gion of the parameter space for small to large $tan\,\beta$ values after an integrated luminosity of 300 fb^{-1}. This is du to the fact that both the direct and the associated production of the h Higgs boson, and its decay branching ratios to $bb/\gamma\gamma$ final states, approach asymptotically to that of the SM Higgs boson for increasing $tan\,\beta$ and/or m_A. The neutral CP-even Higgs bosons, h/H, may be detected simultaneously in the $H \to hh \to bb\,\gamma\gamma\,/\,bb\,bb$ decay modes, at intermediate m_A, $\sim 200 - -350$ GeV for $tan\,\beta <\sim 3$. The $A \to Z\,h \to \ell\ell\,bb$ channel behaves similarly, making it possible to detect The CP-odd neutral Higgs boson, A. Large $tan\,\beta$ region of the parameter plane is covered by the complementary $A/H \to \mu\mu\,/\,\tau\tau$ decay modes. The $\tau\tau$ channel covers a larger area due to its much higher branching ratio, $\sim 10\%$. The $\mu\mu$ final state can on the other hand be extracted more efficiently. In general, as mentioned above, the leptonic final states are favourable in the LHC environment. The charged Higgs boson, $H^{\pm}$, is detectable over a narrow band at low m_A for the entire $tan\,\beta$ range through the $t \to b\,H^{+} \to b\,\tau\nu$ channel.

Chapter 3

ATLAS trigger system

The ATLAS detector should operate in the hostile and high interaction rate environment of the LHC and should manage to select efficiently expected rare interesting physics processes while rejecting much higher-rate background. This is already explained in the opening of the last chapter (see also Figure 2.5 on page 26). Given the high luminosity and center-of-mass energy at the LHC, the real challenge is when one considers the fact that decisions should be taken every 25 ns, corresponding to 40 MHz bunch crossing rate, whether an event is a *good* candidate for new physics or not. On top of these comes the huge number of channels from diverse, complex and large sub-detectors which should be processed in this ultra short time interval. All these considerations necessitate an extremely selective trigger system. A typical electronic signal, as for instance from calorimeter readout cells, have a triangular shape with a duration of about 400 ns. These signals are shaped in order to clip the long decay and to optimize the signal-to-noise ratio. An example of such a signal and the corresponding shaped bipolar signal is shown in Figure 3.1. As seen in this figure the duration of the peak of the shaped signal is about 100 ns, much shorter than the original one. The negative undershoot, with a duration of about 300-400 ns and with a depth about 20% of the peak hight, has though some consequences on the trigger system. Calorimeter signals from $\sim$ 18 consecutive bunch crossings, each containing on average $\sim$ 23 ($\sim$ 2.3) p-p interactions at high (low) luminosity, pile up and influence negatively the accuracy of the energy measurements. These two effects, which collectively go under the notion *pile-up*, tend to degrade the energy measurement capabilities of the detector system which should be compensated by appropriate trigger strategies.

The ATLAS experiment has adopted a three level trigger system [35, 39] to accomplish the extremely difficult task of reducing the event rate from it's nominal 40 MHz down to $\sim$ 100 Hz suitable for storage on tapes or similar recording devices. The ATLAS trigger system is shown in Figure 3.2.

The **LVL1 trigger** [43] accepts coarser granularity data from the calorimeters and the muon chambers at 40 MHz LHC bunch crossing rate. The output rate of the LVL1 trigger is limited to 75 kHz (upgradable to 100 kHz) implying an event reduction of roughly $\sim 10^{-4}$ corresponding, on average, to 1 accepted bunch crossing in every 400. The level-1 trigger must identify unambiguously the bunch crossing containing the interaction of interest and introduce negligible dead-time. The target latency, i.e. the time taken to form and distribute trigger decision, consisting of particle time of flight, detector response, signal collection in the

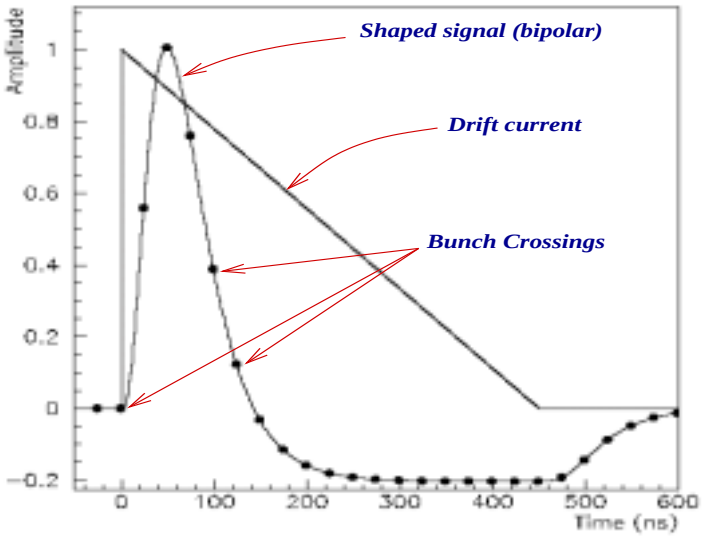

Figure 3.1: *An example of a drift current versus time of an ionization calorimeter, and the corresponding bipolar shaped signal. The dots indicate the bunch crossings.*

detectors, analogue signal processing, digitization, cable delay and digital processing, is $\sim 2\mu s$ with a $0.5\mu s$ contingency. Data from all detector-channels for each bunch crossing, during the LVL1 decision, are stored in front-end (on-detector) pipeline memories. When LVL1 accepts an event, the data from all the pipelines are transferred via optical links to off-detector readout cards containing the level-2 buffer memories, the so called Read-Out Buffers (ROBs). Regions of detectors identified by LVL1 as containing interesting information, referred to as Regions of Interest (RoIs), are sent to the next level trigger in form of pointers in $\eta - \phi$ space.

The **LVL2 trigger** is essentially driven by the full granularity data from the RoIs identified by LVL1. The RoI data* are accessed from the ROBs via the de-randomizer buffers, which absorb the instantaneous LVL1 rate and output data more uniformly. Full precision data from the inner detector are also accessed by this trigger level. The event rate after this stage of trigger should be reduced to $\sim$ 1 kHz. The LVL2 trigger performs fairly complicated processing to find tracks and measure their transverse momenta. Data processing by LVL2 has two phases, feature extraction and feature combination, and is performed in three steps:

1. Building physical quantities within each sub-detector (e.g. clusters and/or tracks) from their cell and/or hit information. This reduces the amount of data.

2. Building objects by combining RoIs from all sub-detectors. Particle identification, if possible, is also performed at this stage.

3. Making global event decision by combining all objects. This should be considered as some kind of topological trigger stage, where certain physics processes could be selected.

*Triggers for B-physics studies at low luminosity should operate in parallel with other triggers also operational at high luminosity. These studies require, in addition to muons with $p_T \gtrsim 6\,GeV$, low p_T electron and hadron triggers at LVL1, which will not be able to produce RoIs for. For this reason the LVL2 trigger system in such cases should also be able to process data without the RoI guidance from LVL1.

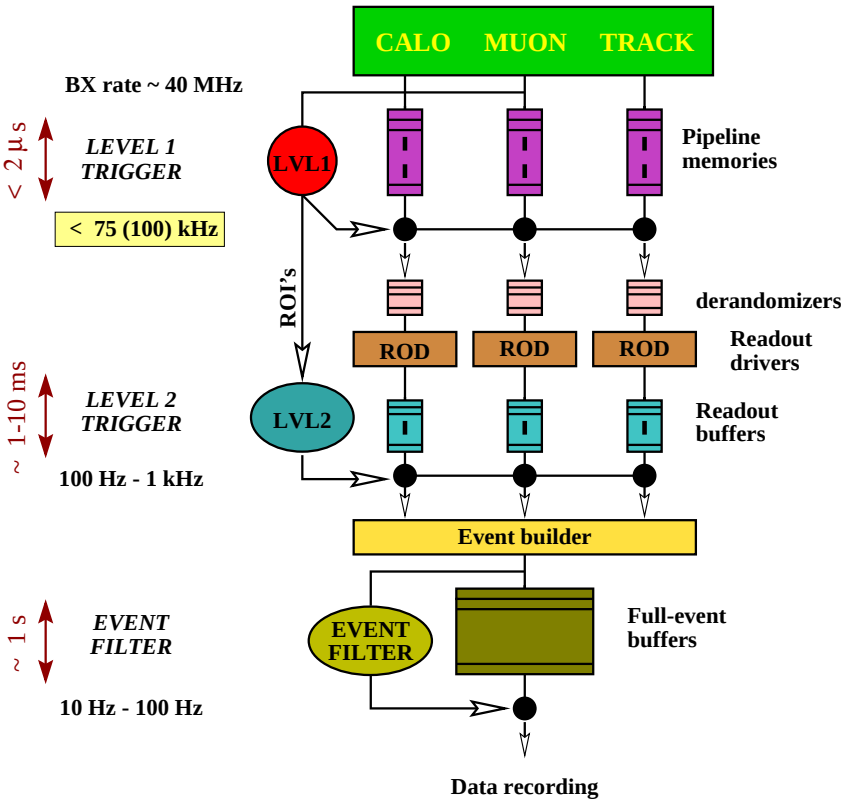

Figure 3.2: *The ATLAS trigger system.*

The first step could be performed in parallel in fast local processors for each RoI in each sub-detector, with the exception of the transition region from barrel to endcap in the TRT and precision tracker detectors. The second step in LVL2 data processing could be performed in parallel for each RoI. The global event selection task is performed by global processors organized in a farm of general purpose processors. The latency of LVL2 trigger is variable, depending on the event complexity, and varies within the range $\sim 1-10\,ms$. The full detector data, for each accepted event by LVL2, are transferred from the ROBs via the Event Builder (EB) to the third and last level of trigger system to perform the final event selection and to store or discard the event.

The **Event Filter** is the third and last level on the online event selection path of the ATLAS trigger system. Full event data from all sub-detectors at full granularity and precision is accessed by the event filter. An important task of the ATLAS Data AcQuisition (DAQ) system is to provide data for the event selected by LVL1/LVL2 triggers to the processor farm (or array) of the event filter. These processors perform, at real time, highly complex offline-like algorithms to select events based on physics signatures. The complete event reconstruction plus the subsequent decision will take, up to, $\sim 1\,s$. The latency depends on the event complexity. The event rate at the output of the event filter is about 10-100 Hz. A combination of event selection and data compression at this level will reduce the total data rate for permanent storage.

3.1 Level–1 Trigger, Functional overview

A functional block diagram of the ATLAS level–1 trigger system is shown in Figure 3.3. The major components, as seen in the figure, are the calorimeter and the muon trigger systems, the Central Trigger Processor (CTP) and the Timing, Trigger and Control (TTC) system. Each trigger system receives input signals/data from the corresponding sub-detector, i.e. the calorimeters and the muon chambers, performs trigger algorithms to identify and localize high transverse energy depositions, and provides on the output data required by the CTP system. The overall trigger decision, based on the combination of the calorimeter and the muon triggers, is then generated in the CTP and distributed to other ATLAS subsystems via the TTC system. As the name implies the TTC distributes in addition several other global information, e.g. event and bunch–crossing numbers.

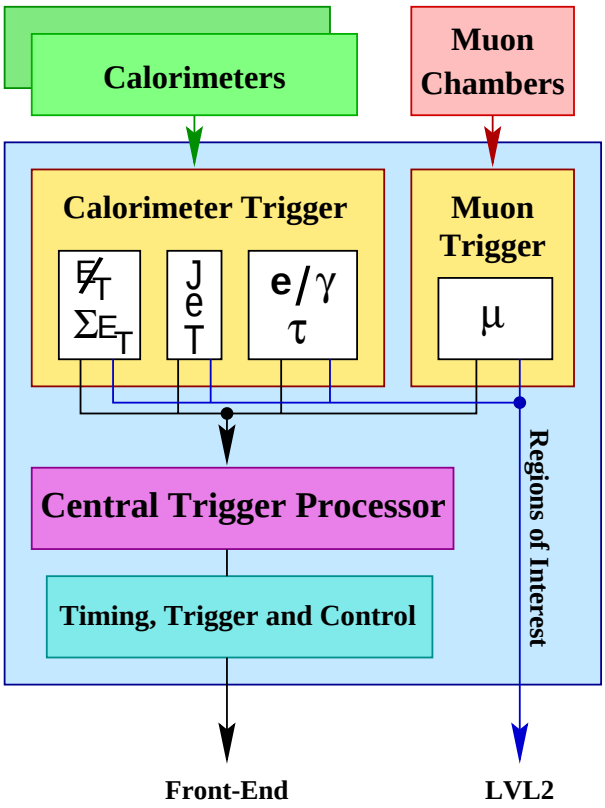

Figure 3.3: *Functional overview of the ATLAS Level-1 Trigger system.*

The LVL1 trigger is a synchronous and pipelined – with custom designed electronic – system running at the full LHC beam crossing rate of 40 MHz. The different algorithms of the trigger systems are hard-wired into specific integrated circuits, either full customized or commercial, programmable only at the parameter level. The level–1 trigger system is therefore a hard-ware trigger. The trigger criteria (or parameters) will be adjusted after gathering some experience from the initial running of the LHC.

3.1.1 Muon trigger

The LVL1 muon trigger is based on dedicated high granularity trigger chambers with a very fast response time, being capable of identifying uniquely the bunch crossing of interest. A schematic view of the trigger chambers together with the implemented muon algorithms is presented in Figure 3.4.

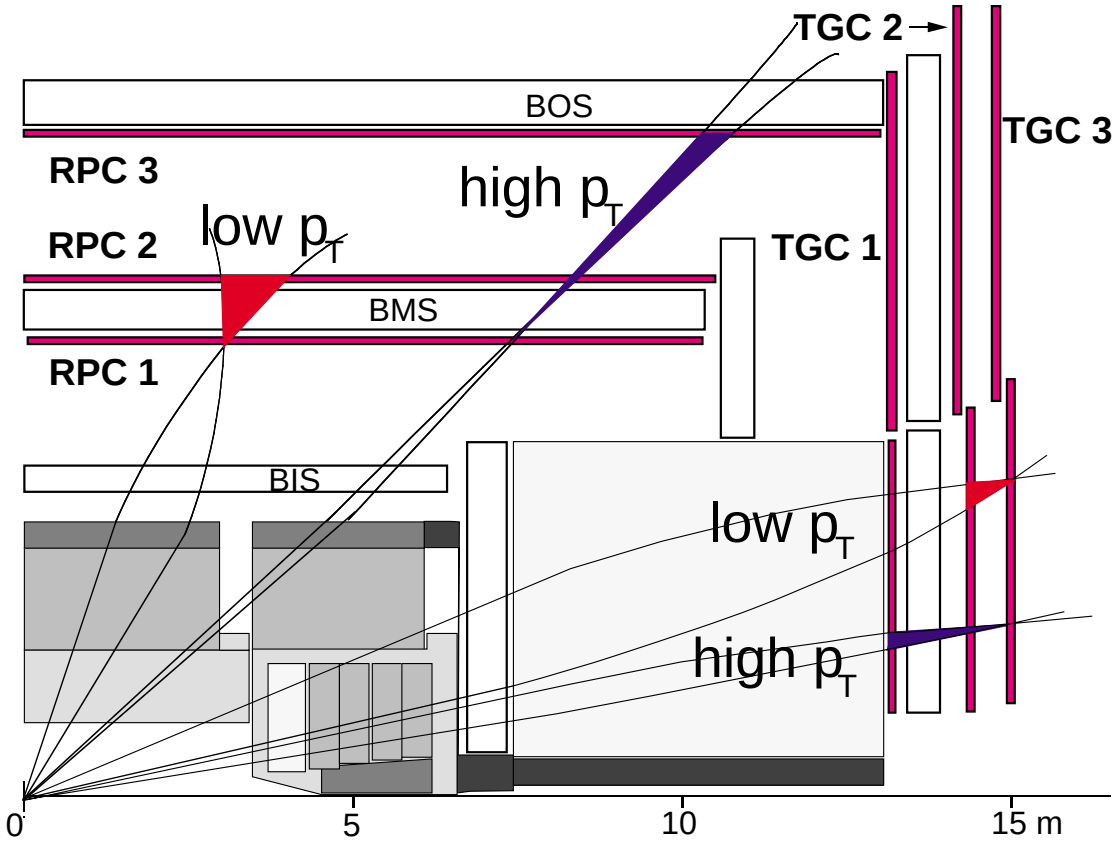

Figure 3.4: *The ATLAS Level-1 Muon Trigger Chambers and algorithms.*

Three stations of trigger chambers, with a 2-coordinate readout ($\eta - \phi$), are used to perform muon trigger algorithms. Triggering on low-p_T muons (thresholds $E_T \sim$ 6-10 GeV) is performed by using the information from only two out of three stations. In the barrel region ($\eta < 1.05$), the first two stations, whereas in the endcap region ($1.05 < \eta < 2.4$) the last two stations are used for low-p_T trigger algorithm. Triggering on high-p_T muons (thresholds E_T ~8-35 GeV) requires information from all three stations. The principle of triggering on muons is also illustrated in Figure 3.4. A hit in the RPC1 (TGC3) station, the so-called pivot plane, in the barrel (endcap) is (virtually) connected to the interaction point. This defines a road which passes through the other stations. The width of the road, depending on the required p_T threshold, is programmable and defines a coincidence window on the other trigger stations. At least one hit within the coincidence window in the second (and third) station is required for low(high)-p_T trigger.

3.1.2 Level–1 Calorimeter Trigger

The calorimeter trigger system is composed of three major components as illustrated in the block diagram of Figure 3.5: The front-end Pre-Processor (PPr), the Cluster Processor (CP) and the Jet/Sum-ET Processor (JEP).

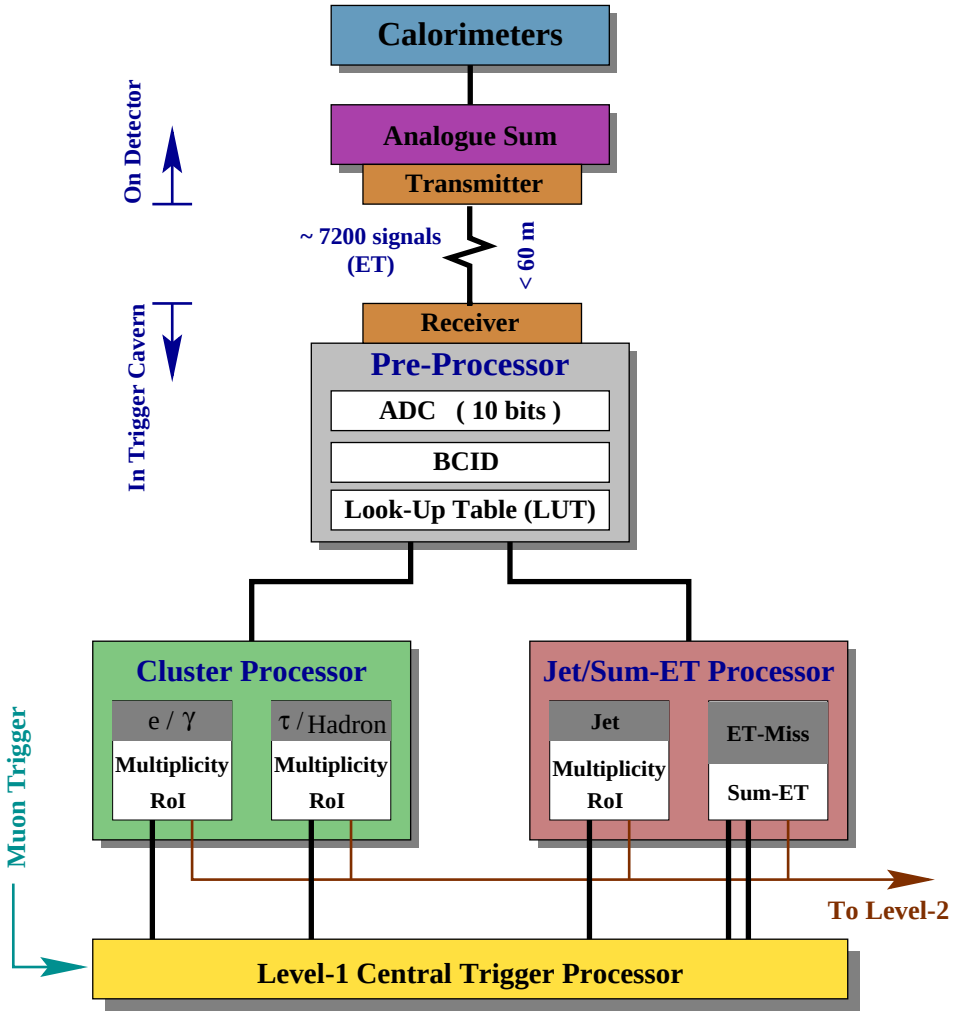

Figure 3.5: *The TLAS Level-1 Calorimeter Trigger.*

Analogue signals from the electromagnetic and the hadronic calorimeter cells are summed on-detector into separate sets of so-called Trigger Towers (TTs). The granularity of the TTs is typically (with some exceptions in $2.5 < |\eta| < 3.2$ region and specially in the FCAL) $(\Delta\eta \times \Delta\phi) \sim (0.1 \times 0.1)$, much coarser than the readout granularity of the calorimeters. An example of this could be seen in Figure 2.9 on page 31 for the barrel ECAL. The TTs are projective, i.e. pointing to the interaction point, and cover the region $|\eta| < 4.9$ (with full coverage in ϕ).

The *Pre-Processor* performs all the necessary signal processing to provide the trigger modules/algorithms with the required inputs. It receives a total of $\sim$ 7200 analogue signals on twisted pairs via the line receivers and performs the following major tasks:

- digitizing the analogue inputs at the sampling rate of 40 MHz. This is done with fast Analogue-to-Digital Converters (ADCs) with 10-bit dynamic range and 250 MeV resolution. This gives a Least Significant Bit (LSB) of 0.25 GeV and a maximum E_T measurement of 256 GeV.
- performing the Bunch crossing Identification (BCID) based on the digitized signal. Actually two tasks are performed here, the calibration of the transverse energy and the assignment of a unique bunch crossing to the TT signal.
- converting the 10-bit digital signal to 8-bit data, and at the same time performing any residual (transverse energy) calibration, like pedestal subtraction and threshold application against noise at the TT level.

Several other more-or-less minor but important tasks are also performed by the PP, which are not described here. For details of these and other related issues see [43] and [50].

The BCID process deserves some explanation here. The BCID is performed by implementing a Finite-Impulse-Response (FIR) filter complemented by a sliding peak-finder to extract the transverse energy deposit and at the same time to identify the bunch crossing of interest. The FIR-filter multiplies, in parallel, the contents of a finite digital pipeline, containing digitized samples of the analogue input signal, with separate filter coefficients. At each bunch-crossing five consecutive ADC samplings are weighted with the corresponding FIR-filter coefficients and summed up to give a measure of the energy deposit. The implemented peak finder algorithm compares the FIR-filter output of BX-1 with the corresponding quantity from BX-2 and BX (BX being the present bunch crossing). The BCID criterion is fulfilled if the BX-1 semi–peak-integral is greater than that of the BX-2 and greater than or equal to that of the present BX. The obtained peak-integral of the BX-1 is then calibrated in the LUT mentioned above. Having determined the peak, the BCID logic could also easily identify the bunch crossing of interest, by virtue of the fact that the rise time of calorimeter signals are essentially constant ($\sim 50\,ns$).

The digital output of the ADC, depending on the characteristic of the input analogue signal, could have two different shapes, which has an impact on the following peak finding algorithm. The analogue signals from trigger towers with a large amount of transverse energy-deposit may become saturated and get a flat-top shape. In such cases the rising edge of the signals are steeper than the non-saturated signals. And in addition the width of the signal peak, e.g. the positive part of the bipolar signals, is in general much larger. The degree of saturation determines the width of the flat-top. The effect would be that the digitized signal would have several samplings with the maximum content, i.e. 250 GeV. The peak finder, in these cases, could not identify a unique peak and the information would be lost. With the high particle multiplicity at the LHC environment and with the relatively large trigger towers this would certainly not be a rare case. For this reason an alternative scheme is also implemented in the BCID logic to handle the saturated pulses, which uses the form of the rising edge of the signal to obtain the bunch crossing of interest. There is actually an overlap between the regions handled by each of these logics.

3.1.2.1 Level–1 Calorimeter Trigger Algorithms

The requirements on the level–1 trigger algorithms are that they should be fast and easy to implement on hardware processors, e.g. on ASICs and/or FPGAs. Some flexibility is though foreseen in form of programmable parameters. The calorimeter trigger algorithms are therefore simple and inclusive. At the level–1 trigger only the individual trigger objects are of importance and not the topology of the event. But the determination of the trigger criteria for different objects is of course based on intensive analysis on trigger rates, efficiencies and their coverage. For an event accepted by LVL1 trigger, all these objects would be refined by higher level triggers.

The LVL1 calorimeter trigger algorithms have very few parameters, related to the characteristic attributes of the corresponding objects. Trigger objects are isolated electrons and photons, selected collectively with the electromagnetic trigger, tauons, identified by single hadron trigger, jets and global quantities: $\sum \mathrm{E_T}$ and $\mathrm{E_T^{miss}}$, with associated triggers. The individual trigger algorithms are performed in specific (sub-)modules, described below. All level–1 calorimeter triggers, except the global ones, are based on a sliding window algorithm to find (isolated) local $\mathrm{E_T}$ maxima in a limited η-region of the calorimeters (ϕ is fully covered). Windows are $n \times n$ trigger elements in $\eta - \phi$ space. A trigger element is the basic component of the trigger algorithms with a dimension which depends on the trigger object. These will be described in the following.

e/γ Trigger

The electromagnetic trigger algorithm, with no distinction between electrons and photons (hence the name), is performed by the *cluster processor* module. The trigger elements input to the e/γ trigger algorithm are the pre-processed trigger tower signals, referred to as the trigger elements, in form of two separate maps for the electromagnetic and the hadronic calorimeters. The e/γ Trigger covers the precision physics region $|\eta| < 2.5$ with an algorithm implemented based on a sliding window of 4×4 trigger elements. Two such windows are considered, in the ECAL and in the HCAL, overlapping each other completely as seen from the interaction point. The central 2×2 trigger elements (or TTs), i.e. the core, in the ECAL is then checked to be a local $\mathrm{E_T}$ maximum. This is realized by requiring the $\mathrm{E_T}$ deposit in the core, to be higher than the $\mathrm{E_T}$ deposit in all possible 2×2 neighbouring clusters to the right and to the top of the core, and at the same time to be higher than or equal to the $\mathrm{E_T}$ deposit in the all possible 2×2 neighbouring clusters to the left and to the bottom of the core. This process is called a de-clustering[†] and the core cluster, if a local $\mathrm{E_T}$ maximum, is known as the RoI cluster. The centare coordinate of the lower left trigger element within the (e.m.) RoI is the RoI coordinate. The local $\mathrm{E_T}$ maximum determination method just explained, the so-called de-clustering, avoids in a simple way any RoI double counting. The de-clustered RoI would now be flagged as an electromagnetic trigger object, i.e. e/γ trigger, if in addition the following conditions are also fulfilled:

$\Rightarrow$ The $\mathrm{E_T}$ deposit in at least one of the 2×1 or 1×2 trigger element combinations, called the e.m. cluster, within the RoI, be higher than the electromagnetic cluster threshold.

[†]Obviously the 9 2×2 ($\equiv (\Delta\eta \times \Delta\Phi) \sim (0.2 \times 0.2)$) clusters within the 4×4 ($\equiv (\Delta\eta \times \Delta\Phi) \sim (0.4 \times 0.4)$) trigger window overlap with all their neighbouring clusters.

It must be noticed that the e.m. RoI cluster is defined differently than the e.m. cluster (they have simply different sizes).

⇒ The total E_T deposit in the electromagnetic isolation ring, i.e. the summed E_T in the 12 trigger elements surrounding the e.m. RoI, be lower than the e.m. isolation threshold.

⇒ The total E_T deposit in the central 2×2 trigger elements in the hadronic calorimeter, right behind the e.m. RoI cluster, be less than the hadronic core veto threshold.

⇒ The total E_T deposit in the hadronic veto (or isolation) ring, right behind the e.m. isolation ring, be less than the hadronic ring veto (or isolation) threshold.

If all these conditions are met, an e/γ trigger candidate has been found. The trigger window is then slid, either in η or in ϕ direction, by one trigger element (or TT). The trigger criteria are then once again for the new window position evaluated. This procedure is repeated till the whole calorimeter is covered ($|\eta| < 2.5$). The simultaneous trigger windows in the ECAL and in the HCAL are always fully overlapping – as seen from the impact point – and slide at the same time to the same direction (or position). A pictorial representation of the trigger elements and criteria is illustrated in Figure 3.6. A total of 8 sets of trigger parameter combinations (E_T thresholds) are foreseen, which serve as a means of classification of the triggers. The multiplicity of the trigger objects passing each trigger set is counted and sent to the CTP for further processing. The maximum number of the multiplicity count, which could be sent to the CTP, for each E_T threshold set is limited to 7 (three bits). The RoI multiplicities sent to the LVL2 trigger do not suffer from this restriction.

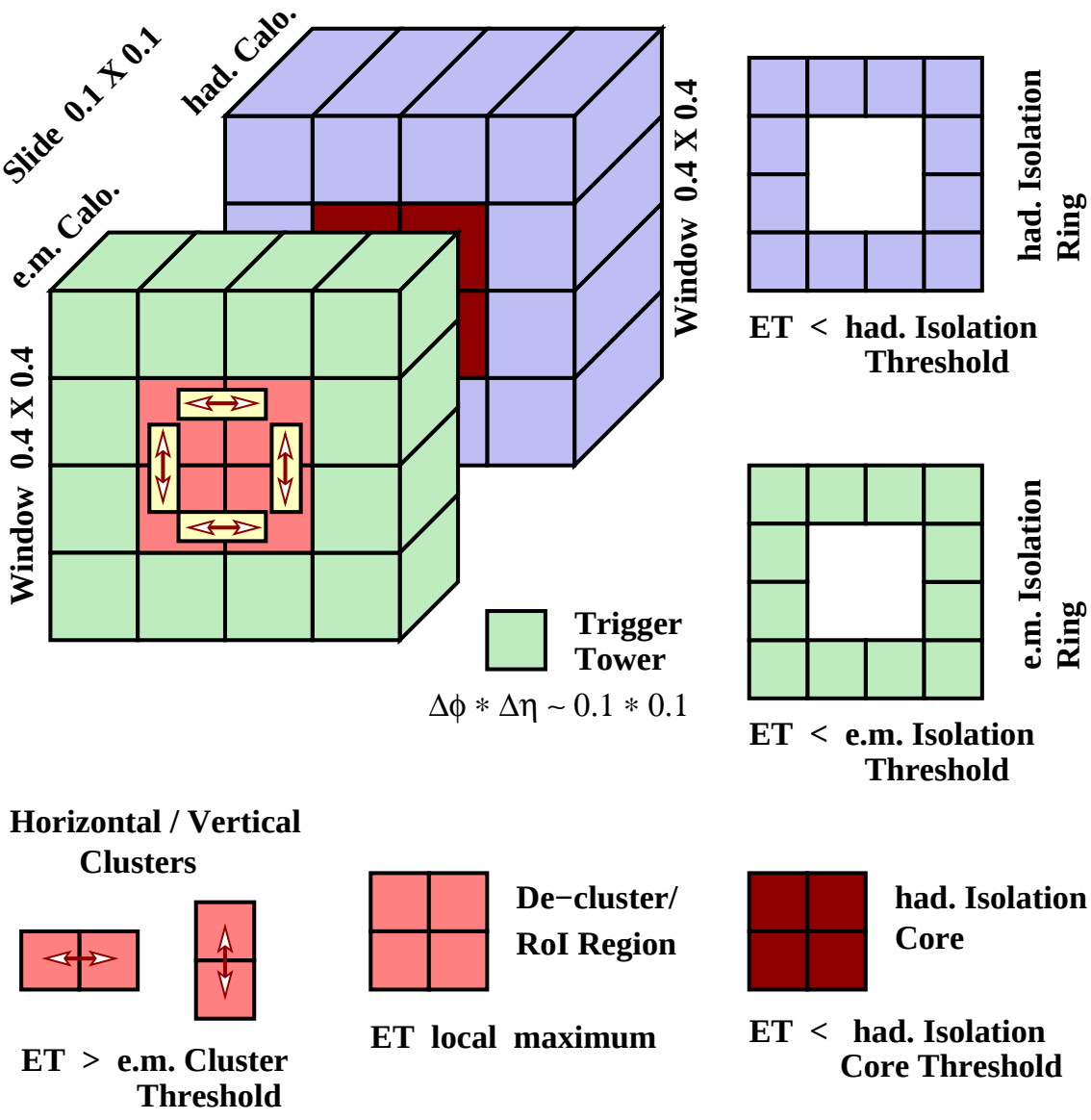

Figure 3.6: *The ATLAS LVL1 electromagnetic trigger algorithm/elements.*

τ/h Trigger

The (isolated) single hadron trigger, constructed to capture τ's decaying hadronically, is also performed by the cluster processor. It is based essentially on the same basic principles as the e/γ trigger, but with few redefinitions of some trigger parameters (or elements). Here the RoI cluster, also used to apply the de-clustering scheme, is the sum of the electromagnetic and the hadronic 2×2 core clusters. The τ RoI cluster is examined to be a local E_T maximum, according to the same scheme applied in the case of the e/γ trigger, in a window of 4×4 e.m+had trigger elements. The trigger criteria in this case are:

- $\Rightarrow$ The E_T deposit in at least one of the $2 \times$ 1e.m.+$2 \times$ 2had. or $1 \times$ 2e.m.+$2 \times$ 2had. trigger element combinations, called the τ cluster, within the RoI, be higher than the τ cluster threshold. The RoI cluster is also in this case different from the τ cluster.
- $\Rightarrow$ The total E_T deposit in the electromagnetic isolation ring, i.e. the summed E_T in the 12 trigger elements surrounding the e.m. 2×2 core, be lower than the e.m. isolation threshold.
- $\Rightarrow$ The total E_T deposit in the hadronic isolation ring, right behind the e.m. isolation ring, be less than the hadronic ring isolation threshold.

Here again the trigger window is slid by one trigger element sideways, i.e. in η and/or ϕ directions, till the region specified for the trigger is completely covered. The τ trigger algorithm together with it's elements are explained in Figure 3.7. The multiplicity and the number of threshold sets for this trigger is exactly the same as for the e/γ trigger.

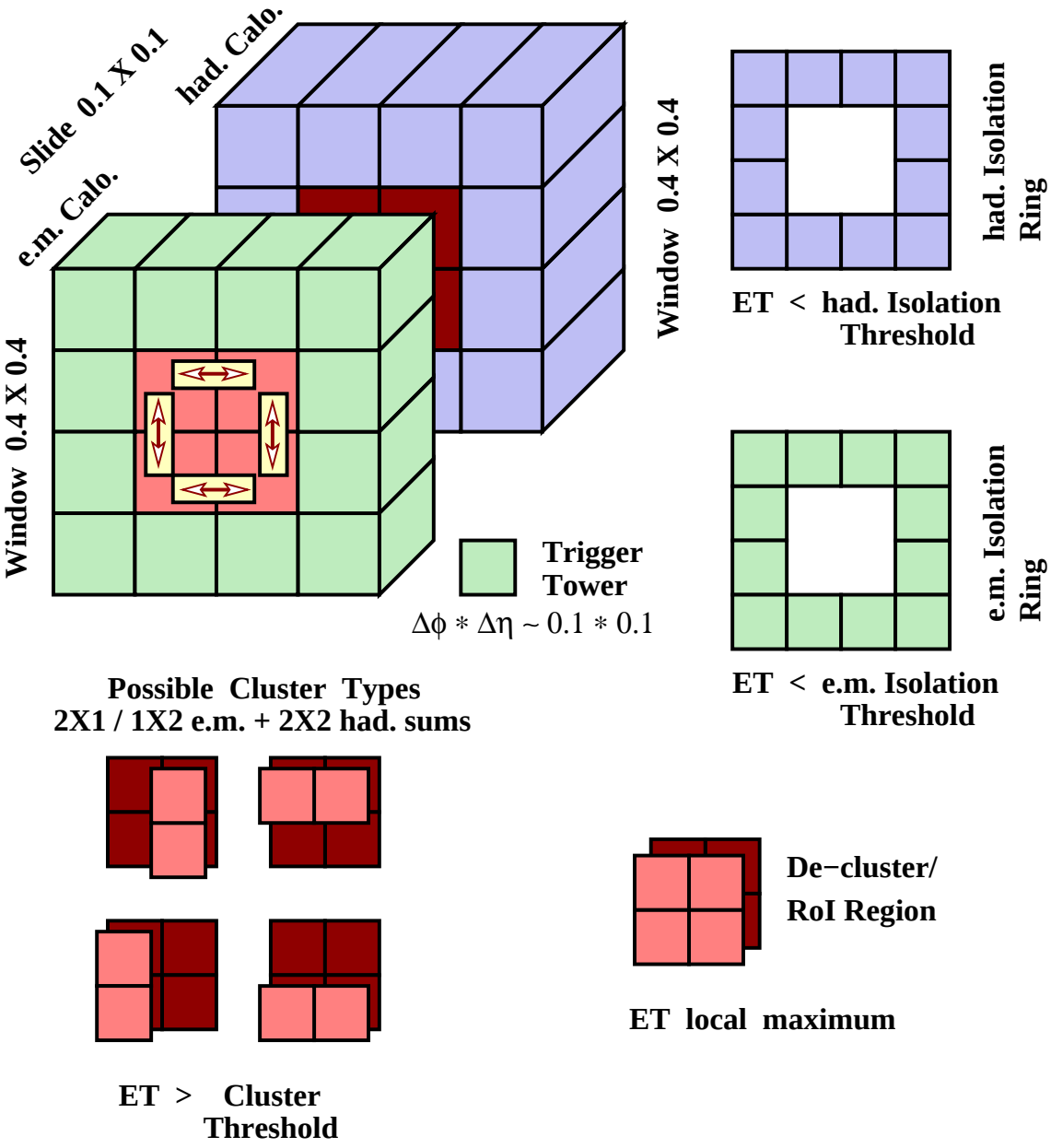

Figure 3.7: *The ATLAS LVL1 Tau/single-hadron trigger algorithm/elements.*

jet trigger

The jet trigger algorithm is performed in the *jet/energy-sum processor* module, which receives as input a e.m+had. map with a courser cell granularity. The trigger elements in this case are basically $(\Delta\eta \times \Delta\phi) \sim (0.2 \times 0.2)$ cells summed in ECAL and HCAL. The basic trigger element (or smallest element entering the trigger algorithm) is referred to as the jet element ($(2 \times 2)_{ECAL+HCAL}$ summed trigger towers) in analogy to the e/γ and the τ trigger. The region covered by the jet trigger is $|\eta| < 3.2$. Three different types of trigger algorithms, distinguished by their cluster, RoI and window sizes, are foreseen for the jet trigger. Like the other triggers discussed so far, the jet trigger is also based on a sliding window algorithm in all three cases. All three types of the jet trigger algorithm and the corresponding elements are displayed in Figure 3.8. The largest trigger window considered is

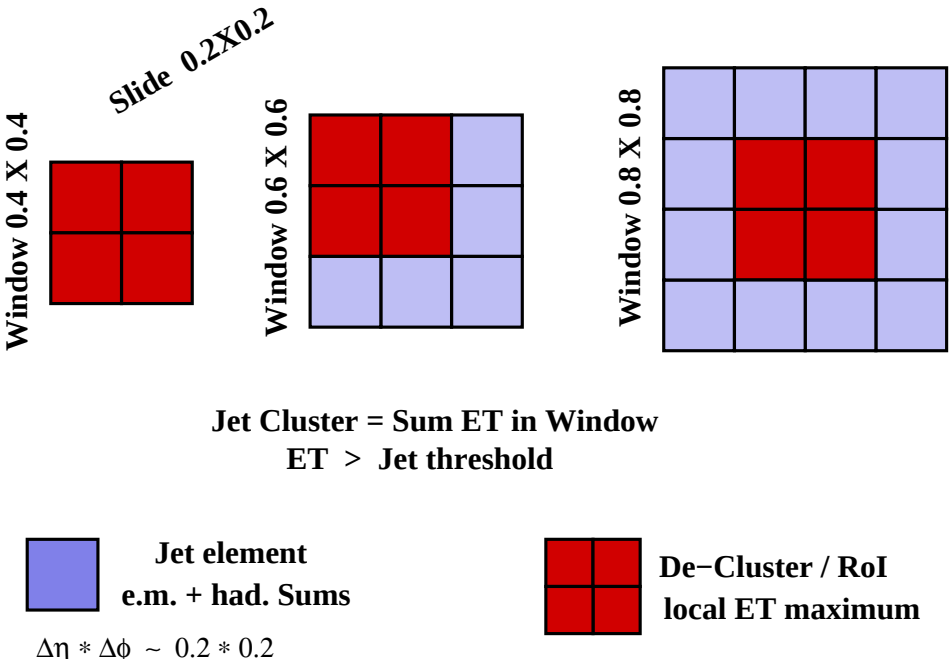

Figure 3.8: *The ATLAS LVL1 Jet trigger algorithms/elements.*

a 4×4 ($\equiv (\Delta\eta \times \Delta\Phi) \sim (0.8 \times 0.8)$) jet element window. The 2×2 core cluster is used as the RoI and de-clustering purposes. The RoI cluster is required to be a local E_T maximum by de-clustering, according to the applied method in the e/γ (or τ) trigger case. The jet cluster though here is defined[‡] to be the window itself. A trigger is accepted when after the de-clustering the total E_T deposit in the jet trigger window is above the jet cluster threshold. The second window size considered for the jet trigger is a 2×2 ($\equiv (\Delta\eta \times \Delta\Phi) \sim (0.4 \times 0.4)$) jet element combination. Here the RoI and the jet cluster are overlapping. The de-clustering information could in principle be extracted from the 4×4 window case (it is actually the same). The conditions for a trigger is the same as those for the 4×4 window size, with the exception of the jet cluster size which is smaller, i.e. 2×2 jet elements. A 3×3 ($\equiv (\Delta\eta \times \Delta\Phi) \sim (0.6 \times 0.6)$) jet element window is another possibility, which obviously fills the intermediate region. The size of the RoI is the same as for the other two window sizes, but

[‡]The RoI then in this case could essentially be considered to be the core and the 12 jet elements in the ring surrounding the core (or RoI) the halo of the jet.

it's location is not restricted to a given position within the trigger window. It could namely be in any corner within the trigger window. The jet cluster E_T is here the total E_T deposited in the window that should pass the jet cluster threshold for a trigger. The de-clustering algorithm though in this case is complicated than the other cases considered so far, and is not fully implemented yet. Therefore in the simulations studying the jet trigger performance, for instance, this option is not fully analyzed. In this case also 8 trigger threshold sets are considered. Multiplicity for each threshold is sent to the CTP system.

$\sum E_T$ and E_T^{miss} triggers

The total and the missing transverse energy deposit in the calorimeters are global quantities evaluated in the range $|\eta| < 4.9$ and are implemented in the jet/energy-sum processor. The basic element size, in this case, is that of the jet elements, input to the JEP module. The $\sum E_T$ and the E_T^{miss} could be considered as a scalar and a vector sum of the E_T deposits of the calorimeter cells – actually deposits in jet elements. The E_T^{miss} quantity is actually calculated in form of the transverse energy imbalance in x and y directions in the transverse plane, using the ϕ information. The E_T^{miss} trigger, specially when combined with other triggers, plays an important role in the LHC experiments (e.g. in the SUSY searches). Four different thresholds for each of these triggers are foreseen.

3.1.3 The level–1 trigger menu

The level–1 trigger algorithms are relatively simple, they look essentially for localized high E_T clusters (apart from E_T^{miss} and $\sum E_T$) in order to be fast. For this reason the LVL1 triggers are inclusive. The level–2 trigger system uses the RoI information from the LVL1 trigger objects in order to optimize the overall trigger items. The Global[§] LVL2 decision performs a final trigger selection which is based on the final state properties of a given process, i.e. based on the event topology. In order to optimize this path of decision taking, several studies have been performed to optimized the performance of the trigger selection procedure. The starting point has been a set of physics signatures of interest, prepared in such a way so as to cover as much as possible of the ATLAS physics goals. A number of benchmark physics channels have been proposed and studied in order to evaluate trigger performance and it's selectivity. The result of such global optimizations has been a set of trigger menus for different trigger levels and physics programs. A complete discussion of these issues with much detailed considerations on trigger menus is given in [47, 39].

Trigger criteria, in order to be able to capture the desired physics, should clearly be efficient. This is what concerns the physics requirements, i.e. high efficiency for physics channels of interest. Whereas what concerns the trigger, in the LHC experiments, is the rate. Clearly the most efficient trigger is one that keeps everything, which is not affordable in this case. The LVL1 trigger suffers from the huge number of QCD jets, which also fake almost all other trigger objects, and muons, which are simply numerous in the LHC environment. A compromise between physics efficiency and limits on trigger rates has motivated these physics-oriented trigger menus. A list of the level–1 trigger menus at low and high luminosities is

[§]The major interest in this section is a discussion of the LVL1 trigger menu and therefore any eventual (and still un-clarified) overlap between the LVL2 trigger and the Event Filter, regarding the final state topology, is irrelevant.

given in table 3.1. This must noted that this trigger menu is not final yet and may be modified when more trigger analysis results are available.

Table 3.1: *The LVL1 low and high luminosity trigger menus and the the corresponding rate for each item. The notation convention in this table regarding the trigger name is as follows. The first one or two letters refer to the trigger object:* MU = μ, EM = e/γ, T = τ/h, J = *jet*, XE = E_T^{miss} . *This is followed by the trigger* E_T *thresholds in GeV. The entry* others *leaves room for triggers for other purposes, like calibration and monitoring. The letter I after some of the thresholds indicates whether the trigger object, in addition to the applied threshold, is also required to be isolated. And multiplication with a number, e.g.* $\times 2$*, stands for the trigger multiplicity.*

Low Luminosity		**High Luminosity**	
Trigger	**Rate (kHz)**	**Trigger**	**Rate (kHz)**
MU6	23	MU20	3.9
		MU6×2	1
EM20I	11	EM30I	22
		MU10 + EM15I	0.4
EM15I×2	2	EM20I×2	5
J180	0.2	J290	0.2
J75×3	0.2	J130×3	0.2
J55×4	0.2	J90×4	0.2
J50 + XE50	0.4	J100 + XE100	0.5
T20 + XE30	2	T60 + XE60	1
others	5	others	5
Total	**44**	**Total**	**40**

The evaluated total level–1 trigger rate, in the trigger menus, of about 40 kHz is less than the canonical 75 kHz rate budget, in order to take into account the uncertainties involved in various simulations. The quoted trigger rates should only be considered as indicative figures. This safety margin leaves certainly also room for extra, and more specialized, entries. It should also be noted that the trigger E_T thresholds quoted in the trigger menus for a given trigger applies to the offline thresholds at the point where LVL1 triggers are 95% efficient. This means that the actual trigger thresholds are set at lower values. For an example of the method to determine and apply the thresholds see the next chapter. Another point which may be in place to mention here is the fact that the inclusive jet trigger thresholds are quite high. The reason for this is that the additional jet rejection capability at LVL2 is small and therefore the LVL1 inclusive jet thresholds should be set at a rather high value in order to reduce the input rate to LVL2 trigger. Finally the combined and multiple trigger entries in the menus should allow the application of lower thresholds on specific objects.

3.2 Level–2 Trigger, Functional overview

Functionally the LVL2 trigger system processes the input data at several stages. The first functional stage in data processing at LVL2 trigger is to collect ROI data from the ROBs for events selected by LVL1 trigger[¶]. The data collection stage at LVL2 may, to a certain extent, be combined with some sort of data preprocessing, e.g. zero–suppression or data compression and/or reformatting, prior to the actual data transmission to the LVL2 processor farm. The second stage of the LVL2 data processing is the feature extraction within each sub–detector separately. Information obtained from different sub–detectors at this stage is combined together in the subsequent one, in the so called object building stage. The global–decision algorithms are applied at the last stage of the LVL2 trigger system[‖]. In the following a brief description is given for each of the stages mentioned above. The full and detailed description is to be found in [39] and references therein.

3.2.1 Preprocessing

Information associated to the RoIs is extracted from the ROBs at this stage. This is a process depending strongly on the sub–detector type. For the precision–tracking detectors, i.e. the SCT and the pixels, adjacent strips or pixels are clustered into *hits* that may correspond to a single track. At this stage space points are determined and the local coordinates of the wafers, in the form of strip/pixel numbers, are converted to $\eta/\phi/r$ global ones. In the transition radiation tracker, TRT, all wires are scanned for hit information. Here the amount of data transmitted from the ROBs is reduced by compacting and reformatting the ROB data associated to a given RoI. In the case of the calorimetry the data is formatted in a manner so that to keep the trigger towers belonging to a given ROB or RoI together. In general the preprocessing in the calorimetry is nothing but collecting the fine–granular cell information belonging to an RoI.

Preprocessing is a very time consuming process and no optimization on the algorithms as such has yet been studied in detail in order to minimize the amount of computing time consumed at this stage.

3.2.2 Feature extraction

Feature extraction algorithms for the LVL2 trigger analyze LVL1 RoI data at the level of individual sub–detector system. This stage of data processing is the main part of the LVL2 trigger system. The overall LVL2 trigger performance in terms of efficiency and background rejection is determined by the power of the algorithms at this step. Being the most important stage, the corresponding algorithms are more complex than both the preceding and the following stages. The algorithms will briefly be explained in the following. However, they are not final and should be considered as prototypes. A major criterion for the algorithms is that they should be fast and therefore relatively simple to implement in the LVL2 trigger.

[¶] This the general case. Data processing without the guidance of LVL1 RoIs will not discussed here.

[‖] Special trigger algorithms are required for B–physics studies. These are described for instance in [39] and are not discussed here.

3.2.2.1 Level–2 muon trigger

The LVL2 muon trigger identifies muon tracks by using the information from the muon spectrometer and calculates the transverse momentum of the muon accurately and at the same time performs extrapolation to the inner tracker and calorimeter. The algorithms are initiated by using the hit information from the fast LVL1 muon trigger, i.e. the RPCs or the TGCs, with very low occupancy. Within the RoIs, provided by LVL1, a pattern recognition of muon tracks in muon chambers, i.e. in MDT chambers, is performed using position information. This is followed by a fit of tracks using drift–time. The last step is a transverse–momentum fit.

3.2.2.2 Level–2 calorimeter trigger

The LVL2 trigger refines the LVL1 global and RoI information using full–granularity, full–precision calorimeter information. The RoI information is in form of (η,ϕ) position and E_T range of the trigger object. The position resolution is $\Delta\eta \times \Delta\phi \sim 0.2 \times 0.2$ for jet triggers and $\Delta\eta \times \Delta\phi \sim 0.1 \times 0.1$ for others. The global information, calculated at LVL1 and provided for LVL2 trigger, is in form of the vectorial and the total scalar E_T sum quantities.

The RoI–associated data from the ROBs are collected by LVL2 in $\Delta\eta \times \Delta\phi$ regions of a size depending on the LVL1 position resolution of the trigger object and on the LVL2 trigger algorithm to be applied. First step is to verify the LVL1 decision by recalculating the cluster and/or isolation E_T parameters for a given trigger object, and improving the cluster position information. All other LVL2 trigger algorithms are performed in windows centered at this position. Because of the steeply falling E_T spectrum of the background, the refined E_T calculation, together with improved luminosity dependent calibrations, makes it possible to optimize various trigger thresholds and to perform tighter E_T cuts at LVL2. This will also make it possible to have a better control on the LVL2 output rate.

The LVL2 photon and electron trigger objects are preselected (and formed) by first applying the so called e/γ (or electromagnetic) cluster trigger, which is a calorimeter–only trigger. The LVL2 e/γ cluster trigger, after E_T and position improvements within the LVL1 RoIs, builds shower shape variables to discriminate electromagnetic clusters from jets. This is done by studying:

- the leakage of the electromagnetic showers into the hadronic calorimeter,
- the lateral shower shape in the second calorimeter sampling,
- the energy deposition in the ECAL (fine–granular) first sampling.

Based on these quantities the LVL2 e/γ trigger verifies whether the LVL1 RoI clusters are compatible with e/γ clusters (e.g. rejecting π^0's or hadronic showers with high e.m. fractions). In this way a rejection with respect to that of LVL1 is achieved before the application of the LVL2 photon and electron triggers. The final particle identification is performed later by combining the tracking information from the inner tracker information explained later.

The LVL2 calorimeter τ algorithm is based on the selection of isolated narrow jets associated with few tracks in the tracking system. The shower shape and isolation quantities within

windows are calculated in each calorimeter type separately. The first step in the LVL2 calorimeter algorithm is to refine and verify the LVL1 decision. The same algorithm as in the LVL1 case is applied here, except that the more accurate and refined cell information is used at LVL2. The second step is the τ identification. Both these steps are performed on quantities calculated using refined calorimeter deposits. The calorimeter quantities are calibrated using the jet calibration, as opposed to the e/γ trigger case above, where the electromagnetic calibration is used. Finally the calorimeter cluster information is combined with the inner tracker information to identify τ candidates.

The LVL2 also treats jets in order to reduce the rate of events containing jets. This is done by improvements in E_T and position calculations of jet measurements, which in turn is achieved by refined energy calibration, refined jet definition and threshold adjustments. An important point here is that in contrast to the e/γ clusters for instance, where jets could be considered as background, jets can not be classified as such.

A reduction of data transfer from the ROBs to the LVL2 system is minimized by building (projecting calorimeter cells into) trigger towers ($\Delta\eta \times \Delta\phi \sim 0.1 \times 0.1$). The LVL2 jet algorithm starts with the application of an E_T cut on calorimeter cells in order to eliminate electronic noise contribution. Only cells passing this cut are included in the tower summation. Further, because of the non–compensating ATLAS calorimetry, the response to jets is optimized by applying a weighting procedure during the cell projection into towers. This weighting procedure is referred to as jet calibration, also mentioned above. The LVL2 jet reconstruction algorithm is a cone algorithm with radius $\Delta R = \sqrt{\Delta\eta^2 + \Delta\phi^2} \sim 0.4$ applied on LVL2 trigger towers within a $\Delta\eta \times \Delta\phi \sim 1.0 \times 1.0$ window around each LVL1 RoI.

3.2.2.3 Level–2 tracking trigger

The information from the inner detector regarding the presence of a high-p_T track is an important component in the reduction of the LVL1 e.m. cluster trigger rate from di-jet events. Simple and fast algorithms search for track segments separately in the precision tracker and in the TRT. The low-p_T tracks required by B-physics necessitates full scan of the TRT. The identified LVL2 RoIs are then extended back to the precision tracker. The combined information of the SCT and the pixel detectors (the precision tracker) is fed into a common feature extractor. In addition, a stand alone pixel trigger is also implemented that will make possible an impact-parameter measurement with good resolution, which provides a b-tag (b-jet trigger).

3.2.3 Building and identification of trigger objects

The identification of trigger objects at LVL2 is performed by first combining the feature information from different sub–detectors to form objects. The work to develop algorithms in this area for the LVL2 trigger and also in the offline reconstruction software are in progress. Therefore the algorithms are not final and not completely optimized. For details of the algorithms and the selection cuts, together with the performance issues see [**?**].

The muon trigger rate could be reduced, with respect to that of the LVL1 and the subsequent LVL2 feature extraction (described above), further by using information from the inner

tracker. Calorimeter information is used to determine whether the muon is isolated or not. A core size with a radius of $\Delta R \sim 0.07(0.1)$ in (η, ϕ) in the ECAL (HCAL), with an isolation halo extending to $\Delta R \sim 0.3$ is considered at the moment to discriminate between the isolated muons and the muons within jets (except high–p_T muons coming from b–decays which are isolated).

The photon identification is based on the quantities used for LVL2 e/γ trigger. In order to reject jets, two further quantities are also calculated. These are the shower shape in η direction in the ECAL in the second and in the first samplings, which is broader for jets than for photons. The electron identification requires a track inside the inner detector associated with the reconstructed calorimeter cluster. This reduces the trigger rate due to jets faking electromagnetic trigger. The τ trigger rate is reduced by likewise using the information from the inner tracker.

For completeness it must be noted that the global LVL1 quantities, i.e. the $x-y$ components of the E_T^{miss} and the total scalar E_T are recalculated at LVL2. These quantities will essentially be used in combination with other triggers.

3.2.4 The level–2 trigger menu

As in the case of the LVL1 trigger, a set of trigger items, optimized for specific benchmark physics channels, are determined and put together in form of trigger menu. The current LVL2 trigger menus for low and high luminosity runs are compiled in Table 3.2. As could be seen from this table, the trigger items are quite similar to those given in the LVL1 trigger menu. Due to the more accurate energy measurement at LVL2, the indicated thresholds are (in most of the cases) the actual trigger thresholds applied. For the low luminosity case a B-physics trigger menu is also implemented, which goes under the "B-physics" entry in Table 3.2 and specializes in the low momentum muon trigger combined with other relevant signatures, e.g. reconstructed di-electron mass or B-meson mass, for CP violation studies in B-sector.

It must be noted that in addition to the trigger items tabulated in form of trigger menus for LVL1/LVL2 trigger combinations, specialized triggers to cover specific physics topics, e.g. QCD studies, are likewise under investigation. Perhaps one of the most important and crucial trigger item belonging to this latter category is the implementation of a b-jet tag trigger using the impact-parameter measurement in the precision tracker. This special trigger will prove useful in reducing the LVL1 jet trigger rate for multi b-jet final state signals.

Table 3.2: *The LVL2 low and high luminosity trigger menus and the the corresponding rate for each item. The notation convention in this table regarding the trigger name is similar to that of the LVL1 case, except that the greek letters are used to indicate the objects, and small roman letters to specify signal characteristics, like isolation (an appended "i" after the threshold). The entry* others *leaves room for triggers for other purposes, like calibration and monitoring. The B-physics trigger item covers the very low* p_T *muon trigger for CP violation studies and is not discussed further here.*

Low Luminosity		**High Luminosity**	
Trigger	**Rate (Hz)**	**Trigger**	**Rate (Hz)**
μ20	200	μ20i	200
		μ6×2 + m_B	10
		μ10×2	80
e20i	100	e30i	600
e15i×2	∼few Hz	e20i×2	20
γ40i	100	γ60i	400
γ20i×2	5	γ20i×2	200
j180	100	j290	120
j75×3	80	j130×3	80
j55×4	40	j90×4	80
j50 + xE50	250	j100 + xE100	∼few 100
τ20 + xE30	400	τ60 + xE60	∼few 100
μ6i + e15i	15	μ10i + e15i	20
B-Physics	1130		
others	100	others	100
Total	**2400**	**Total**	**2000**

Chapter 4

The level–1 calorimeter trigger rates from fast simulation

A first attempt to estimate the LVL1 trigger rates has been performed by using a fast simulation* containing a simplified parameterization of the detector response and a complete implementation of the LVL1 calorimeter trigger chain as explained in [54]. The trigger rates presented in this chapter have either a global character, e.g. E_T^{miss} , or are objects built of several trigger towers, e.g. jets, which therefore, to first approximation, are basically not affected by the fine details of the detector performance issues. Trigger objects implemented to capture electromagnetic particles, i.e. the e/γ trigger, and the hadronic decay of the τ lepton, i.e. the $\tau/hadron$ trigger, which rely heavily on the internal structure of the shower developments, e.g. the isolation criterion, can not be studied reliably in this way and will need the extentions/modifications explained in chapter 5.

4.1 Introduction

Missing transverse energy will be one of the distinct signatures at LHC to select interesting physics processes. Many extensions of the Standard Model include weakly interacting particles which, if produced, at LHC, will escape detection. Their presence will however be signaled by an imbalance of transverse momentum. Among the basic building blocks of the level–1 calorimeter trigger is the summation of the total transverse energy deposited in the calorimeters. Together with the scalar sum $\sum E_T$ also the components E_x and E_y in the plane transverse to the beam axis are computed in the jet/energy-sum processor of the level–1 trigger system. Although the E_T^{miss} trigger itself is not included in the basic level–1 triggers [47], it's combination with the single jet and tau triggers is important to allow for triggering on interesting events with low jet or tau thresholds.

Due to the large cross section, QCD 2–jet events dominate the E_T^{miss} trigger rate at low values of missing transverse momentum [53, 54]. Their contribution depends strongly on the achievable E_T^{miss} resolution. This resolution is mainly determined by the detector acceptance, the calorimeter response and resolution and the hardware realization of the E_T^{miss} trigger.

*For a detailed description of these issues and extensions/modifications to these see chapter 5 and 6.

These effects have been studied using the same simulation chain as the one used to obtain the results presented in this chapter and can be found in [51]. In the following some trigger rates obtained at low and at high luminosities are presented and some conclusions are extracted, which are discussed in the last section.

4.2 Level–1 Trigger Rates at Low Luminosity

4.2.1 Contributions to the E_T^{miss} Spectrum from QCD Jet Events

The calculation of the inclusive E_T^{miss} spectrum is affected by large uncertainties, since in addition to the contributions from physics channels, also contributions from instrumental effects are important which can not be calculated reliably at present. Among such effects are machine induced backgrounds, beam gas interactions as well as contributions resulting from extreme tails in the detector performance.

In the present note an attempt is made to calculate the contribution of QCD jet and minimum bias events to the E_T^{miss} spectrum. These events will add a significant contribution to the E_T^{miss} trigger rate given their high production cross section together with resolution effects of the missing transverse energy measurement in the trigger.

In order to simulate the total inelastic proton-proton cross section of 70 mb, the following procedure has been applied: in the QCD jet simulation using the PYTHIA Monte Carlo program [56, 57] the P_T cutoff value, which has to be introduced in order to cutoff the divergent tree-level cross sections, has been chosen such that the total QCD jet cross-section corresponds to 70 mb. This cross section value is obtained for a cutoff value of 4.3 GeV. Applying this procedure assumes that typical minimum bias events can be described by low P_T tree level QCD jet production. Since in any case the contributions of low P_T jet or minimum bias events to the E_T^{miss} spectrum are small for large values of missing transverse momentum, the uncertainty introduced by using this method is considered to be small. For the low luminosity simulation the E_T^{miss} spectrum as well as the trigger rates have been calculated without pile-up as well as with the superposition of 2.3 minimum bias events on average.

The reconstructed E_T^{miss} spectra at the trigger level for the simulated events are shown in Figure 4.1. Due to the degraded E_T^{miss} resolution the spectrum is found to be slightly harder if on average 2.3 minimum bias events are added.

These spectra can be directly turned into level-1 E_T^{miss} trigger rates. They are shown in Figure 4.2 as a function of the E_T^{miss} threshold.

In Figure 4.3 the P_T spectrum of the generated leading parton is plotted for the case where 2.3 minimum bias events have been added. On the same figure the accepted cross sections of events passing E_T^{miss} thresholds of 40 and 60 GeV are shown. As can be seen, no events with low P_T partons contribute to the accepted trigger rates for high E_T^{miss} at low luminosity.

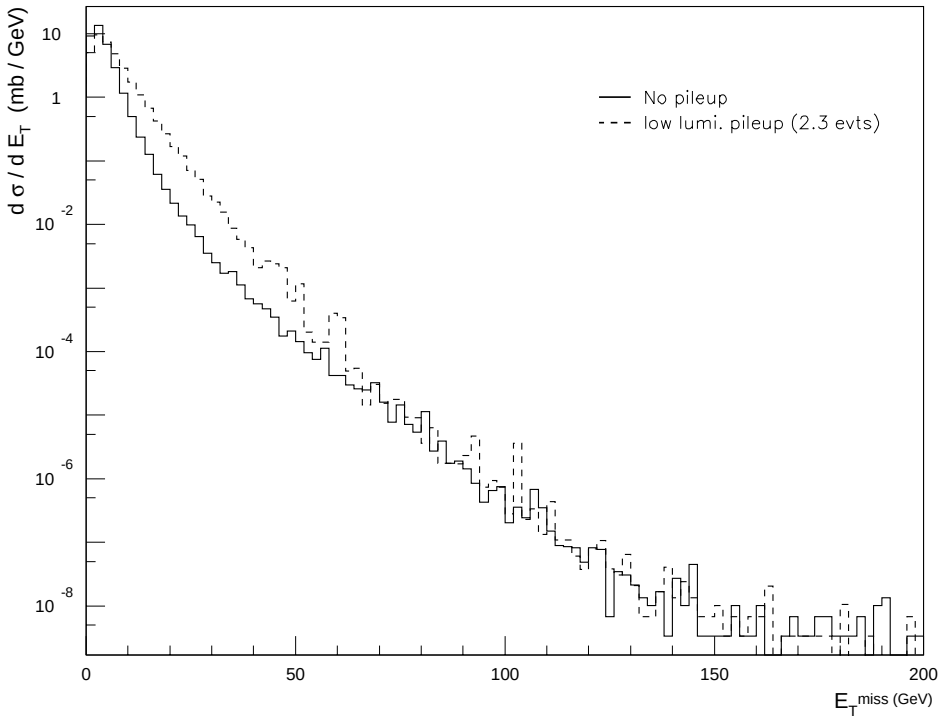

Figure 4.1: *Contribution of QCD two jet events to the E_T^{miss} spectrum with and without the superposition of low luminosity pile-up.*

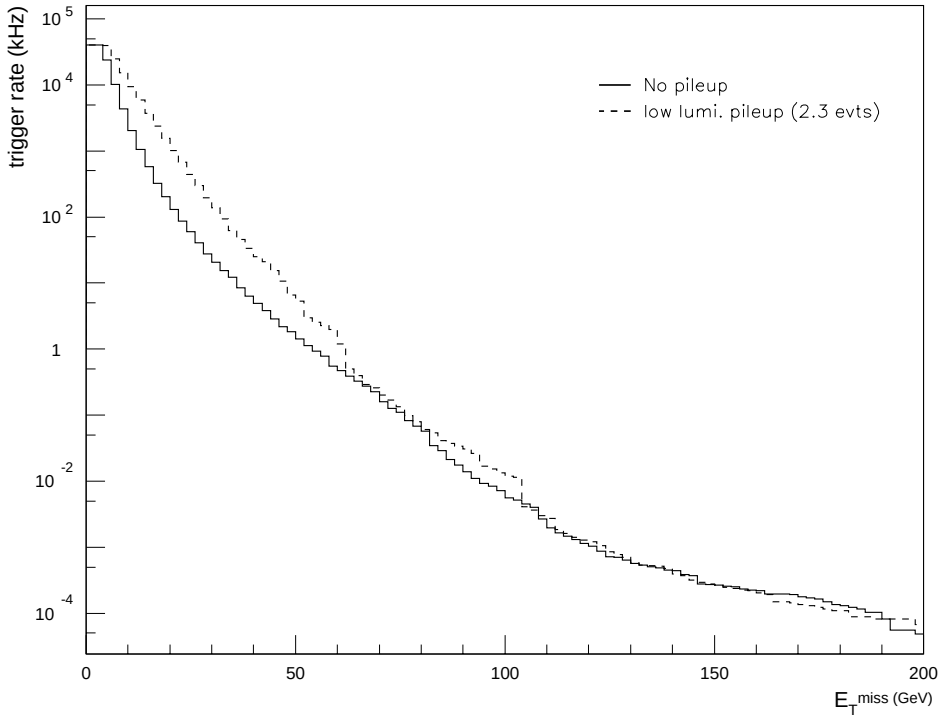

Figure 4.2: *Inclusive E_T^{miss} trigger rates from QCD jet events as a function of the* $\mathrm{E_T^{miss}}$ *threshold used in the level–1 trigger.*

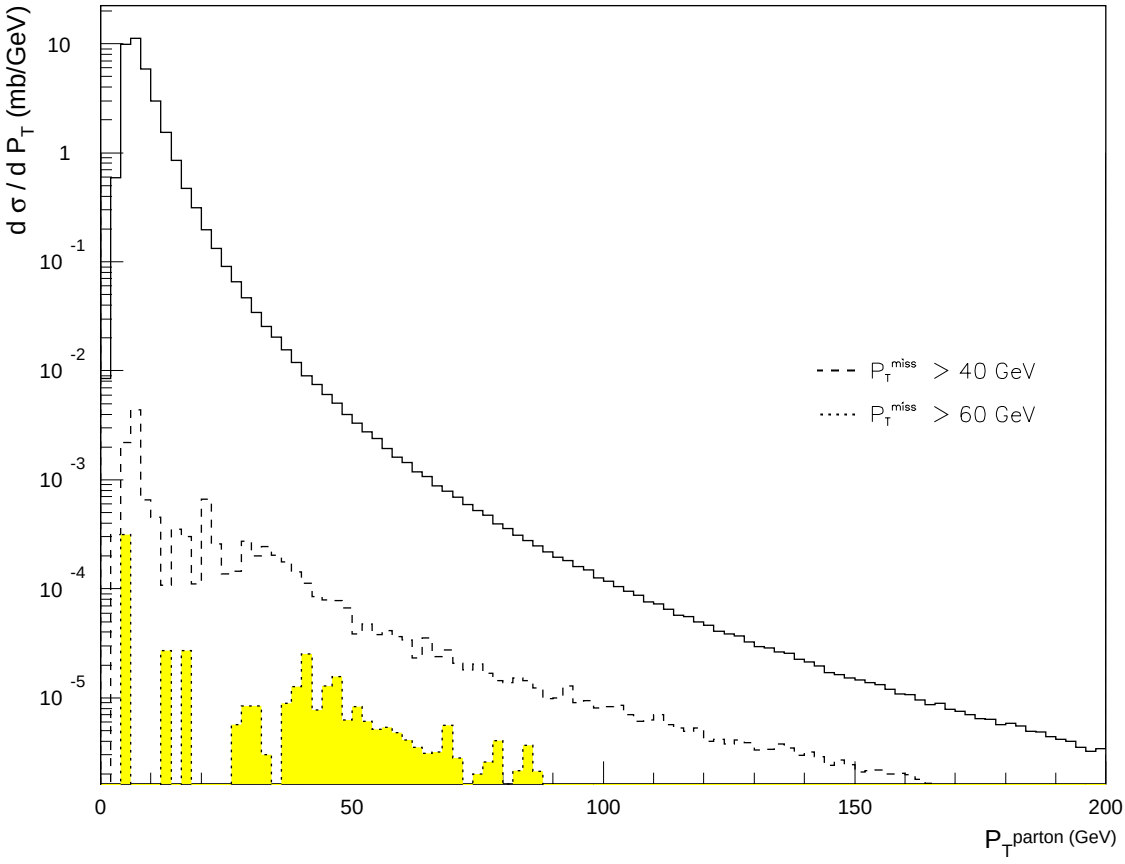

Figure 4.3: *The P_T spectrum of the leading parton of the generated QCD jet events. The fraction of events accepted passing various E_T^{miss} thresholds is indicated by the dashed curves.*

4.2.2 Combined Trigger Rates: Jet + $\mathbf{E_T^{miss}}$

A combination of the E_T^{miss} trigger in association with the single jet trigger is among the basic level–1 triggers of ATLAS. Before the combined trigger rates are evaluated, it is important to establish the relation between the jet energy scale and the level–1 jet trigger scale. Differences between these scales might arise from the different geometrical size of the jet windows, since a cone with a radius of 0.4 or 0.7 is used in the reconstruction while a fixed window of $\Delta\eta \times \Delta\phi$ = 0.8 × 0.8 is used in the trigger. In the following a comparison is made between the jets reconstructed offline by using the ATLFAST algorithm [67] and the so called level–1 jets.

In Figure 4.4 the trigger acceptance is shown as a function of the reconstructed offline jet transverse momentum. Only jets with a P_T above 15 GeV are used. The acceptance has been determined for various trigger thresholds with values at 10, 20, 30, 40 and 50 GeV. In addition, Figure 4.5 shows the ratio between the energies reconstructed at the trigger level to the ones reconstructed offline using the full calorimeter information. Part a) shows the correlation between the ratio of trigger energy to jet energy as a function of the jet P_T. In part b)-f) this ratio is shown for various bins of the jet P_T. As can been seen, the distributions are broad at low P_T values, which indicates that low thresholds have to be used to trigger with high efficiency on low P_T jets. This on the other hand will lead to a significant increase in trigger rate resulting from fluctuations in the underlying event structure. From these curves, the trigger cluster thresholds have been determined such that the reconstructed jets of a given E_T will be accepted with an efficiency of 95%.

Using these thresholds the trigger rates have been determined. The results are shown in Figure 4.6 for the case where 2.3 minimum bias events have been superimposed on average. The rates are given as a function of the E_T^{miss} threshold for different jet thresholds. Trigger rates for specific combinations of jet and E_T^{miss} thresholds are also given in Table 4.1 for the case where no pile-up events are superimposed and in Table 4.2 for the case where on average 2.3 minimum bias events are added. As mentioned above, these rates have been determined for a threshold setting on the trigger clusters which correspond to an efficiency of 95 % with respect to the offline jets. As can be seen, for low E_T^{miss} thresholds there is a significant increase in trigger rate due to the pile-up addition. This increase is moderate for E_T^{miss} thresholds beyond $\sim$ 50 GeV. If instead of the trigger clusters the thresholds of the reconstructed jets are used directly, i.e. with an ideal threshold curve, the rates as given in Table 4.3 are obtained. They can be considered as lower limits for the combined jet+E_T^{miss} trigger rates at level–2. The deviations from the true level–2 rates will be smaller the closer the level–2 scale is to the offline jet scale.

Table 4.1: Level–1 trigger rates (in kHz) for various combinations of E_T^{miss} and jet E_T thresholds, without the superposition of minimum bias pile-up.

E_T^{miss} (GeV)	20	30	40	50	60	80	100
E_T^0(jet) > 0 GeV	129.3	20.5	4.89	1.38	0.45	0.052	0.003
E_T^0(jet) > 20 GeV	67.9	13.6	3.80	1.17	0.40	0.049	0.003
E_T^0(jet) > 30 GeV	37.0	7.7	2.34	0.80	0.30	0.032	0.002
E_T^0(jet) > 40 GeV	23.1	4.9	1.40	0.49	0.18	0.029	0.002
E_T^0(jet) > 50 GeV	15.4	3.5	0.97	0.35	0.13	0.023	0.002
E_T^0(jet) > 60 GeV	9.7	2.7	0.77	0.26	0.10	0.018	0.002
E_T^0(jet) > 80 GeV	4.3	1.7	0.53	0.17	0.06	0.014	0.001

Table 4.2: Level–1 trigger rates (in kHz) for various combinations of E_T^{miss} and jet E_T thresholds, including 2.3 minimum bias events (low luminosity).

E_T^{miss} (GeV)	20	30	40	50	60	80	100
E_T^0(jet) > 0 GeV	1003.5	138.9	24.89	5.24	1.17	0.056	0.010
E_T^0(jet) > 20 GeV	764.5	124.3	23.72	4.98	1.08	0.054	0.009
E_T^0(jet) > 30 GeV	338.0	74.2	14.71	4.50	0.99	0.050	0.009
E_T^0(jet) > 40 GeV	131.2	25.9	5.19	1.95	0.19	0.033	0.003
E_T^0(jet) > 50 GeV	65.1	14.6	1.41	0.45	0.15	0.027	0.002
E_T^0(jet) > 60 GeV	32.0	6.9	1.03	0.34	0.11	0.021	0.002
E_T^0(jet) > 80 GeV	5.7	2.0	0.64	0.19	0.07	0.008	0.001

Table 4.3: Level–1 trigger rates (in kHz) for various combinations of E_T^{miss} and jet E_T values, assuming an ideal threshold behaviour. On average 2.3 minimum bias events have been superimposed. These rates can be considered as a crude estimate (lower limit) of the level–2 rates.

E_T^{miss} (GeV)	20	30	40	50	60	80	100
E_T^0(jet) > 0 GeV	1003.5	138.9	24.89	5.24	1.17	0.056	0.010
E_T^0(jet) > 20 GeV	41.4	9.8	2.73	0.81	0.26	0.048	0.009
E_T^0(jet) > 30 GeV	21.1	5.6	1.66	0.55	0.17	0.037	0.003
E_T^0(jet) > 40 GeV	12.2	3.8	1.13	0.37	0.13	0.030	0.002
E_T^0(jet) > 50 GeV	6.9	2.5	0.78	0.26	0.095	0.019	0.001
E_T^0(jet) > 60 GeV	4.3	1.8	0.63	0.20	0.068	0.009	0.001
E_T^0(jet) > 80 GeV	1.7	0.8	0.35	0.13	0.048	0.006	0.001

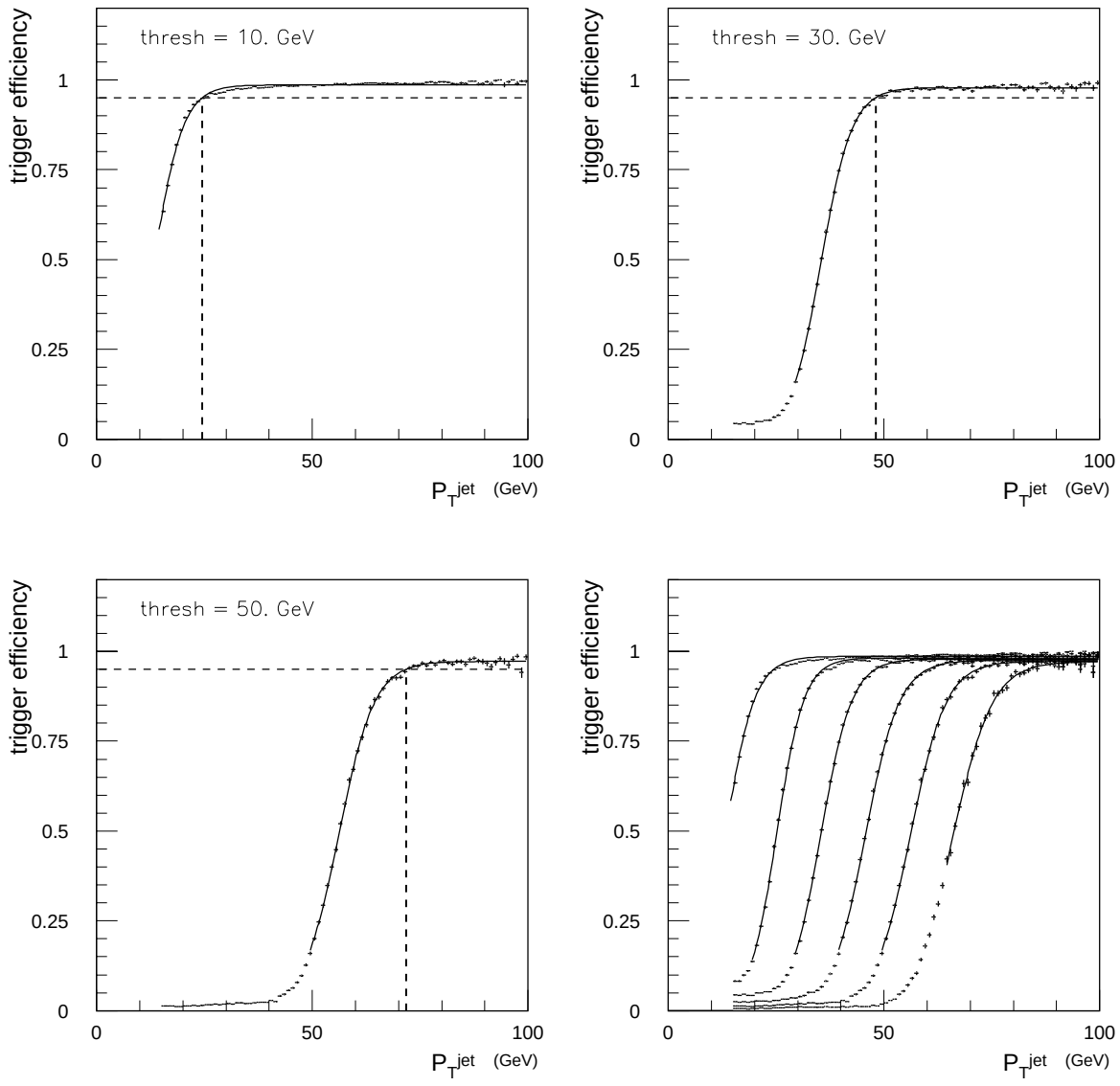

Figure 4.4: *Examples of trigger efficiency curves for trigger cluster thresholds in the range 10 – 60 GeV in 10 GeV steps. The reference scale is the reconstructed jet energy of ATLFAST using a cone algorithm with a radius of 0.7.*

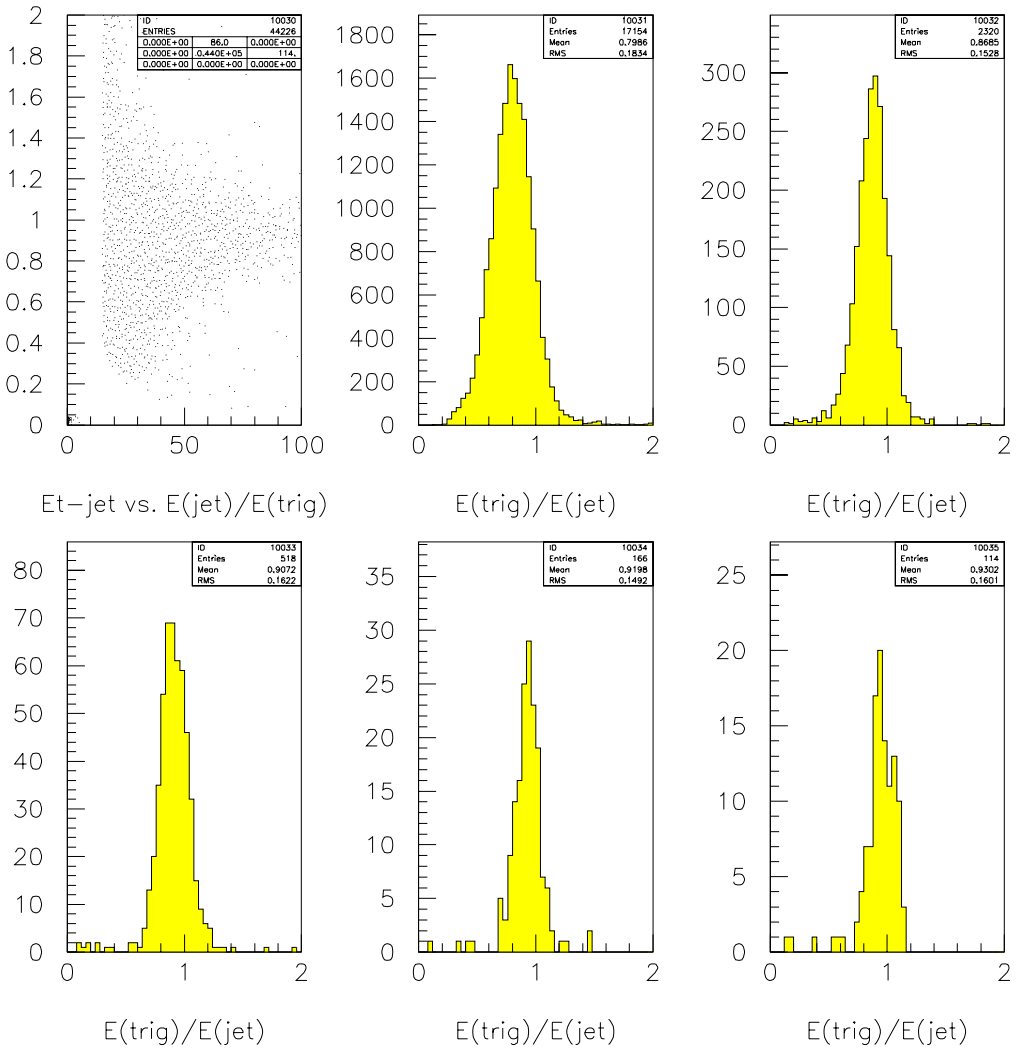

Figure 4.5: *Ratios between the energy in the trigger cluster and the reconstructed ATLFAST jet energy using a cone algorithm with a cone radius of 0.7. Plot a) shows the ratio as a function of the jet E_T, plots b) – f) show the ratio for various bins of the jet E_T.*

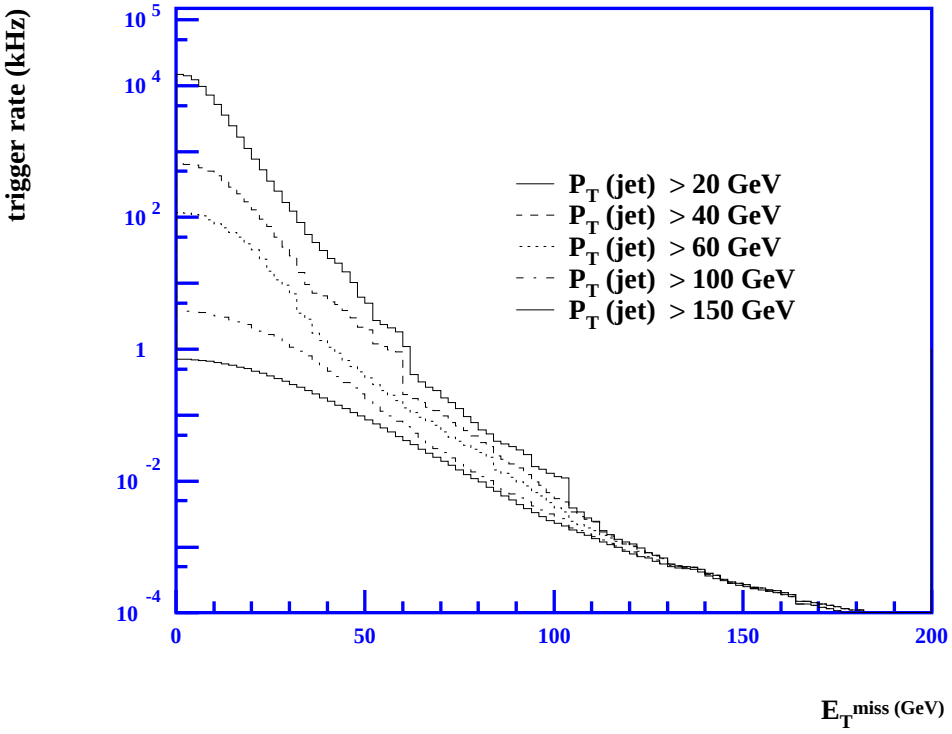

Figure 4.6: *Level–1 trigger rates at low luminosity using the combined jet and E_T^{miss} signatures. The rates are given as a function of the E_T^{miss} threshold for different jet thresholds. On average 2.3 minimum bias events have been added to the hard collision.*

4.3 Level–1 Trigger Rates at High Luminosity

4.3.1 Combined Trigger Rates: Jet + E_T^{miss}

The analysis described above has been repeated for a high luminosity scenario at LHC. In this case 23 minimum bias events have been added on average on the hard scattering process. The calorimeter shaping functions, the complete pulse history and the BCID algorithm are applied as described in Section 2.

The results obtained for the E_T^{miss} spectrum and for the accepted events at the parton level are given in Figure 4.7 and Figure 4.8. Clearly visible is the degradation in the E_T^{miss} resolution, which is reflected by the much broader spectrum. At high luminosity also events with small parton E_T values pass the E_T^{miss} cuts of 40 and 60 GeV.

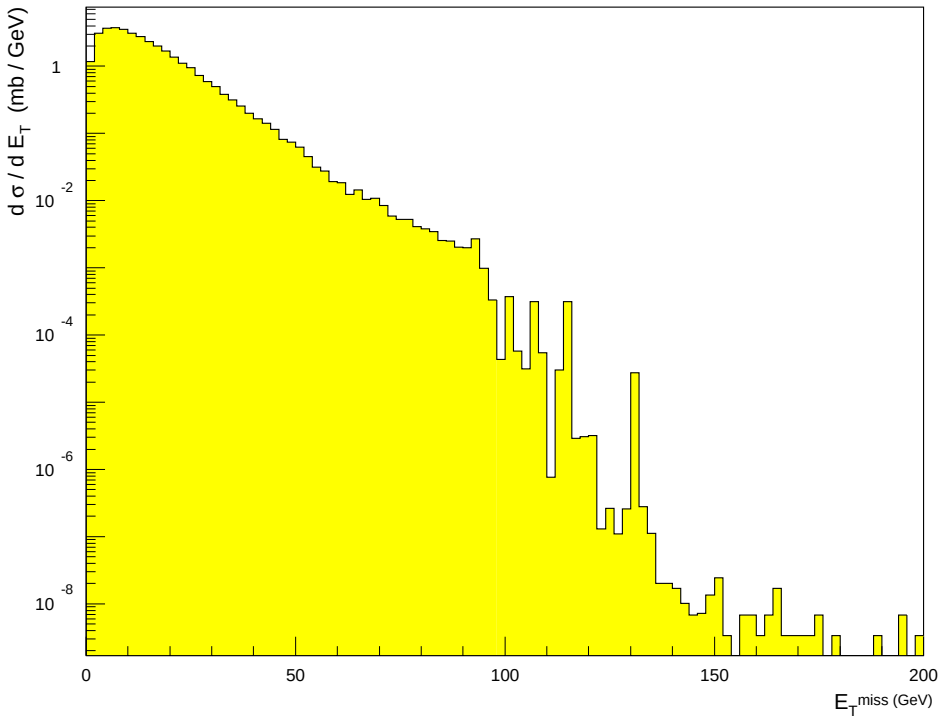

Figure 4.7: *Contribution of QCD two jet events to the E_T^{miss} spectrum, high luminosity.*

The inclusive E_T^{miss} trigger rate and the combined rates including jet requirements are given Figures 4.9 and 4.10. In order to obtain trigger rates in the kHz range, E_T^{miss} threshold around 100 GeV have to be set.

As in the case of low luminosities the trigger rates for specific combinations of jet and E_T^{miss} thresholds are given in Table 4.4. These rates have been determined for a threshold setting on the trigger clusters which correspond to an efficiency of 95 % with respect to the offline jets. If instead of the trigger clusters the thresholds of the reconstructed jets are used directly, i.e. with an ideal threshold curve, the rates as given in Table 4.5 are obtained. They can be considered as lower limits for the combined jet+E_T^{miss} trigger rates at level–2. The deviations from the true level–2 rates will be smaller the closer the level–2 scale is to the offline jet scale.

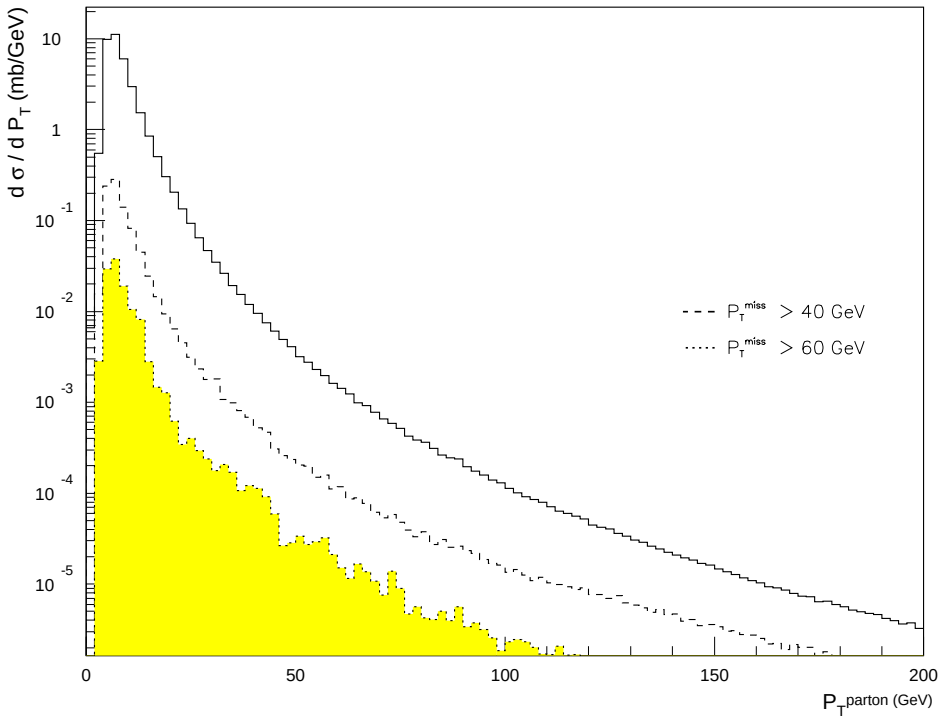

Figure 4.8: *Fractions of accepted events in the E_T^{miss} trigger from QCD jet events for various E_T^{miss} thresholds, high luminosity.*

Table 4.4: Level-1 trigger rates (in kHz) for various combinations of E_T^{miss} and jet E_T thresholds, including 23 minimum bias events (high luminosity).

E_T^{miss} (GeV)	60.	80.	100.	120.
E_T^0(jet) > 60. GeV	484	93	7	0.6
E_T^0(jet) > 80. GeV	298	59	0.1	< 0.1
E_T^0(jet) > 100. GeV	112	58	< 0.1	< 0.1
E_T^0(jet) > 120. GeV	110	58	< 0.1	< 0.1
E_T^0(jet) > 150. GeV	41	0.2	< 0.1	< 0.1

Table 4.5: Level-1 trigger rates (in kHz) for various combinations of E_T^{miss} and jet E_T values, assuming an ideal threshold behaviour. These rates can be considered as a crude estimate (lower limit) of the level-2 rates.

E_T^{miss} (GeV)	60.	80.	100.	120.
E_T^0(jet) > 60. GeV	2	0.4	< 0.1	< 0.1
E_T^0(jet) > 80. GeV	1.1	0.2	< 0.1	< 0.1
E_T^0(jet) > 100. GeV	0.6	0.1	< 0.1	< 0.1
E_T^0(jet) > 120. GeV	0.4	0.1	< 0.1	< 0.1
E_T^0(jet) > 150. GeV	0.1	< 0.1	< 0.1	< 0.1

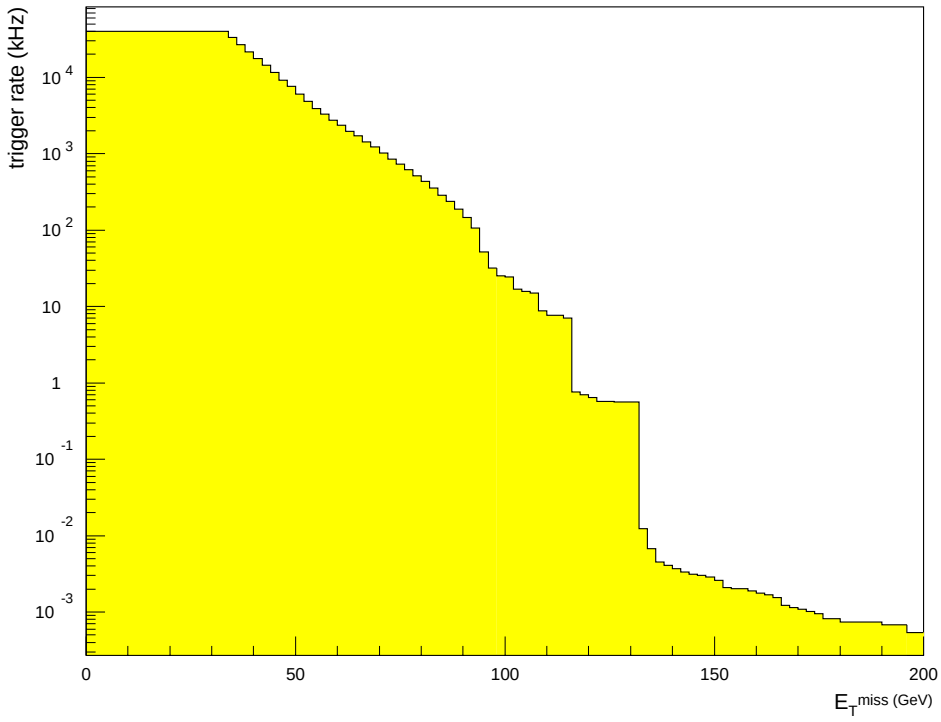

Figure 4.9: *Inclusive E_T^{miss} trigger rates at high luminosity from QCD jet events as a function of the E_T^{miss} threshold used in the level–1 trigger.*

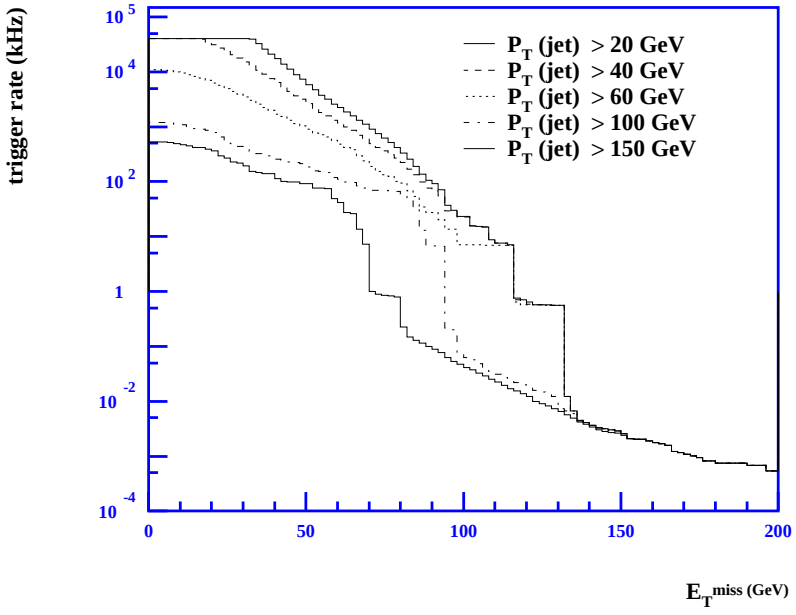

Figure 4.10: *Combined trigger rates at high luminosity, jets + E_T^{miss}.*

4.4 Conclusions

In this section the level–1 rates for triggers using the E_T^{miss} signature have been estimated. Together with the inclusive E_T^{miss} rate the rates for various combinations of the E_T^{miss} trigger with other triggers like the jet and the tau trigger have been estimated for both low and high luminosity run scenarios. The trigger rates are found to be dominated by QCD two jet production. The superposition of minimum bias pile-up events leads to a degradation of the E_T^{miss} resolution and therefore to an increased trigger rate at a fixed threshold.

At low luminosity, trigger rates in the kHz range could be achieved for an E_T^{miss} threshold of $\sim$60 GeV. This threshold can be lowered if in association to the E_T^{miss}-signature at least one jet is required above a certain E_T. For example, the combinations of 60/0, 40/60 or 30/100 GeV for the E_T^{miss}/E_T(jet) thresholds lead to trigger rates in the kHz range.

At high luminosity, this rate can only be kept if the E_T^{miss} threshold is raised significantly. Without any jet requirements a threshold in the order of 120 GeV has to be set. Also in this case, the threshold can be lowered if in addition a jet with $E_T > 100$ GeV is required.

Chapter 5

Simulation framework

Monte Carlo simulations in experimental particle physics are general composed of three layers. The innermost layer, the kernel (or the core), is the simulation of physics processes. The next layer contains detailed simulation of the detector and it's effects. The outermost layer is the simulation of a trigger system along with the corresponding algorithms. In ATLAS simulations, the inner most layer, the kernel, is almost exclusively performed by the PYTHIA [57] package. Nevertheless there exist several good event simulation packages which are and have been used for specific processes. Experimental observations and theoretical/phenomenological improvements are constantly used to update these packages in order to supply physicists with tools rich in physics. Computations in this layer, thanks to the rapid technological progress in the computing branch, is not a time consuming process. The output of this layer is a set of 4–momentum information of stable (or upon request also unstable) final state particles. This is the input to the next layer.

The second layer, namely the detector modeling level, is the bottle neck of the overall simulation process. A detailed parameterization of the various sub–detector materials, the active and absorbing parts together with the dead material present in the support constructions of the detector, and the simulation of the response of different sub–detectors to different particle types are among the tasks of the second layer. Simulations in this layer contain, among others, the shower development in the detector system based on various material compositions of the sub–detectors. These simulations are often referred to as the full simulations. In ATLAS, the full simulations are performed by the package combination DICE+GEANT. The GEANT package [62] is a detector material and geometry description tool. It is a general detector description package which could be used to define a user specific detector system. The DICE package [63] is the ATLAS interface to GEANT. The combination of these two packages goes under the nick name GEANT. Test beam results are iteratively used to fine–tune the performance of this package. This part of the simulation consumes a lot of computing time. Therefore, one is usually restricted to partial events with low statistics, or to a limited number of single particle samples.

The last layer in the simulations is the trigger performance. It receives as input the output from the foregoing layer, in the form of hit information or energy deposition in detector cells. The official ATLAS trigger simulation utility is the ATRIG* package. Different levels of the

*Another closely related tool is the ATRECON [64] package, which reconstructs different ATLAS relevant quantities. This package is used internally by ATRIG [65].

ATLAS trigger system are simulated in this layer. A full simulation based on these three layers is very expensive, regarding time consumption issues, and produces large amount of data. Certainly the former is the most important of both.

It would be therefore desirable to have a simulation of the central layer, the detector performance layer, which contains the major impact of the relevant sub–detector and is fast enough to allow production of large samples for high statistics studies. The ATLAS Level–1 Calorimeter Trigger Fast Simulation (**L1CT**) package[†] is such a simulation tool developed to perform both offline analyzes and trigger specific studies. The L1CT simulation tool is not only able to perform a relatively fast study of the LVL1 calorimeter trigger effects and its impact on physics processes, but is also able to carry out realistic off–line physics analysis on account of its realistic parameterized calorimetry features. The overall structure (or flowchart) of the simulation code is depicted in Figure 5.1. The simulation starts by generating an event using the PYHTIA5.7 [56] physics generator. The output is fed into several routines, which simulate the calorimeters and trigger chain. The effect of the solenoidal magnetic field on the charged particles is then simulated in an approximate manner. Calorimeter simulations contain: parameterized calorimeter response (including the effects of the inner detector material and the Barrel/EndCap transition region) and resolution effects, electromagnetic/hadronic shower profile parameterization as well as the addition of pile-up. Resolution, response and shower profile parameterizations are performed on data obtained from fully simulated **DICE/GEANT3** single particle samples. Hence, the inner detector effects are implicitly contained in the response and resolution parameterizations of the calorimeters. Results from this stage are compiled in the form of trigger tower maps in the electromagnetic and in the hadronic calorimeters, which are then fed into the next level of simulation, i.e. the trigger. A complete simulation of the LVL1 calorimeter trigger chain is incorporated into the existing code: • signal shaping, • tower building, • electronic noise, • signal digitizing, • BCID as implemented in the hardware, • LUT and • implementation of the trigger algorithms (e/γ, $\tau/hadron$, jet, $\mathrm{E_T^{miss}}$ and $\sum \mathrm{E_T}$). In addition pile-up is modeled in a realistic fashion. Several results obtained with an earlier version of this package (with no shower parameterization) have already been published as ATLAS notes [47, 54, 55, 55]. An analysis on the effect of the different trigger steps on the resolution of the $\mathrm{E_T^{miss}}$ distribution could also be found in [51]. Further, some results obtained with (the old version of) this package is presented in different ATLAS trigger and physics TDRs. An exhaustive description of the simulation code is unfortunately not possible here, and the above mentioned notes and/or documents should be consulted.

[†]Accessible from: http://www.kip.uni-heidelberg.de/∼mahboubi/l1ct.html

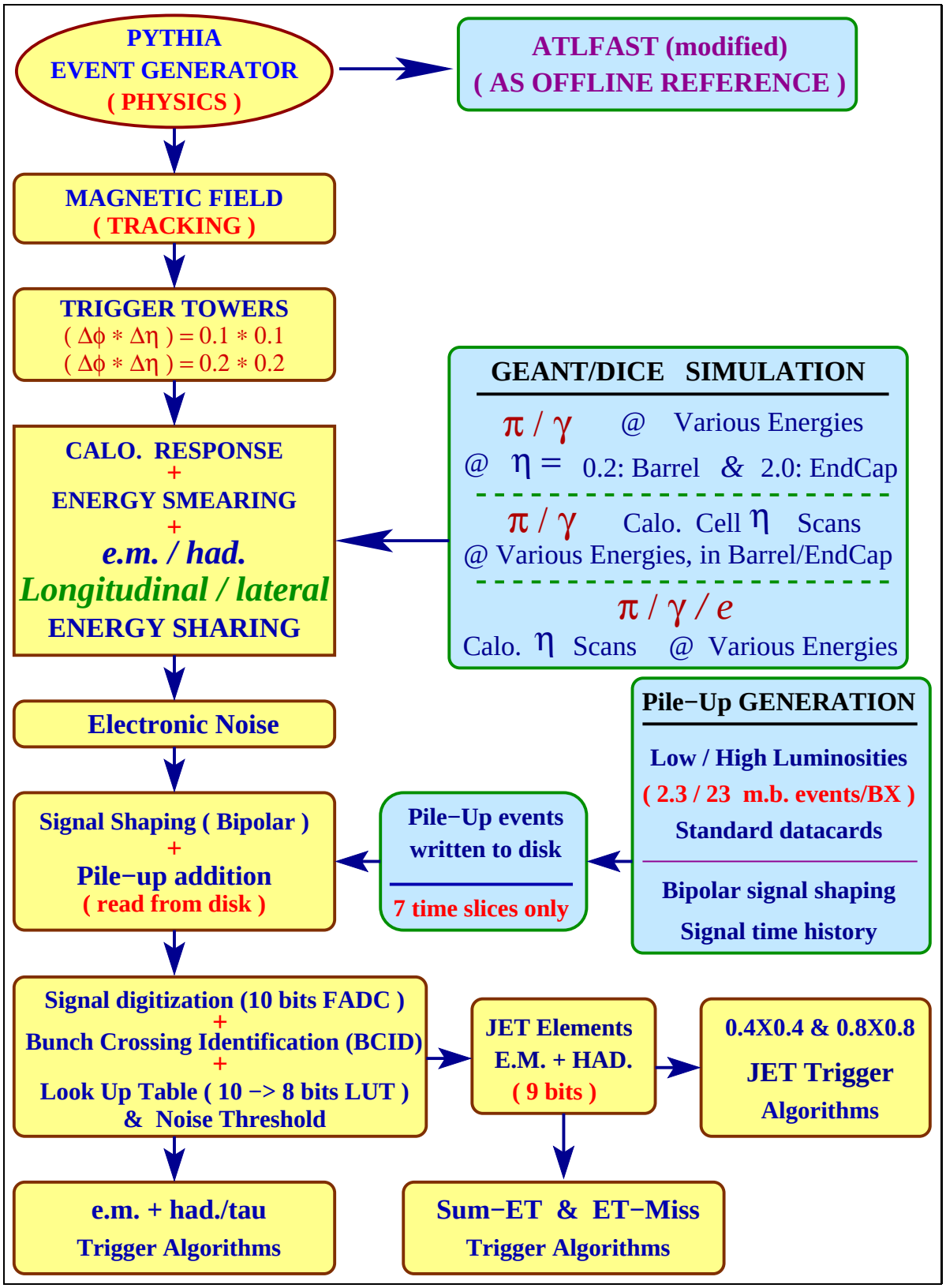

Figure 5.1: *Block diagram of the L1CT package showing important aspects of the simulation environment.*

Introduction

The effects of the calorimetry, such as energy response and resolution, shower development within a given calorimeter type and energy sharing between the hadronic and the electromagnetic calorimeters, are parameterized based on the data extracted from fully simulated **DICE/GEANT3** single particle samples. The electromagnetic and hadronic particles, in these full simulations, are represented by photons (γ) and charged pions (π^+) respectively. In some occasions electrons have also been used to extract the effect of the calorimetry. A shower shape parameterization is performed on a cell map with the granularity of the level–1 calorimeter Trigger Towers (TTs), i.e. $(\Delta\phi \times \Delta\eta) \sim (0.1 \times 0.1)$ in ECAL and HCAL, with no segmentation in the longitudinal direction in any of the calorimeters. Energy deposits in different cells are reconstructed using modified **ATRECON** [64] and/or **ATRIG** [65] packages.

Two features of the L1CT code are of special importance which have a non-negligible effect on physics analyzes. These effects are essentially absent in other physics studies performed by fast simulations so far. And even if included they are in a very crude and probably optimistic and naive manner. These are the effects of the pile-up and the calorimetry, e.g. calorimeter response to different types of particles, longitudinal and lateral shower developments and the transition region. Pile-up simulations, even in the full simulations, is quite limited, i.e. only a few number of fully simulated pile-up events are available. Pile-up simulation and it's incorporation into the code does deserve some explanation. It takes into account, depending on the luminosity, the average number of minimum bias (or low p_T) events, at each bunch crossing plus the time history of the shaped signals. This means that a trigger tower signal at a given time slice (or bunch crossing) has contributions not only from the average number of minimum bias events but also from all the $\sim$23 bunch crossings earlier in time. These simulations are quite time consuming (specially at high luminosity) and are therefore simulated once and for all, for both luminosities, and are dumped into separate files for future usage. The implemented BCID algorithm needs data from at least 7 consecutive bunch crossings. Therefore, per event, 7 time slices about the peak are written to pile-up files. During the actual physics simulation, a pile-up, either low or high luminosity, is read from the appropriate pile-up file and added to the signal.

After this general explanation of the simulation tools, a more specific topic, namely the parameterization of the calorimetry effects is presented here. It must be noted that only the general idea is outlined, and no numerical results and no fine–details of the parameterizations are given. The layout of this chapter is as follows. Data sets used in the parameterizations are explained in section 5.1. parameterization of the energy response and resolution and studies on energy calibration are presented in section 5.2. The effect of the transition region on the energy response is discussed in section 5.3. The method applied to parameterize and simulate shower profiles in the longitudinal, i.e. the energy sharing between the ECAL and the HCAL, and in the lateral directions, i.e. within each calorimeter type separately, is explained in detail in section 5.4. And finally some conclusions and final remarks are discussed in section 5.5.

5.1 Data samples

Different data sets have been used to extract parameters to describe the behaviour of the calorimeters for different particles, electromagnetic and hadronic, at various energies, ranging from low to moderate and/or high, at selected η and/or η ranges. Data samples together with the information extracted from each set is compiled in Table 5.1. In all these samples the inner detector, the magnetic field and all the calorimeters are switched on. (The muon chambers are also switched on although they are of no importance in the studies presented here.) Electronic and pile-up noise are switched off. Also no calibration and/or threshold is applied on cell deposits.

Table 5.1: *Fully simulated* **DICE/GEANT3** *data samples.*

Particle	Energy (GeV)	η	Extracted
γ	0.2, 0.3, 0.4, 0.5 1.0, 2.0, 5.0, 10.	0.2, 2.0	Resolution/Response
π^+	0.2, 0.3, 0.4, 0.5, 1.0, 2.0, 5.0, 10., 20., 50.	0.2, 2.0	Resolution/Response ECAL/HCAL Energy Sharing
γ	10., 20., 50., 100.	0.2 – 0.3 1.9 – 2.0	Longitudinal (ECAL/HCAL) Lateral Energy Sharing
π^+	10., 20., 50., 100.	0.2 – 0.3 1.9 – 2.0	Lateral Energy Sharing
γ	15., 30., 90.	0.0 – 2.6	Response/calibration
e^-	15., 30., 90.	0.0 – 2.6	Response/calibration
π^+	15., 30., 90.	0.0 – 3.2	Response/calibration

5.2 Energy resolution and response

Two different types of scans have been performed in order to study and parameterize the energy resolution and response of different particle types, i.e. electromagnetic and hadronic, in different calorimeter regions, e.g. transition region. The generated scans are:

- ⊙ Energy scans at discrete energies ranging from 0.2GeV to 50GeV for pions, and from 0.2GeV to 10GeV for photons. Each energy is generated at two fixed η's, i.e. η=0.2 and η=2.0, representing each calorimetry region, i.e. barrel and endcap respectively. (First two rows in Table 5.1)
- ⊙ Pseudo-rapidity scans at 15GeV, 30GeV and 90Gev with electrons, photons and pions. The η scans cover a range from 0. to 2.6 for e/γ and from 0. to 3.2 for π^+ samples. (Last three rows in Table 5.1)

5.2.1 Electromagnetic particles

Electromagnetic particles, as mentioned above, are represented by photon samples. The energy deposit of photons are reconstructed by performing a (weighted) sum of the deposits in the Pre-Sampler (PS), ECAL and HCAL calorimeters according to the formula:

$$E_{Reco.} = E_{PS} + E_{ECAL} + E_{HCAL}\,,$$

where $E_{Reco.}$ is the reconstructed energy. When possible, the distribution of the reconstructed photon energy, normalized to it's nominal energy, is described with a Gaussian fit function. Some examples of these distributions are shown in Figure 5.2. As seen in this figure, the distribution of the reconstructed energies of photons with an energy below 1.5 GeV have large tails toward low fractional energy deposits. For photons in this very low energy range, the reconstructed energy does not follow a pure Gaussian distribution because of the relatively high energy loss in the material (including the inner detector) in front of the electromagnetic calorimeter.

The energy resolution, i.e. the ratio of the sigma to the mean of the gauss fit to the reconstructed energy, as a function of the nominal energy is shown in Figure 5.3. The dotted curve is a parametric resolution function of the form: $\frac{a\%}{\sqrt{E}} \oplus b$, with the sampling a and the constant b terms, fitted to the data. It should be noted that the resolution function for photons used in the ATLFAST package, obtained from test beams, describes this energy dependence quite well down to energies above 1.5 GeV. The coefficients obtained here and those quoted in the ATLFAST package are very similar. On the other hand, the lower the energy of the photon the higher the fractional energy loss in the material in front of the ECAL. For photons with an energy less than 1.5 GeV, the ECAL energy distribution is broad (in fact completely smeared) with no well–defined mean, and is shifted toward lower fractions so that it cannot be described by parameterized functions of this type. This behaviour of the response to very low energy photons, i.e. $E_\gamma < 1.5GeV$, which is of great importance for the trigger performance, is therefore handled differently in the L1CT code. Histograms at discrete energies (below 1.5Gev in the energy scan samples) are filled with these distributions, and are used to randomize the ECAL energy deposit of low energy photons.

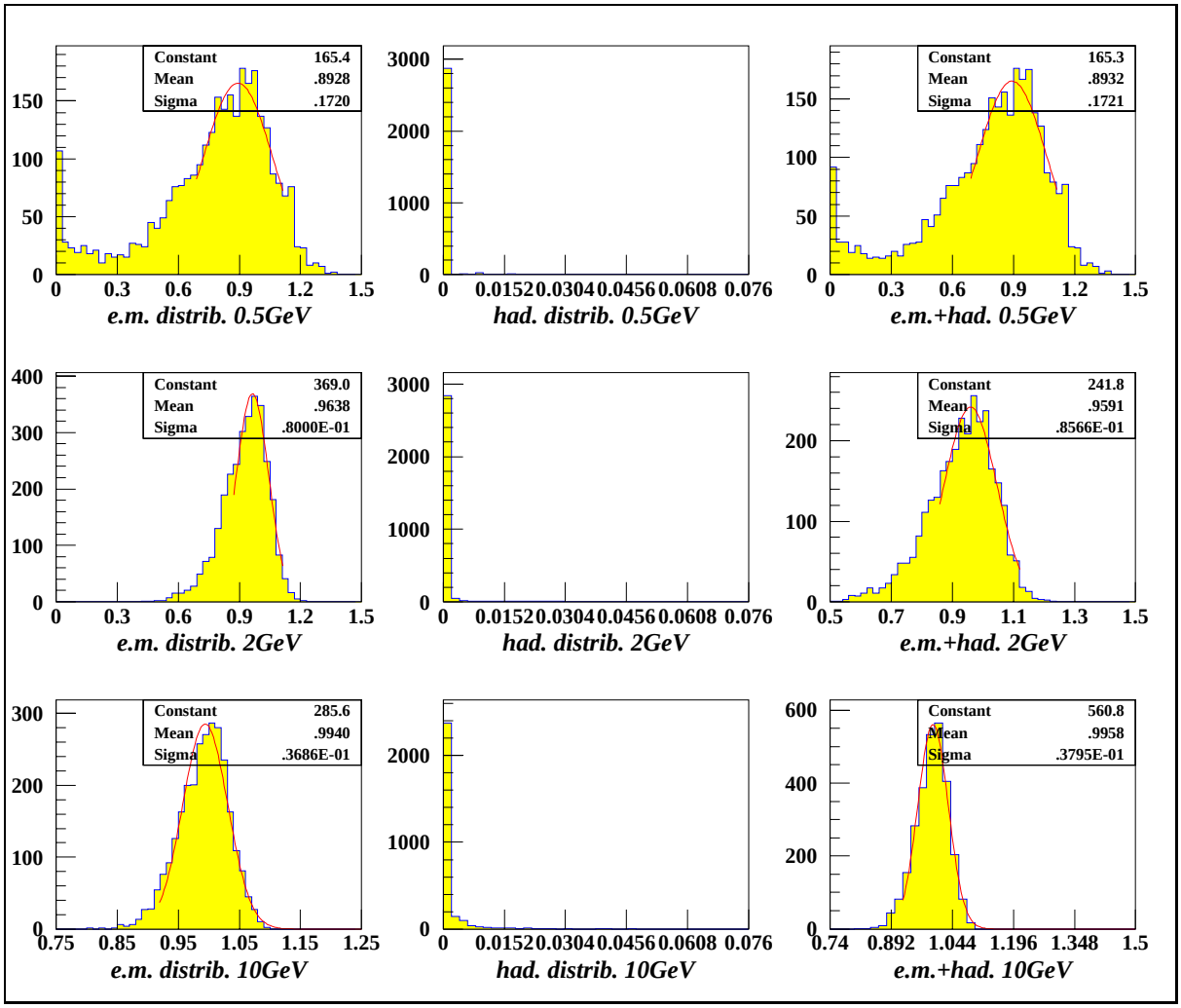

Figure 5.2: *Examples of the reconstructed photon energy (normalized to the nominal energy). The corresponding Gaussian fits (when possible) are also shown.*

To study the response to photons, the ratio of the means of the Gaussian fits, corresponding to the average visible energy in the calorimeters, to the incident energies $\frac{\mu_\gamma}{E_\gamma}$, are plotted, in Figure 5.4, against the corresponding nominal energies. It is seen clearly in this figure that the response of the calorimetry to photons with an energy in excess of a few GeV is very close to unity. The superimposed dotted curve in Figure 5.4 is a parameterized response function describing the data points. For photons with an energy less than 1.5 GeV, a slightly different approach is applied. Instead of taking the mean of the Gaussian fit, the average value of the distribution is considered and a response curve is produced which is only used for intra- or extrapolation purposes (see next paragraph).

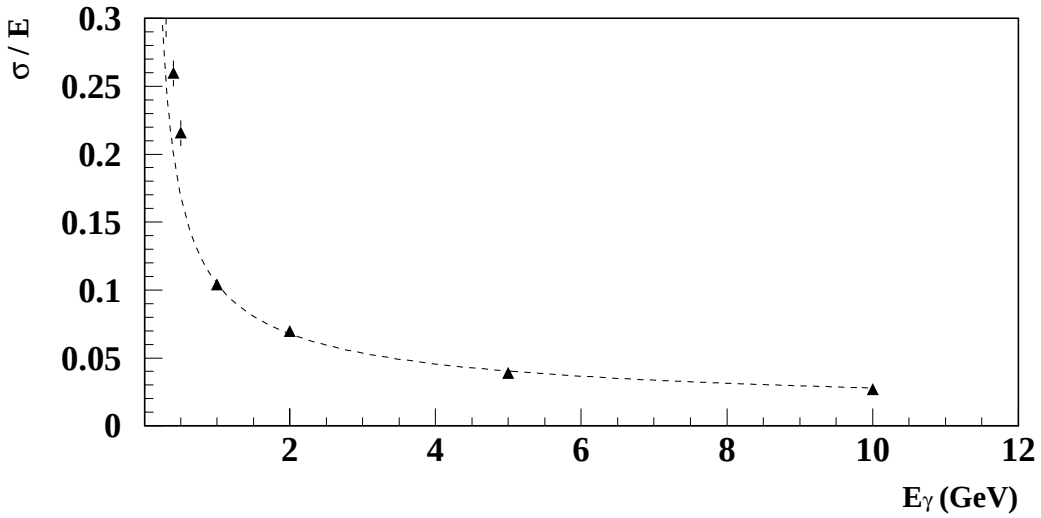

Figure 5.3: *Fractional energy resolution for photons as a function of the nominal energy. The dotted curve is a parameterized function describing the data points.*

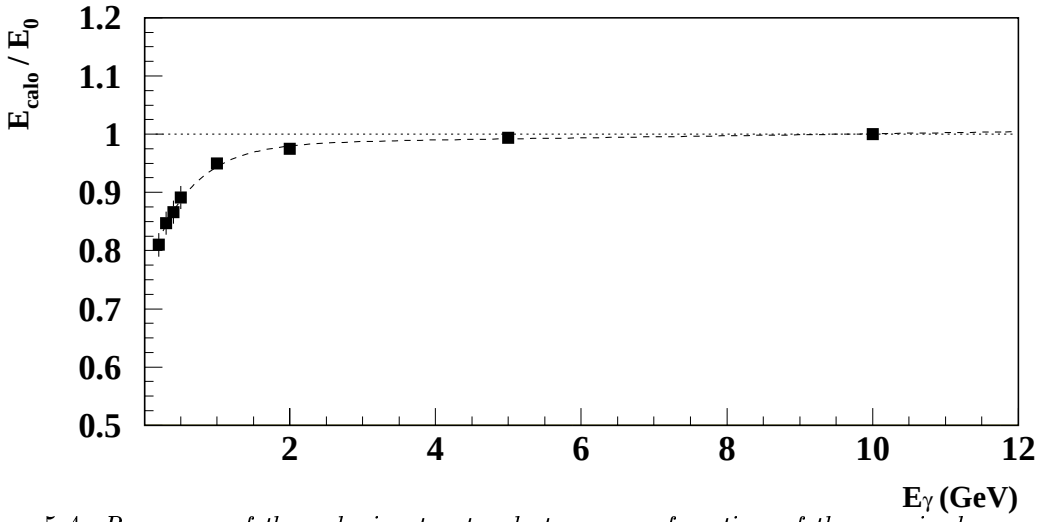

Figure 5.4: *Response of the calorimetry to photons as a function of the nominal energy. The dotted curve is a parameterized function describing the data points.*

In the fast simulation, for a given photon energy falling in the low energy range ($E_\gamma < 1.5 GeV$), the energy fraction deposited in the ECAL is randomized from the energetically nearest histogram and the response is scaled to the correct energy by inter- or extrapolation using the corresponding response curve. For photons with energies of 1.5 GeV or more the ATLFAST resolution function, which is essentially the same as the one in Figure 5.3, and the above explained response functions are used to smear the energy.

5.2.2 Hadronic particles

Hadrons are represented by samples of charged pions, i.e. π^+. Some examples of the distributions of the energy deposit of charged pions in the electromagnetic[‡] and in the hadronic calorimeters, normalized to the incident energy, are shown in Figure 5.5. The reconstructed

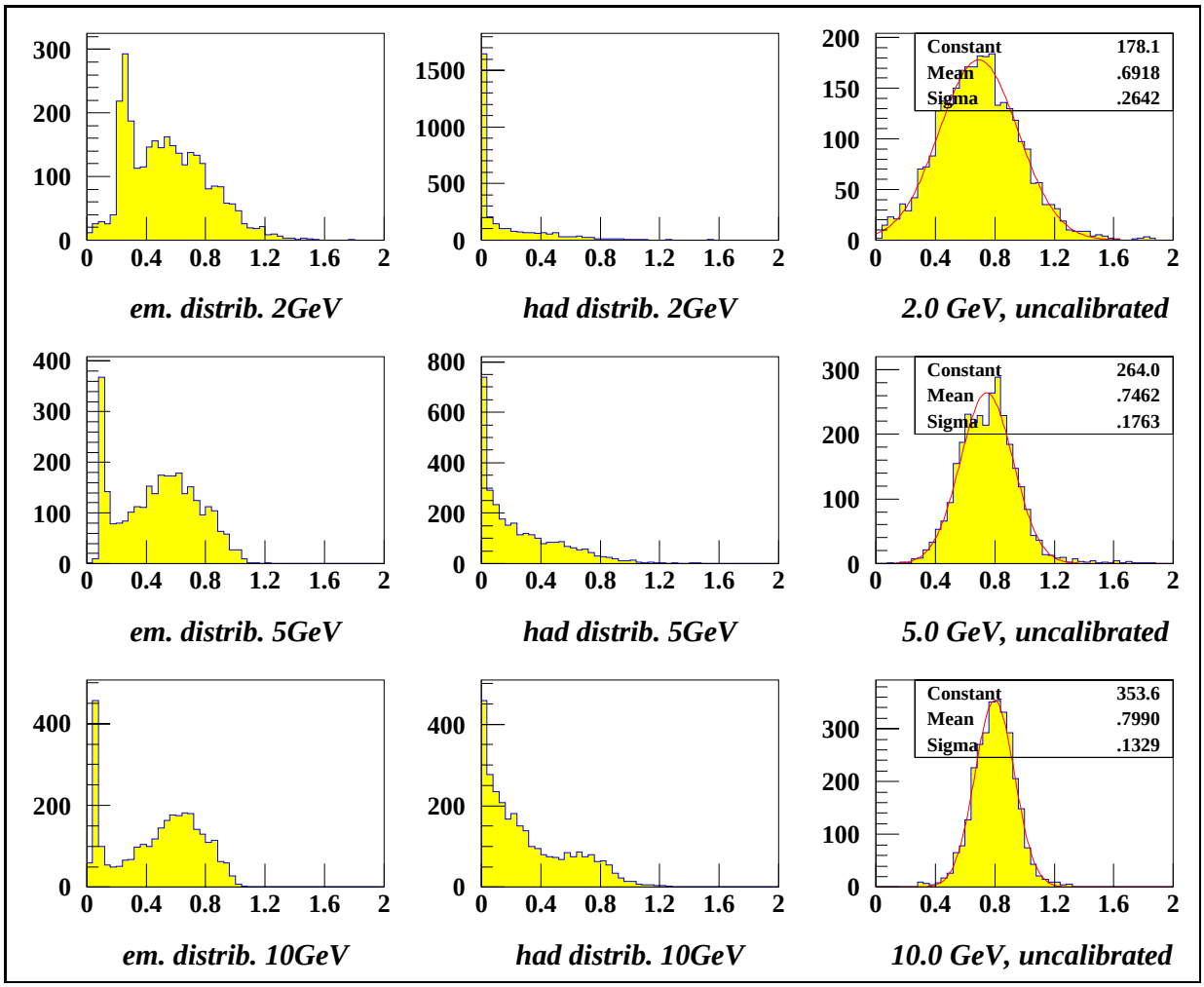

Figure 5.5: *Total energy deposit of pion in the calorimeters, normalized to the nominal pion energy.*

energies, obtained by summing the electromagnetic and the hadronic contributions, normalized to the nominal particle energy, is also shown in the same figure. The visible energy of a hadron with an energy in excess of 10 GeV is about 20% lower than the nominal energy. This is due to the non-compensating effect of the calorimetry in ATLAS: hadrons are seen on the electromagnetic scale. Here again a Gaussian fit to the total reconstructed energies has been performed and the ratio of the sigma to the mean of these fits are then plotted against the nominal energies. The obtained resolution curve is shown in Figure 5.6. Superimposed on this plot is a fitted parametric resolution function which describes the data points.

[‡]The electromagnetic in this case means the sum of the energies seen in the ECAL and in the Pre-Sampler.

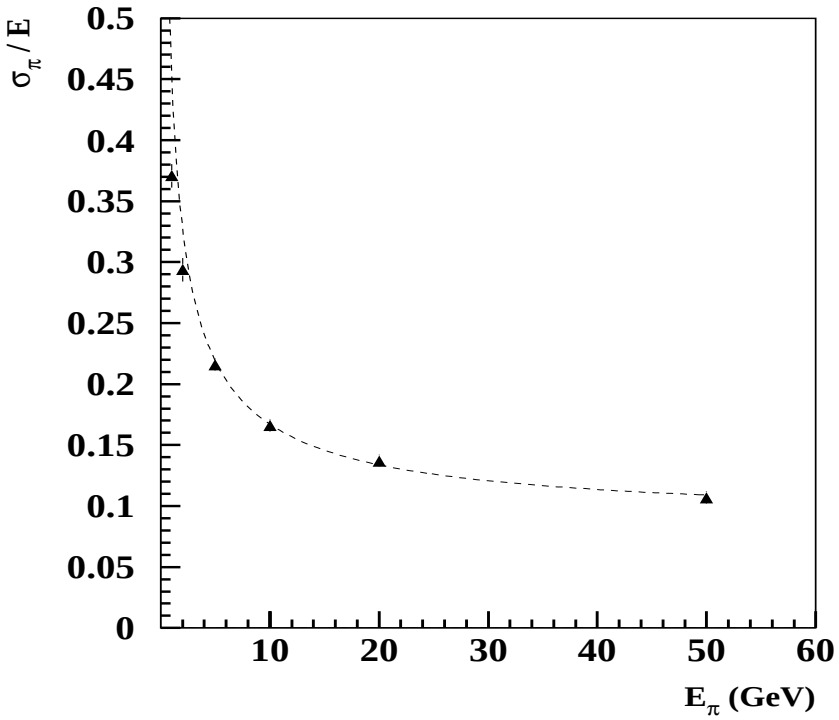

Figure 5.6: *Fractional energy resolution for pions as a function of the nominal energy. The dotted curve is a parameterized function describing the data points.*

The response to hadrons is studied by first calibrating the reconstructed energy given by

$$E_{Reco.} = \alpha \cdot (E_{PS} + E_{ECAL}) + \beta \cdot E_{HCAL},$$

where α and β are calibration constants which are, essentially, energy and pseudo-rapidity independent. These calibration (weight) factors are determined by performing, in the MINUIT [66] environment, a minimization of the quantity:

$$\chi^2 = \sum_{E_j} \sum_{i=1}^{N_j} \left(\frac{E_{i,Reco.} - E_j}{\sigma_j} \right)^2,$$

where N_j is the number of events in a given sample with energy E_j. The σ_j's are the resolutions at E_j energies. The result is: $\alpha \simeq 1.30 \pm 0.02$, $\beta \simeq 1.13 \pm 0.03$. An example of the application of these calibration factors on the energy deposits of 20 GeV positively charged pions is demonstrated in Figure 5.7. As seen in this figure the resolution gets worse by about 3% as a result of the minimization.

The value of the means of the Gaussian fits to the reconstructed (or calibrated) energies normalized to the corresponding nominal energies are plotted against the corresponding incident energies in Figure 5.8.

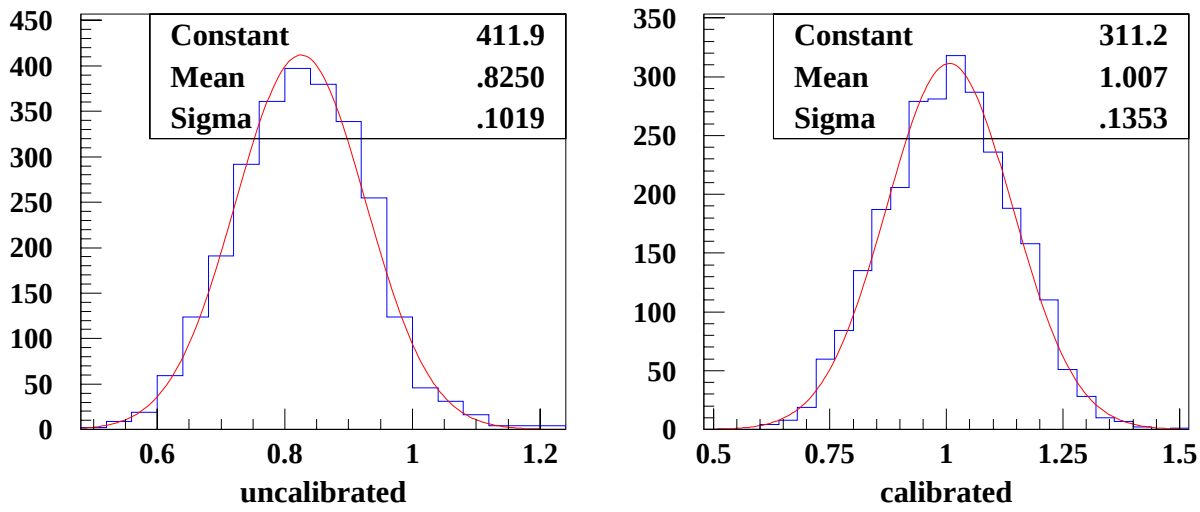

Figure 5.7: *Reconstructed energy of a 20 GeV positively charged pion in the barrel before (left) and after (right) application of the calibration factors. The mean of the Gaussian fit which is at about 82% before calibration is shifted to 100% after calibration, with a corresponding loss in resolution.*

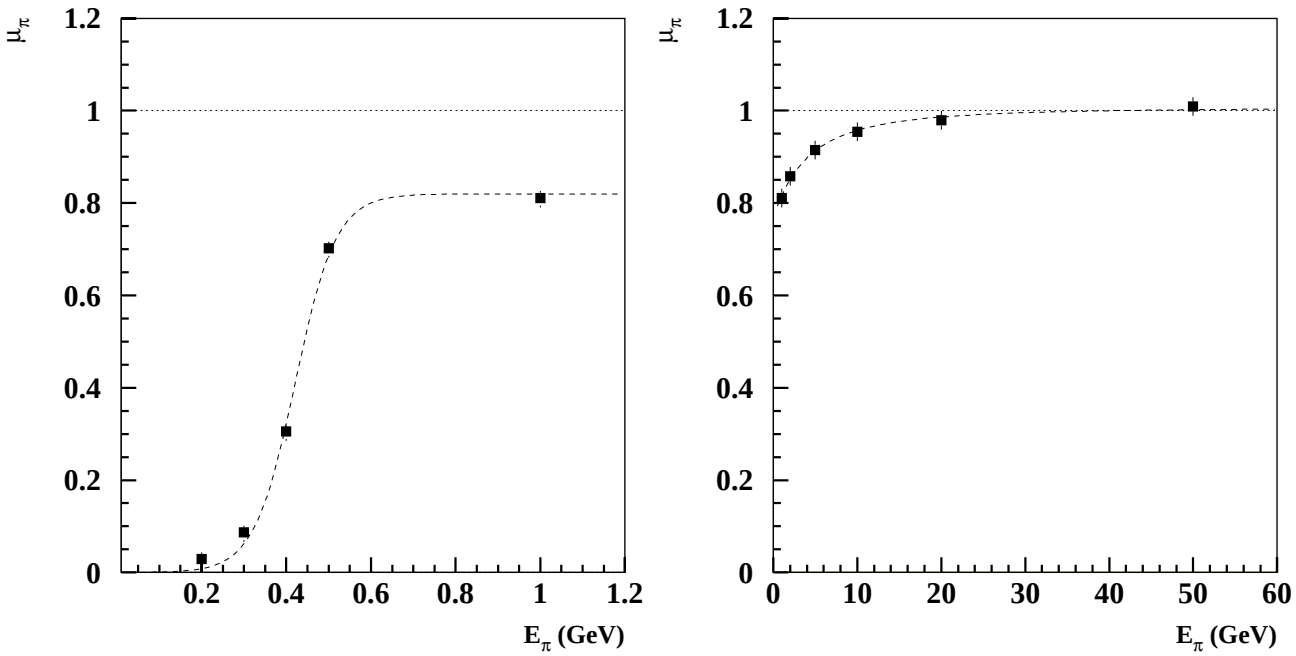

Figure 5.8: *Response of the calorimetry to pions as a function of the nominal energy. The dotted curve is a parameterized function describing the data points.*

In order to be able to describe the behaviour of the calorimeters' response to pions, the response function is divided in two regions, below and above 1GeV. Two different parametric functions are fitted to the data points, which are also plotted on the corresponding plots. It should be noticed on the response curves in Figure 5.8 that pions with an energy below half a GeV practically do not enter the calorimeters.

An instructive study has been the correlation between the fractional energy deposits in the ECAL and in the HCAL. This is shown in Figure 5.9 which plots these two fractions against each other for some representative energies. There are several points which should be noticed on these plots. Low energy pions (in the MeV range) often deposit most of their energy in the electromagnetic calorimeter. For higher energy pions, one observes a band of data points showing both the effect of the resolution and response of the calorimeters. Another point which is of importance is the high density region on this band at very low electromagnetic energy fractions which in fact shifts to even lower values with increasing pion energies. This high density region is seen as a narrow peak at low values of the distributions for the fractional energy deposit in the ECAL in Figure 5.5. This effect is discussed later in section 5.4.

In the fast simulation, the fractional energy loss in the ECAL and in the HCAL is randomized from the energetically nearest histogram, and the response (for $E_\pi \geq 0.15 GeV$) and/or resolution (for for $E_\pi > 1 GeV$) is rescaled to the correct energy by inter- or extrapolation. For pions with a very low energy ($E_\pi < 150 MeV$) no rescaling of the random fractions obtained from the lowest energy histogram is performed.

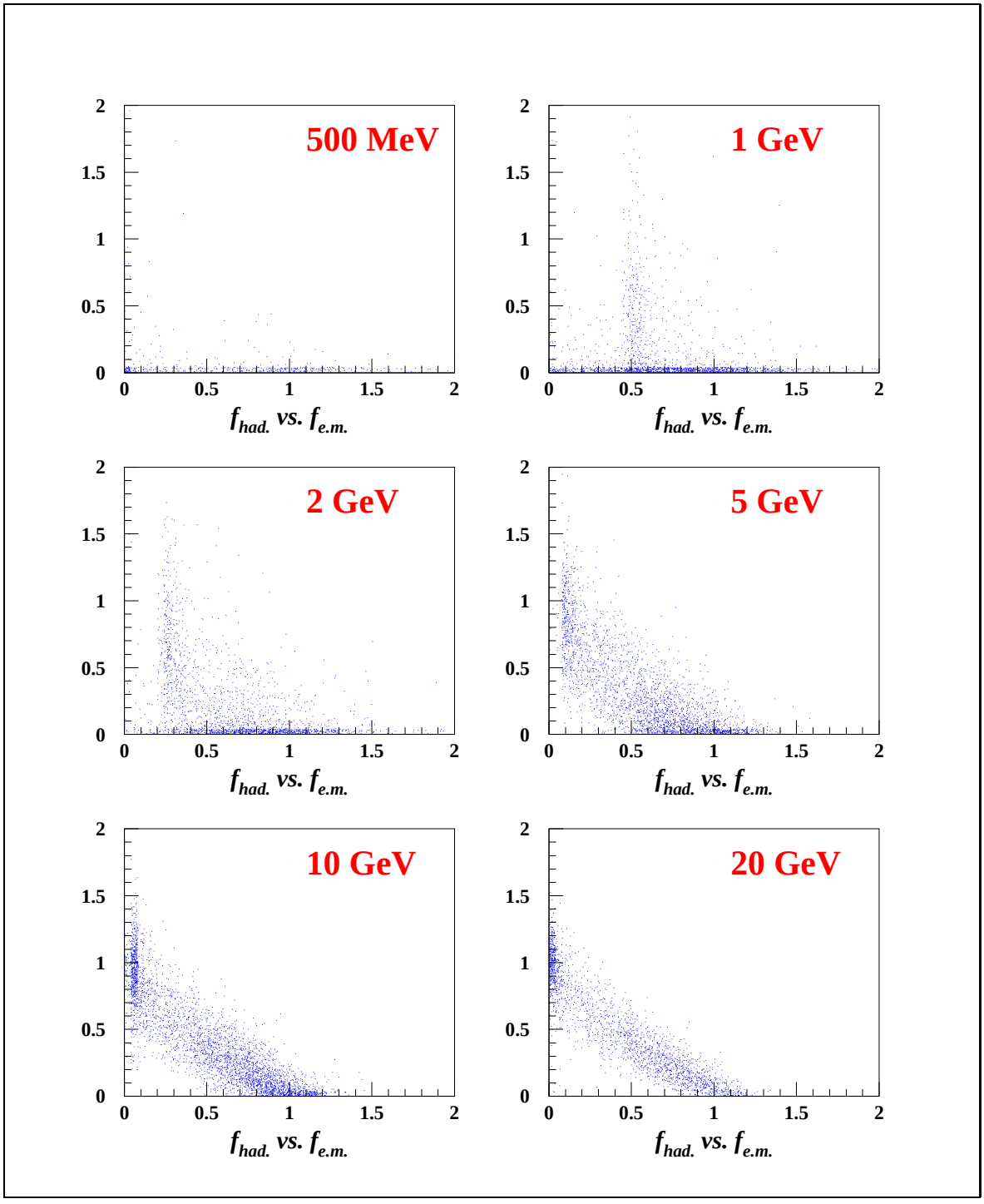

Figure 5.9: *Correlation between the fractional ECAL and HCAL energy deposits for pions.*

5.3 Barrel–EndCap transition region

The effect of the transition region on the energy response has been studied for photons, electrons and charged pions by performing η scans across the transition region. These scans serve also as a check of the η dependence of both the calibration factors (used for energy reconstruction) and the response functions alike.

Figure 5.10 shows the effect of the transition region on the response of the calorimetry to electromagnetic particles, i.e. e/γ.

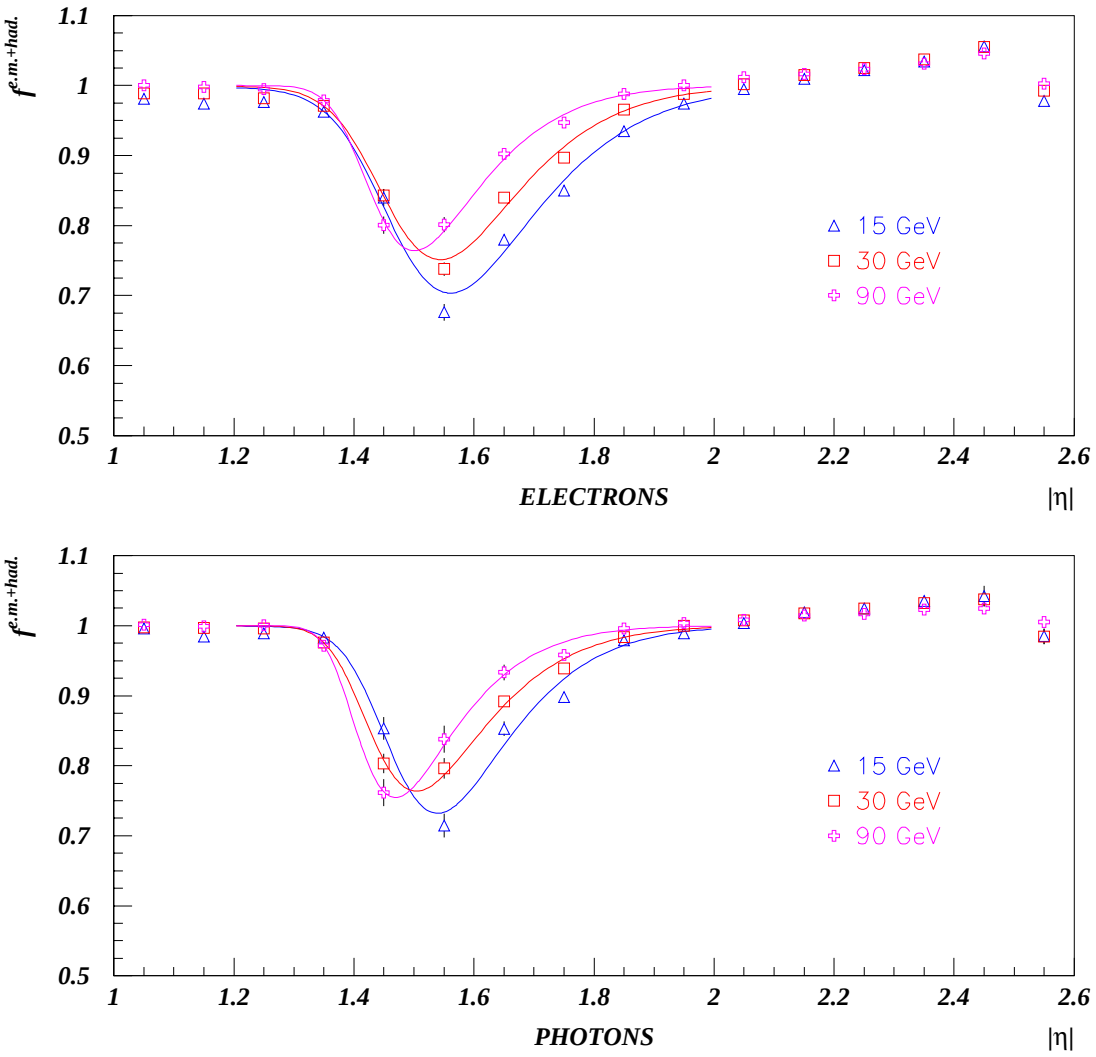

Figure 5.10: *The effect of the transition region on e/γ energy response.*

It is seen in Figure 5.10 that the energy response in the range $1.4 < |\eta| < 1.8$ is decreased and goes through a minimum at about $|\eta| \approx 1.5$. The effect for the transition region for electrons and photons is parameterized by

$$\mathcal{R}(\eta) = 1 - exp\left\{-b \cdot (\eta - a)^2 - d \cdot exp\left(-c \cdot (\eta - a)^2\right)\right\},$$

where a, b, c and d are constant parameters. This means that the slight difference of the response to electrons and photons, with the same energy, across the transition region is neglected. Another effect, which is obvious from figure 5.10, is the energy dependence of the response to electromagnetic particles. This is already corrected for, when the response from previous section, obtained from energy scans, is applied (these are both multiplicative factors on the visible energy). It must be noted that this energy loss of the electromagnetic particles in the transition region affects predominantly ECAL deposits.

The response to charged pions, e.g. 30GeV, across the transition region is shown in Figure 5.11 (the filled dots). In this case, since the energy deposits in both calorimeter types, i.e. electromagnetic (e.m.) and hadronic (had.), are of importance, the change in the fractional deposits in both calorimeters are considered. The observed dips in the overall response, i.e. e.m.+had., at $|\eta|$ about 1.0 and 1.5 could be related to the feed–through and the Barrel–EndCap transition region respectively. The energy loss on the border of the hadronic endcap region is due to incomplete shower containment – a larger fraction of the shower energy is deposited in the forward calorimeters as the showering particle approaches the border of the endcap. This is more prominent for the HCAL deposits, most probably due to the transverse size of the shower.

The behaviour of the response of the calorimeters to charged pions is described by a parametric (cubic) spline function. Two sets of spline functions have been fitted to the *e.m.+had.* and *e.m.* responses, and the parameters are determined. The response of the hadronic calorimeter is then derived from the fitted distributions. The result of this parameterization is also shown in Figure 5.11 (the empty boxes).

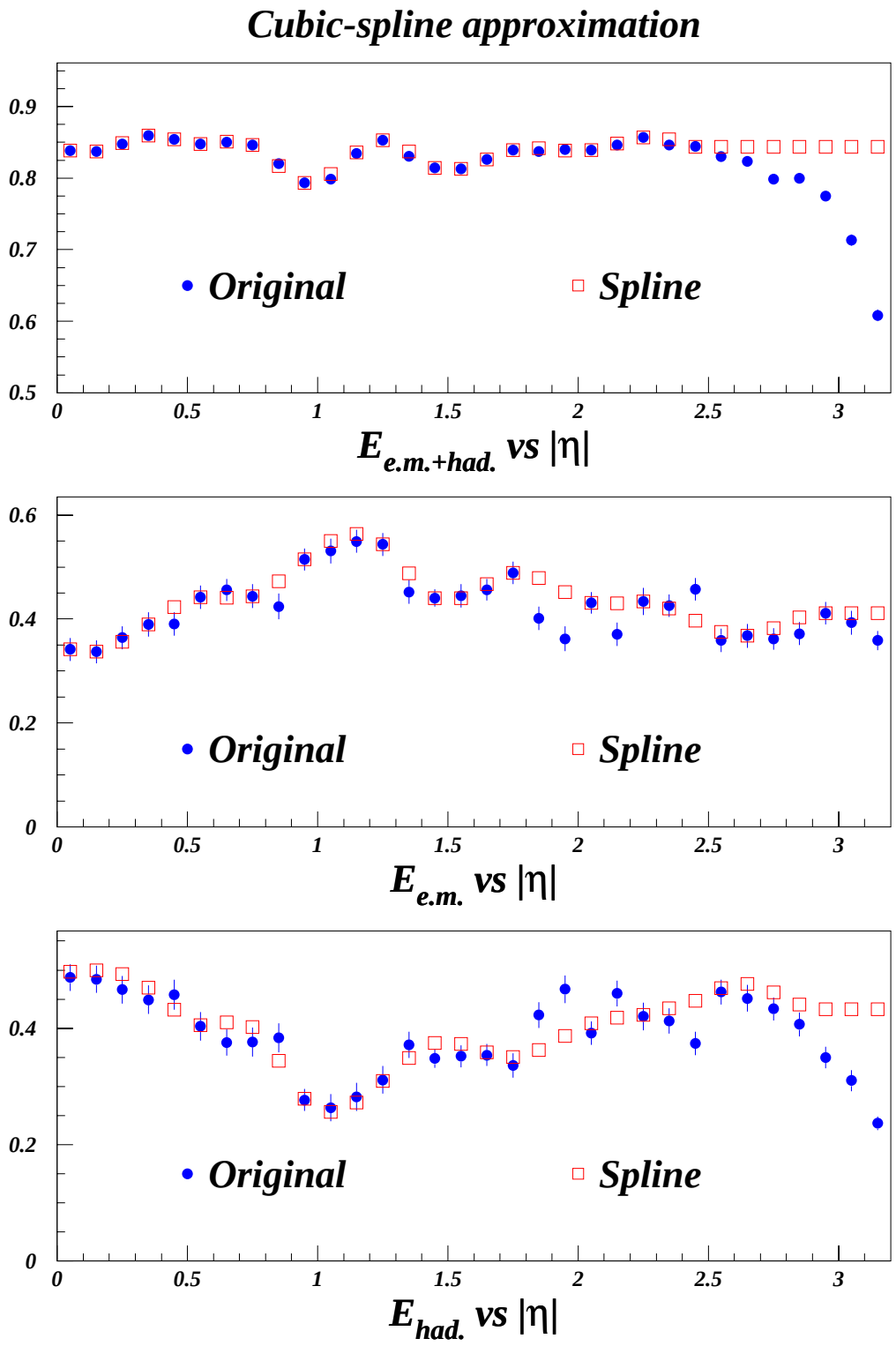

Figure 5.11: *η scan of the response of the calorimeters to 30 GeV π^+, the filled bullets labeled as original, showing different effects, like the depth of the calorimeters and the feed-through/transition region etc. . The empty boxes on the upper two plots show parametric (cubic) spline fits to describe the data points. These two functions are used to derive the response superimposed on the lower plot.*

5.4 Shower profiles

Having studied and parameterized the energy resolution, response and loss in the transition region for electromagnetic and hadronic particles, a parameterization of the shower profiles has been performed. Major aspects of this parameterization is described in this section. Data samples used to study shower profiles are single particle scans in both η and ϕ directions uniformly distributed within a trigger cell (see 3rd and 4th rows in Table 5.1 on page 78). Two different cell positions, in the Barrel and in the endcap, are considered.

Before proceeding, the nomenclature (or definitions), used in the following, are clarified. A given simulated single particle (γ or $\pi^{\pm}$), after traversing the inner detector (and other material in front of the ECAL) and moving through the magnetic field, enters the electromagnetic calorimeter. The point, on the front face of the ECAL, where the particle enters the calorimetry is referred to as the impact point. The coordinate of the impact point, (ϕ_{IP},η_{IP}), is used to identify the trigger cell (or tower, in the LVL1 terminology,) hit by the particle. This cell is referred to as the hit cell, and the coordinate of the center (ϕ_C,η_C) of the hit cell is determined. The ϕ, η components of the distance of the impact point to the center of the hit cell are calculated as: $(\Delta\phi, \Delta\eta) = (\phi_{IP} - \phi_C, \eta_{IP} - \eta_C)$. The hit cell, depending on $(\Delta\phi, \Delta\eta)$, is divided in four quadrants. The quadrant containing the impact point is called the hit quadrant. Figure 5.12 explains these pictorially. Quadrants are further numbered counter clockwise with the number 1 being the upper right quadrant, in the figure.

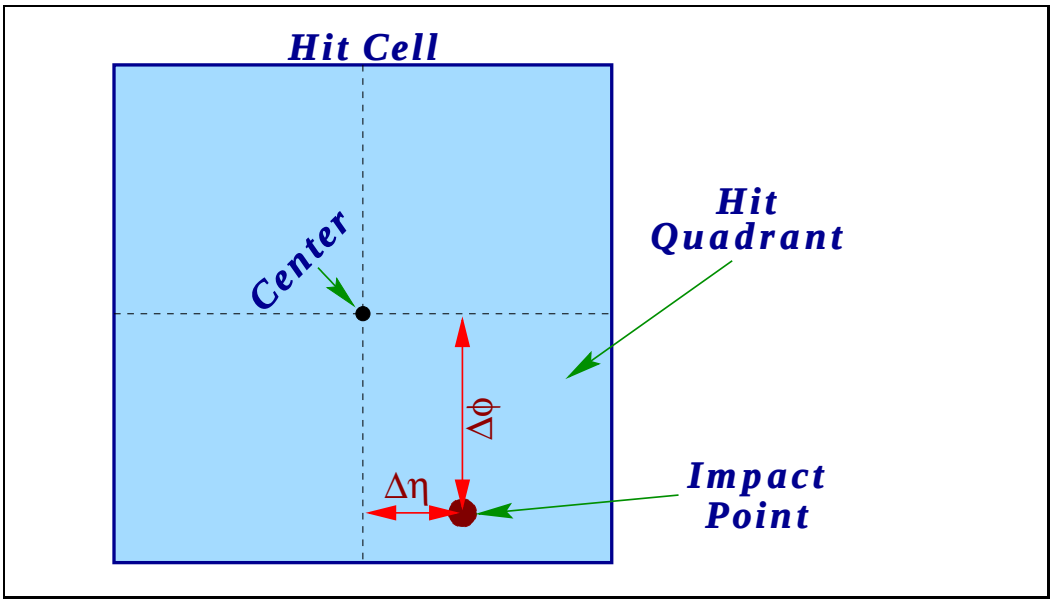

Figure 5.12: *Definition of the impact point, hit cell and hit quadrant explained in the text.*

5.4.1 Electromagnetic showers

The energy of a showering electromagnetic particle is almost entirely deposited in the electromagnetic calorimeter. The very small leakage of the electromagnetic showers into the hadronic calorimeter is modeled in the fast simulation by depositing it in a single trigger cell in the HCAL right behind the hit cell (in the ECAL), see next section. In the electromagnetic calorimeter, on the other hand, a cluster, composed of a number of trigger cells, would be needed for a complete shower containment. A 3×2 trigger cell matrix[§] about the hit cell, has proved to be adequate as the electromagnetic cluster (Core + Halo). The parameterization goes as follows. Trigger cells within a 3×3 cell matrix, centered on the hit cell, are considered in the parameterization procedure, which are numbered in a counter clockwise fashion. For a given hit quadrant, an appropriate 3×2 sub-matrix (i.e. the electromagnetic cluster) is parameterized. These are graphically displayed in Figure 5.13.

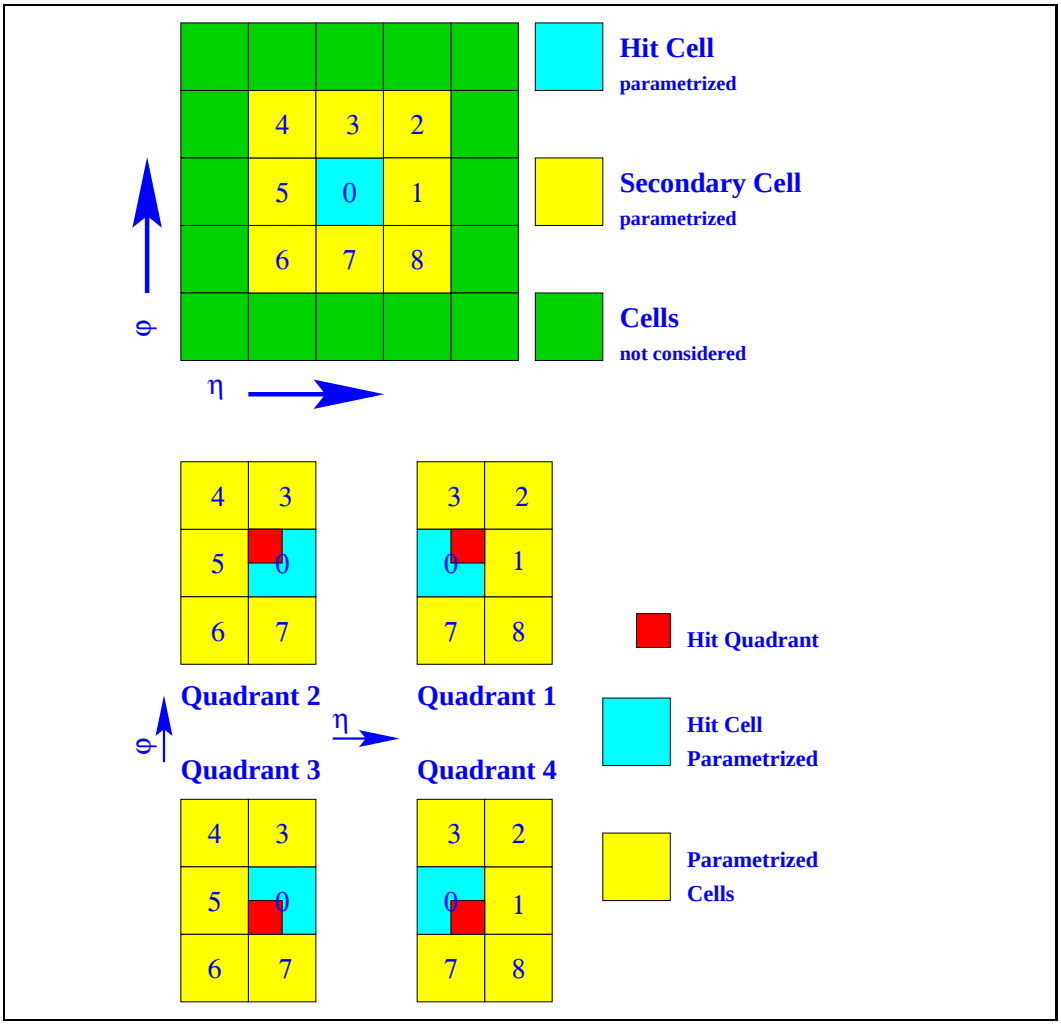

Figure 5.13: *Trigger cell and hit quadrant numbering scheme.*

[§]The convention adopted for the indices, in this and in the following sections, is that the first index always refers to the ϕ and the second index to the η direction.

5.4.1.1 Longitudinal

The first step in the shower parameterization is to determine the fraction of the incident particle energy deposited in the HCAL. This is done by parameterizing the normalized cumulative distribution of the fractional HCAL deposit. An example of the HCAL distribution together with the corresponding normalized integrated distribution is shown in Figure 5.14.

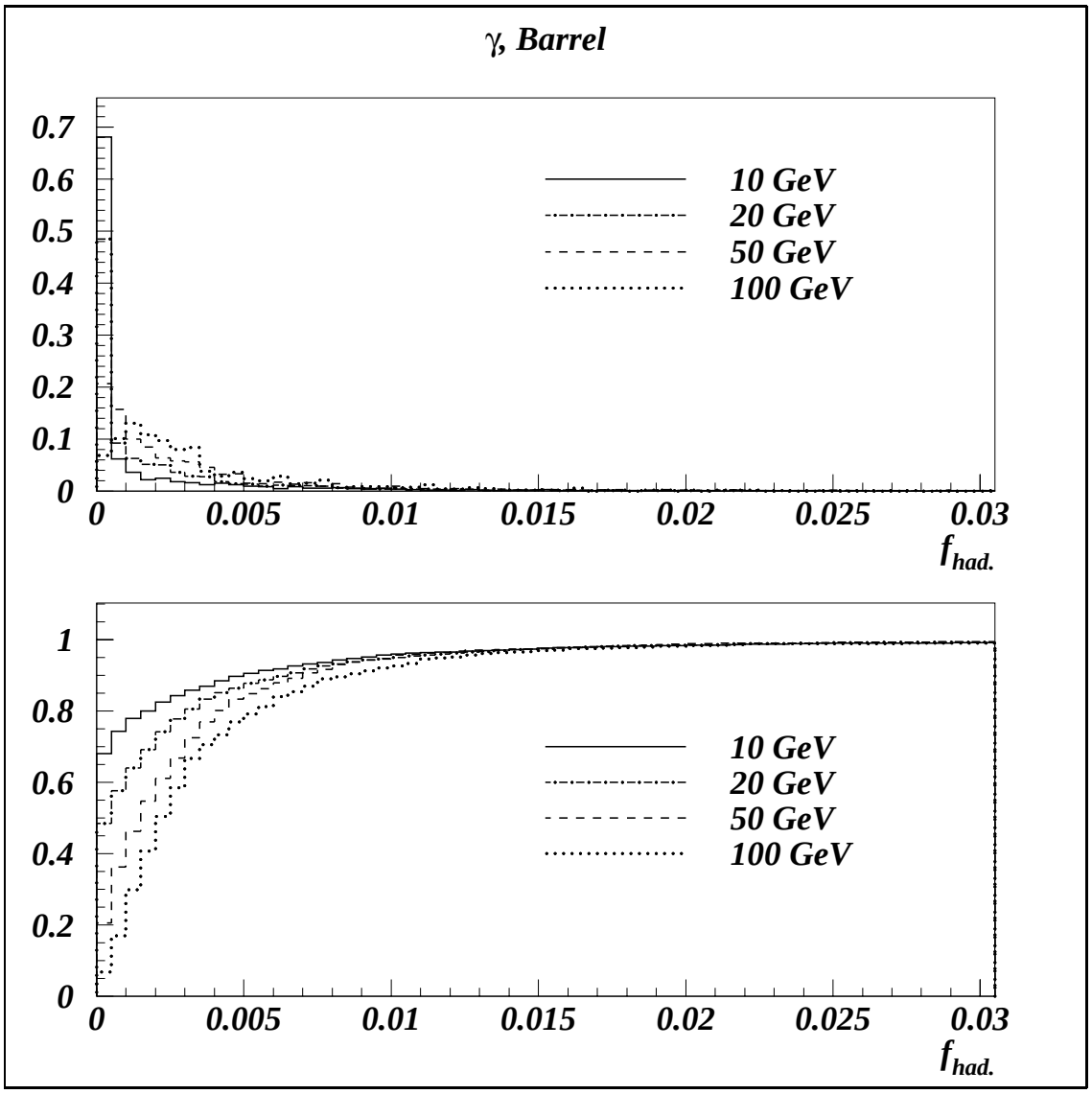

Figure 5.14: *Normalized distribution (top) of the fractional deposit in the HCAL, and the corresponding normalized cumulative distribution (bottom).*

As seen on the abscissa of the plots in this figure, HCAL deposits are very low fractions of energy (of the order of 1% and less). A parameterized (modified Fermi-Dirac) function is then fitted to the cumulative distribution at each energy. The parameters of the fit function, determined in this way, depend on the incident particle energy. The energy dependence of

the parameters is then described by an appropriate functions with constant coefficients as a function of the particle energy. The same procedure is applied both to the Barrel and to the EndCap samples. This means that two sets of, in general, energy dependent parameters, for the Barrel and for the EndCap regions, are obtained. The Barrel set is used for $\eta < 1$ and the EndCap set for the rest of the η coverage. In Figure 5.15 an example of the original fitted function and the function obtained using the parameters derived[¶], using this method, is shown.

At the time of the simulation, depending on the η region, it is decided whether the Barrel or the EndCap parameter set should be used. Being energy dependent, the values of the parameters in the selected set are then calculated for the corresponding incident energy. The fraction of the energy deposited in the HCAL, defined as

$$f_{had.}(E_{nominal}; \eta) = \frac{E_{HCAL}}{E_{nominal}},$$

is then calculated by inserting these parameters in the inverse of the parameterized normalized cumulative function (the parametric fit function). This fraction of the energy is then deposited in the trigger cell, in the HCAL, right behind the hit cell in the ECAL.

[¶]The original distribution could then be regenerated by randomizing from the inverse of the parametric function.

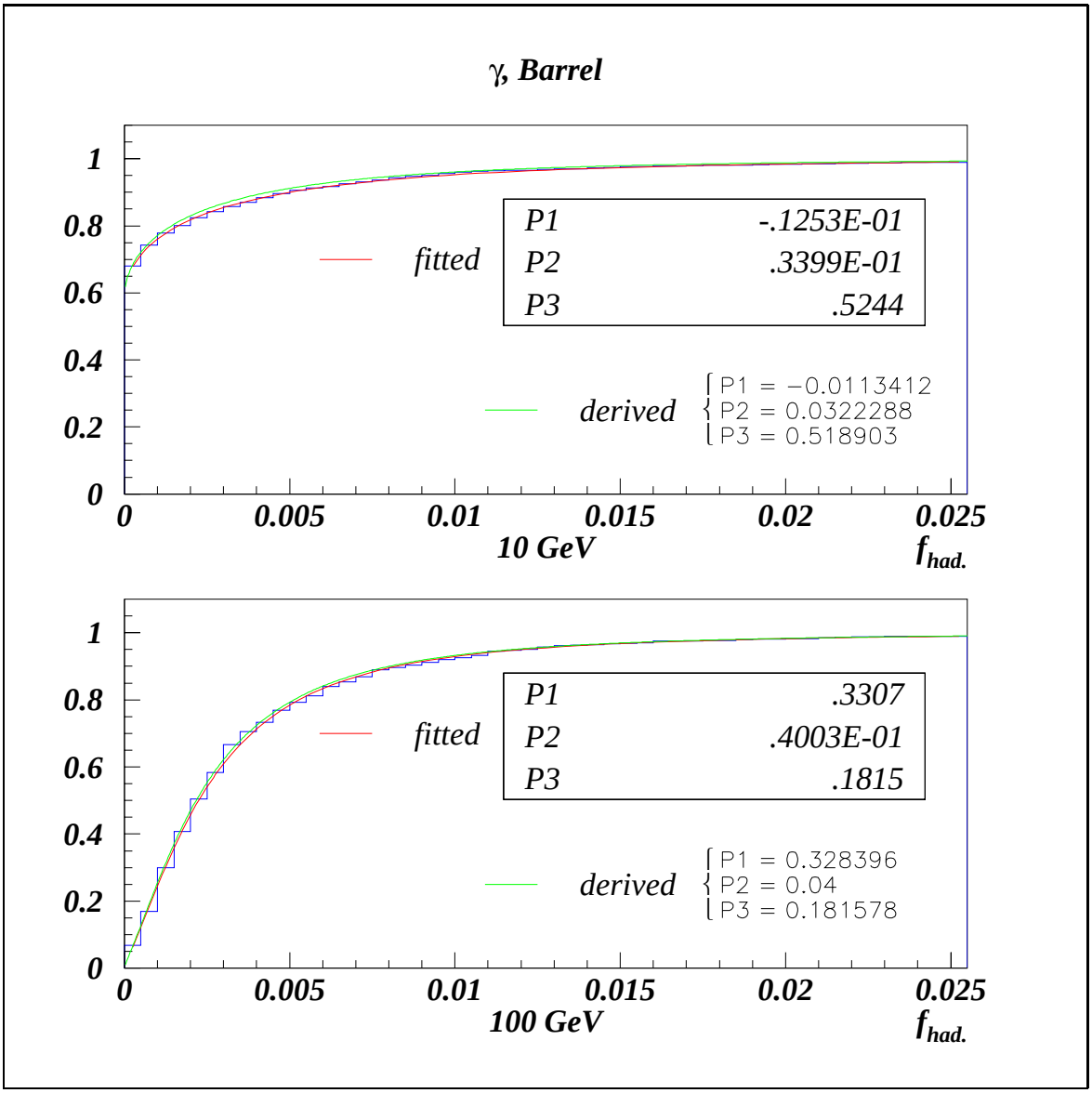

Figure 5.15: *Examples of the parameterized normalized cumulative distribution of the fractional energy deposit in the HCAL. To be seen on the plots are the original histogram, the fitted function and the resulting function obtained by inserting the derived parameters, for 10Gev (top) and 100GeV (bottom) photons in the barrel.*

5.4.1.2 Lateral

An electromagnetic shower, in the ATLAS environment, is more smeared in ϕ direction than in the η. This is because of the solenoidal magnetic field within the inner detector which deflects charged particles inside the shower in ϕ direction. Therefore depending on the hit quadrant (containing the impact point) six cells, 3 in ϕ and 2 in η directions, including the hit cell, are considered to parameterize the lateral shower profile. The possible 3×2 clusters, corresponding to the hit quadrant, are described in Figure 5.13. The adopted numbering scheme is also indicated in this figure. The distribution of the fraction of the energy deposit in the ECAL, given by (note the normalization)

$$f_{e.m.} = \frac{E_{ECAL}}{E_{nominal}} = 1 - f_{had.},$$

within these six trigger cells should now be parameterized. From now on all quantities are normalized to the energy deposit in the ECAL, i.e. all fractions refer to the ECAL deposits. The distribution of the fractional energy deposit in the hit cell plus it's two ϕ neighbours, i.e. the three cells numbered as 3, 0 and 7 in Figure 5.13, is defined as:

$$f_{307} = \frac{E_3 + E_0 + E_7}{E_{ECAL}} = f(|\Delta\eta|),$$

as a function of the absolute value of the distance in η of the impact point to the center of the hit cell, $|\Delta\eta|$, is shown in Figure 5.16. The interpretation of the result is straight forward: the closer the hit point to the center of the hit cell, i.e. $|\Delta\eta| \to 0$, the larger the fractional energy deposit in the central slice of the trigger cells, i.e. in the 3, 0 and 7 cell combination.

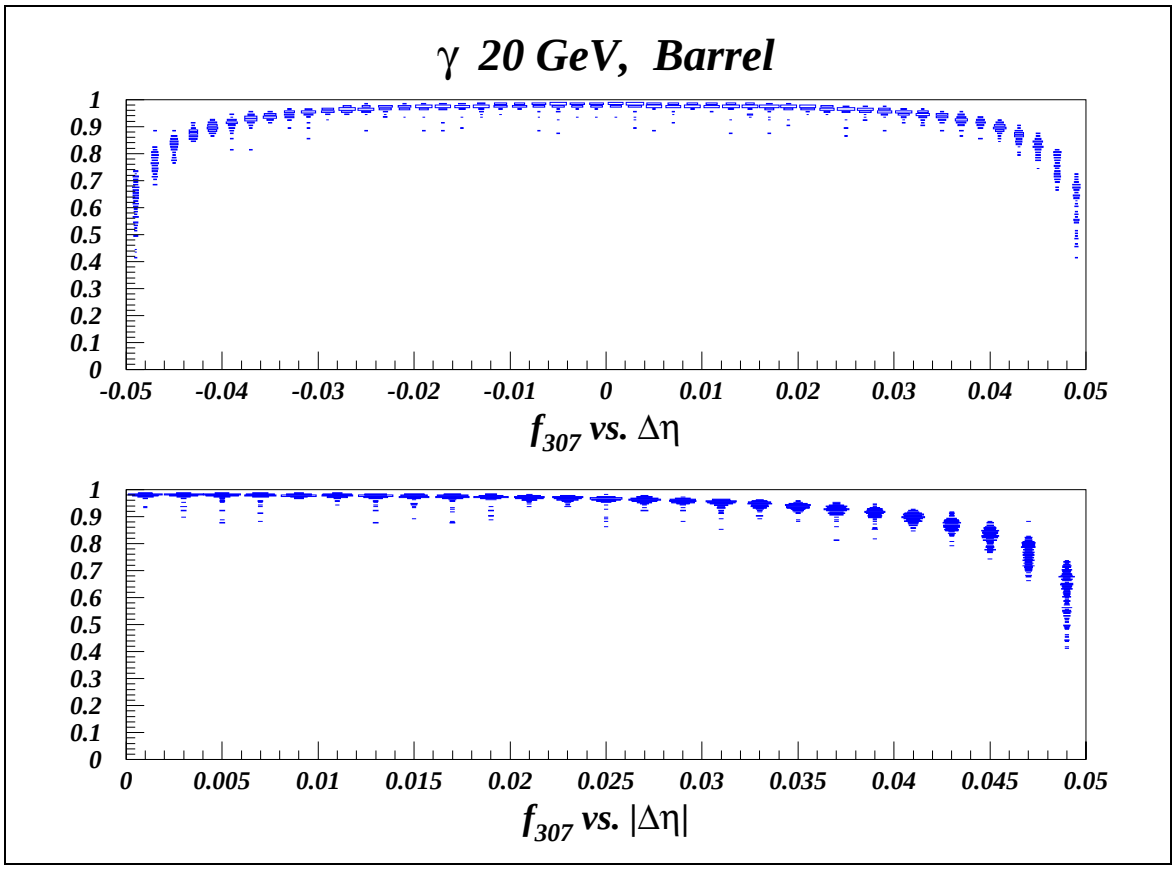

Figure 5.16: *Fractional energy distribution in the ECAL, deposited in the hit cell and it's two nearest ϕ neighbours. On the plot on the bottom, because of the symmetry of the distribution about the cell center in η, obvious from the top plot, the same distribution is plotted against the numerical value of the impact point distance to the center of the hit cell.*

The two dimensional distribution in Figure 5.16, for a given energy, is partitioned on the $|\Delta\eta|$ axis in several slices, and the distribution within each slice is projected onto the f_{307} axis. In the f_{307} distributions within a given slice a prominent peak with a tail at low fractions is observed. The location and width of the peak and the tail fraction are position dependent, i.e. $|\Delta\eta|$ dependent. The peak in each slice is fitted with a gauss function and the integral of the tail of the distribution outside 3σ of the mean of the gauss fit is determined. Some examples of these gauss fits are shown in Figure 5.17.

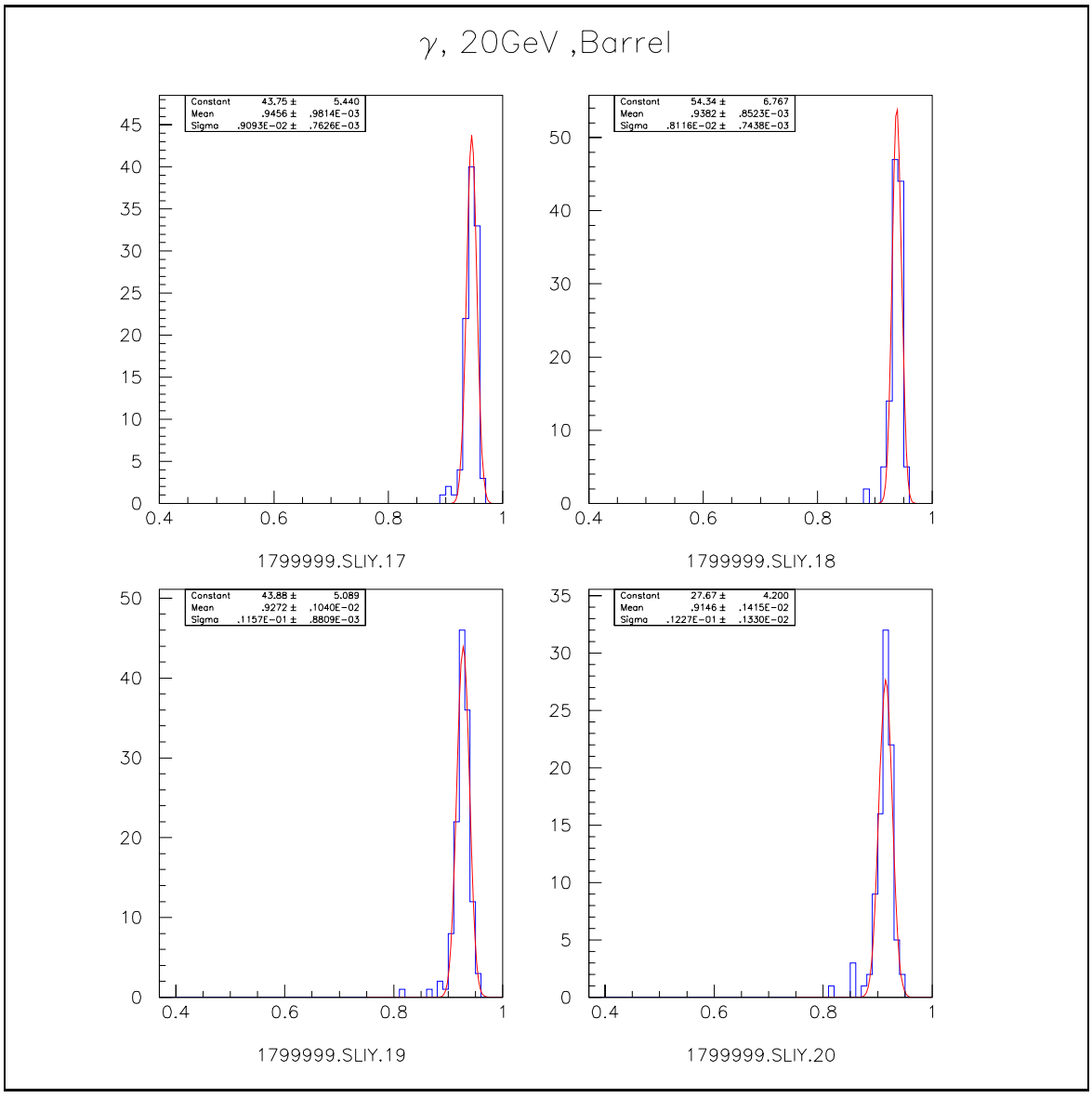

Figure 5.17: *Some examples of the gauss fits to the peak of the f_{307} distributions within each $|\Delta\eta|$ slice (see text).*

The mean and sigma of the Gaussian fits, as well as the tail fraction in each slice, is now fitted with parametric functions as a function of $|\Delta\eta|$. An example of these fits is shown in Figure 5.18. Fit parameters obtained in this way are now, in general, energy dependent. The energy dependence of the parameters, for the Barrel and for the EndCap samples, is then separately described by appropriate functions with constant coefficients. The constants are determined through a fit procedure. In addition, the shape of the tail of the distributions is also modeled in an approximate way, e.g. flat or triangular.

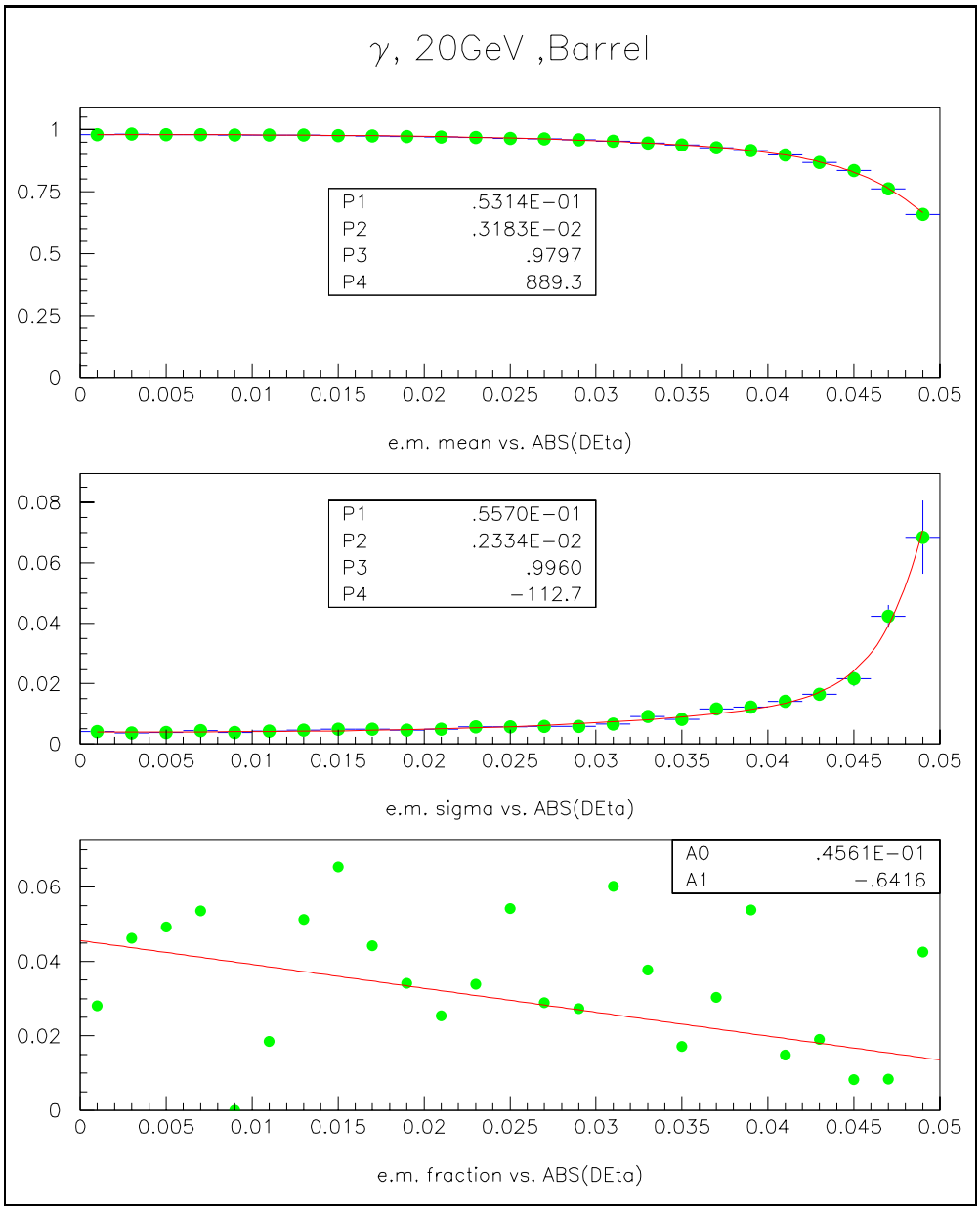

Figure 5.18: *Examples of parameterization of the mean and the sigma of the gauss fits and of the tail fractions.*

Next, the ratio of the fractional energy deposit in the hit cell, i.e. f_0, to that of the hit cell plus the two nearest ϕ neighbours, i.e. f_{307}, are parameterized. A plot of this ratio, denoted in the following by $\frac{f_0}{f_{307}}$, versus the distance of the impact point to the center of the hit cell in ϕ, i.e. $|\Delta\phi|$, is shown in Figure 5.19.

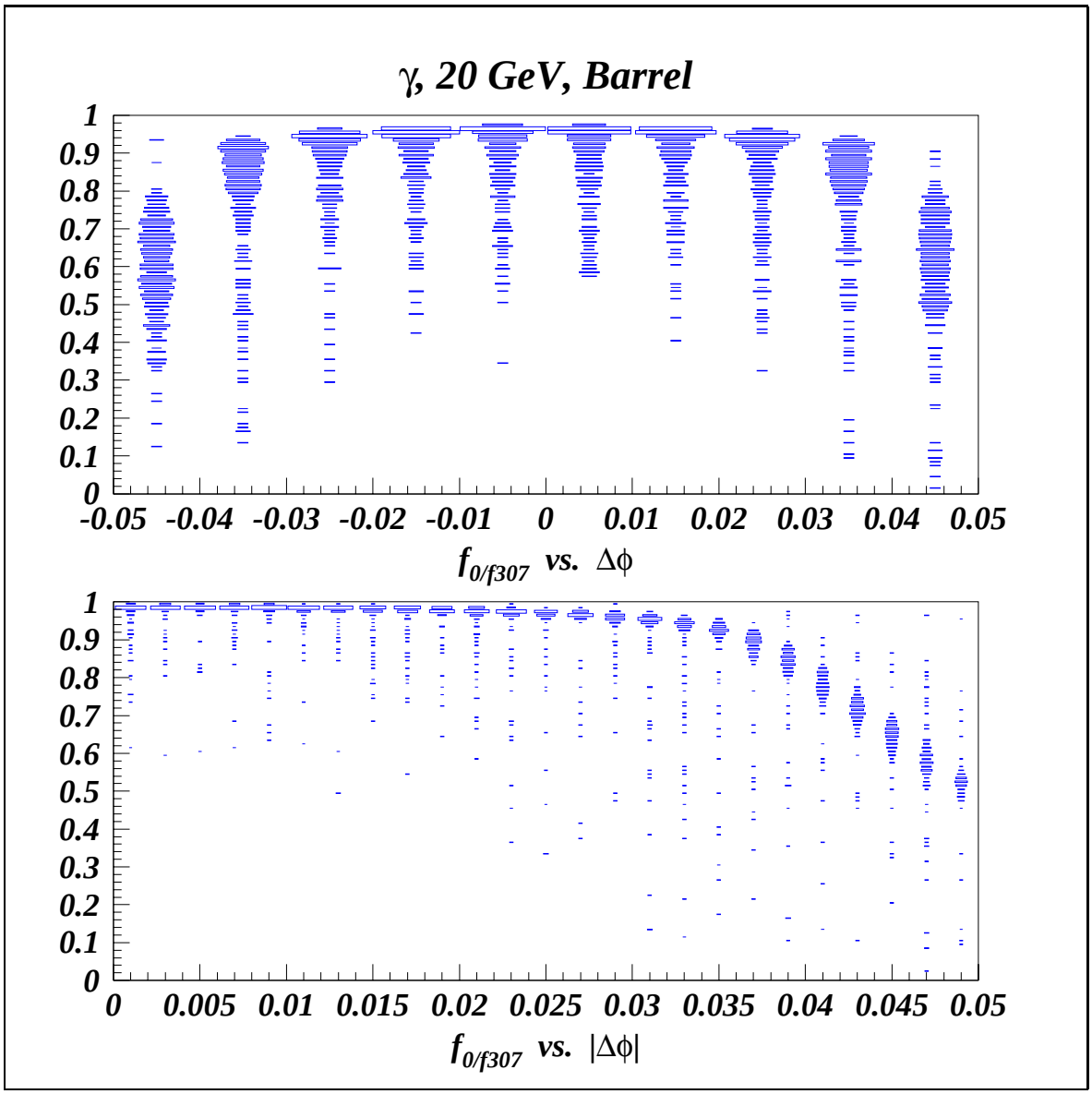

Figure 5.19: *Distribution of the fractional energy deposit in the hit cell as a function of* $\Delta\phi$ *(top), normalized to* f_{307} *(see figure 5.16). Because of the symmetry about* $\Delta\phi = 0.$*, the folded distribution about the* ϕ *center of the hit cell is considered for the parameterization of* $\frac{f_0}{f_{307}}$.

The $\frac{f_0}{f_{307}}$ versus $|\Delta\phi|$ distribution is parameterized in a similar manner as described in the f_{307} case above. Some differences are, for instance, the form of the parametric functions and the fraction and the shape of the tail. Here again, depending on η, two different sets of parameters, for the barrel and for the endcap, are obtained. At this stage the fraction of the energy deposit in the ECAL, which should be deposited in the hit cell, is fully determined (parameterized).

In Figure 5.20 the correlation between the fractional energy deposit in the nearest ϕ neighbour and the hit cell, both normalized to the energy deposit in the hit cell plus it's two nearest ϕ neighbours, i.e. to f_{307}, is shown. The nearest ϕ neighbour of the hit cell is, according to the cell numbering scheme adopted here, either 3 or 7, whichever one is closer to the hit quadrant (see Figure 5.13). This distribution is parameterized by slicing the distribution on the $\frac{f_0}{f_{307}}$ axis and approximating the peaks in each slice by a half Gaussian with a mean at $\mu(\frac{f_3 \text{ or } f_7}{f_{307}}) = 1 - \frac{f_0}{f_{307}}$ and a sigma parameterized as a function of $\frac{f_0}{f_{307}}$. The other ϕ neighbour of the hit cell gets the rest, i.e. $\frac{f_7 \text{ or } f_3}{f_{307}} = 1 - \frac{f_0}{f_{307}} - \frac{f_3 \text{ or } f_7}{f_{307}}$.

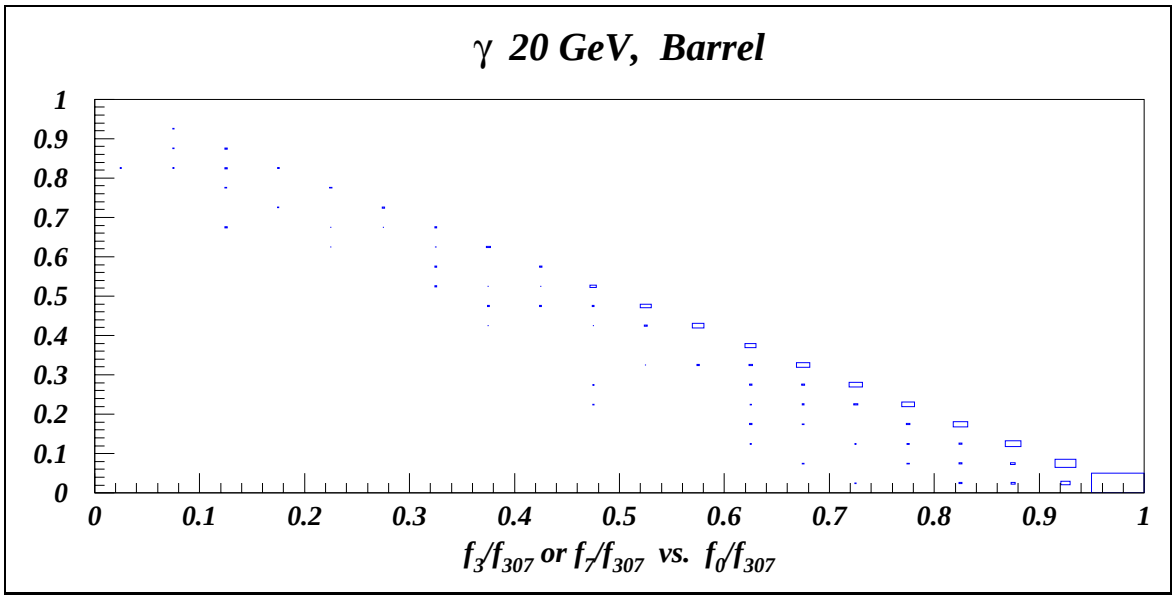

Figure 5.20: *Correlation between the energy deposits in the hit cell and in it's nearest ϕ neighbour, both normalized to the f_{307} fraction.*

In order to respect the topology of the shower, the correlation between the hit cell's nearest ϕ cell and it's nearest η cell closest to the hit quadrant (one corner of this cell touches in fact one edge of the hit quadrant) is also parameterized. Notice that the former is normalized to the deposit in the hit cell plus it's two nearest ϕ neighbours, whereas the latter is normalized to the energy deposit in itself plus the other two (nearest and next to nearest) ϕ cells, which are touching the hit cell. An example plot showing this correlation is found in Figure 5.21. The histogram title on these plots describes the normalization scheme just explained.

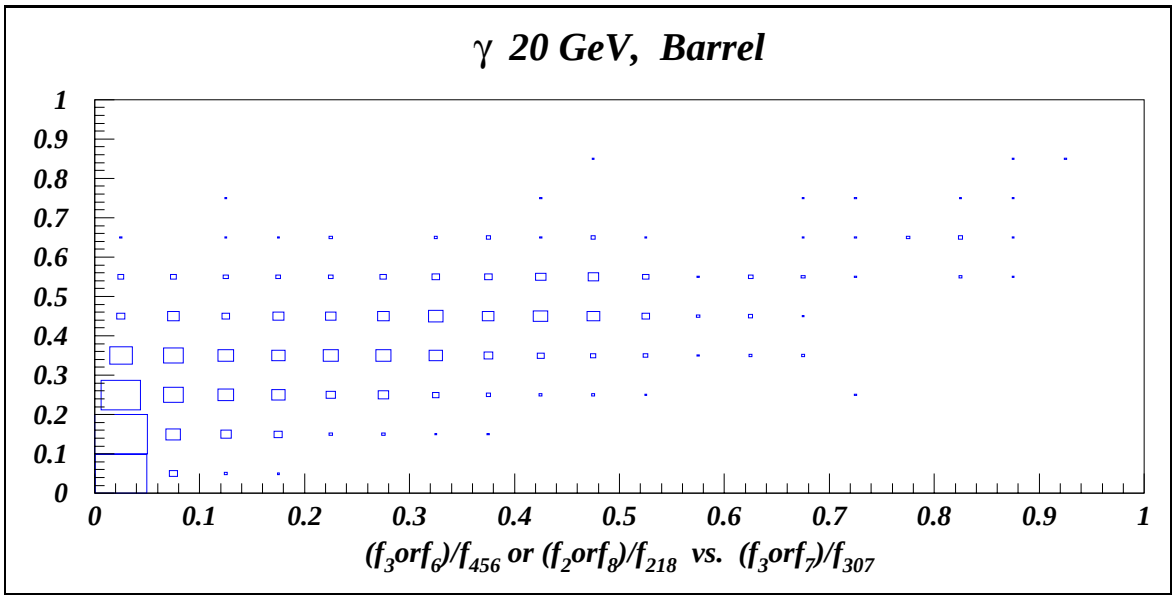

Figure 5.21: *Correlation between the energy deposits in the hit cell's nearest ϕ neighbour and it's nearest η cell closest to the hit quadrant. For details see text. For cell numbering see Figure 5.13.*

This distribution is parameterized by dividing it in two sections. The content of the first bin on the plot in Figure 5.21, i.e. $\frac{f_3 \text{ or } f_7}{f_{307}} < 5\%$, is approximated with a Gaussian, and the rest of the distribution is sliced on the abscissa axis where each slice is approximated with Gaussian fit functions. Finally, the mean and sigma of these gauss fits are parameterized as a function of $\frac{f_3 \text{ or } f_7}{f_{307}}$. Example of these fits are reproduced in Figure 5.22.

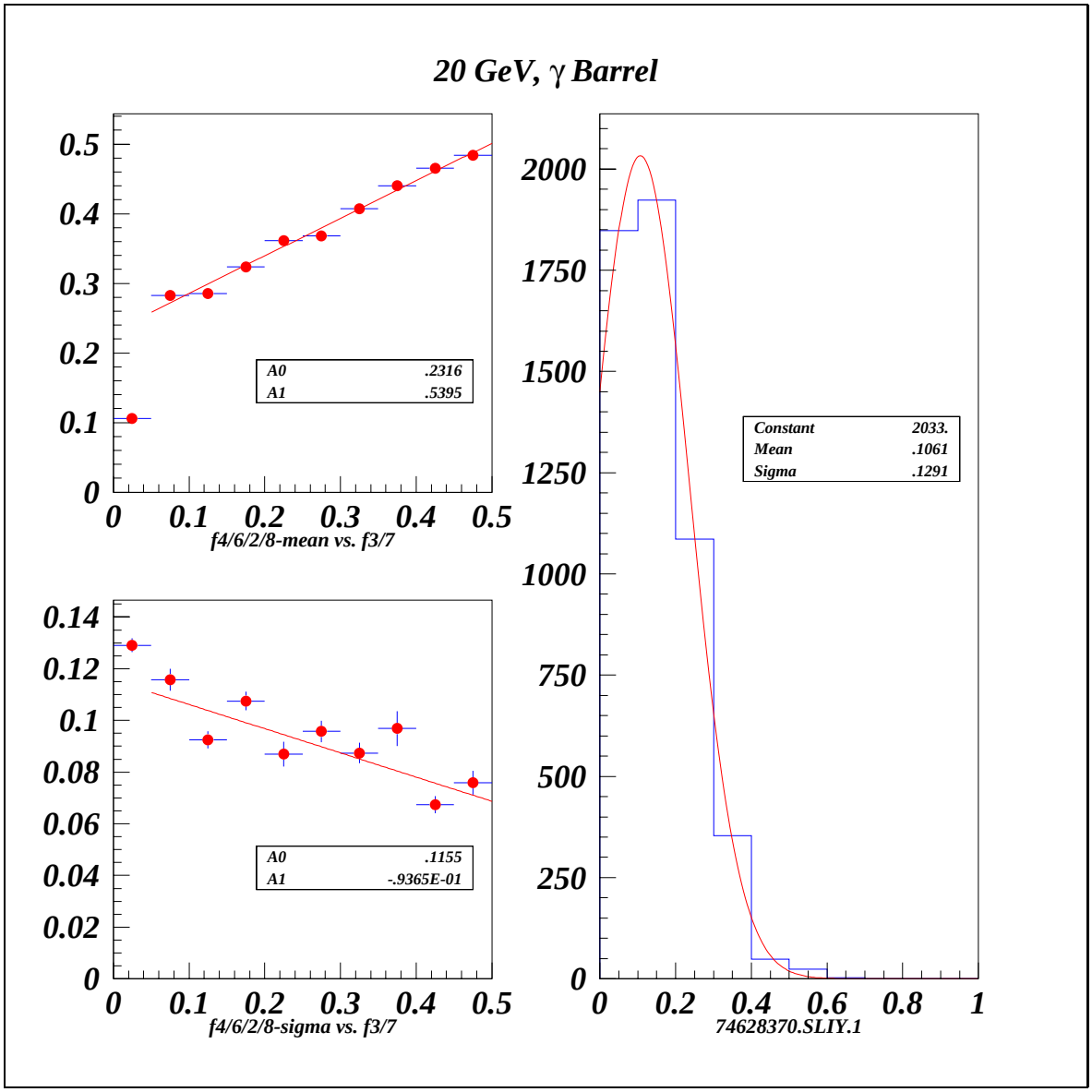

Figure 5.22: *Fit procedure to the distribution of Figure 5.21. See text for details.*

At this point the energy content of four cells of the original six trigger cells (the 3×2 matrix in Figure 5.13) is parameterized. A short cut is now applied: the remaining energy, seen in the ECAL, is divided between the remaining two cells[‖] in the same ratio as the deposits of their corresponding neighbours in η direction η cell deposits.

[‖] The remaining two cells are: the hit cell nearest neighbour in η direction closest to the hit quadrant and its neighbouring cell in ϕ direction farthest from the hit quadrant.

5.4.2 Hadronic showers

Hadronic showers are parameterized by considering a 5×4 trigger cell matrix in HCAL and/or ECAL. A 3×2 sub-matrix, in HCAL and/or ECAL, has proven to be adequate to describe the core of the charged pion shower. In order to contain as much of the shower as possible, 14 cells surrounding the core matrix are considered to describe the shower halo. To make cell references more clear, a numbering scheme is also introduced in this case. Core cells are numbered as in the electromagnetic case in previous sections. Trigger cells within halo are numbered depending on their position relative to the hit quadrant**. For a graphical description of these see Figure 5.23.

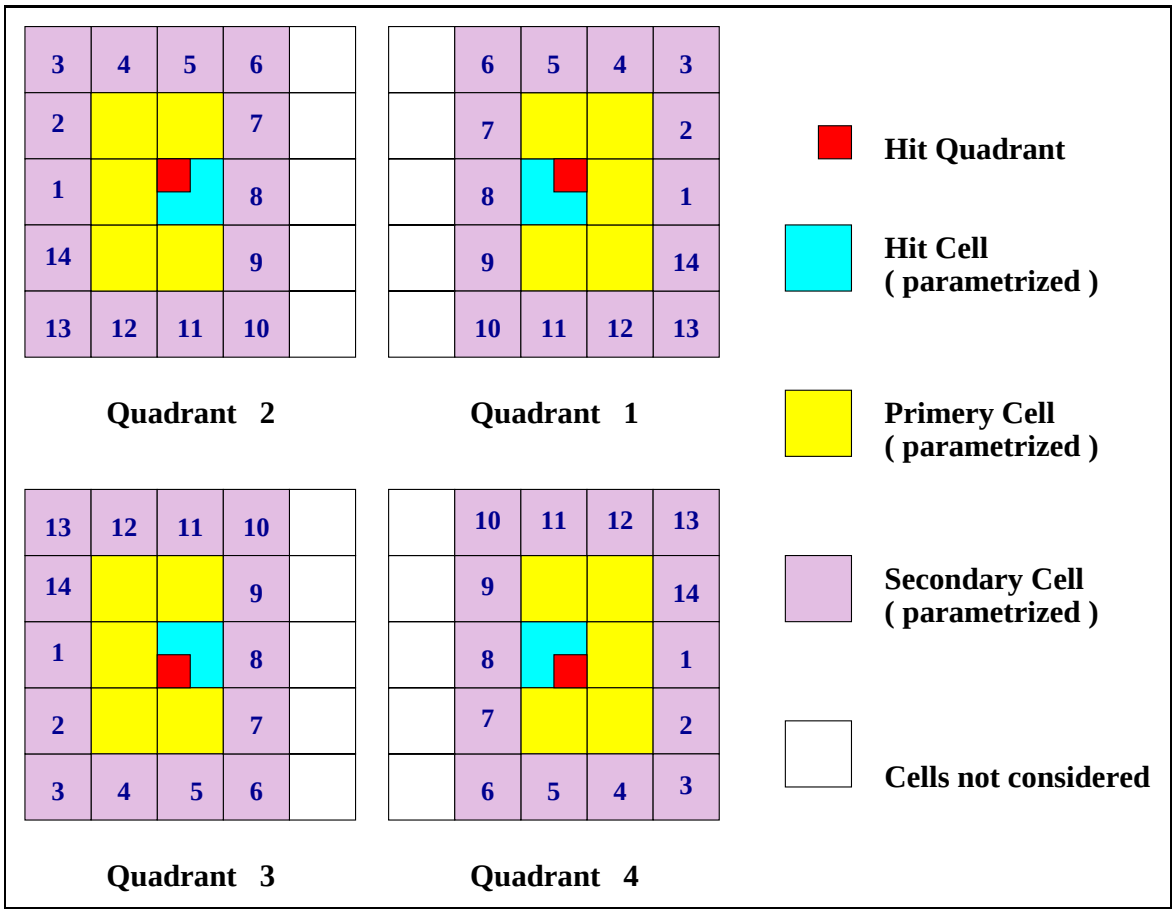

Figure 5.23: *Numbering scheme of the trigger cells within the halo of a hadronic shower (either ECAL or HCAL).*

**For instance trigger cell 8 is always closest to the hit quadrant.

5.4.2.1 Longitudinal

The longitudinal shape of the hadronic showers is implemented by randomizing from pre-filled 2–D histograms at different η positions for a number of discrete energies. As already explained in detail in section 5.2.2, these histograms contain the fractional energy deposit in the ECAL and in the HCAL against each other.

5.4.2.2 Lateral

The basic cluster size for a hadronic shower has been taken to be a 5×4 trigger cell matrix in HCAL and/or ECAL. Hadronic showers exhibit two distinct profiles. The distribution of the fractional energy deposit in the ECAL, obtained by projection on the ECAL axis in Figure 5.9, contains a large narrow peak at small energies. As explained in section 5.2.2 the position of this peak moves to smaller fractions with increasing energy. They actually correspond to a fixed energy of the order of 500 MeV, which is clearly seen in Figure 5.9 for the $1GeV$ pion case. This energy deposit corresponds simply to the energy lost by a minimum ionizing particle, *mip*. A *mip* signal within the ECAL indicates that the hadron has penetrated the ECAL, and has started showering in the HCAL. For this reason this type of shower is referred to as a *late shower*. Another type of a hadronic shower is when the showering starts already in the ECAL, known as an *early shower*. Hadronic shower types are visualized in Figure 5.24.

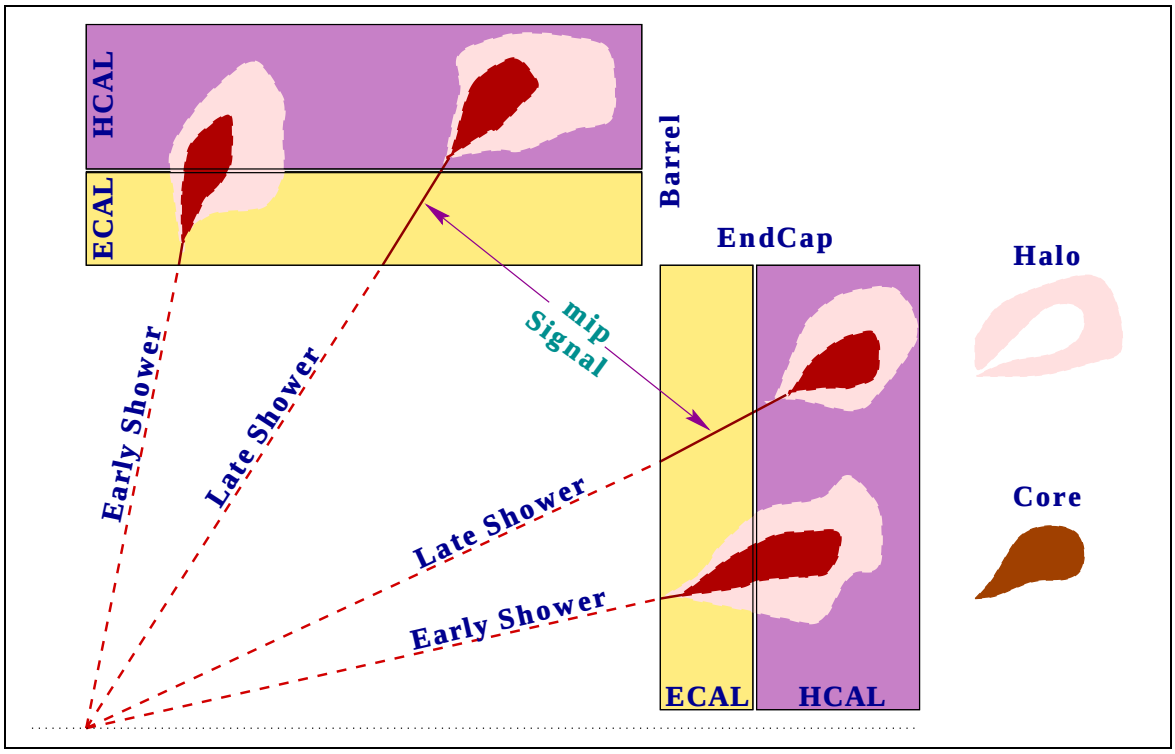

Figure 5.24: *Different types of hadronic showers explained in the text.*

Late showers

Late showers are parameterized as follows. Parameterizing the ECAL energy fraction is easy. The *mip* deposit in the ECAL is put entirely in the hit cell. The energy fraction deposited in the HCAL, i.e. $f_{HCAL} = \frac{E_{HCAL}}{E_0} = 1 - f_{ECAL}$, is now distributed among the trigger cells within a 5×4 matrix, chosen according to the hit quadrant illustrated in Figure 5.23. This is done by first parameterizing the distribution of the fraction of the HCAL deposit contained in the 3×2 core sub-matrix, i.e. $f_{Core} = \frac{E_{Core}}{E_{HCAL}}$. The same method as the one used to parameterize the longitudinal leakage of the electromagnetic showers into the HCAL is also applied here. Parameters of the fit obtained in this way are energy dependent and are described by appropriate functions, with constant coefficients, as a function of the energy. Normalizing to the energy content of the shower core, the energy fractions of the trigger cells within the 3×2 core sub–matrix are then parameterized according to the same strategy used to parameterize the lateral profile in the case of the electromagnetic showers. Finally, the halo deposit is parameterized. The distribution of the fractional energy deposit in each of the 14 trigger cells in the shower halo, normalized to the HCAL minus the core deposit, is shown in Figure 5.25.

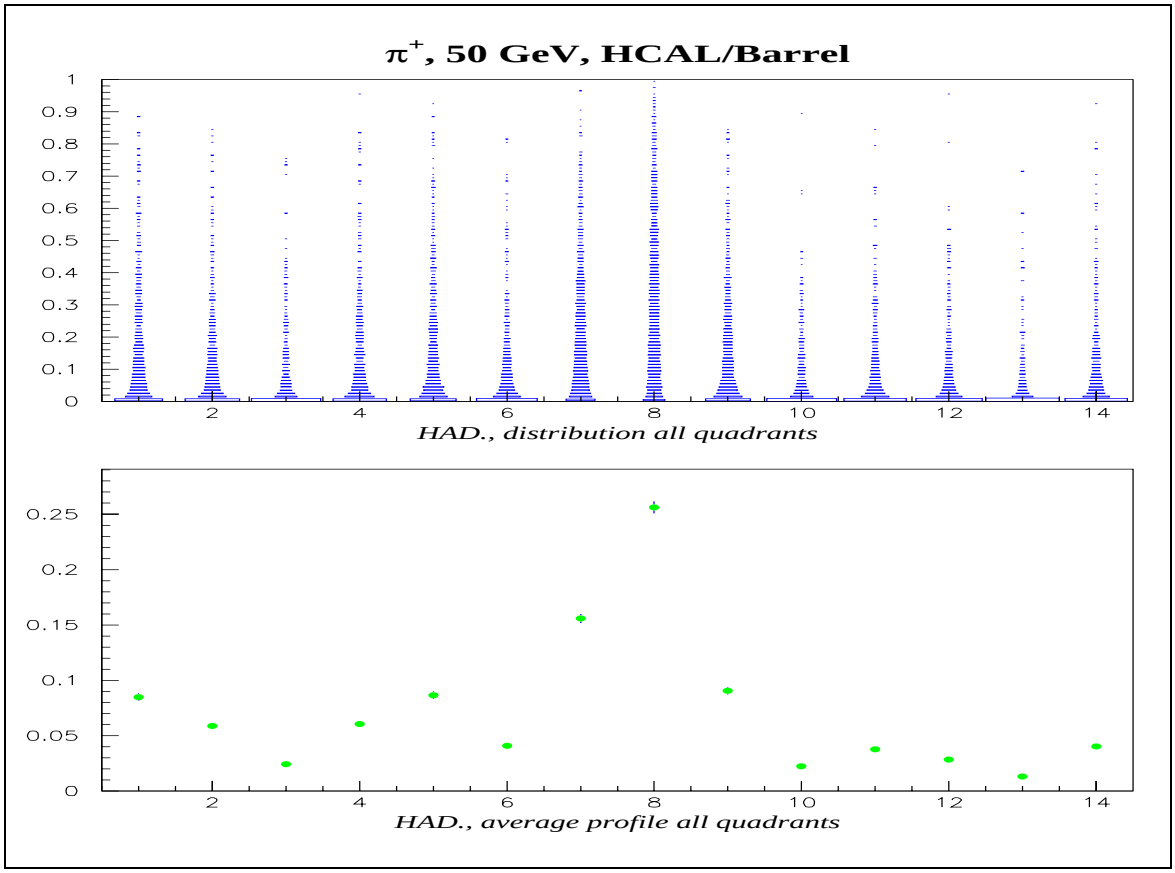

Figure 5.25: *Fractional energy distribution among trigger cells within shower halo.*

It is not straight forward to parameterize this distribution, hence the following short cut is applied. A hint of a pattern is observed in the distribution of the average fractional energy content of each cell within the halo, normalized to the halo energy, when considering the position of the cells relative to the hit quadrant. This can be seen in Figure 5.25 the bottom plot. From this figure it is seen that trigger cells can be ordered according to their average content, starting from cell number 8 with the highest average content and so on. This pattern (or order) does not change drastically for different energies (for cells with high fractional content this is a very good approximation). The fraction of the entries below 1% for each cell is then parameterized, as a function of energy. At the time of simulation, starting at the top of the ordered list of cells, it is decided, based on a random number, whether a fraction below 1% should be deposited in that cell or not. (The 1% limit for that cell is first obtained by the energy dependent parametric functions.) A fraction below 1% is generated for that cell if this is the case, otherwise a randomized fraction between 0.01 and 1 is deposited in that cell. The amount of the energy which should be deposited in the next cell in the ordered list is then determined with the same method. This procedure is continued until either the available energy is used up or the last cell in the list is processed. The remaining energy, if any, is then distributed between the cells in the same ratio as their energy content (after the first pass).

Early showers

The parameterization in this case goes essentially along the lines explained above for the hadronic part of the late hadronic showers. Both ECAL and HCAL deposits are handled in the same way.

5.5 Summary and global performance examples

The parameterization described here makes it possible to perform detailed and at the same time relatively fast simulations of the ATLAS calorimeters' response to different particle types. It provides a powerful tool to generate samples with high statistics for physics analyzes, needing a realistic detector performance effects, very fast. As a result of the parameterization the visible energy – obtained from the nominal energy by applying such calorimeter effects like response, resolution, non-compensation (in the case of hadrons) and transition region – of an incident particle is deposited in a collection of cells, of 0.1×0.1 granularity, in both the ECAL and the HCAL. Effectively the shower is described through its average profile, with fluctuations superimposed. Hence, as opposed to other fast simulations, the electromagnetic and hadronic showers:

- are not pencil–like, which deposit all their energy in only one trigger cell,
- do not deposit all their energy in only one calorimeter type, either in the ECAL or in the HCAL,
- and do not deposit all the energy in the calorimetry, not taking into account effects like response and transition region effects.

In the following some examples of the performance of the fast simulation explained here is presented. In Figure 5.28 the distribution of the electromagnetic cluster energy obtained from the fast simulation is compared to that from the full simulation, for photons in the barrel at four different energies. It is seen that the shape of the distributions, i.e. the peaks and in particular the shape of the tails, are well described. In Figure 5.27 the corresponding efficiency curves for a 20 GeV photon in the barrel as a function of the e.m. isolation threshold for 4 different hadronic leakage are compared. Thus a 95% efficiency for an e.m. isolation of 2 GeV and a had. leakage of 2 GeV is required both in the full and fast simulations. The important point is that the curves agree very well in all these four cases.

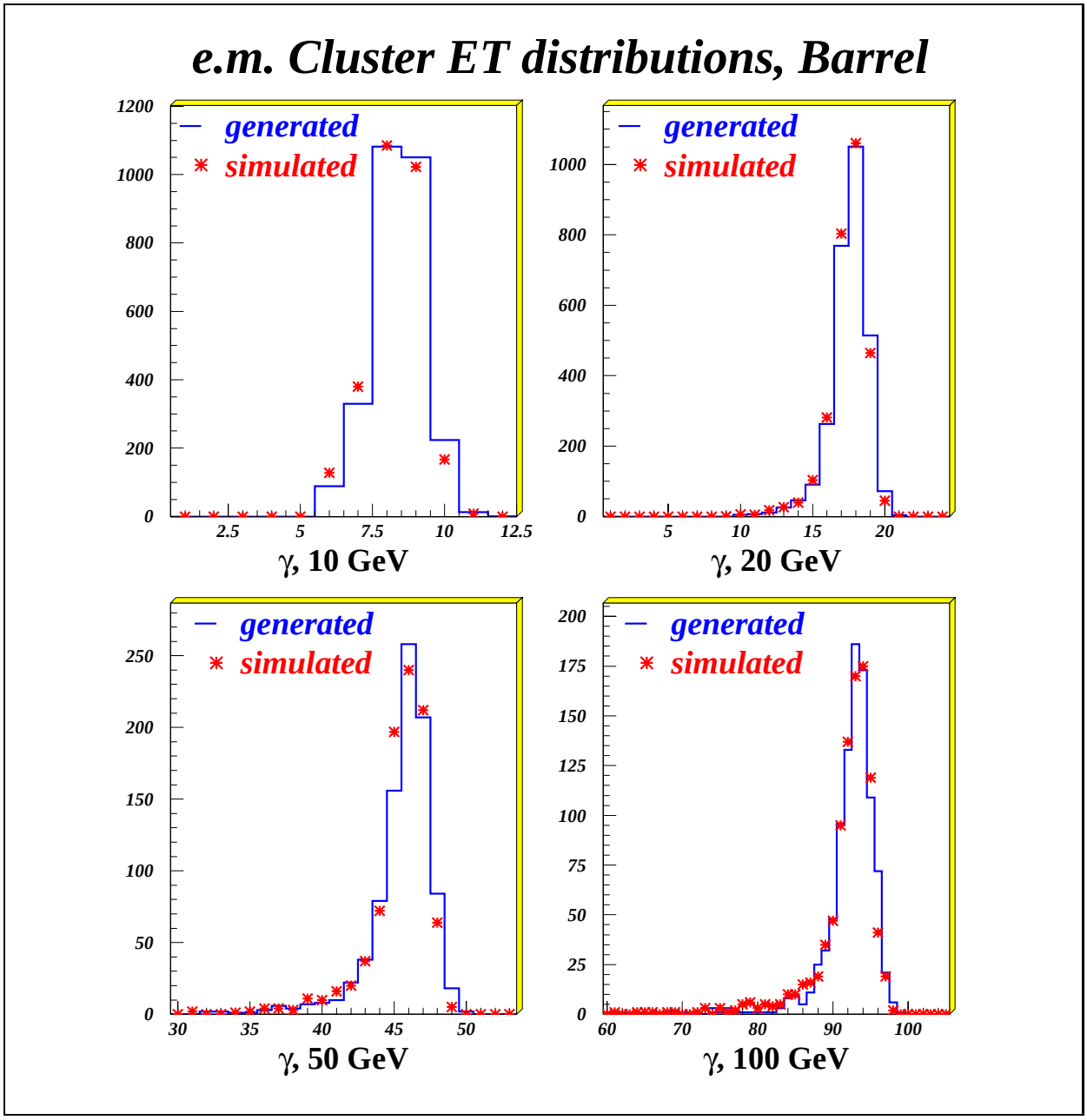

Figure 5.26: *Comparison of photon e.m. cluster energy distributions at different energies in the barrel obtained form the fast (asterisk) and from the full (histogram) simulations. Generated refers to the fully simulated sample whereas simulated to the fast version.*

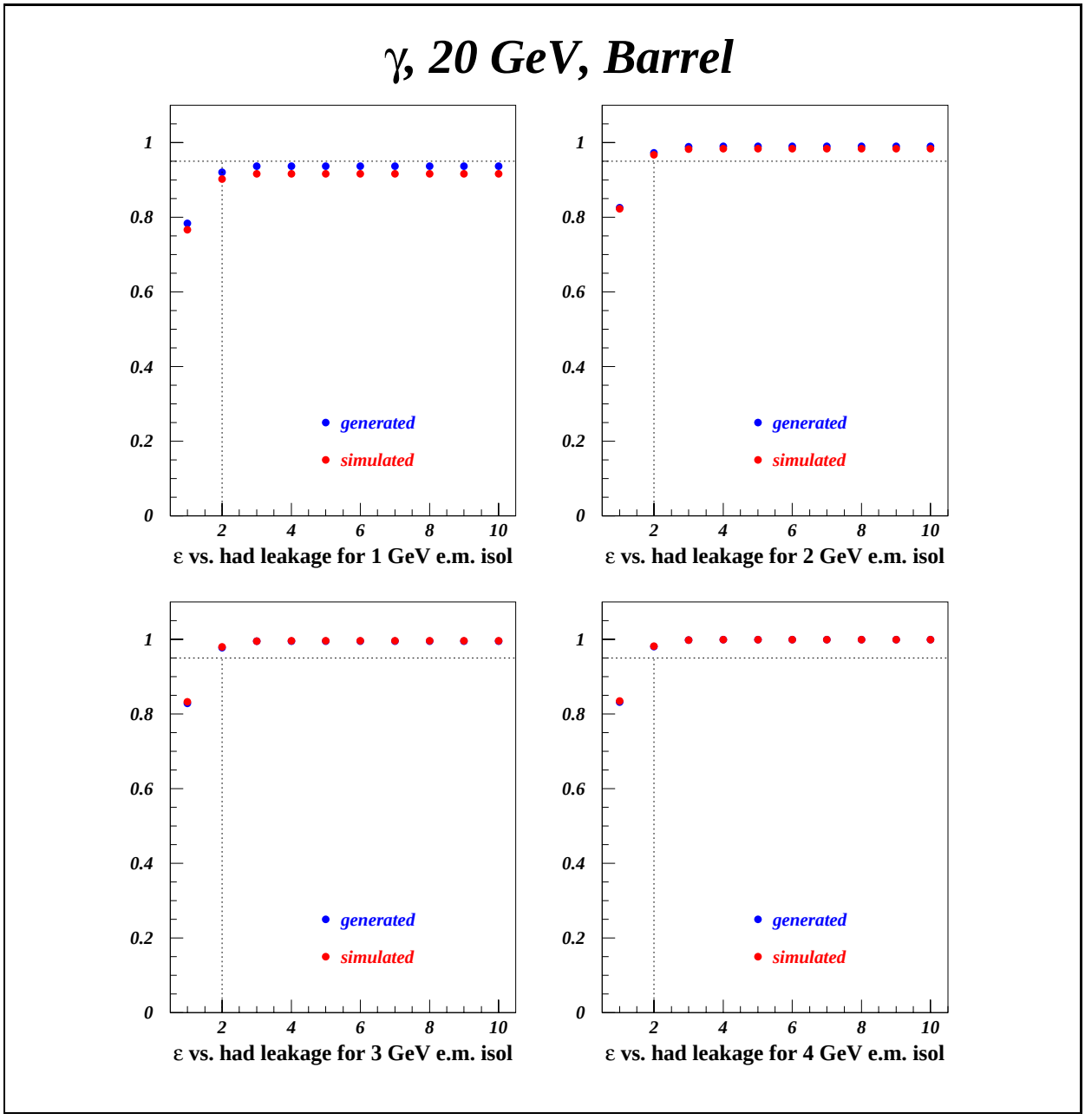

Figure 5.27: *Efficiency plots for a 20 GeV photon in the barrel for the full () and the fast () simulations. The 95% efficiency points are shown with dotted lines.*

Finally, for 50 GeV charged pions the e.m. and had. deposits (separately, together and against each other) and the transverse profiles (in the ECAL, HCAL and both) of the shower are shown in Figures 5.28 and 5.29 respectively.

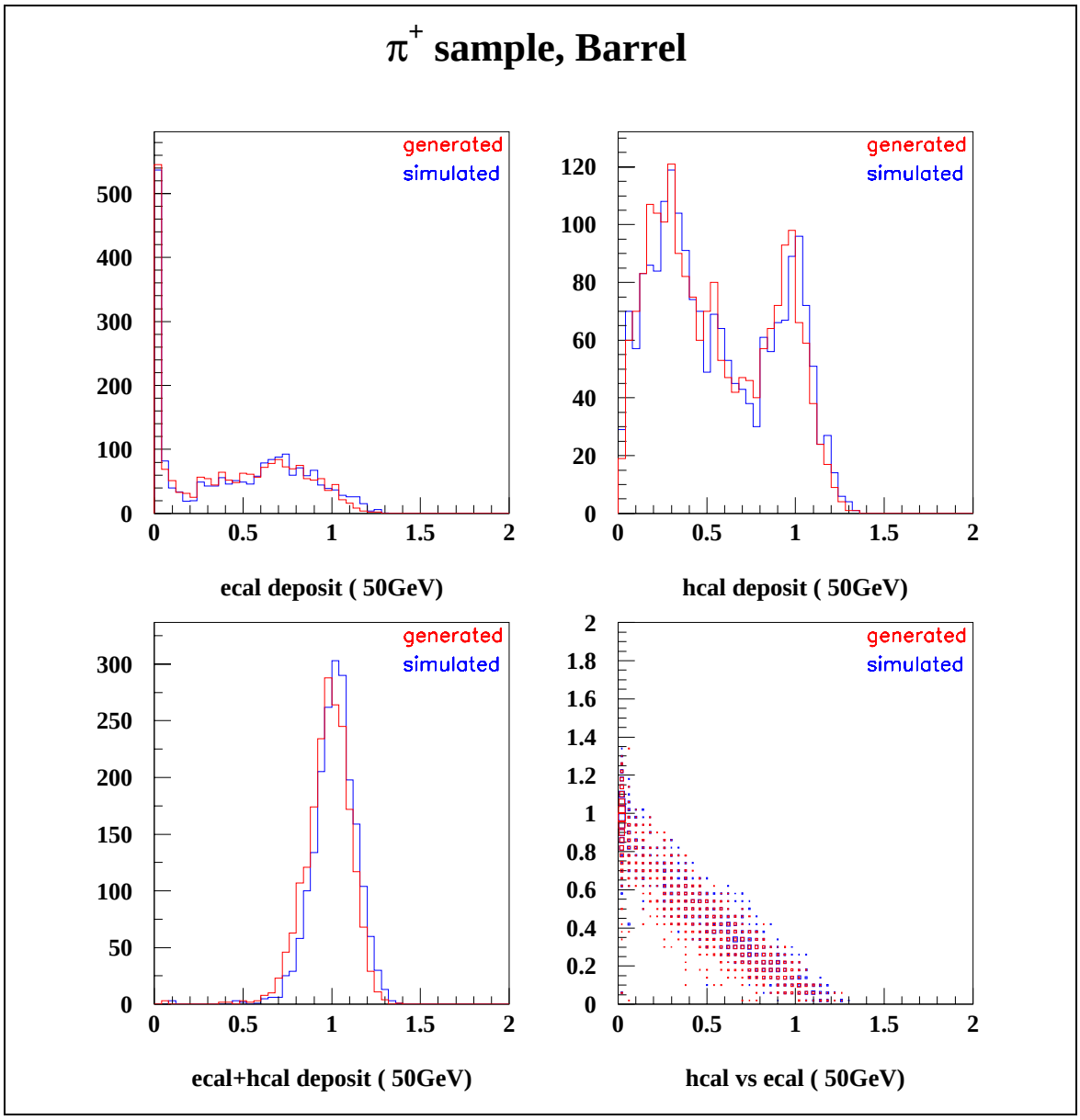

Figure 5.28: *Distributions of the energy deposits of 50 GeV charged pions in the barrel in e.m., had. and e.m.+had. calorimeters, plus the e.m. versus had. distribution.*

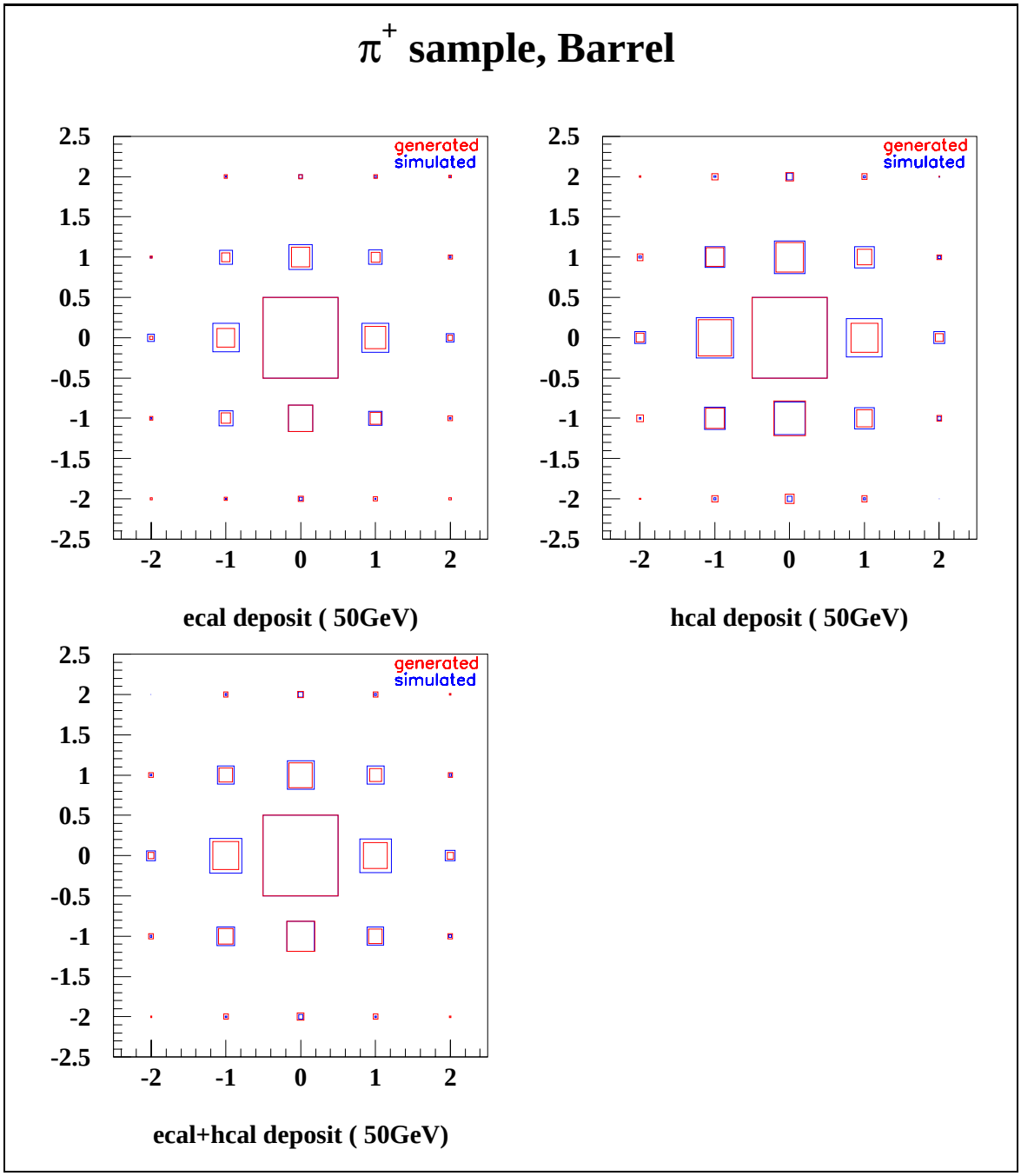

Figure 5.29: *Average lateral shower profile for 50 GeV charged pions in the barrel.*

A set of efficiency plots for tauons obtained by the fast simulation is shown in Figure 5.30. To be noticed, for instance, is that for a hadronic isolation less than 4 GeV the 95% efficiency can not be achieved no matter how high the e.m. isolation.

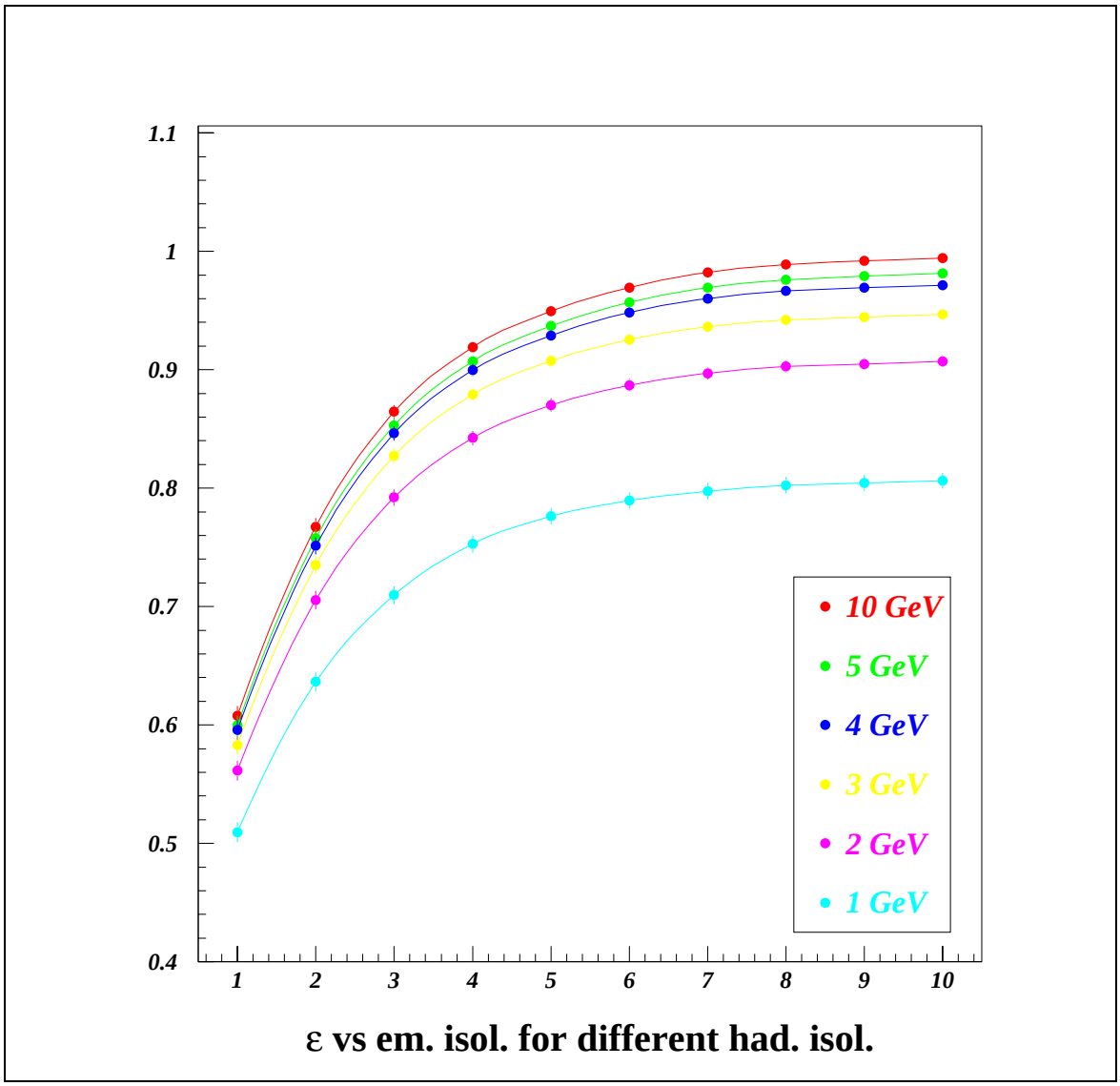

Figure 5.30: *Efficiency plots for a tauon as a function of the e.m. isolation threshold for various had. isolation.*

Chapter 6

Jet calibration and rate

The L1CT package, introduced in the previous chapter, has an interface to the fast simulation tool called ATLFAST [67], which is considered as the offline reference. This means that quantities like acceptance, trigger threshold and/or efficiency for the level–1 trigger objects are determined based on the corresponding entities in the ATLFAST so–called banks (or common blocks), which are considered as the offline quantities. An example of such a threshold determination for the level–1 calorimeter jet triggers will be worked out in the following sections. Being too optimistic a simulation tool, in terms of the calorimeter response and pile-up effects, the original ATLFAST package and its interface are modified in several ways. The details of these modifications is discussed in this section.

6.1 Introduction

In the original ATLFAST package for all stable (and, in the calorimetry, visible) particles, i.e. electromagnetic and hadronic, only one type of calorimeter map is filled, referred to as the cell map. Further, particles do not develop showers and deposit all their energy in a single cell. Pile-up effects in ATLFAST are modeled in a very simple way, and transition region effects are missing. For these reasons, and in order to have a coherent picture in the analysis on the level–1 calorimeter trigger impact in particular, a modification of the ATLFAST package has been performed. A first step in modifying the ATLFAST code is to combine and interface the L1CT calorimeter maps to the ATLFAST cell-map. In this way the modifications will be transparent to the ATLFAST package and the usual, i.e. default, cluster finding algorithms can be applied on this new map. The modification is done by first summing the ECAL and HCAL trigger maps filled by the L1CT package, after the application of the response (including the transition region effects), resolution, longitudinal/lateral shower simulation and addition of pile-up, and then copying this map onto the corresponding cell-map in ATLFAST. As explained above, ATLFAST applies it's cluster finding routine, which uses a cone algorithm method, on this map and classifies different entities like electrons, photons and jets. The transverse energy of the electromagnetic quantities suffer, at this stage, from the transition region effects and should be corrected. Hence, the transverse energy of electrons and photons falling in the transition region are modified by using the inverse of the corresponding function in Figure 5.10 on page 87.

6.1.1 Jet calibration

Due to the non–compensating effects of the ATLAS calorimetry, the visible energy of a jet is in general less than the energy of the parton initiating it. Therefore the transverse energy of the jets should be calibrated to their correct values. For this purpose, large samples of prompt photon processes are generated in PYTHIA, utilising the modified version of the interface explained above. The transverse energy of the jet is then normalised to the transverse energy of the photon. In order to do this properly and unambiguously, both initial and final state radiation are switched off in the event generation phase in PYTHIA. In this case the outgoing jet and photon in the final state are back–to–back in the transverse plane, i.e. in a plane perpendicular to the beam axis. Three cases are considered, namely samples with no pile-up, and samples with low and high luminosity pile-up. In order to populate a wider energy range for jets, two samples for each case are generated, one with $p_T < 100$ GeV at the parton level and one with $p_T > 100$ GeV. The jet finding algorithm, as already mentioned, is the ATLFAST default, namely the cone algorithm. The cone radius, $\Delta R = \sqrt{\Delta\eta^2 + \Delta\phi^2}$, is at low luminosity taken to be $\Delta R = 0.5$ and at high luminosity to be $\Delta R = 0.4$. When no pile-up is added the cone size is as in the low luminosity case. The jet E_T calibration factors, α and β, are defined according to the condition:

$$E_T^{jet}(calibrated) = \alpha(E_T,\eta)\, E_T^{ECAL} + \beta(E_T,\eta)\, E_T^{HCAL} \equiv E_T^{\gamma}\,,$$

where $E_T = E_T^{ECAL} + E_T^{HCAL} = E_T^{jet}(uncalibrated)$. The quantity $E_T^{jet}(uncalibrated)$ refers to the transverse energy of the jet reconstructed by the ATLFAST package based on the new cell-map. The jet calibration constants are then determined by minimising the quantity:

$$f = \frac{E_T^{\gamma} - (\alpha(E_T,\eta)\, E_T^{ECAL} + \beta(E_T,\eta)\, E_T^{HCAL})}{E_T^{\gamma}}\,,$$

using the MINUIT [66] program. The jet calibration factors depend both on the transverse energy of the jet and on its η (direction). Therefore a two dimensional minimisation is performed by dividing E_T^{jet} in several intervals, and by binning η in each of these intervals. Some examples of the energy dependence of the jet calibration constants in different η bins are shown in Figure 6.1. In each η bin an energy dependent function is fitted to the data points. The result of this calibration is shown in Figure 6.2. Calibration constants obtained in this way span a two dimensional surface. Separate sets of calibration factors are determined for low and high luminosities and and also for the case with no pile-up added. No parameterisation on the η dependence of the factors is performed. The parameters of the fit functions become vectors in each E_T^{jet} bin, with indices indicating the relevant η bin. The three sets of calibration factors, obtained in this way, are then incorporated into the ATLFAST code. This means that a given identified jet is calibrated to the nominal parton energy according to its E_T and its η-value using these calibration factors. The resulting calibration constants are then incorporated into the ATLFAST code. It must be noticed that in the prompt photon samples, used for the jet calibration, jets are either from gluons and/or from light quarks. As a result the jet calibration factors are average values, and might need some minor, or in some cases major, corrections based on the type of the parton initiating the jet, like a b-jet. Hence, the application of the same calibration factors to the b-jets, will, in general, not reproduce the b-parton E_T . These should then be re-calibrated to their correct nominal energies, which will be explored in the next chapter.

The complete package, i.e. L1CT plus the modified ATLFAST and the implemented interface, is then used to perform the analysis presented in the next chapter. A block diagram, illustrating the simulation framework as described here, is given in Figure 6.3. As indicated in the figure, the transverse energy of the jets in the ATLFAST package are also corrected for the E_T of any muons happen to fall within the jet cone, the so-called non-isolated muons.

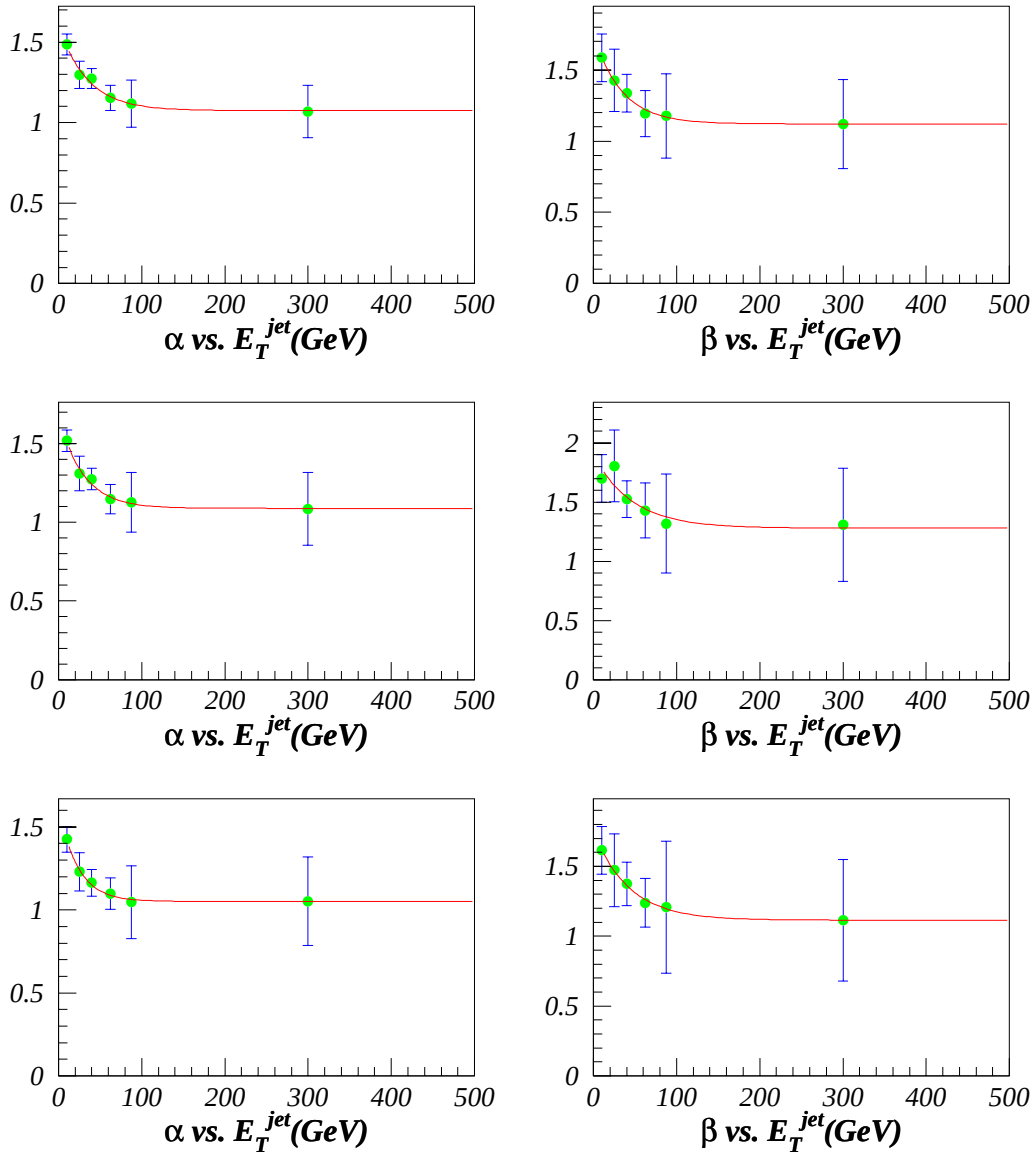

Figure 6.1: *Dependence of the calibration parameters α (left column) and β (right column) on the reconstructed transverse jet energy, E_T^{jet} (uncalibrated). Three η bins, barrel (top), transition region (middel) and endcap (bottom), are shown as examples of the behaviour of the ECAL (α) and HCAL (β) calibration factors.*

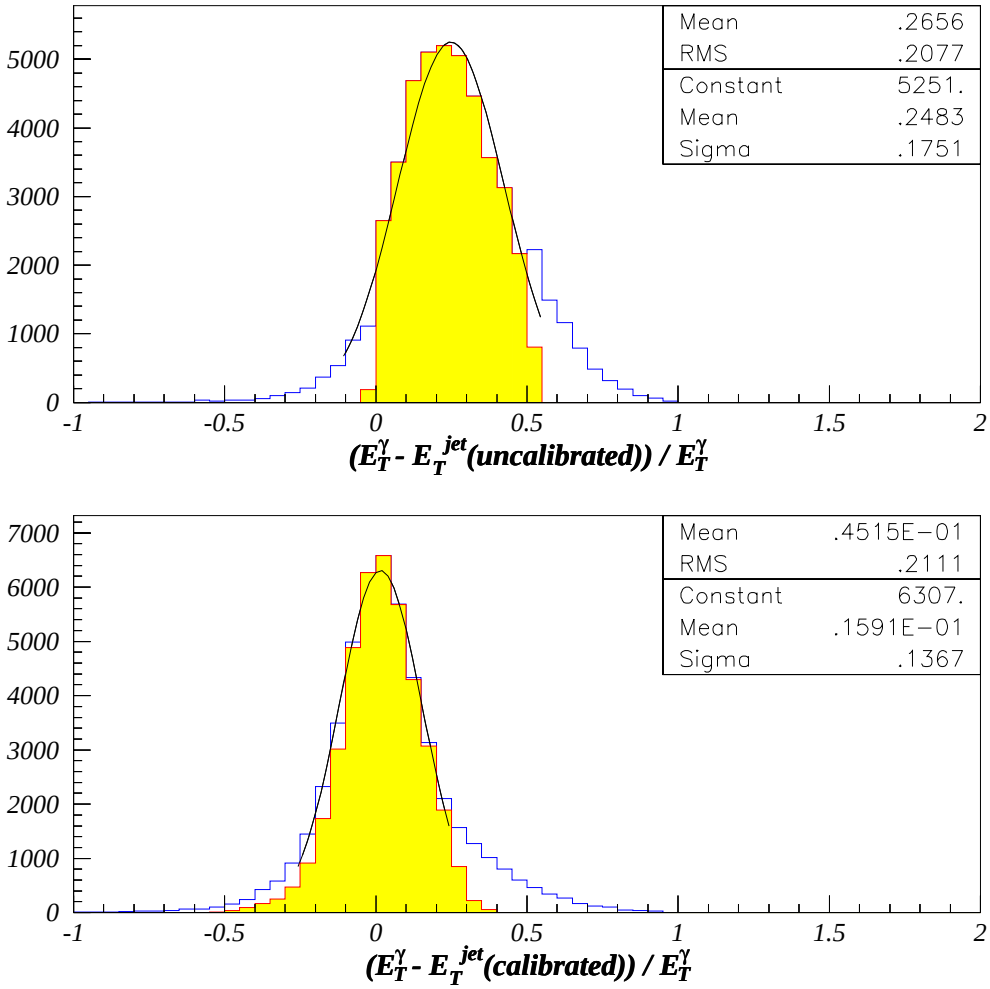

Figure 6.2: *Calibrated (top) and un-calibrated (bottom)* $(E_T^{\gamma} - E_T^{jet}) / E_T^{\gamma}$ *distributions. Only entries in the shaded part of the histogram are considered in the minimisation procedure.*

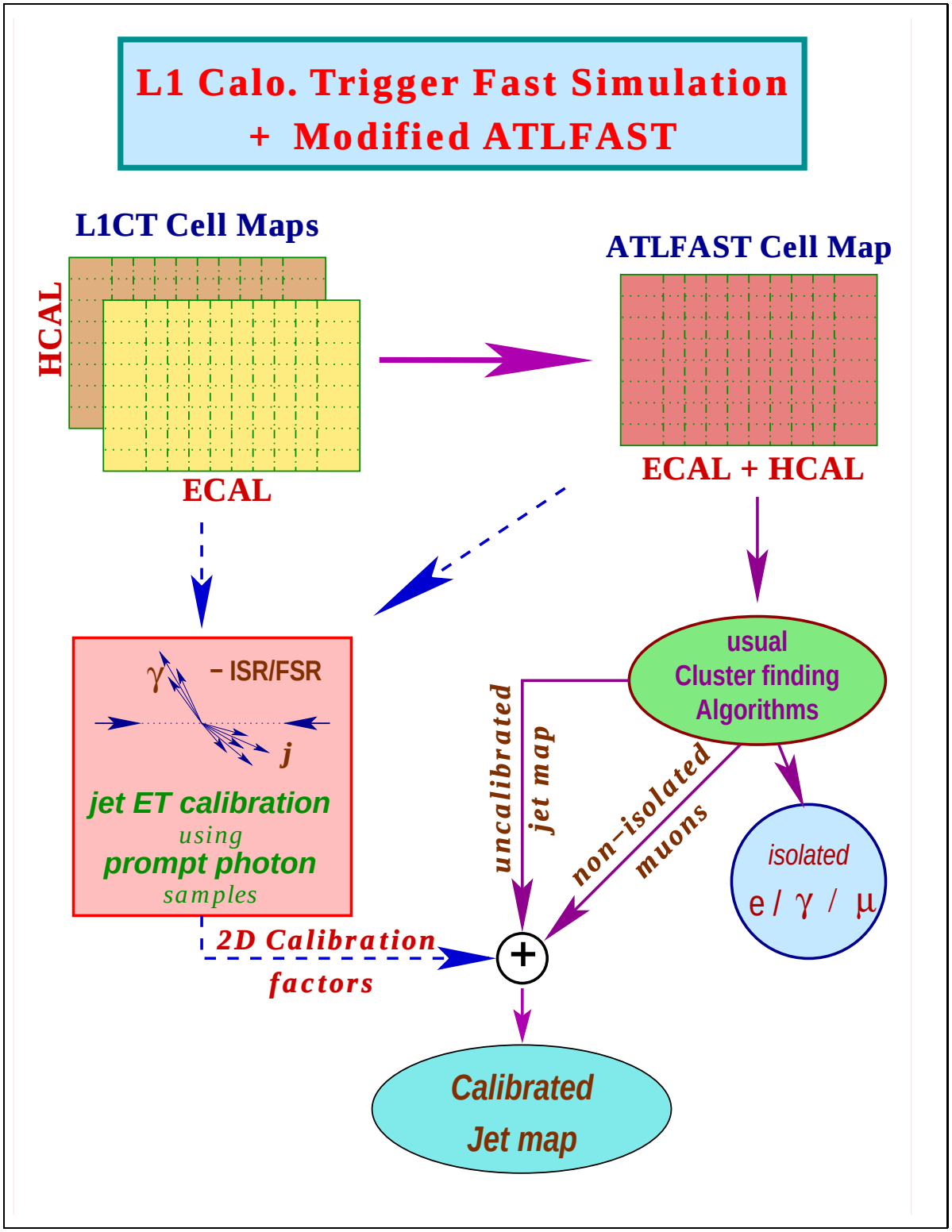

Figure 6.3: *Block diagram of the L1CT interface to the modified ATLFAST package. See text for details.*

6.2 The level–1 calorimeter jet triggers

The ATLAS level–1 trigger menu, explained in chapter 4, has foreseen three types of jet triggers. These are the inclusive, the three–jet and the four–jet triggers, with the corresponding (luminosity dependent) off–line thresholds. In order to be able to study the LVL1 calorimeter jet trigger acceptance, jet trigger thresholds must be determined. This is done by first assigning to each offline jet, reconstructed by the modified ATLFAST package, a corresponding LVL1 calorimeter trigger jet in the L1CT package. An offline jet has a radius of $\Delta R = \sqrt{\Delta\eta^2 + \Delta\phi^2} = 0.5\ (0.4)$ at low (high) luminosity. A LVL1 trigger jet, on the other hand, is a $8 \times 8 \equiv 0.8 \times 0.8$ ($4 \times 4 \equiv 0.4 \times 0.4$) trigger–tower window at low (high) luminosity. The smaller window size at high luminosity reduces the contribution of the larger pile-up effects at high luminosities to the jet E_T at LVL1. Jets at LVL1 are found by the jet algorithms explained in chapter 4. The direction of an offline jet is the E_T weighted (ϕ, η) coordinate of the offline cells taking part in the reconstruction of the jet. That of a LVL1 jet, on the other hand, is given by the RoI coordinate, which as explained in chapter 4 is the coordinate of the lowest left jet element (0.2×0.2) within the 2×2 RoI cluster.

Assignment of a LVL1 jet to an offline jet is performed as follows. Both jet maps, i.e. offline and LVL1, are ordered in descending E_T . The distance of all offline jets to all LVL1 jets, defined as $\Delta R = \sqrt{(\eta_{RoI} - \eta_{jet})^2 + (\phi_{RoI} - \phi_{jet})^2}$, are plotted in Figure 6.4. A cut has been applied on this distribution in order to be able to correlate a LVL1 jet to an offline jet. Starting from the offline jet with the highest E_T , LVL1 jets are scanned, also starting from the highest E_T , as can be seen from the figure, for their RoI distance to the offline jets direction. The first LVL1 jet which falls within a distance of 0.3 of the offline jet is flagged and assigned to that offline jet. This procedure is continued till the offline jets or the LVL1 jets (which ever sooner) are exhausted. Clearly several ambiguities, regarding the eventual correlation between E_T and distance, are involved. However, they don't occur that often, and hence don't affect the threshold determination drastically.

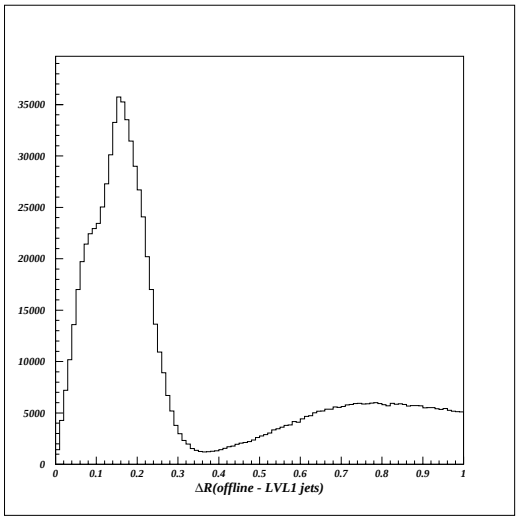

Figure 6.4: *Distribution of the distance, ΔR, between the direction of the offline jets and the RoI of LVL1 jets as defined in the text.*

6.2.1 Jet trigger thresholds

The correlation between the reconstructed offline jets and the corresponding LVL1 trigger jets, obtained as described in the previous section, is illustrated in Figure 6.5.

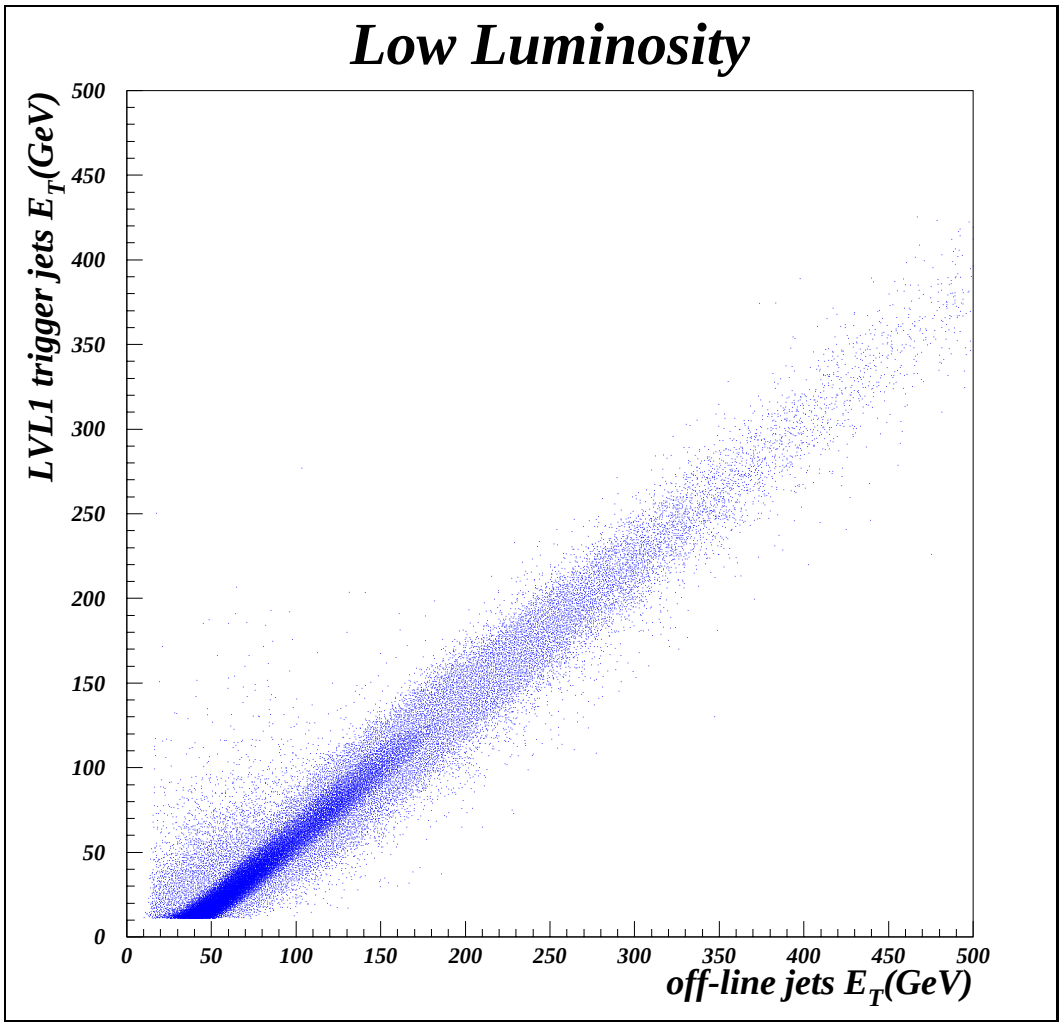

Figure 6.5: *Correlation between the LVL1 calorimeter trigger jets, calculated in L1CT, and the (calibrated) offline jets, computed by the modified ATLFAST. The distribution is not diagonal which is due to:* 1) *the much larger cone size of the offline jets relative to the size of the correspoding tLVL1 jet trigger window,* 2) *the digitization of the trigger tower signals and the limited dynamic range of the jet element construction of the (pre-)summing in the pre-processing and/or jet processing stage of the LVL1 trigger system.*

The LVL1 jet trigger thresholds, for 90% efficiency at a desired offline jet E_T , are determined from this 2–dimensional distribution. To do this the offline jet E_T axis is sliced in several intervals and each slice (or interval) is projected separately on the LVL1 trigger jet E_T axis. In each slice a jet trigger threshold is determined such that the E_T of, at least, 90% of the jets in that slice be above the threshold. Examples of such threshold determinations are shown in Figure 6.6 for three different thresholds used by the jet triggers in the LVL1 trigger menu at low luminosity. The determined thresholds in all of the offline jet E_T slices, both at low and high luminosities, plotted against the E_T of the corresponding offline jet E_T are shown in Figure 6.7.

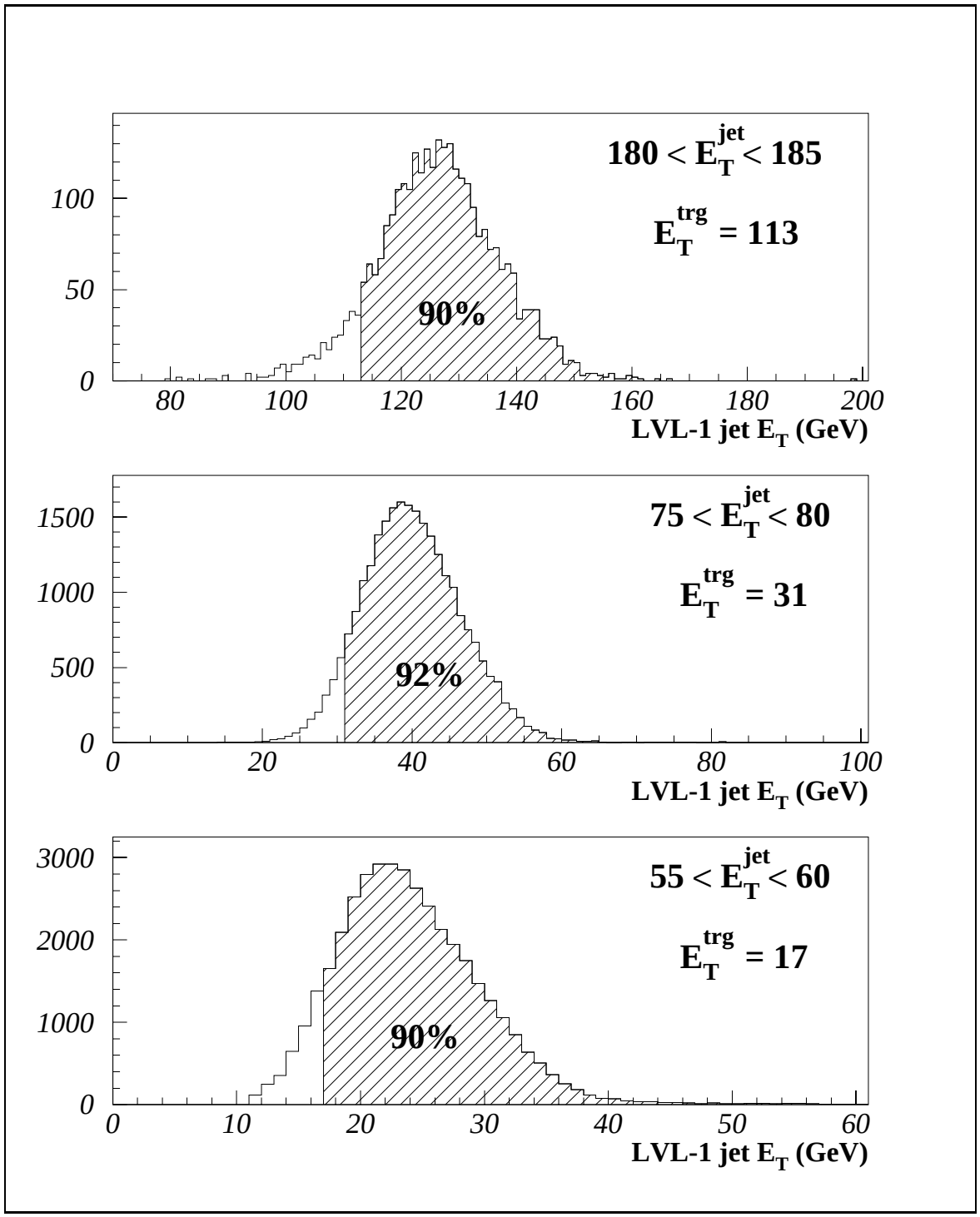

Figure 6.6: *Examples of the LVL1 calorimeter jet trigger threshold determinations. The illustrated examples correspond to jet thresholds used in the LVL1 trigger menu. The required thresholds for at least 90% (offline) efficiency, indicated by the hatched areas, are also given on the plots. (The thresholds are obtained assuming inclusive triggers within the indicated jet* E_T *intervals.)*

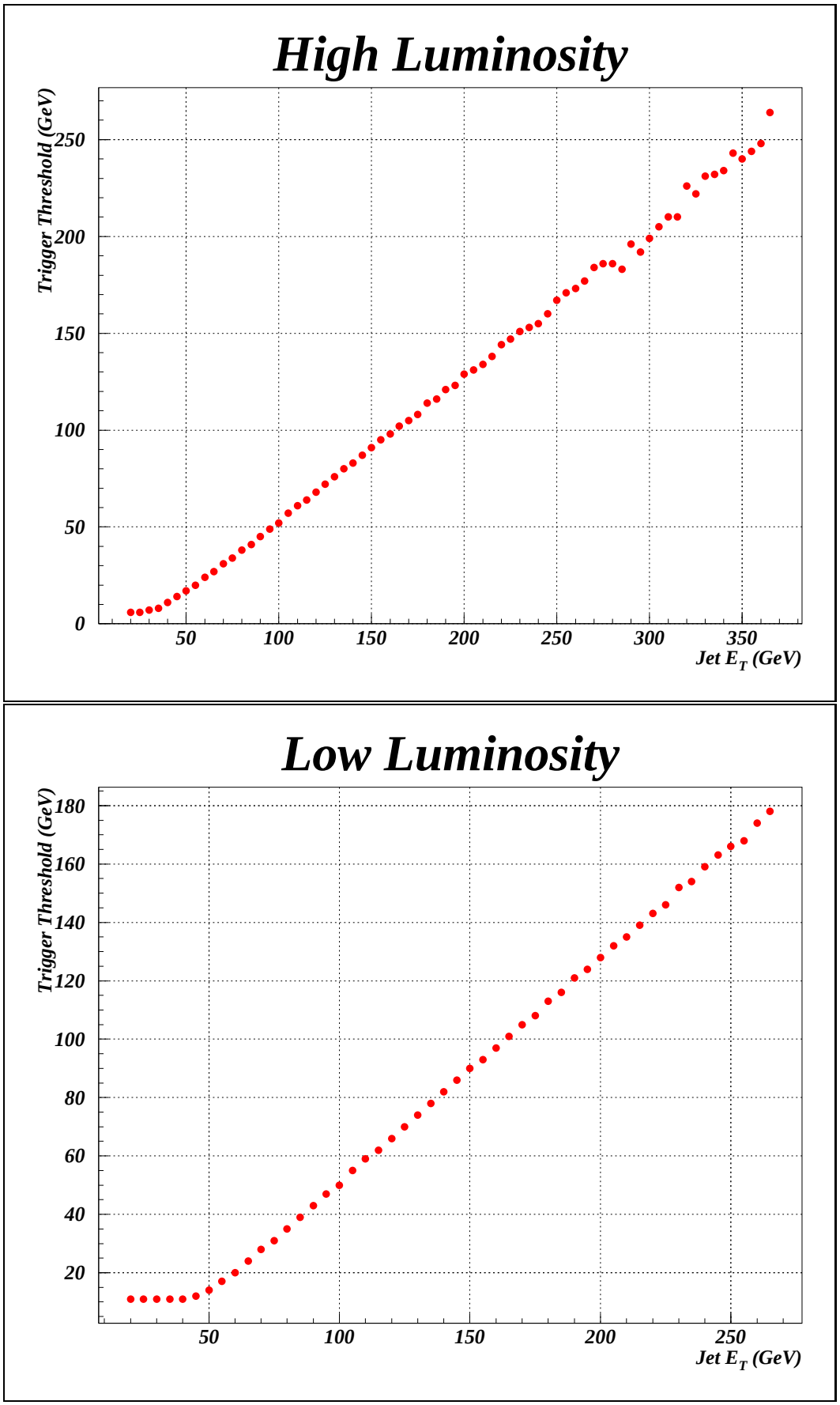

Figure 6.7: *Inclusive (or single) jet trigger threshold curves as a function of the offline jets for 90% efficiency at high and low luminosities.*

6.2.2 The LVL1 jet trigger rates

The LVL1 calorimeter jet trigger thresholds, corresponding to 90% efficiency at the offline jet E_T , can be read–off from the plots in Figure 6.7. Using these thresholds the LVL1 jet trigger rates for the low and high luminosity cases, displayed in Figure 6.8, can be estimated for any offline jet E_T for 90% efficiency.

The trigger rates read from the figure are roughly 600 Hz at low and about 300 Hz at high luminosity for each jet trigger type. It should be noted that these jet rates are larger than the corresponding rates quoted in the trigger menus. One major difference between the two evaluations is the pile-up simulation, which is more detailed here. Another point is the jet definition, in terms of the cone size for offline jets, which is not unique and well–defined, and consequently may be different in each case. Yet another difference is the effect of the calorimeter response being simulated in more detail here. In addition the thresholds can be determined either to obtain a given rate or a given efficiency.

Considering the jet triggers in the LVL1 trigger menu the following thresholds are obtained:

- **Low Luminosity:** single/three/four jet trigger: 113/31/17 GeV,
- **High Luminosity:** single/three/four jet trigger: 196/76/45 GeV,

These trigger thresholds will be applied on the signal and background samples in the next chapter to obtain an estimate on the signal acceptance and the just quoted background rate.

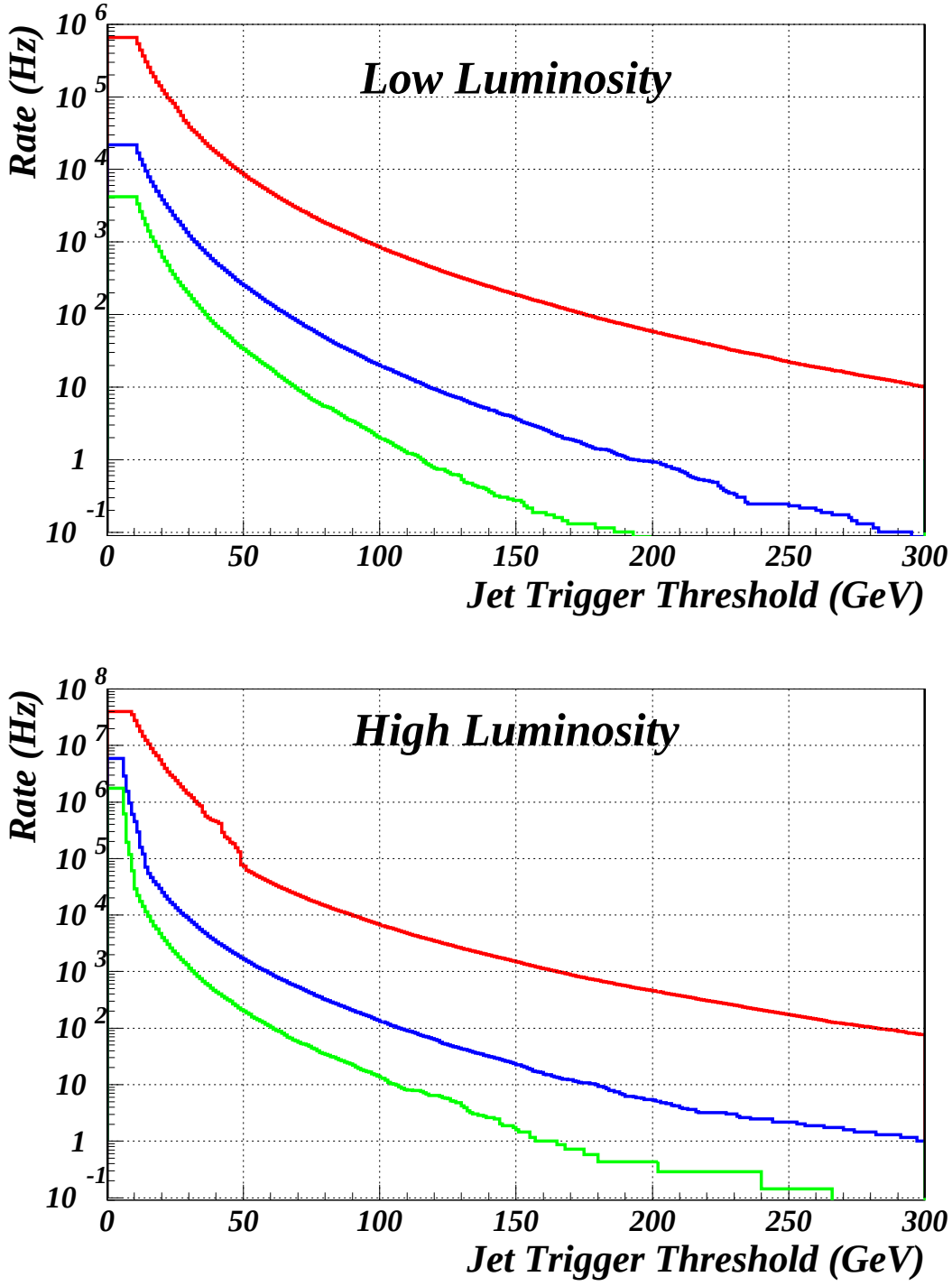

Figure 6.8: *The LVL1 jet trigger rates as a function of the applied threshold. The LVL1 jet trigger thresholds for the LVL1 trigger menu entries are given in parentheses for each jet trigger type.*

Chapter 7

Observability of the neutral MSSM Higgs bosons in multi *b*-jet decay channels

In this chapter a detailed study on the observability of the neutral MSSM Higgs bosons in the decay channels with multi b-jet final state topologies* in the ATLAS environment will be presented. These channels are the $b\bar{b}\,H \rightarrow b\bar{b}\,b\bar{b}$ and the $H \rightarrow h\,h \rightarrow b\bar{b}\,b\bar{b}$ decay modes, at low and high $tan\,\beta$ values respectively. The production cross-section and the branching ratios for both channels are high for the $tan\,\beta$ and mass values studied. The selectivity of the combined LVL1/LVL2 jet triggers are essential for these channels, which suffer from the huge QCD multi-jet background. Having to do with b-jet final states, the ability of the LVL2 specialized b-tag jet trigger is essential to reject the dominant jet activity from QCD multi-jet processes. Representative offline selection algorithms, with adjustable parameters, are analyzed, and, based on specific choices of parameters, estimates on the ATLAS discovery potential, in terms of the statistical significance defined as the ratio of the signal to the square-root of the background contribution, are obtained. In what follows, the impact of the LVL1 calorimeter jet triggers on the acceptance of these processes is presented and possible improvements in the acceptance of the combined LVL1/LVL2 trigger system are discussed.

7.1 Introduction

In order to evaluate the level-1 calorimeter jet trigger acceptance and, at the same time, to perform the required offline analysis, large samples of the signals and the QCD background have been generated using the PYTHIA physics generator. The signal samples are generated using a modified version of PYTHIA, which is improved in the MSSM Higgs sector, containing radiative corrections to masses cross-sections and branching ratios for instance. The cross-sections and the branching ratios, quoted in the following, stem, however, from more accurate Monte-Carlo programs [60] and differ slightly from the values obtained from this modified version. Hence, all results regarding the rates are normalized to these more accurate values.

*For other discussions/analyzes on this topic see for instance [70, 69, 46].

While 2-loop corrections to the production cross-sections of the signal samples are available, the same is not the case for all the background processes. For this reason the K-factors on the signal channels are not included in the calculations. In the following, after a description of the so called b-jet recalibration procedure, the essential characteristics of the QCD multi-jet sample, being the common background to both channels studied here, is described first.

7.2 Re-calibration of b-jets

The jet calibration procedure, explained in the previous chapter, averages the gluon and the light quark jets, which generally have different internal topologies than the jets initiated by the b-quarks. As mentioned in chapter 1, the hadronization of heavy quarks is well described by the peterson fragmentation. Hence the fragmented B-hadron will in general have a higher $\mathrm{p_T}$ distribution. In addition a B-hadron does, in almost 20% of the cases, also decay semi-leptonically into muonic or electromagnetic final states, with missing transverse energy due to the associated lepton neutrinos. The jet calibration implemented in the simulation environment does not take this into account. Hence, the visible energy of a b-jet will in general be lower than its nominal energy. For this reason, before being able to perform offline analysis on the signal and on the background, the final state b-jets must be re-calibrated to their correct $\mathrm{E_T}$.

To re-calibrate the b-jets, and in order to be able to cover a larger $\mathrm{E_T}$ range, signal samples with heavy neutral (CP-even) MSSM Higgs with a mass of 300/500 GeV decaying into $b\bar{b}$ final states, i.e. the $b\bar{b}\,H \rightarrow b\bar{b}\,b\bar{b}$ decay channel, are used to derive the energy dependent b-calibrating factor, $\alpha(E_T^b)$. The transverse energies of the b-jets are then recalibrated to their nominal values according to: $E_T^b(calibrated) = \alpha(E_T^b) \cdot E_T^b(uncalibrated)$. The mass of the heavy Higgs is reconstructed by using the offline jets labeled as b-jets coinciding with a parton b-jet. The coincidence is determined based on the criteria that a parton b-jet should be the closest jet falling within a cone of radius $\Delta R = \sqrt{\Delta\eta^2 + \Delta\phi^2} = 0.1$ about the $\mathrm{E_T}$ weighted center of gravity[†] of a b-labeled offline jet. Further, only the two b-jets, which according to the information in the partonic part of the event history are emitted in the decay of the Higgs boson H, are used for the mass reconstruction and the following recalibration procedure. The associated offline b-jets are excluded from the recalibration procedure. The reconstructed bb-mass appears in a lower value than the nominal H Higgs mass, when using the uncalibrated b-jet transverse energies. To move this bb mass peak to its correct location the $\mathrm{E_T}$ of the contributing b-jets should be calibrated accordingly. The calibration is performed by dividing the transverse energy of the b-jets in several sub-intervals. The η dependence of the calibration factors are averaged out. The calibration factor in each of the b-jet transverse energy interval is determined by performing a common global minimization using MINUIT, according to the function:

$$\sum_{n=1}^{N} \left(\frac{m_{bb}(\alpha_i(E_T^{b1}), \alpha_j(E_T^{b2})) - m_H}{\sigma_H} \right)^2 ,$$

where σ_H is the width of the uncalibrated bb-mass distribution. The summing in the formula above runs over the number of events and the indices i and j refer to E_T^b intervals. The

[†] This is the usual definition of the jet direction (or axis) in the (η, ϕ)

superscripts $b1$ and $b2$ on the transverse energies of the b-jets correspond to each of the b-jets from the Higgs decay. The obtained calibration factors, for low and high luminosities, as a function of the transverse energy of the b-jets are shown in Figure 7.1 for $tan\,\beta = 30$ case. The calibration factors do not depend on $tan\,\beta$ and vary slightly with the H mass. The slight dependence on the mass of the Higgs is neglected in the determination of the b-jet recalibration factors. As seen in the figure the recalibration factors approach asymptotically to value of about 1.30 at high transverse energies. At low transverse energies ($E_T <\sim 80$ GeV) the calibration factors are approximated with constants, in order not to introduce artificial boost in the E_T of the jets in this region.

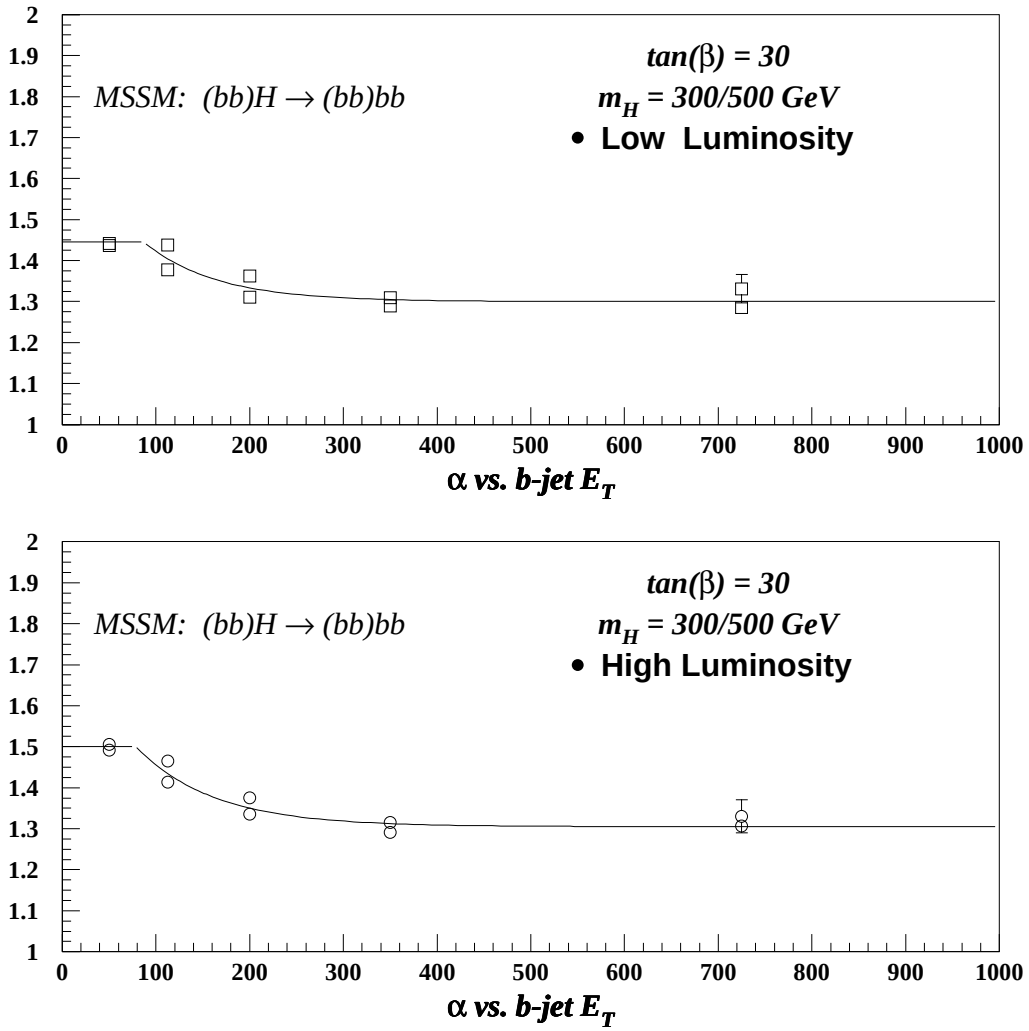

Figure 7.1: *The b-jet recalibration factor as a function of its* E_T *for* $tan\,\beta = 30$ *with a heavy Higgs mass of 300/500 GeV. The factors are obtained by correcting the mass distribution of the two b-jets, produced in the* $H \to bb$ *decay, to the nominal Higgs mass. For details of the procedure see text.*

The performance of the calibration is illustrated in Figure 7.2, which shows the Higgs mass distribution constructed with (to the right) and without (to the left) the application of the b-jet calibration factors. As seen the position of the bb mass distributions, after recalibration, are shifted to their correct mass. The price to pay is a degradation of about 30% in the width of the distributions.

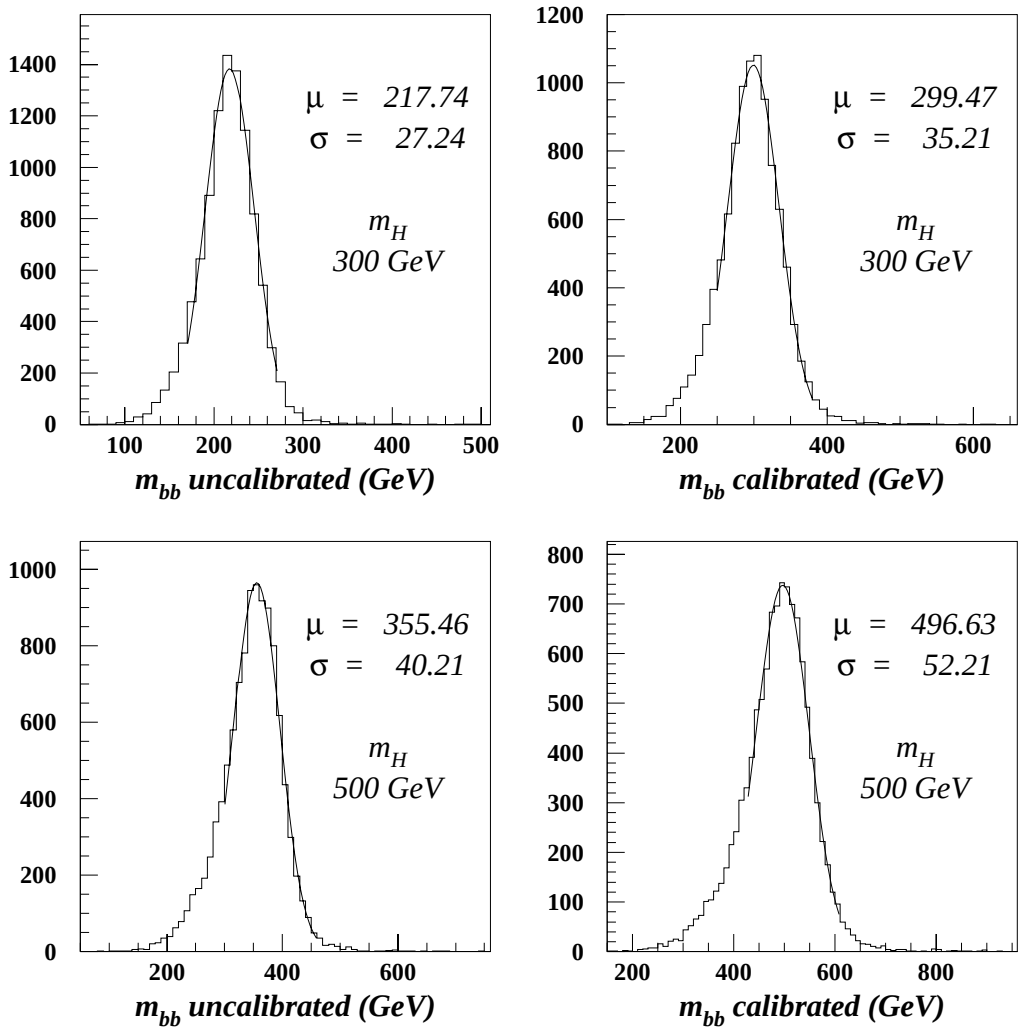

Figure 7.2: *The uncalibrated (to the left) and calibrated (to the right) bb mass distribution in the $H \rightarrow bb$ decay process for an H Higgs mass of 300/500 GeV as indicated on the plots. The calibrated m_{bb} is obtained by recalibrating the corresponding b-jets according to the calibration factors shown in figure 7.1.*

7.3 The QCD multi-jet background sample

The special multi-jet final state signals studied in this chapter both suffer from the overwhelming QCD multi-jet background. This is the dominant background relevant for these channels, being a mixture of both reducible and irreducible background. The largest contribution to the QCD multi-jet sample is from the $gg \rightarrow b\bar{b}$ process followed by the $gb \rightarrow gb$ and the $gg \rightarrow gg$ processes with gluon radiation together with gluon splitting into $b\bar{b}$. The necessary low p_T cut-off, to regulate the diverging tree-level matrix element calculation, is set such that the total inelastic, non-diffractive, pp cross-section of $\sim 70\ mb$ is obtained. In order to cover a wide range of jet transverse energies, the QCD background samples are divided in four intervals, also referred to as bins, as follows[‡]:

- $4.3\ \text{GeV} < p_T < 20\ \text{GeV} \Rightarrow \sigma \sim 68\, mb$,
- $20\ \text{GeV} < p_T < 50\ \text{GeV} \Rightarrow \sigma \sim 0.6\, mb$,
- $50\ \text{GeV} < p_T < 100\ \text{GeV} \Rightarrow \sigma \sim 21\, \mu b$,
- $p_T > 100\ \text{GeV} \Rightarrow \sigma \sim 1.44\, \mu b$,

where p_T refers to the transverse energy of the partons. Each interval enters into calculations weighted according to it's cross-section. The E_T distribution of the four leading jets in each QCD sub-sample is shown in Figures 7.3 and 7.4 at low and high luminosities respectively.

The expected LVL1 jet trigger rates based on the thresholds determined in the previous chapter are shown in Figure 7.5. It is seen that the rate at the low luminosity case is almost double as much as in the high luminosity case. The reason for this behaviour is the high thresholds applied at high luminosity.

[‡]The samples are generated based on the CTEQ2L parameterization of the parton distribution functions.

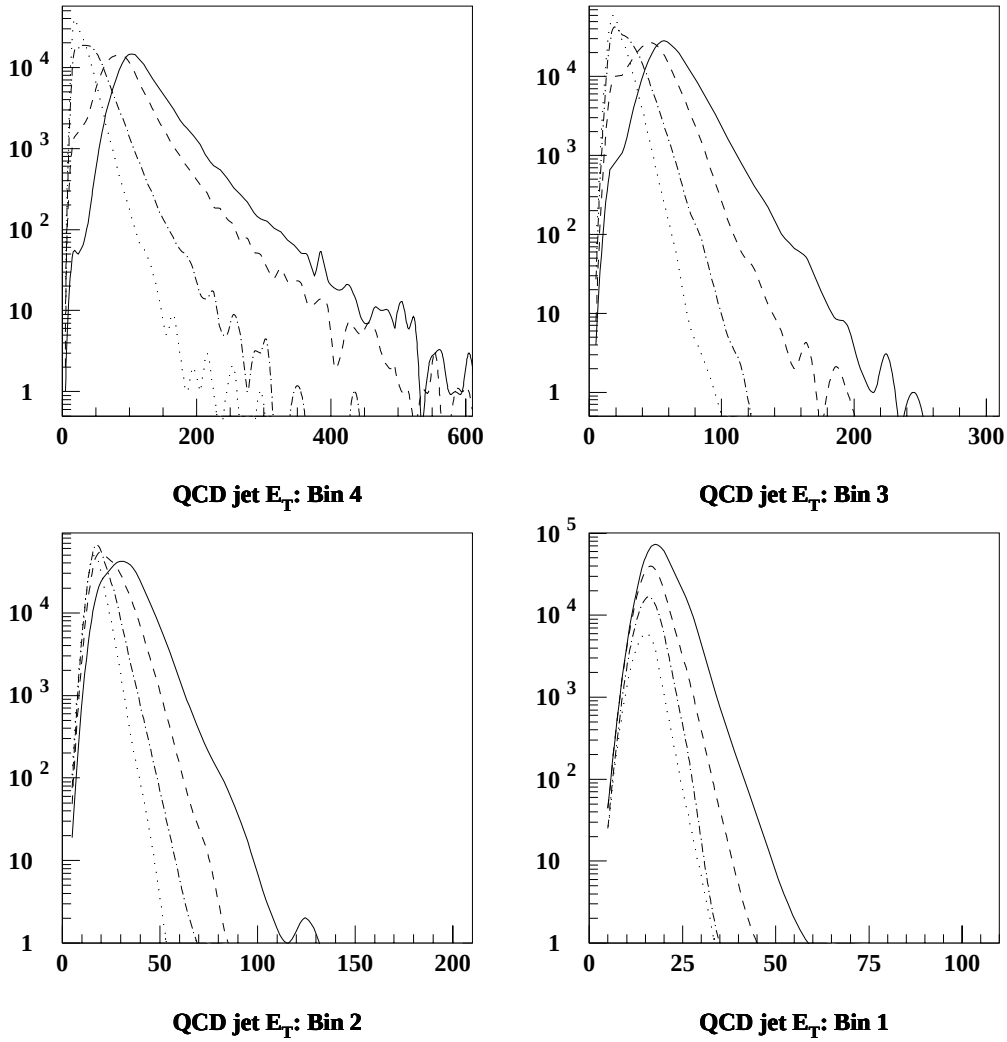

Figure 7.3: *The* E_T *distribution of the four leading jets in each QCD sub-sample (corresponding to the* E_T *intervals explained in the text) in the QCD multi-jet sample at low luminosity. The jet transverse energies plotted here are all b-jet recalibrated quantities. For more discussion on this see sections 7.5.3 and 7.6.3.*

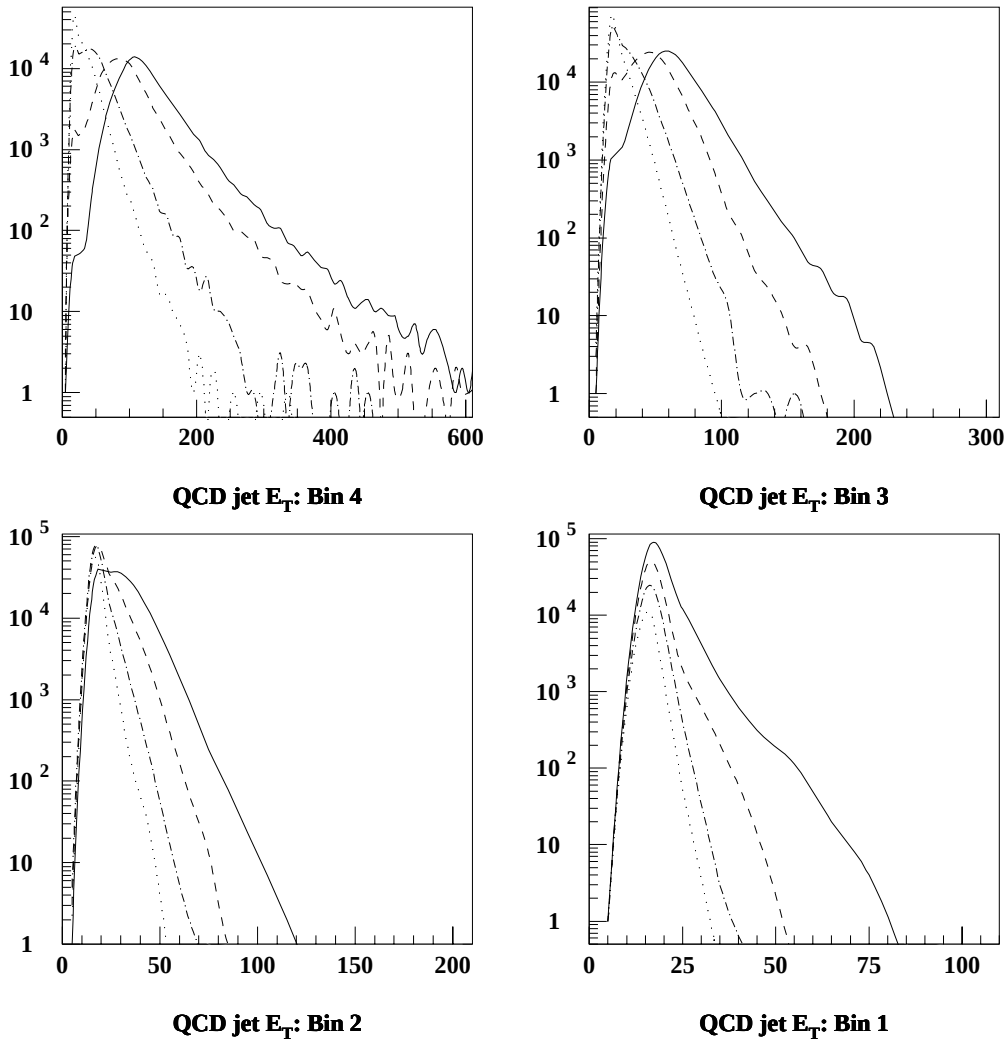

Figure 7.4: *The same as Figure 7.3, but at high luminosity.*

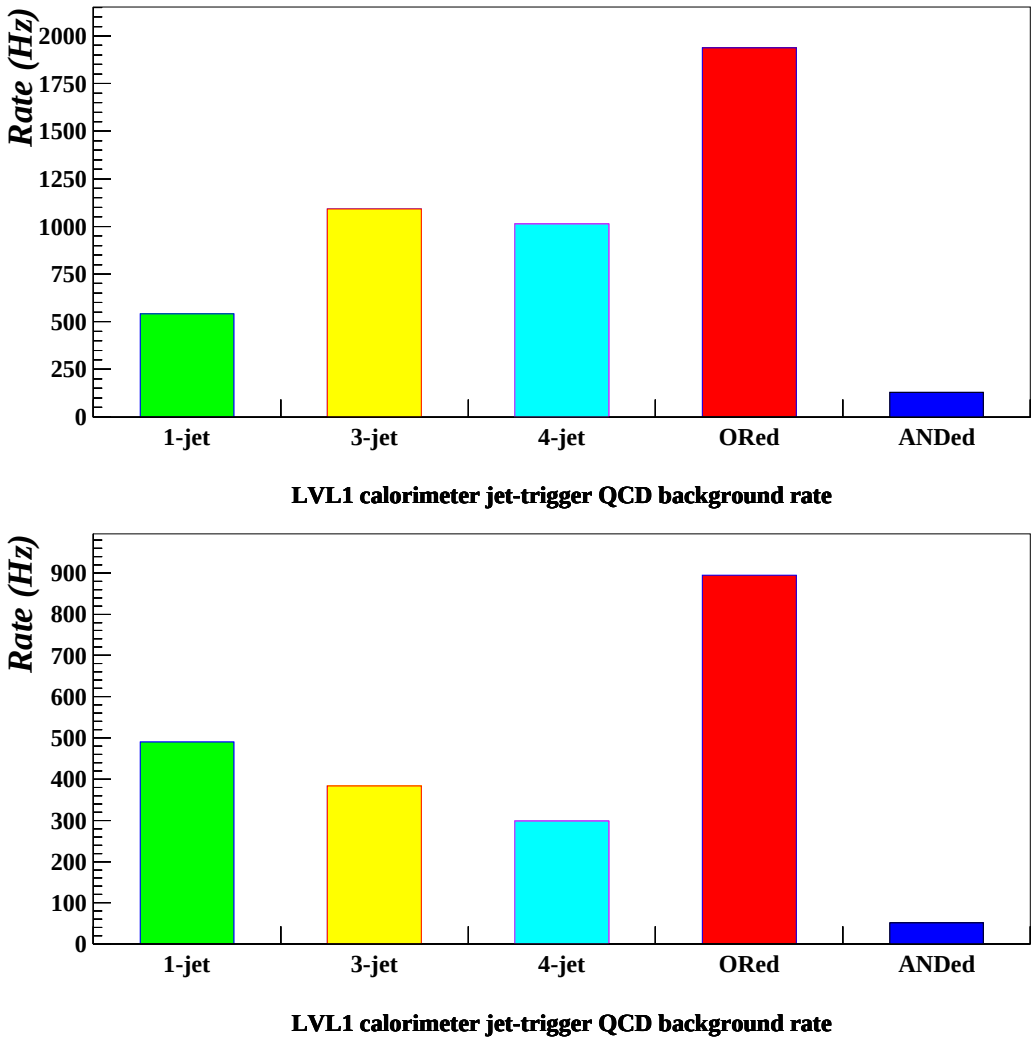

Figure 7.5: *LVL1 calorimeter jet trigger rates at low (top) and high (bottom) luminosities as obtained using the jet trigger thresholds determined in the previous chapter. Column four gives the overall LVL1 jet trigger rate. The last column serves only to illustrate the overlap between different jet triggers (inclusive, 3- and 4-jet triggers).*

7.4 Offline analysis, general aspects

Features of the offline analysis that is common to both of the signal samples studied here are discussed in this section, while details on the selection criteria depending on the kinematics and/or topology of the specific signals is discussed later in their appropriate sections. The corresponding offline analysis of the QCD background is, in one important aspect, handled in a different manner than the signal samples, which will also be explained here.

The extraction of these multi b-jet final state signals, with respect to the offline analysis, and at the same time the rejection of the huge QCD multi-jet background, relies to a large extent on an *efficient* b-tagging feature of the ATLAS LVL2 trigger system. In principle the b-tag efficiency is correlated to the rejection against other jet types, R_j , $j = u$, d, s, c, g, the higher the b-tag efficiency the lower the jet rejection. This behaviour is illustrated in Figure 7.6. The commonly used average efficiencies for b-tagging is about 60% for low and about 50% for high luminosity. This gives an average rejection of u-type jets of about 100 (200), and of g-jets of about 50 (100) and of c-type jets of about 7 (10) at low (high) luminosity. See [39].

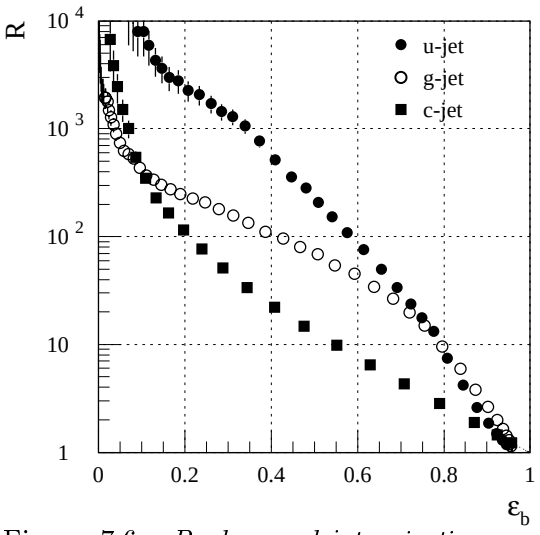

Figure 7.6: *Background-jet rejections as a function of b-tag efficiency. Taken from [39].*

In general the jet rejection factors are both η and p_T dependent, degrading with increasing $|\eta|$ and decreasing p_T , being most significant at low p_T ($< 30\ GeV$). This is shown in Figure 7.7. In addition a b-mistag probability for c-jets of about 10% and for light jets of about 1% both at low and high luminosities are also applied.

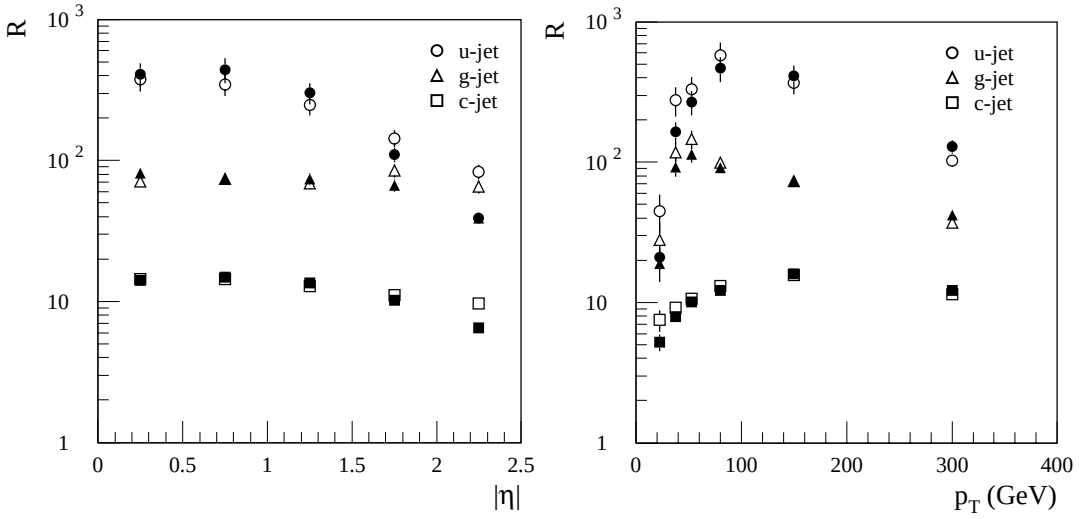

Figure 7.7: *Background jet rejections as a function of* $|\eta|$ *(left) and* p_T *(right) for* $\varepsilon_b = 50\%$. *Full and open symbols refer to different algorithms. See [39].*

To analyze the signal, all jets in the samples undergo a randomized b-tagging procedure. The tagging is performed by flagging each jet as a b-jet, in the following referred to as a b-tagged jet, or as a non-b-jet. This is performed by using the information on the *id* of each jet stored in the jet bank of the event. Hence a b-jet, based on the b-tag efficiencies just discussed, is tagged as a b-jet in 60% (50%) of the cases at low (high) luminosity. On the other hand a c-jet, based on the b-mistag probability, is tagged as a b-jet in about 10% of the cases. A light quark or a gluon jet is in 1% of the cases tagged as a b-jet. The appropriate selection criteria, like kinematical cuts, are then applied on these b-tagged jets.

The situation is radically different for the QCD background sample, being dominated by light quark or gluon jets. Considering the multi b-jet final states for the signals and the smallness of the b-mistag probabilities, a background sample with a huge number of events will be required to be able to obtain enough statistics after the application of the signal extraction criteria. For this reason the background samples are handled in the following way. All jets are assumed to be b-tagged and participate in the offline analysis procedure at equal footing. A given jet carries, so to speak, a weight factor equal to its probability to be identified (or more correctly to be tagged) as a b-jet. These weight factors are nothing but the above described b-tag/mistag (depending on the jet type) probabilities. A jet combination passing all the event selection cuts contributes with a weight obtained as the product of the weight factors of the contributing jets. If several jet combinations pass a selection algorithm, the event weight is obtained by summing the corresponding weights obtained for each of these combinations. In principle the concept of weighted events is equally well applicable in the case of the signal samples and should reproduce the results obtained by the randomized b-tagging procedure (probably $\pm$ a few %).

However, before being able to perform offline analysis, all b-jets must be re-calibrated to their correct E_T . The b-jet re-calibrations, discussed in the previous section, are applied to all b-tagged jets in the event. For the QCD background sample, all jets are re-calibrated.

7.5 $H \rightarrow h\,h \rightarrow b\bar{b}\,b\bar{b}$

To be specific two representative points in the conventional (m_A , $tan\,\beta$) plane have been considered in order to study this channel. The MSSM parameter set are selected such that all the supersymmetric particles are too heavy (fixed at $\sim$ 1 TeV) to be allowed as decay products of either of the Higgs bosons. Hence all SUSY decay modes of both the heavy and light neutral CP-even Higgs bosons, H and h respectively, are kinematically closed (or forbidden). The mass of the neutral CP-odd Higgs boson, A, is taken to be $m_A \sim 300$ GeV. Two values of the ratio of the vacuum expectation values of the neutral components of the two Higgs isodoublets, namely $tan\,\beta = 1.5$ and $tan\,\beta = 3.0$, are considered. The former gives the light neutral CP-even Higgs, h, the mass $m_h \sim 80$ GeV, whereas the latter results in a slightly heavier h boson with $m_h \sim 100$ GeV. The masses of the heavier neutral CP-even Higgs, H, and the neutral CP-odd Higgs, A, are degenerate for this choice of m_A, irrespective of $tan\,\beta$. With this specific parameter set in the (m_A , $tan\,\beta$) plane, with $2\,m_h < m_H < 2\,m_t$, the $H \rightarrow V\,V$ decay (, with V representing a vector boson,) is strongly suppressed with respect to that of the SM case (except for $tan\,\beta < 1$). On the other hand, the $H \rightarrow h\,h$ decay mode is open, whilst the $t\,\bar{t}$ final state is kinematically not available. In addition the top and bottom trilinear couplings, A_t and A_b respectively, and the Higgs mass parameter, μ, are set to zero[§]. The variation of m_H and m_h as a function of m_A for the two $tan\,\beta$ values considered here are illustrated in Figure 7.8. These masses are obtained using the HDECAY package [58] and include the most significant two-loop radiative corrections. As seen on this plot the H and A boson masses are (to a good approximation) degenerate in the range $m_A > 250\ GeV$. The mass of the h boson saturates at its, in general $tan\,\beta$ dependent[¶], maximum for $m_A > 200\ GeV$.

The production cross-section of the neutral CP-even Higgs, H, via the gluon fusion through triangular top-quark loop, as calculated in HIGLU program [59, 60], is shown in Figure 7.9 as a function of m_A, for the two $tan\,\beta$ values considered here. This is, as in the case of the SM Higgs, the most important production mechanism at LHC. Other production mechanisms, as shown in Figure 2.11 on page 35, due to vertex correction factors in Table 1.3 on page 12, are strongly suppressed and contribute with negligible amounts. The production cross-sections in Figure 7.9 are calculated to Leading and Next-to-Leading Order (LO/NLO) in the strong coupling (constant) α_s. The corresponding K-factors, i.e. the ratio of the NLO to the LO cross-sections, are also superimposed on the plots. It is seen that the higher order diagrams have a large effects on the production cross-sections, e.g. ~ 1.6 at $m_A \sim 300\ GeV$. Nevertheless, in the analysis presented here only the Leading order cross-sections are taken into account, since the corresponding K-factors for the QCD background processes are not completely calculated and/or not known.

[§] This corresponds to the minimal (squark) mixing scenario, which, for a given set of (other) parameters, results in a lightest possible light neutral CP-even Higgs boson h.

[¶] Of course the maximum accessible mass of the h boson does not increase without limit with increasing $tan\,\beta$, but in turn saturates itself to a value depending on the specific model under consideration. The absolute maximum, as discussed in chapter 1, is about 130 GeV, which is obtained in the case of maximum mixing.

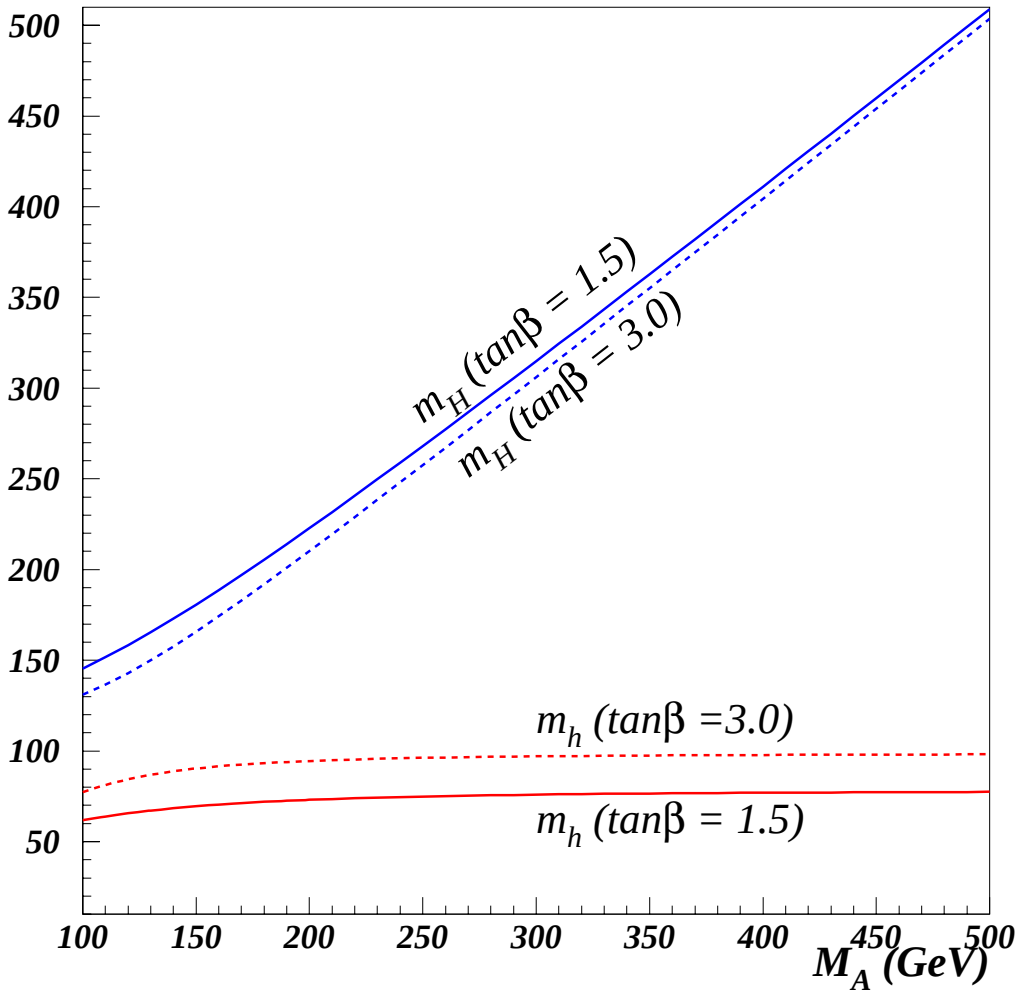

Figure 7.8: *MSSM neutral Higgs sector mass correlations as obtained from HDECAY [58], for two different tan β values discussed in the text.*

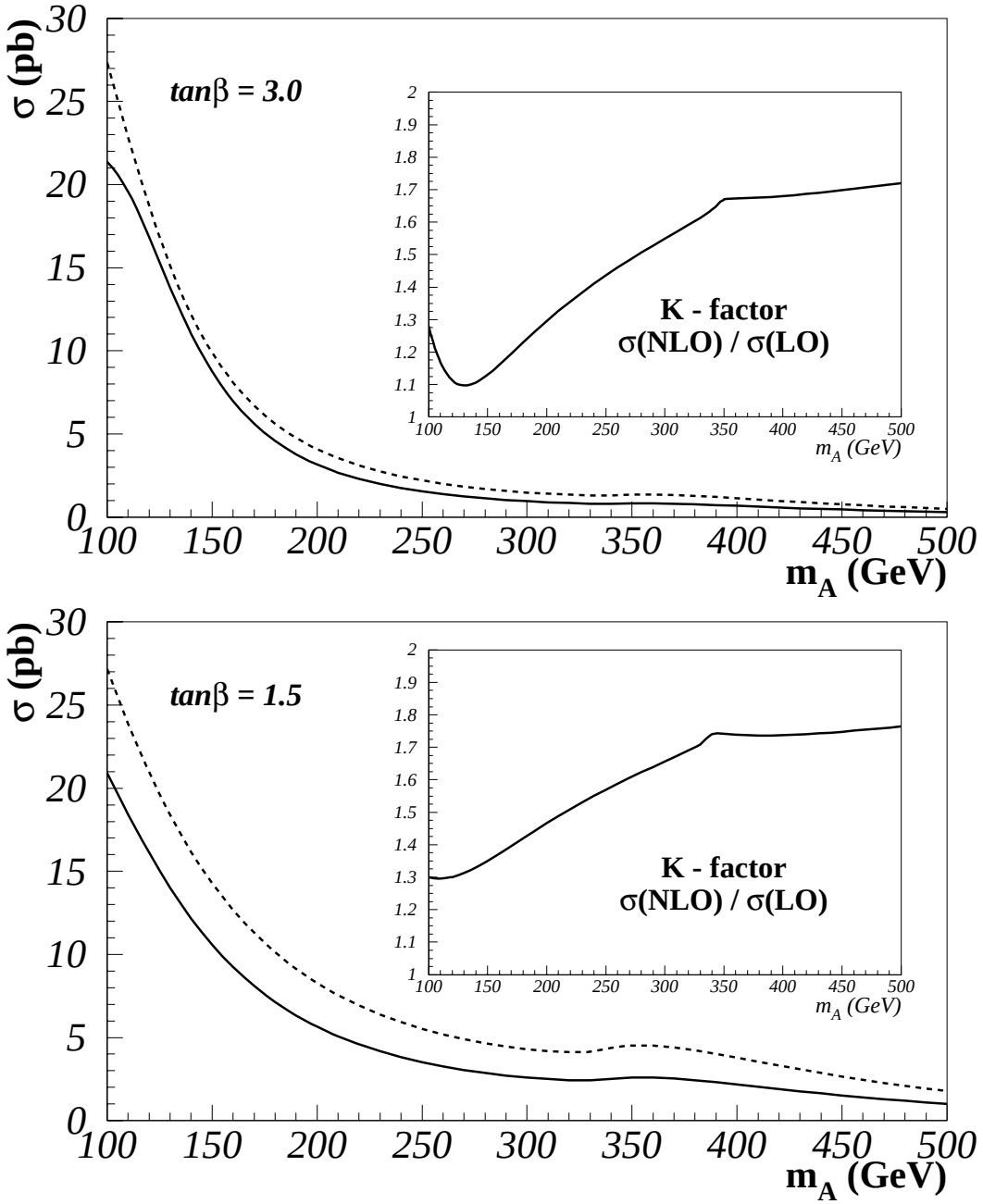

Figure 7.9: *The $gg \to H$ production cross-sections of the neutral CP-even heavy Higgs, H, at one- (full curve) and two-loop (dashed curve) for $\tan\beta$ values discussed in the text. The corresponding K-factor, defined as the ratio of the two- to one-loop cross-section, is also superimposed in each case. The Monte-Carlo program HIGLU [59, 60] have been used to obtain these plots.*

In Figure 7.10 the $H \to hh$ and $h \to bb$ branching ratios, as obtained from HDECAY Monte-Carlo program, for $tan\,\beta$ values considered here, are shown on plots: (a) and (b). It is seen that the $h \to bb$ branching ratio is almost constant over the entire range of m_A and do not vary much with $tan\,\beta$. On the other hand, the $H \to hh$ branching ratio shows large variations with both m_A and $tan\,\beta$. This behaviour is understood by considering (c) and (d) plots in the same figure. The difference in the shape of the $H \to hh$ branching ratio for $m_A < 160\ GeV$ for the two $tan\,\beta$ cases is due to the fact that for small $tan\,\beta$ the light neutral CP-even Higgs boson, h, is very light so that kinematically the heavier neutral CP-even Higgs boson, H, can decay into hh final states with the $H \to bb$ and $H \to WW$ branching ratios suppressed. Whereas for the larger $tan\,\beta$ this is not the case, and the h boson is heavy enough so that the $H \to hh$ decay channel is kinematically closed for $m_A < 170\ GeV$, and $H\,bb$ and $H \to WW$ branching ratios are important.

As seen in Figure 7.10, for $m_A \sim 300\ GeV$, the $H \to hh$ branching ratio is roughly 65%, and the $h \to bb$ branching ratio is of the order of 90%. This means that the overall branching ratio for this channel is about 50%. The $gg \to H$ production cross-sections (at one-loop level) together with the $H \to hh$ and $h \to b\bar{b}$ branching ratios, as obtained form HIGLU and HDECAY Monte-Carlo's, for the case under study here are compiled in Table 7.1.

Table 7.1: *The $gg \to H$ production cross-sections and the $H \to hh$ and $h \to b\bar{b}$ branching ratios for the parameter sets in the (m_A, $tan\,\beta$) space studied here.*

$\boldsymbol{m_H = 300\ GeV}$	$\boldsymbol{tan\,\beta = 1.5}$	$\boldsymbol{tan\,\beta = 3.0}$
$\boldsymbol{m_h}$	76 GeV	97 GeV
$\boldsymbol{\sigma_{LO}(gg \to H)}$	2.71 *pb*	0.95 *pb*
$\mathbf{BR}(\boldsymbol{H \to hh})$	69%	60%
$\mathbf{BR}(\boldsymbol{h \to b\bar{b}})$	86%	84%
$\boldsymbol{\sigma \times \mathbf{BR}}$	1.5 *pb*	0.5 *pb*

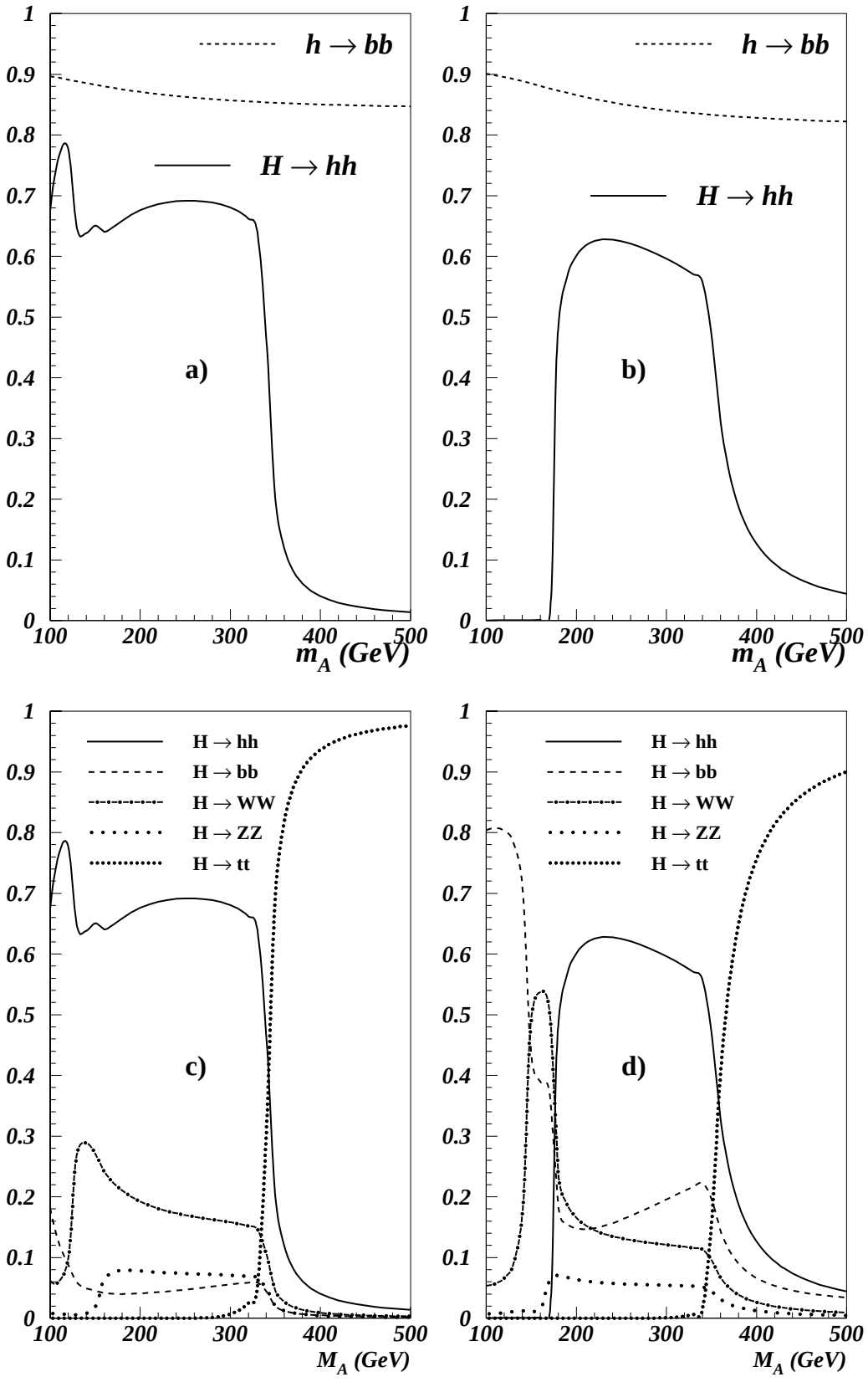

Figure 7.10: *Branching ratio plots, as obtained from HDECAY, for the light and heavy neutral CP-even Higgs bosons, H and h respectively, for $\tan\beta$ values discussed in the text. In the figure, a) and c) are for $\tan\beta = 1.5$, whereas b) and d) are for $\tan\beta = 3.0$.*

The E_T distribution of the recalibrated b-jets and the coinciding final state b-parton jets, produced in the decay of the h bosons are illustrated in Figure 7.11. It is seen that the b-jet recalibration procedure has, to a good approximation, reproduced the corresponding partonic distributions. To be observed is that the mean E_T , of the b-parton jets, ranges from about 100 GeV to about 40 GeV. Needless to say, the E_T distributions of the partonic b-jet are independent of the luminosity, hence a similar result is also obtained in the high luminosity case. These observations justify the kinematical cuts applied on the recalibrated E_T of the b-tagged jets in, so to speak, the preselection phase of signal extraction algorithm to be discussed in a later section.

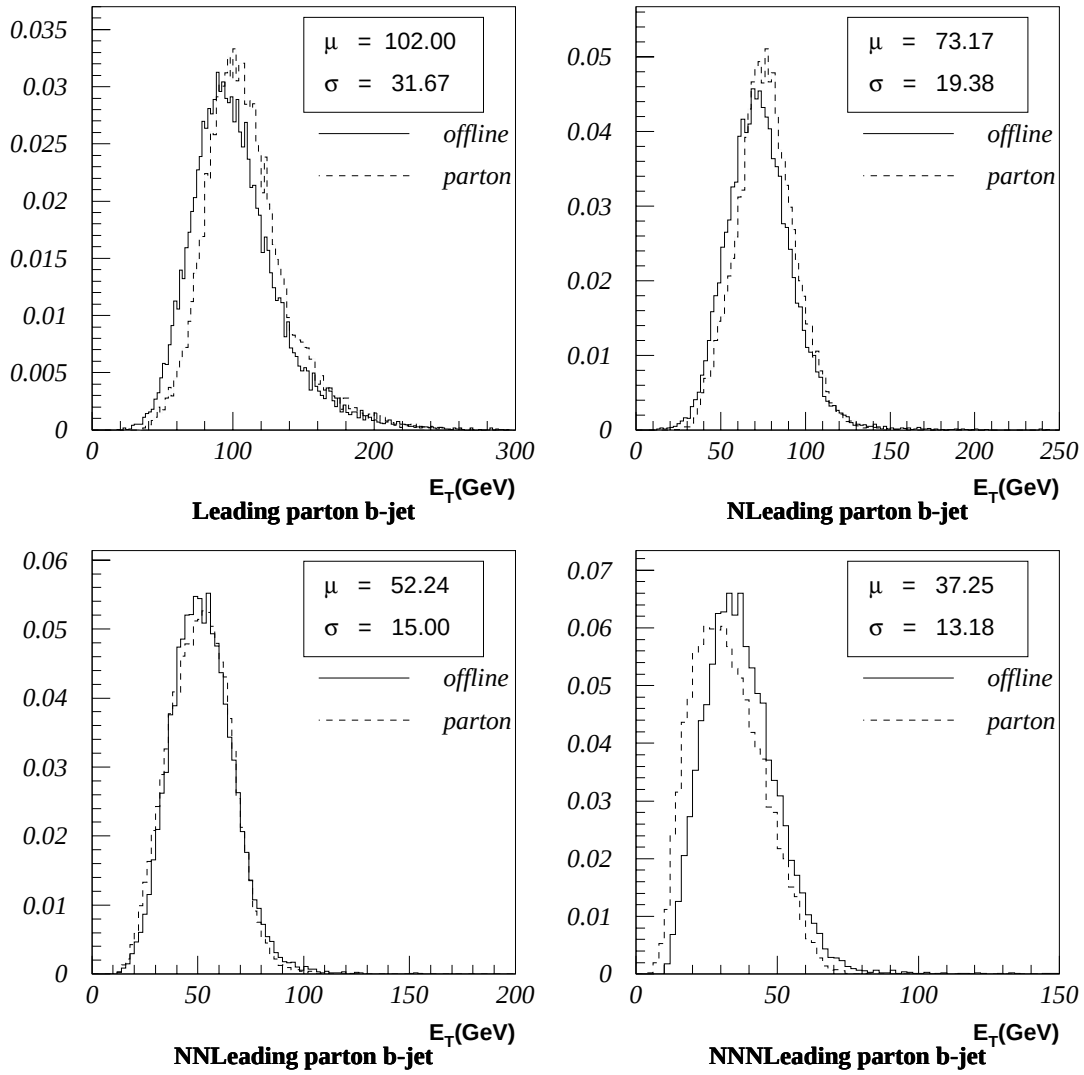

Figure 7.11: *The* E_T *distribution of the parton b-jets and the corresponding recalibrated offline b-labeled jets, produced in the* $hh \to b\bar{b}\,b\bar{b}$ *decay, ordered in* E_T *. The distributions correspond to the* $\tan\beta = 1.5$ *case (at low luminosity). In the labeling on the plots "N" stands for "Next-to".*

The reconstructed jets in an event are ordered according to their E_T . The position of a given jet in this ordered list is referred to as the jet *index* in the following. Hence, the leading jet in the event have the index 1, and so on. In addition, true b-jets in the event are referred to as b-labeled jets. A set of interesting plots is the distribution of the index of the b-labeled and the b-tagged jets initiated by the parton b-jets produced in the decay of the h decays. Various distributions are illustrated in Figure 7.12 for the low luminosity case. Figure 7.12 illustrates, for the low luminosity case, various distributions of the index of the b-labeled and the b-tagged jets initiated by the parton b-jets produced in the decay of the h decays. The **a)** and **b)** histograms show the distribution of the index and the index-sum, respectively, of the b-tagged jets for the accepted events. The histograms in **c)** show the distributions of the number of b-labeled jets before and after b-tagging procedure. It is seen that only about 5% of events have four b-tagged jets. whereas before the b-tagging more than 25% of the events have four true b-jets, corresponding to a reduction of roughly $(\varepsilon_{b-tag})^4 \sim (0.60)^4 \sim 0.13$. From **a)** and **b)** histograms it could be seen that although in about 30% of the accepted events the four b-tagged jets are the leading jets in the event, the probability of having the four b-tagged jets among the six leading jets is not negligible, and should only be neglected if background rejection issues are of importance. These observations do also justify the selection criteria to be mentioned in the signal extraction section later.

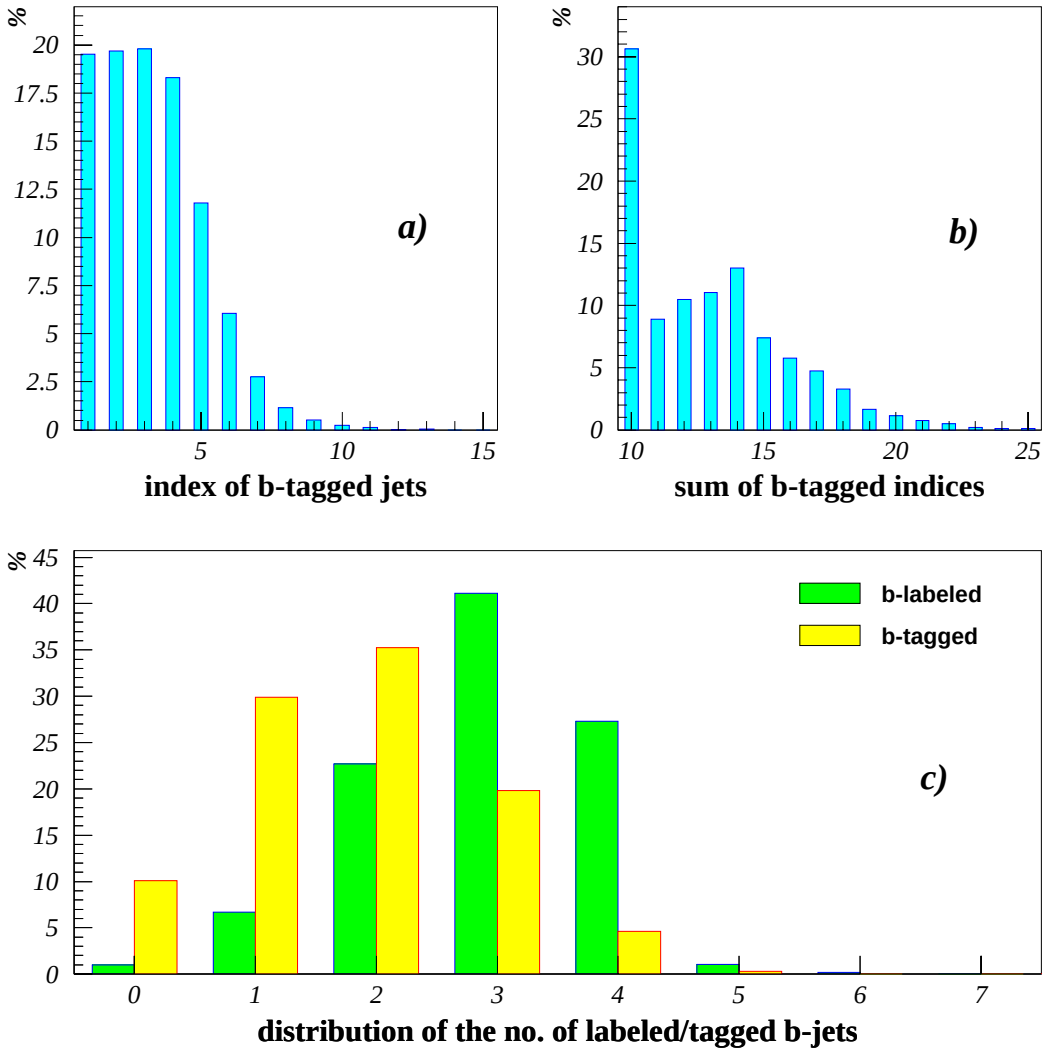

Figure 7.12: *The distribution of index of labeled/tagged b-jets, produced in the $h \to b\bar{b}$ decays. The distributions correspond to the $\tan\beta = 1.5$ case. In* **a)** *the occupation percentage of the four b-tagged jet indices is plotted for accepted events (i.e. each accepted event has 4 entries in this histogram). In* **b)** *the sum of the indices of the entries in* **a)** *are plotted (i.e. 1 entry per accepted event). In* **c)** *the percentage of the b-labeled/tagged jets in the b-tag η acceptance region are plotted.*

7.5.1 The LVL1 signal acceptance

The LVL1 calorimeter jet trigger acceptance is obtained by applying the LVL1 jet triggers on the signal samples. An example of the obtained results is shown in Figure 7.13. The acceptance does not depend on $tan\,\beta$, and therefore only the results for the $tan\,\beta = 1.5$ point for both low and high luminosities are shown. The LVL1 calorimeter jet trigger acceptance is a combination of all jet trigger acceptances, which is the fourth bin in the histograms plotted in the figure. The overall acceptance at low luminosity, as seen in the figure, is about 68%. At high luminosity the acceptance is as low as about 9%. The first three bins indicate the acceptance for each jet trigger acting alone. And finally the last bin shows the overlap between the jet triggers in the LVL1 menu. As seen on this figure the acceptance at high luminosity is quite low and essentially, with this set of trigger thresholds, the signal could not be selected efficiently. Lowering the trigger thresholds will help to increase the efficiency, but at the same time the jet trigger rate will increase. For a discussion see section 7.7.

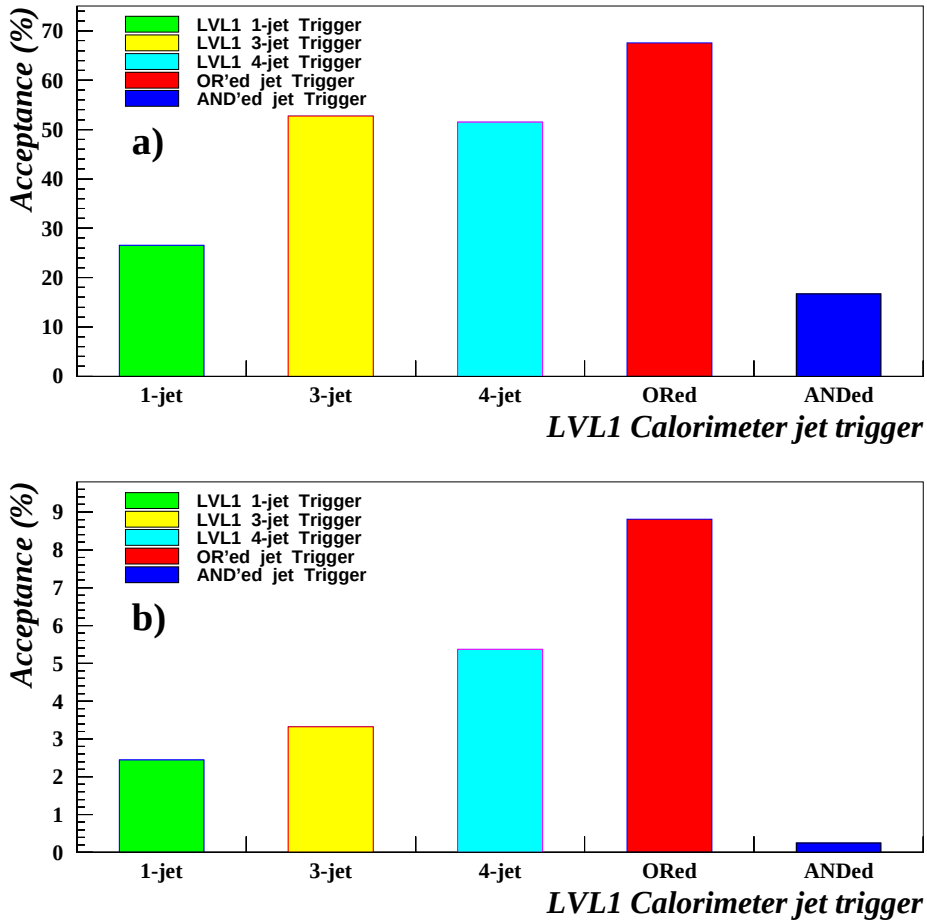

Figure 7.13: *Signal acceptance of the LVL1 calorimeter jet trigger (menu) at* **a)** *low and at* **b)** *high luminosities. The first three columns on each plot give the acceptance for each jet trigger type. The "ORed" column is actually the real LVL1 acceptance. The "ANDed" column represents a measure of the overlap between the jet trigger types.*

7.5.2 Signal extraction

The $H \rightarrow h\,h \rightarrow b\bar{b}\,b\bar{b}$ signal is extracted by selecting events according to the following requirements:

- There have to be at least four b-tagged jets within the region $|\eta| < 2.5$ each with $p_T > 15$ GeV ($p_T > 40$ GeV) at low (high) luminosity. These p_T cuts are applied on the re-calibrated b-tagged jets as explained above. (In fact several p_T cuts have been studied which will be explained below.) The invariant mass for all possible $b\,b$ combinations are constructed for events passing this cut.

- There have to be at least two exclusive $b\,b$ combinations with an invariant mass, m_{bb}, within a mass window of ± 20 GeV about m_h. (Here exclusive means that the four b-tagged jets should be different.) The $4b$ invariant mass, i.e. m_{4b}, is reconstructed for all of these complementary $b\,b$ combinations within the m_h mass window.

- At least one m_{4b} need to be within a window of ± 26 GeV about m_H. The four-momenta of the b-tagged jets within this window is rescaled[‖] according to $m_{bb} = m_h$, in order to get an improved m_{4b} invariant mass reconstruction, i.e. a better mass resolution.

The quoted mass windows in the above selection criteria cover a range of about 1.5–2 $\cdot\sigma$ about the nominal masses of the Higgs bosons, with σ being the mass resolution in each case. Several variations of the above selection criteria, all affecting the acceptance after the first step of event selection algorithm above, have been investigated. Four different p_T cuts on the b-tagged jets, i.e. 15 GeV, 20 GeV, 30 GeV and 40 GeV, both at low and high luminosities have been applied. In addition, in each case, the selection is supplemented with the extra requirements that the b-tagged jets entering the event selection procedure are within the four, five or six leading E_T jets in the event. An additional analysis with no restriction on the position of the b-tagged jets has also been performed.

In Figure 7.14 an example of such an event selection procedure for $tan\,\beta = 1.5$ at low luminosity is illustrated for $p_T^{b-jet} > 15\ GeV$. The dark-gray hatched histogram in these plots refer to the distributions obtained without the application of the LVL1 calorimeter jet trigger, and the superimposed light-gray hatched histograms, in each case, illustrate the same but after the application of the LVL1 trigger. Plot **a)** shows the distribution of the reconstructed invariant $2b$ mass for all bb combinations in the events. The vertical full lines indicate the window about m_h. Plot **b)** shows the invariant $4b$ mass distribution for all exclusive bb combinations falling within the h mass window. This is the second step in the event selection explained above. The vertical lines indicate the mass window about m_H. An event is selected if it has at least one entry in this mass window. For the signal events in almost all the cases only one $4b$ combination per event is reconstructed within this window. But this may not necessarily be the case for the QCD background sample. Therefore in order to reduce the background contribution (or rate) to the selected events, and extra condition may be supplemented to the above criterion. By considering only the $4b$ combination inside the m_H mass window, which minimizes the value of the expression $\sqrt{(m_1(bb) - m_h)^2 + (m_2(bb) - m_h)^2}$, where indices 1

[‖] The application of the rescaling of the four-momenta of the b-tagged jets to their parent h boson, serves only to obtain a better resolution on the reconstructed m_{4b} and does not affect the overall offline acceptance for this channel.

and 2 label the two reconstructed $2b$ masses within the m_h mass window, one could reduce the contribution from the QCD background. The E_T of all four b-tagged jets contributing with their invariant $4b$ mass to this window are then rescaled to the nominal mass of their parent h boson, i.e. m_h. The reconstructed invariant $4b$ mass using these rescaled E_T of the b-tagged jets is shown on plot **c)**. Plot **d)** is also derived from **b)** and shows the same distribution as in **c)** but with the extra minimization just pointed out.

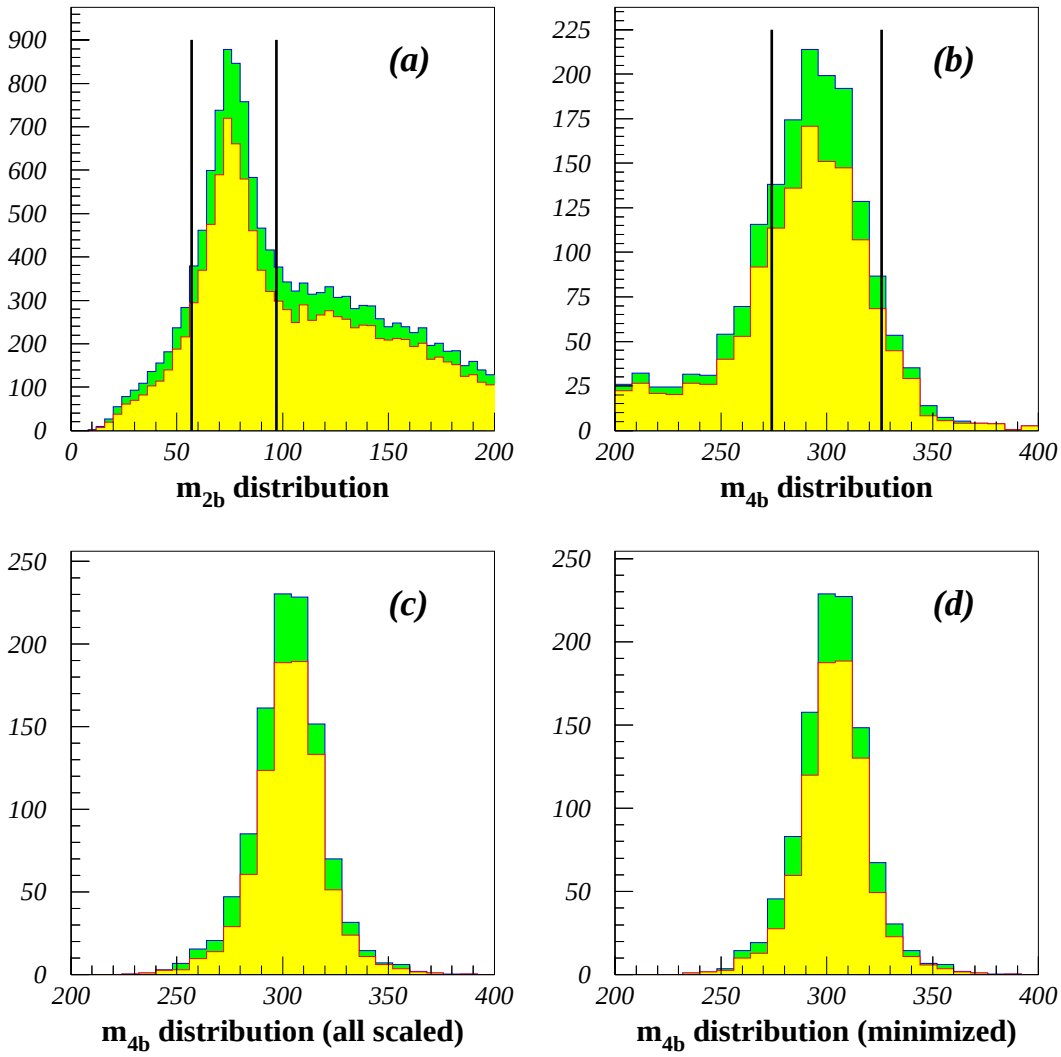

Figure 7.14: *Example of the signal extraction procedure for* $\tan\beta = 1.5$ *at low luminosity.*

The overall acceptance of the offline event selection for this channel is illustrated in Table 7.2, which also summarizes the average percentage of events surviving after each offline cut as explained above. At low luminosity an overall acceptance of about 2% of the signal is to be expected for both $tan\,\beta$ values. In case of the high luminosity the acceptance is quite small, basically due to the large transverse energy cut on the b-tagged jets. The application of level-1 trigger will of course reduce these fractions further. The effect of LVL1 calorimeter jet trigger on the offline acceptance of the signal is shown in Table 7.3. It is seen that the effect at low luminosity is acceptable, whereas at high luminosity the already small offline acceptance is dramatically reduced to a very tiny fraction of the events. As mentioned earlier reducing the jet trigger requirements (in the trigger menu) the situation will improve, with the side effect that the background jet rate will also increase. Giving that the extra jet rejection capability at LVL2 is quite limited, this choice may not be a desirable solution. But any definite conclusion requires more analysis on this part. The increased acceptance of the signal at LVL1, due to a reduction of the applied LVL1 jet trigger thresholds, is illustrated in Table 7.4 for two reduced threshold sets.

Table 7.2: *Signal acceptance after each offline selection cut at low and high luminosities for $tan\,\beta$ values under study. For more information on each cut criterion see the text.*

Low Luminosity					
$\boldsymbol{tan\,\beta}$	$\geq$ **4 jets with** $\boldsymbol{\lvert\eta\rvert < 2.5}$	$\geq$ **4 jets with** $\boldsymbol{p_T > 15\,GeV}$	$\geq$ **4 jets** $\boldsymbol{b}$**-tagged**	$\boldsymbol{m_h}$ **mass window**	$\boldsymbol{m_H}$ **mass window**
1.5	95.8%	28.5%	4.7%	4.0%	2.1%
3.0	96.5%	30.2%	5.2%	4.4%	2.0%
High Luminosity					
$\boldsymbol{tan\,\beta}$	$\geq$ **4 jets with** $\boldsymbol{\lvert\eta\rvert < 2.5}$	$\geq$ **4 jets with** $\boldsymbol{p_T > 40\,GeV}$	$\geq$ **4 jets** $\boldsymbol{b}$**-tagged**	$\boldsymbol{m_h}$ **mass window**	$\boldsymbol{m_H}$ **mass window**
1.5	95.4%	9.9%	0.7%	0.50%	0.3%
3.0	96.1%	10.1%	0.7%	0.6%	0.3%

Table 7.3: *The offline, LVL1 calorimeter jet trigger and the LVL1 plus offline acceptances at low and high luminosities for tan β values considered here. The LVL1 calorimeter jet trigger thresholds are the nominal thresholds determined in the previous chapter.*

Low Luminosity			
tan β	**offline acceptance**	**LVL1 Trig. acceptance**	**LVL1 + offline acceptance**
1.5	2.0%	67.6%	1.6%
3.0	2.0%	67.0%	1.5%

High Luminosity			
tan β	**offline acceptance**	**LVL1 Trig. acceptance**	**LVL1 + offline acceptance**
1.5	0.3%	8.8%	0.04%
3.0	0.3%	7.7%	0.03%

Table 7.4: *Same as Table 7.3 but only for the high luminosity and for two different sets of successively lower LVL1 calorimeter jet trigger thresholds to illustrate the enhanced offline+LVL1 acceptance. The (offline) jet thresholds are indicated on the title row in each table. The applied LVL1 jet trigger thresholds, as usual, correspond to 90% efficiency for the offline jets with the given* E_T .

J×1: 250 GeV J×3: 100 GeV J×4: 70 GeV			
tan β	**offline acceptance**	**LVL1 Trig. acceptance**	**LVL1 + offline acceptance**
1.5	0.3%	25.9%	0.1%
3.0	0.3%	24.4%	0.1%

J×1: 225 GeV J×3: 85 GeV J×4: 60 GeV			
tan β	**offline acceptance**	**LVL1 Trig. acceptance**	**LVL1 + offline acceptance**
1.5	0.3%	38.3%	0.2%
3.0	0.3%	36.8%	0.2%

7.5.3 Background contribution

Applying the signal extraction criteria to the background sample, by utilizing the weighted event procedure explained earlier, an estimate of the background contribution is obtained. All exclusive $4b$ combinations within each event are considered in this case and no minimization criteria is applied. The total number of events, remaining after the selection criteria, in each p_T interval of the QCD background sample is then normalized based on its cross-section and each selected event is weighted with its probability as explained above. The obtained $2b$ and $4b$ mass distributions, corresponding to those of the signal, are shown in Figure 7.15.

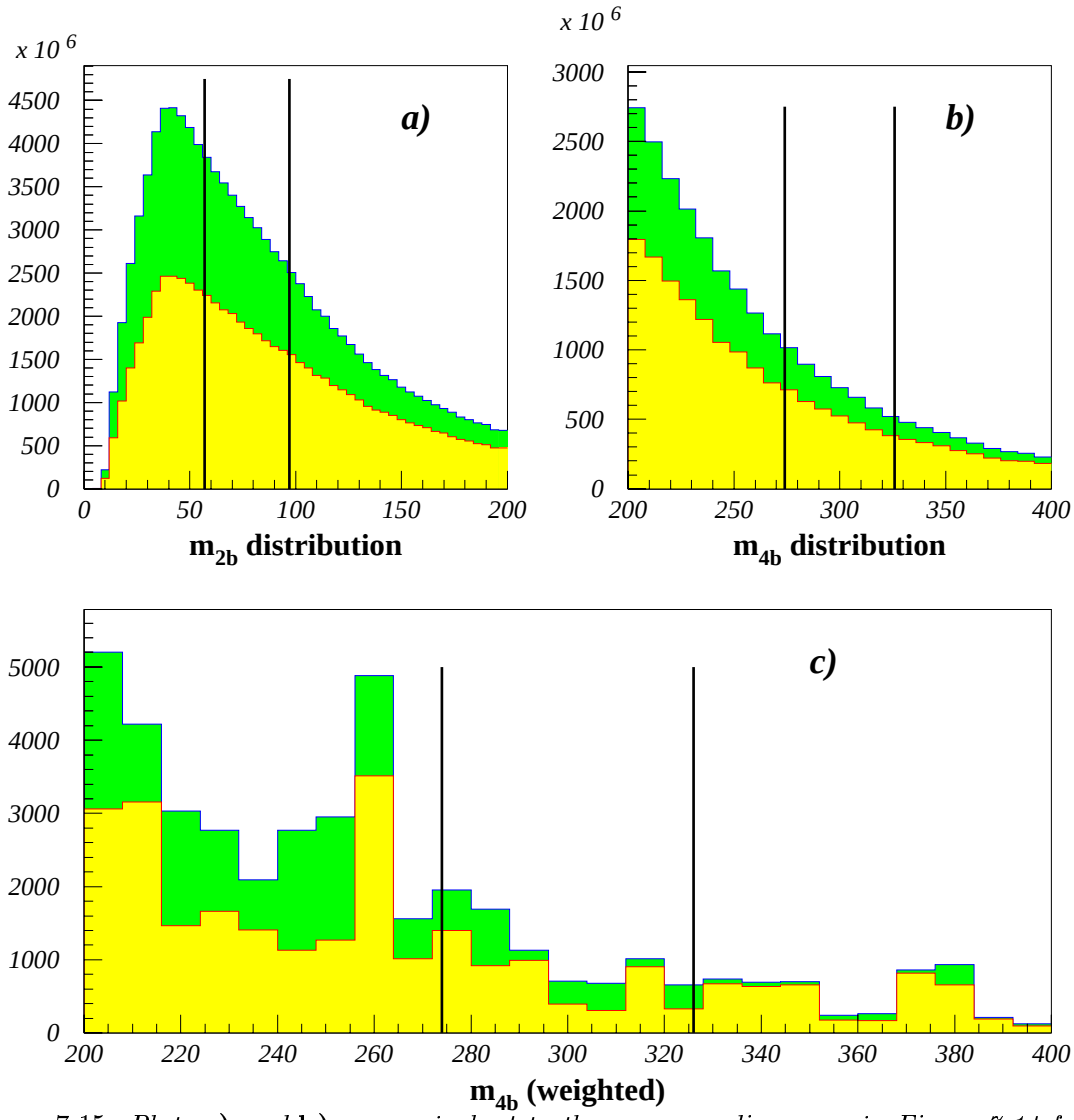

Figure 7.15: *Plots* **a)** *and* **b)** *are equivalent to the corresponding ones in Figure 7.14 for the signal. Plot* **c)** *is derived from* **b)** *by applying the concept of weighted events. The dark- and light-gray hatched histograms show the results before and after the LVL1 calorimeter jet trigger algorithm. The mass windows are indicated with parallel lines. By selecting only one of the entries in the mass window in* **c)** *the contribution of the background could be reduced.*

A visual comparison of the signal and background is illustrated in Figure 7.16. It must be noted that the minimization requirement mentioned above is not applied on any of these distributions.

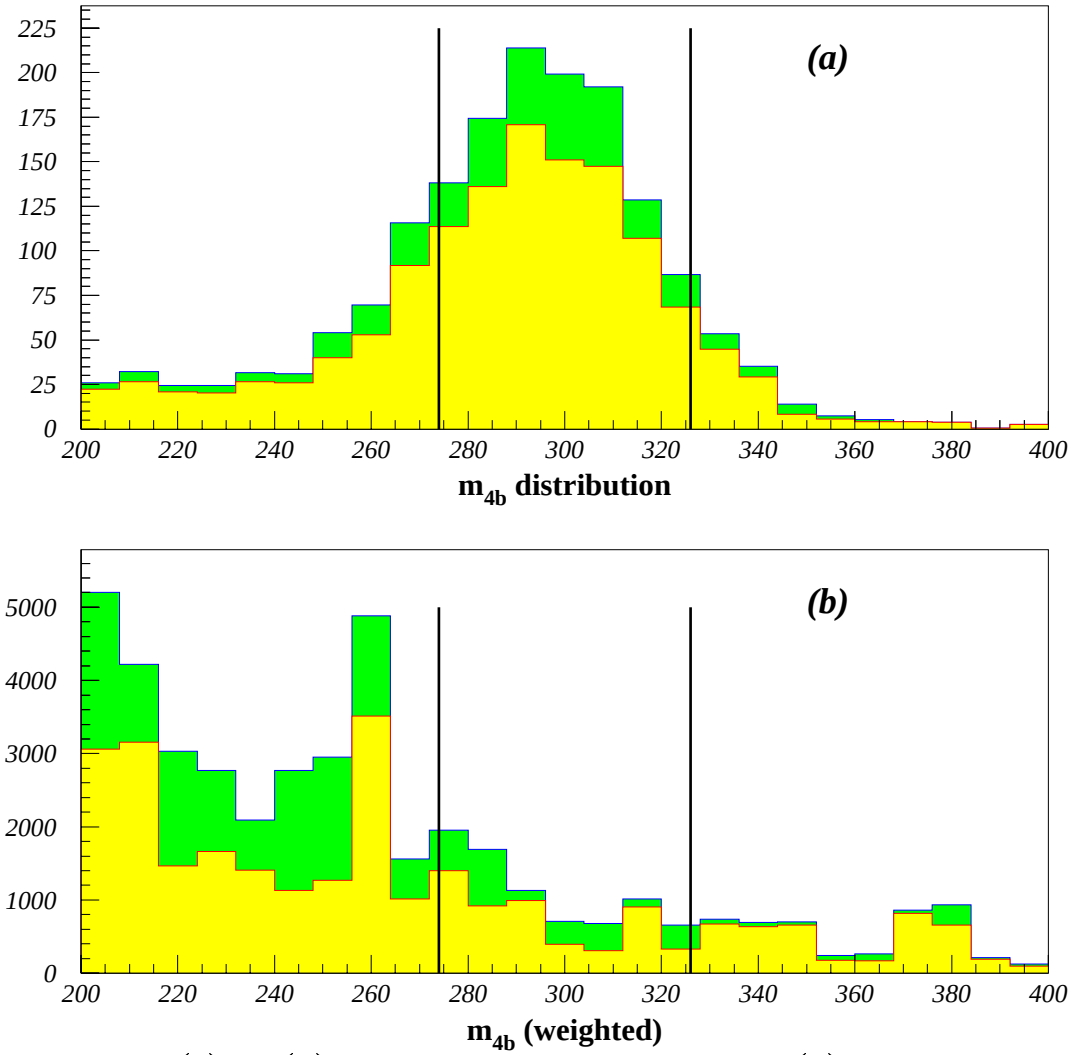

Figure 7.16: *The* **(a)** *and* **(b)** *plots in this figure correspond to plot* **(b)** *for the signal in Figure 7.14 and to plot* **c)** *for the background in 7.15 respectively. They serve only to illustrate the shape of the distributions for the two cases.*

7.5.4 Results

The signal observability in terms of signal (S) to background (B) ratio and the statistical significance of the signal, defined as the ratio of the signal to the square-root of the background, are tabulated in tables 7.5–7.8. For each luminosity four different p_T cuts, i.e. 15 GeV, 20 GeV, 30 GeV and 40 GeV, on the jets for each $tan\,\beta$ value are studied. The signal and background rates for 3 years low and high luminosity runs are also reproduced in the tables. It must be noted that the figures in these tables do not include the effect of the minimization procedure mentioned in the previous section for the background sample. But the signal sample does contain this effect. This means that the entries in the table are worst cases. Considering these statistical signal significances only, several selection criteria may be suited to extract this channel efficiently. Choosing a 15 GeV (40 GeV) jet p_T cut at low (high) luminosity and in addition requiring the 4 b-tagged jets, used to reconstruct the H mass, to be within the first 5 highest E_T jets in the event, the 5σ discovery contour plot shown in figure 7.17 is obtained.

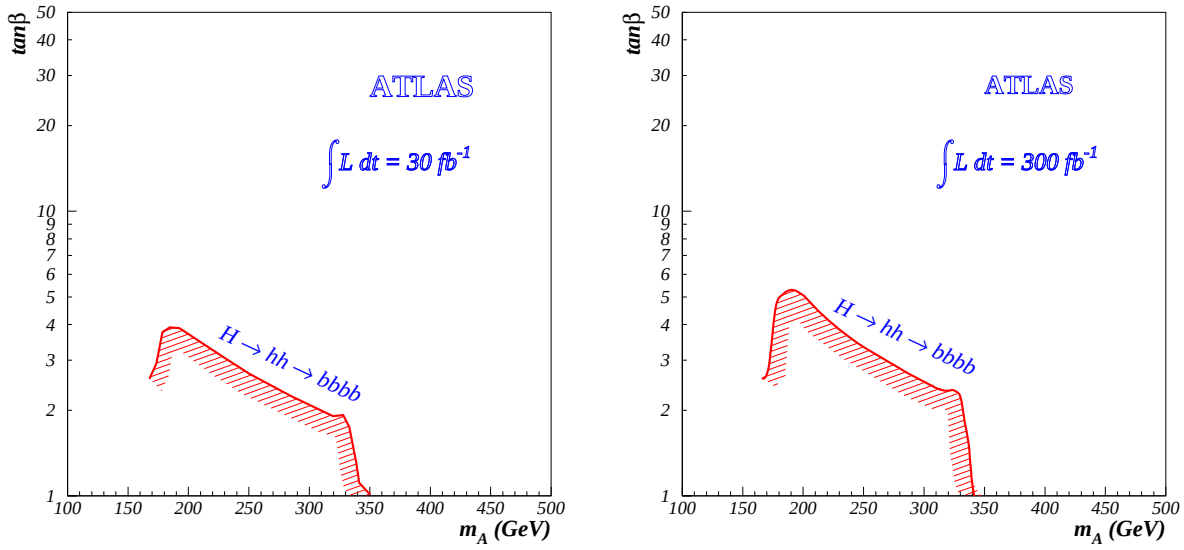

Figure 7.17: *The 5-σ discovery contours for low (left) and high (high) luminosities for the decay channel studied in this section.*

Table 7.5: Expected number of signal and background events after having accumulated 30 fb^{-1} (low) and 300 fb^{-1} (high) luminosity. The corresponding signal (S) to background (B) ratio in percentage and significance is also given. For more details see text.

4 jets: ET $>$ 15 GeV		all jets		6 leading jets		5 leading jets		4 leading jets	
$tan(\beta)$	*sample/ratio*	Low $\mathcal{L}$	High $\mathcal{L}$	Low $\mathcal{L}$	High $\mathcal{L}$	Low $\mathcal{L}$	High $\mathcal{L}$	Low $\mathcal{L}$	High $\mathcal{L}$
1.5	S	836	726	647	285	464	124	187	–
	B	29602	12330	14981	2568	4914	463	1070	–
	$S/B(\%)$	2.8	5.9	4.3	11.1	9.4	26.8	17.5	–
	$S/\sqrt{B}$	4.9	6.5	5.3	5.6	6.6	5.8	5.7	–
3.0	S	347	234	279	109	204	66	64	–
	B	54193	14284	20550	1797	7077	283	2032	–
	$S/B(\%)$	0.6	1.6	1.4	6.1	2.9	23.3	3.1	–
	$S/\sqrt{B}$	1.5	2.0	2.0	2.6	2.4	3.9	1.4	–

Table 7.6: Expected number of signal and background events after having accumulated 30 fb^{-1} (low) and 300 fb^{-1} (high) luminosity. The corresponding signal (S) to background (B) ratio in percentage and significance is also given. For more details see text.

4 jets: ET $>$ 20 GeV		all jets		6 leading jets		5 leading jets		4 leading jets	
$tan(\beta)$	*sample/ratio*	Low $\mathcal{L}$	High $\mathcal{L}$	Low $\mathcal{L}$	High $\mathcal{L}$	Low $\mathcal{L}$	High $\mathcal{L}$	Low $\mathcal{L}$	High $\mathcal{L}$
1.5	S	783	617	629	264	457	119	186	–
	B	18223	5209	12902	1962	4359	242	1032	–
	$S/B(\%)$	4.3	11.8	4.9	13.5	10.5	49.2	18.0	–
	$S/\sqrt{B}$	5.8	8.6	5.5	6.0	6.9	7.7	5.8	–
3.0	S	324	198	272	104	202	66	64	–
	B	31974	5607	16757	1133	5905	126	1965	–
	$S/B(\%)$	1.0	3.5	1.6	9.2	3.4	52.4	3.3	–
	$S/\sqrt{B}$	1.8	2.6	2.1	3.1	2.6	5.9	1.4	–

Table 7.7: Expected number of signal and background events after having accumulated 30 fb^{-1} (low) and 300 fb^{-1} (high) luminosity. The corresponding signal (S) to background (B) ratio in percentage and significance is also given. For more details see text.

4 jets: ET > 30 GeV		all jets		6 leading jets		5 leading jets		4 leading jets	
$tan(\beta)$	*sample/ratio*	Low $\mathcal{L}$	High $\mathcal{L}$	Low $\mathcal{L}$	High $\mathcal{L}$	Low $\mathcal{L}$	High $\mathcal{L}$	Low $\mathcal{L}$	High $\mathcal{L}$
1.5	S	591	430	505	197	393	98	174	–
	B	3819	1600	3616	602	2296	128	923	–
	$S/B(\%)$	15.5	26.9	14.0	32.7	17.1	76.6	18.9	–
	$S/\sqrt{B}$	9.6	10.8	8.4	8.0	8.2	8.7	5.7	–
3.0	S	253	123	225	91	175	54	62	–
	B	8360	2982	6632	629	3030	116	734	–
	$S/B(\%)$	3.0	4.1	3.4	14.5	5.8	46.5	8.4	–
	$S/\sqrt{B}$	2.8	2.3	2.8	3.6	3.2	5.0	2.3	–

Table 7.8: Expected number of signal and background events after having accumulated 30 fb^{-1} (low) and 300 fb^{-1} (high) luminosity. The corresponding signal (S) to background (B) ratio in percentage and significance is also given. For more details see text.

4 jets: ET $>$ 40 GeV		all jets		6 leading jets		5 leading jets		4 leading jets	
$tan(\beta)$	*sample/ratio*	Low $\mathcal{L}$	High $\mathcal{L}$	Low $\mathcal{L}$	High $\mathcal{L}$	Low $\mathcal{L}$	High $\mathcal{L}$	Low $\mathcal{L}$	High $\mathcal{L}$
1.5	S	343	228	306	129	258	83	136	–
	B	1016	681	1001	335	963	114	565	–
	$S/B(\%)$	33.8	33.5	30.6	38.5	26.8	72.8	24.1	–
	$S/\sqrt{B}$	10.8	8.7	9.7	7.0	8.3	7.8	5.7	–
3.0	S	142	75	131	54	105	38	47	–
	B	1153	668	1103	254	1064	112	534	–
	$S/B(\%)$	12.3	11.2	11.9	21.3	9.9	34.0	8.8	–
	$S/\sqrt{B}$	4.2	2.9	3.9	3.4	3.2	3.6	2.0	–

7.6 $b\bar{b}\,H \rightarrow b\bar{b}\,b\bar{b}$

Four different representative points in the conventional (m_A, $tan\,\beta$) plane have been considered for this study. As before the supersymmetric particles are assumed heavy (fixed at $\sim$ 1 TeV) so as the decay into SUSY particles is forbidden (i.e. the SUSY-OFF case). The $tan\,\beta$ values considered here are 30 and 50, each with a heavy neutral CP-even Higgs, H, of mass 300 GeV and 500 GeV. At large $tan\,\beta$ values the associated production of the neutral CP-even/odd heavy MSSM Higgses, i.e. $b\bar{b}\,H/A$, is enhanced. The A and H are mass degenerate from about $m_A \sim 150\ GeV$ at these high $tan\,\beta$ values, with similar production cross-sections and $b\bar{b}$ decay branching ratio's.

The total production cross-section of the neutral (CP-even) MSSM heavy Higgs boson associated with $b\bar{b}$ quarks through gluon scattering and $q\bar{q}$ interactions (through Higgs radiation or Higgsstrahlung from vector bosons), i.e. $gg\,q\bar{q} \rightarrow b\bar{b}\,H$, as a function of m_A is plotted in Figure 7.18. The cross-sections are calculated for $tan\,\beta = 30,\ 50$ at one- and two-loop orders using the HQQ Monte Carlo program [60]. In what follows only the leading order results are considered in the calculations.

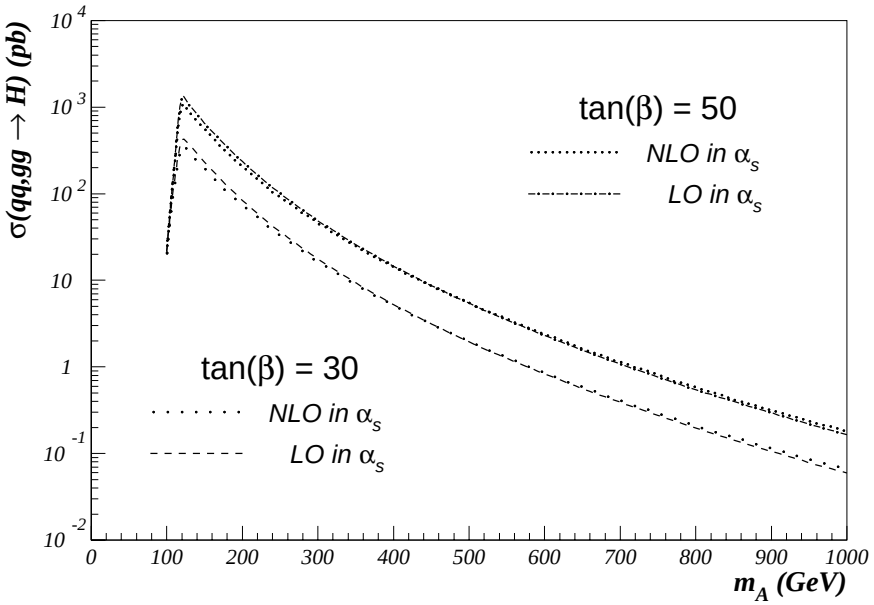

Figure 7.18: *MSSM neutral CP-even heavy Higgs associated production cross-section,* $\sigma(gg,\ q\bar{q} \rightarrow b\bar{b}\,H)$ *for* $tan\,\beta = 30,\ 50$ *as obtained from HQQ program [60].*

The corresponding $H \rightarrow b\bar{b}$ branching ratio's, as obtained from HDECAY, are shown in figure 7.19. The $H \rightarrow \tau^+\tau^-$ branching ratio contributes with about 11-14% to the decay width of H/A Higgses for these $tan\,\beta$ values. To be observed is that, whereas the cross-section decreases rapidly with increasing m_A (or m_H), the branching ratio's are almost constant over the mass range $m_A > 200\ GeV$.

The cross-sections (at one-loop level) and the $H\,bb$ branching ratios for the parameter sets studied here are compiled in Table 7.9.

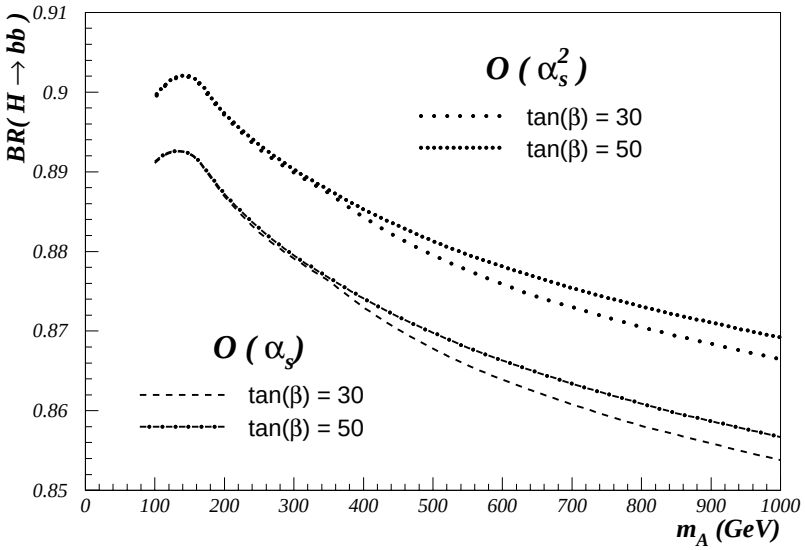

Figure 7.19: *MSSM neutral CP-even heavy Higgs, H, branching ratios for* $\tan\beta = 30\,,\ 50$ *as obtained from HDECAY [58] using* $O(\alpha_s)$ *(LO) and* $O(\alpha_s^2)$ *mass formulas.*

Table 7.9: *The* $gg,\ q\bar{q} \to b\bar{b}\,H$ *production cross-section and the* $H\,bb$ *branching ratios for the four parameter sets in the* $(m_A,\ \tan\beta)$ *space studied here.*

m_H/m_A [GeV]	$\tan\beta = 30$	$\tan\beta = 50$
300	$\sigma_H(LO) = 17.65\ pb$ $\sigma_A(LO) = 17.71\ pb$ $\mathrm{BR}(A/H \to b\bar{b}) = 88\%$ $\sigma\times\mathrm{BR} = 31.12\ pb$	$\sigma_H(LO) = 48.60\ pb$ $\sigma_A(LO) = 49.20\ pb$ $\mathrm{BR}(A/H \to b\bar{b}) = 88\%$ $\sigma\times\mathrm{BR} = 86.06\ pb$
500	$\sigma_H(LO) = 1.96\ pb$ $\sigma_A(LO) = 1.94\ pb$ $\mathrm{BR}(A/H \to b\bar{b}) = 87\%$ $\sigma\times\mathrm{BR} = 3.39\ pb$	$\sigma_H(LO) = 5.46\ pb$ $\sigma_A(LO) = 5.38\ pb$ $\mathrm{BR}(A/H \to b\bar{b}) = 87\%$ $\sigma\times\mathrm{BR} = 9.43\ pb$

In Figure 7.20, the E_T distributions of the partonic b-jets, are plotted for the associated (left column) as well as for the H decay product (right column) b-jets, at H masses 300 GeV (upper row) and 500 GeV (lower row). These distributions are essentially independent of the $tan\,\beta$ values. In each case the E_T distribution of the harder (the full line) and the softer (the dashed line) b-jet is shown. It is seen that the the E_T distributions for the associated b-jets are in general broader than those of the b-jets produced in the decay of the Higgs boson. An important observation is that while the peak position of the E_T distributions for the b-jets from H decay (for the leading and the next-to-leading jet separately) are at higher values compared to the corresponding ones from the associated b-jets, the mean of the distributions are almost comparable.

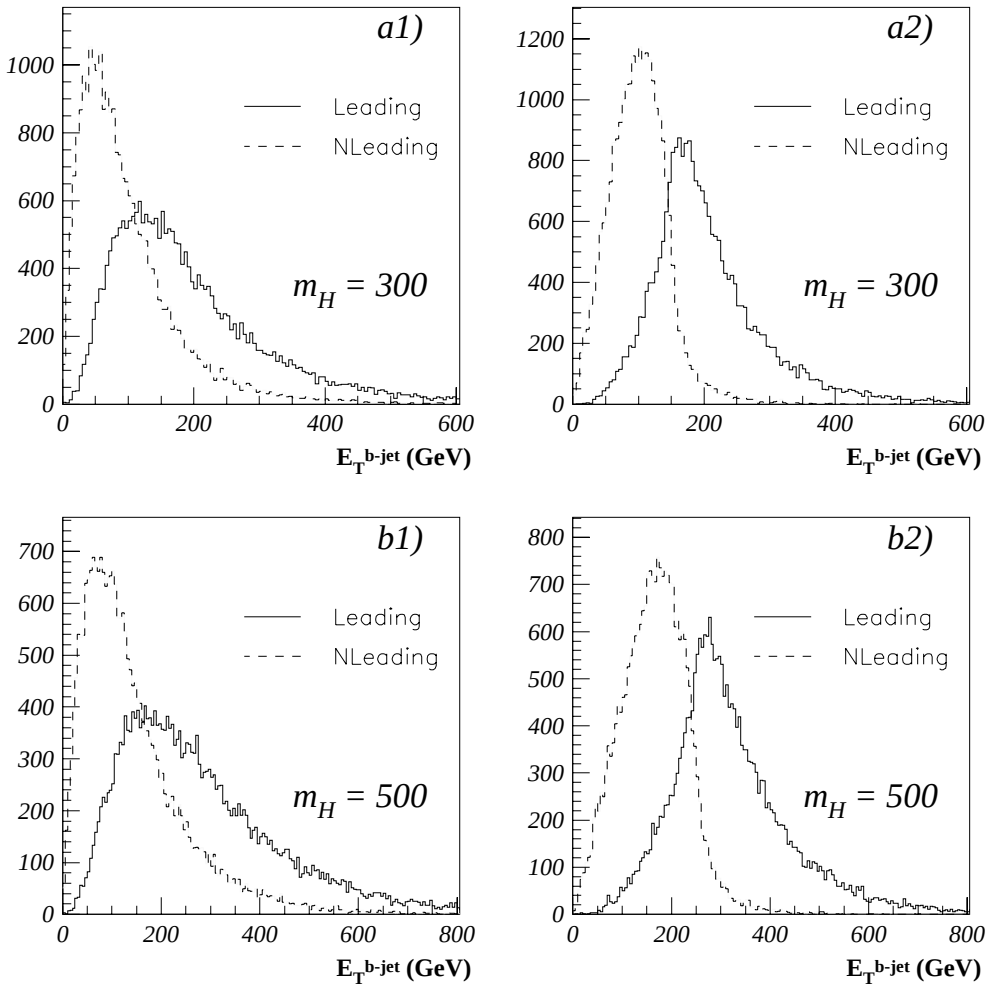

Figure 7.20: *The* E_T *distribution of the partonic b-jets produced in the* $bb\,H \to bb\,bb$ *process. The a plots are for the* $m_H = 300$ *GeV and the b plots for the* $m_H = 500$ *GeV case. The* E_T *distributions of the associated b-jets is suffixed with the digit* 1 *and that of the H decay product b-jets is suffixed with the digit* 2*. In each case the leading (full-line) and the next-to-leading (dashed-lin) jet distributions are shown.*

The E_T distribution of the recalibrated offline b-jets, coinciding with the partonic final state b-jets for the low luminosity scenario, is illustrated in Figure 7.21. The distributions shown on the plots in this figure are similar to those in Figure 7.20. An important point to be noted here is that b-jets enter these plots only if both members of the corresponding b-jet pair are detected. As can be seen the plots for the associated b-jets are less populated than those for the H decay product b-jets. This means that the η distribution of the associated b-jets is broader than that of the H decay b-jets, i.e. in most of the cases only one of the associated b-jets fall within the b-tag η-acceptance window ($|\eta| < 2.5$).

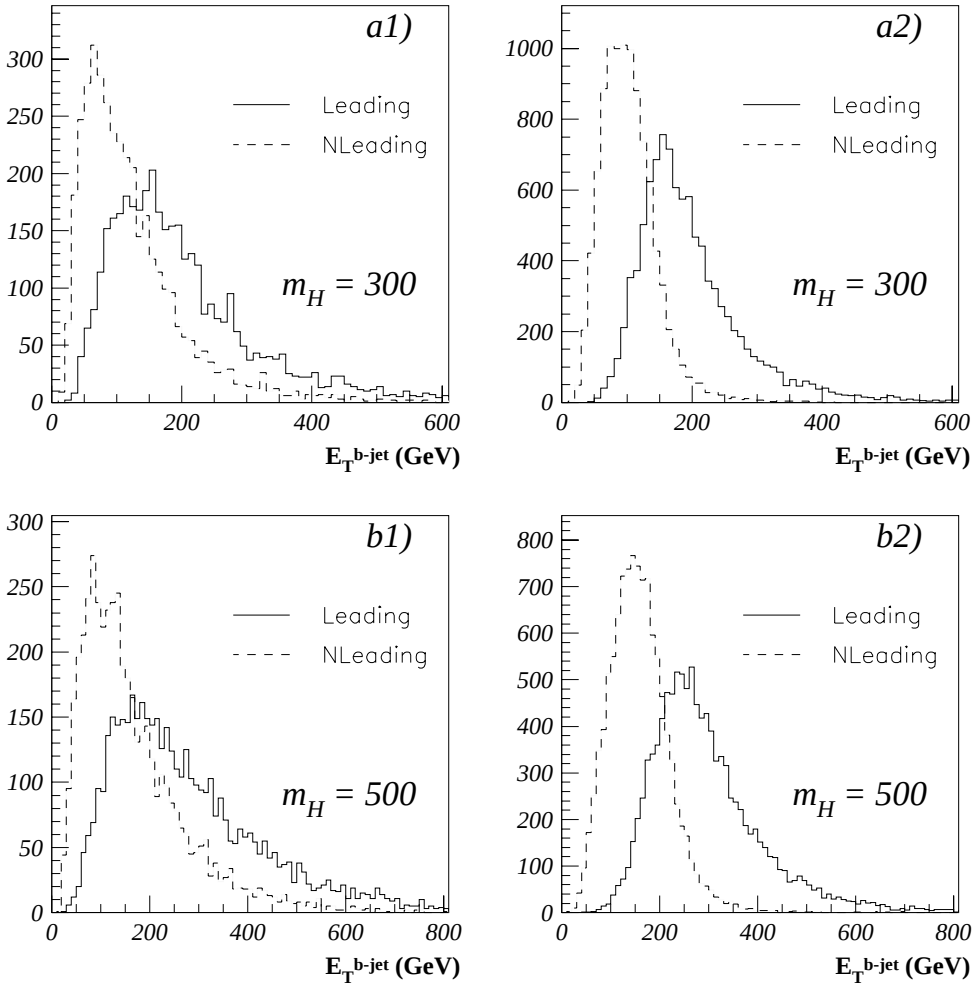

Figure 7.21: *The* E_T *distribution of the offline b-jets produced in the* $bb\,H \rightarrow bb\,bb$ *process. The a plots are for the* $m_H = 300$ *GeV and the b plots for the* $m_H = 500$ *GeV case. The* E_T *distributions of the associated b-jets is suffixed with the digit* 1 *and that of the H decay product b-jets is suffixed with the digit* 2*. In each case the leading (full-line) and the next-to-leading (dashed-lin) jet distributions are shown.*

The correlation of the E_T of the two offline b-jets resulting from the decay of the H boson is in turn shown in figure 7.22. This distribution could be used to optimize event selection by applying cuts on the jets in order to reduce contamination from b-identified jets not being the interested ones. It is seen that the distributions are almost independent of $tan\,\beta$.

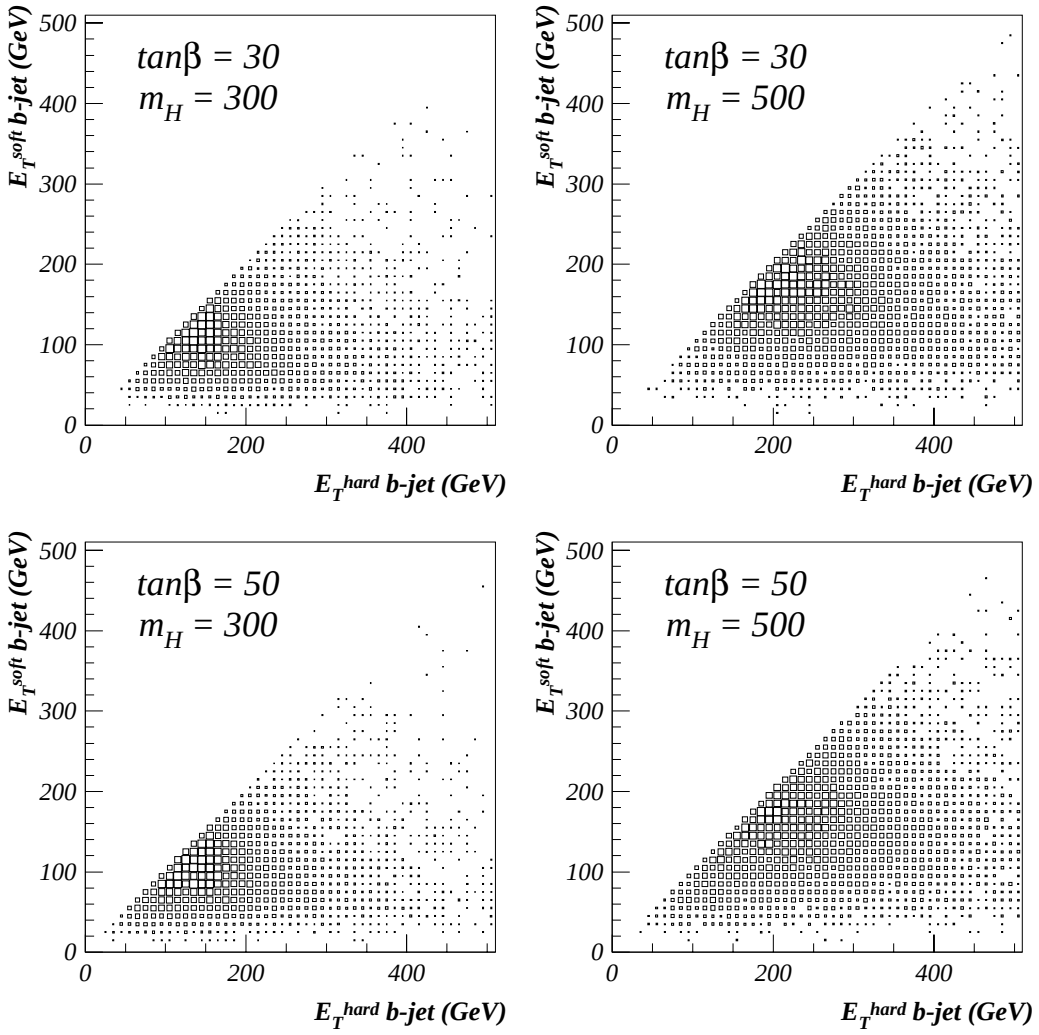

Figure 7.22: *The correlation between the* E_T *of the leading and the next-to-leading b-jets produced in the decay of the H Higgs boson at low luminosity.*

The index (right column) and the sum of the indices (left column) of the b-jets produced in the decay of the Higgs boson, after ordering the offline jets in descending E_T , are shown in figure 7.23. The entries in these plots have passed the kinematical cuts (b-tagged, η acceptance and E_T cuts) to be defined later in the event selection section. The important point to be observed here is that as seen on these plots the decay product b-jets are in most of the cases within the four leading jets of the event, with the $(1,4)$, $(2,4)$ and $(3,4)$ combinations less favored. This observation is confirmed by considering the plots in the right column in the figure, showing the sum of the indices of the b-jets from the H decay.

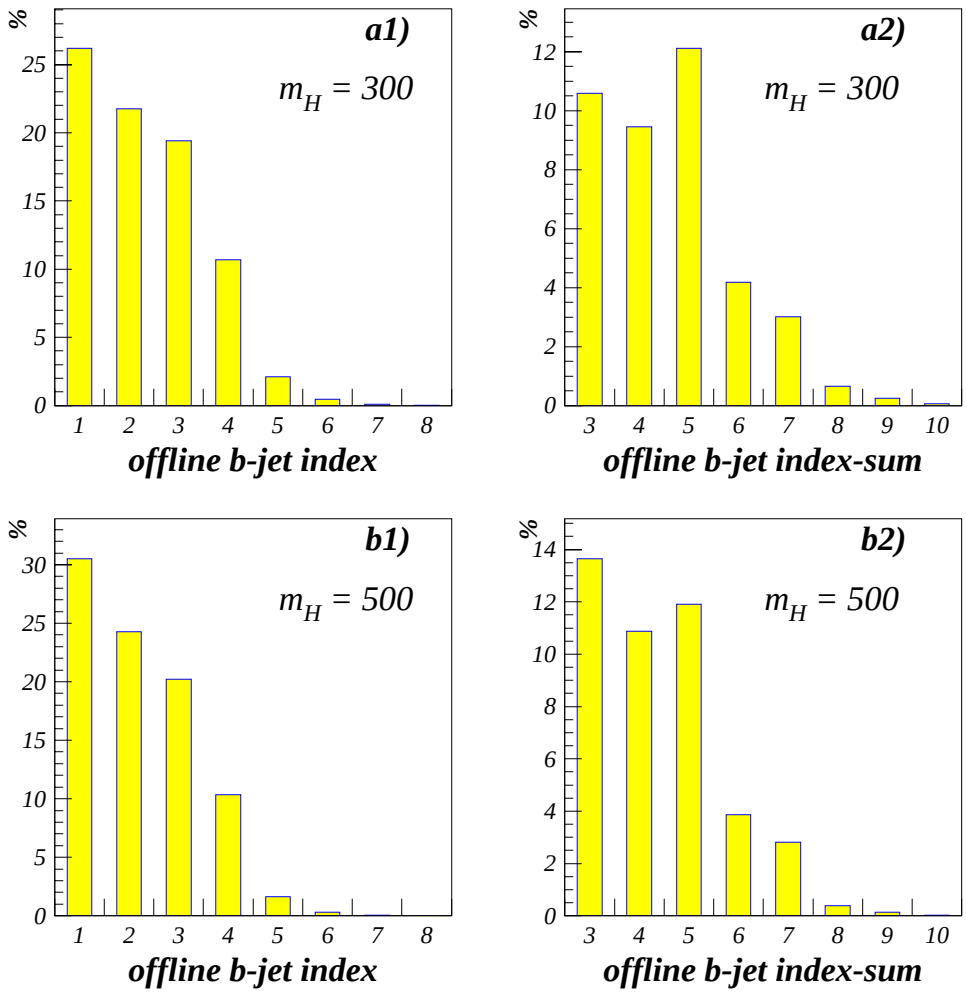

Figure 7.23: *The distributions of the indices, and the corresponding sums, of the b-jets initiated from H decay products. The a plots refer to* $m_H = 300$ *GeV and the b plots to* $m_H = 500$ *GeV. The plots with the suffix* 1 *show the indices of these b-jets in the (descending in* E_T *) ordered list of the event jets, whereas the plots with the suffix* 2 *show the sum of these indices. The contributing events have passed the kinematical cuts defined in event selection section.*

7.6.1 The LVL1 signal acceptance

The acceptance of the LVL1 calorimeter jet trigger(s) at low and high luminosities are shown in Figure 7.24 for the jet trigger thresholds obtained in the previous chapter. An interesting point here is the rather high LVL1 jet trigger acceptance (column 4 in the plots) for both cases, of the order of 90%. Another point is the high acceptance of the individual jet triggers, i.e. the inclusive (first column), the three (second column) and the four (third column) jet triggers. Considering the LVL1 jet trigger rate plots of the QCD background in Figure 7.5 on page 131.

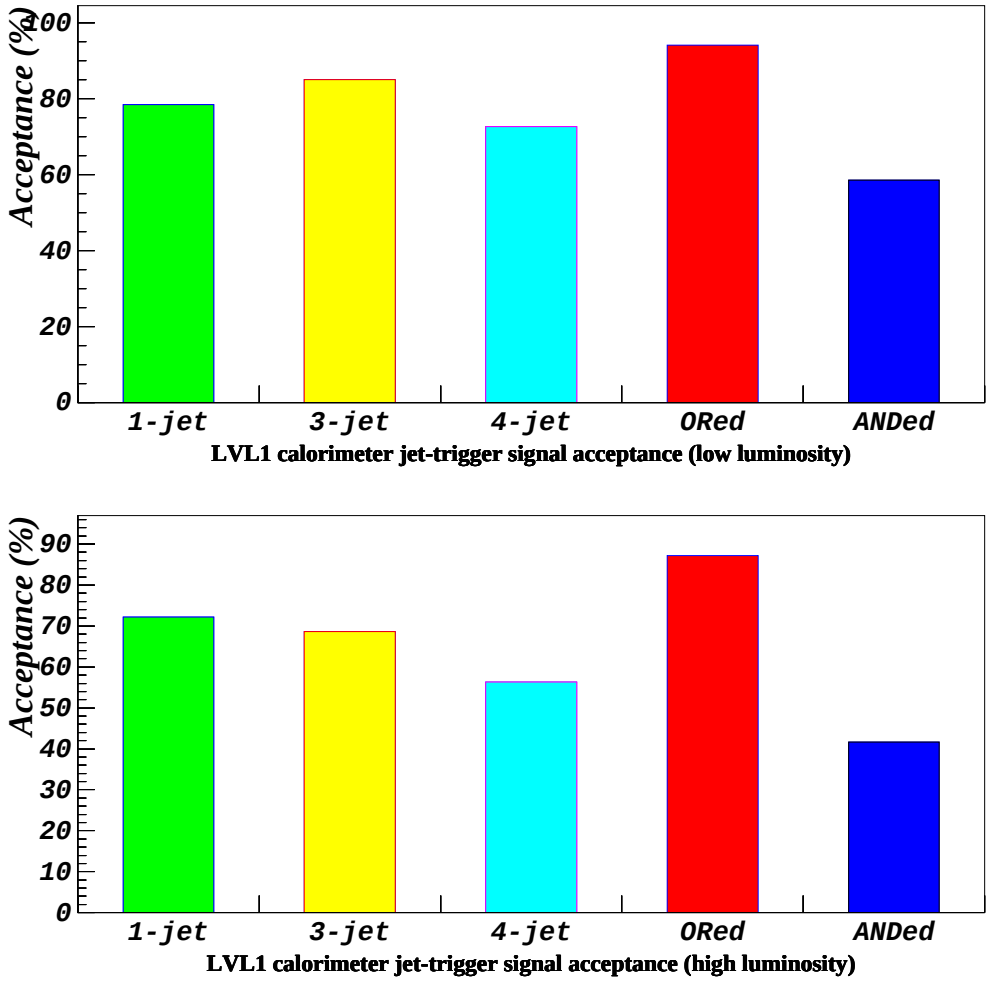

Figure 7.24: *The LVL1 calorimeter jet trigger acceptance at low (top) and high (bottom) luminosities. The first three columns indicate the acceptance of each of the LVL1 jet trigger algorithms, i.e. the inclusive, three and four jet triggers. The fourth column is the overall LVL1 calorimeter jet trigger acceptance. Whereas the last column serves only to illustrate the overlap of the jet triggers.*

7.6.2 Signal extraction

The $b\bar{b}\,H \rightarrow b\bar{b}\,b\bar{b}$ signal is extracted by applying the following cuts:

- At least four b-tagged jets in the event. At this point a geometrical cut is implicitly also applied. This is because a b-tag requires the jet to be within the b-tag η acceptance range, i.e. $|\eta| < 2.5$.
- The four leading jets of the event should be tagged as b-jets.
- The leading jet, passing the previous cut, should have an E_T in excess of 100 GeV (150 GeV) for $m_H = 300\ GeV$ ($m_H = 500\ GeV$). The next-to-leading along with the other jets in the event, also passed the previous cut, should have an E_T greater than 50 GeV (70 GeV) for $m_H = 300\ GeV$ ($m_H = 500\ GeV$). The same E_T cuts are applied both at low and at high luminosity.
- The m_{bb} invariant mass is reconstructed and events with at least an entry within a mass window of about $1.5 \times \sigma_H$, where σ_H is the mass resolution, about the parent Higgs mass are accepted. Three different methods are used to reconstruct m_{bb}: **a**) only the two leading jets, passing the previous cuts, **b**) all bb combinations within the three leading jets, and **c**) all bb combinations within the four leading jets are considered. The mass window is about ± 60 GeV for $m_H = 300\ GeV$ and about ± 80 GeV for $m_H = 500\ GeV$. See mass plots in Figure 7.2 on page 127.

The above cuts could be justified as follows. The only obvious offline handle for this channel is the reconstruction of the bb-mass which should give back the mass of the parent H boson. Additional kinematical cuts applied on the E_T of the b-tagged jets could improve the selectivity of the signal and at the same time reduce the background contribution. By considering the correlation plots in Figure 7.22 and the corresponding E_T profiles of the leading and the next-to-leading b-jets, from the Higgs decay, in Figure 7.21 and at the same time taking into account the index of these b-jets as shown in Figure 7.23, the applied kinematical cuts can be justified. The kinematical cuts on the leading and next-to-leading b-tagged jets are determined in such a way as to keep about 90% of the entries in each profile plot in Figure 7.21, so as to keep the heavily populated region in the correlation plots in Figure 7.22. From the E_T distributions, shown in Figures 7.3 and 7.4 for the QCD samples, these E_T cuts will reduce the background contribution to large extent. For a given mass the selected E_T cuts do not depend on $tan\,\beta$, and depend only on the Higgs mass, and to first approximation the applied cuts are not optimized for the relatively small luminosity effects (with the argument that different jet cone sizes adopted, namely 0.5 at low and 0.4 at high luminosity, remedies the effect.)

The corresponding reconstructed m_{bb}, at low luminosity, is shown in Figures 7.25 and 7.26 for $m_H = 300\ GeV$ and for $m_H = 500\ GeV$ respectively. By selecting the entry with a reconstructed m_{bb} closest to the real Higgs mass, the reconstructed distributions, superimposed as shaded histograms on the corresponding distributions, are obtained (see figure captions).

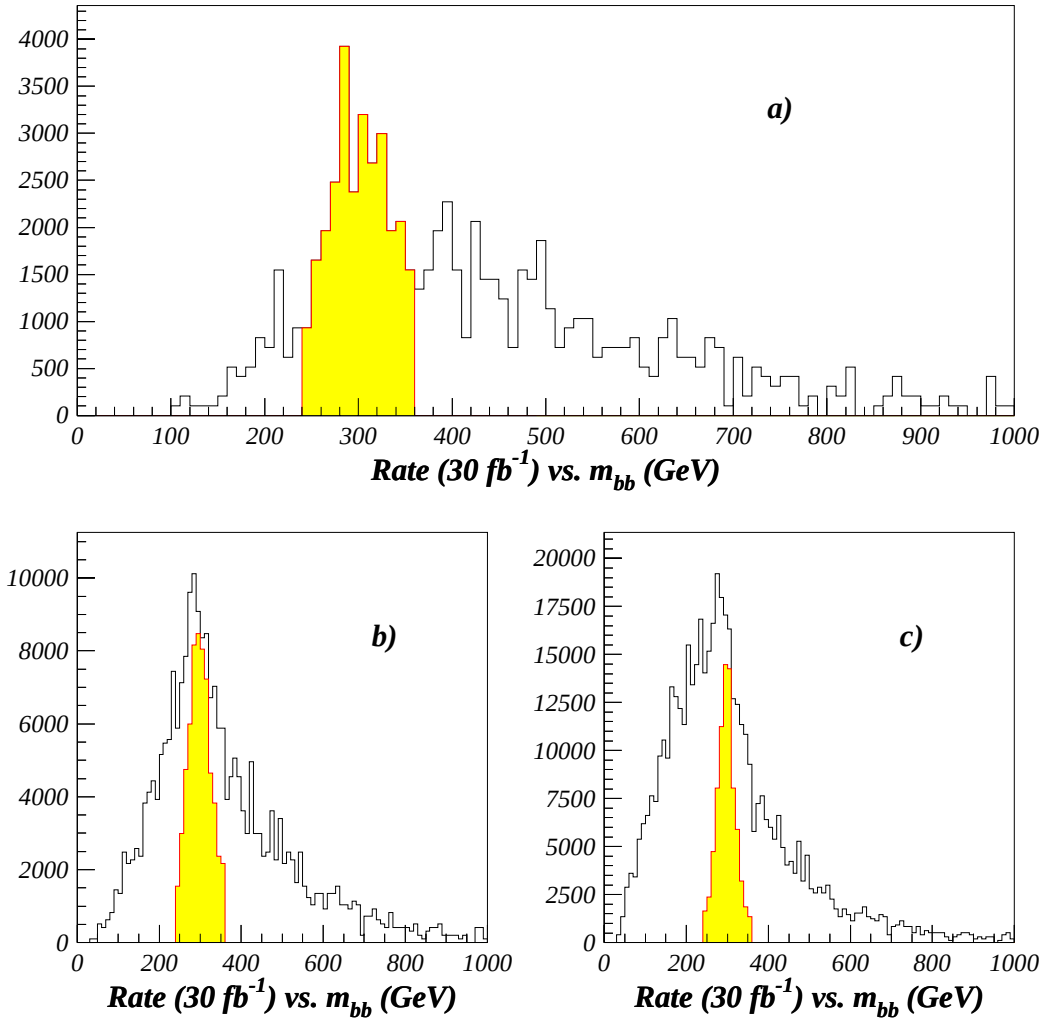

Figure 7.25: *The m_{bb} distributions for $m_H = 300$ GeV for an integrated luminosity of $30\,fb^{-1}$. Only events with four leading jets tagged as b-jets and passing the geometrical/kinematical cuts contribute to the distributions. The invariant m_{bb} is reconstructed by using:* **a)** *only the two leading b-tagged jets (the tight cut),* **b)** *all bb combinations within the three leading ones,* **c)** *all bb combinations within the four b-tagged jets. The entries in the shaded histograms superimposed on the plots correspond to the accepted events with an entry within the applied mass window, and serve only to illustrate: 1) the position and width of the applied mass window and 2) the rate of accepted events. For an explanation of the various selection criteria see text.*

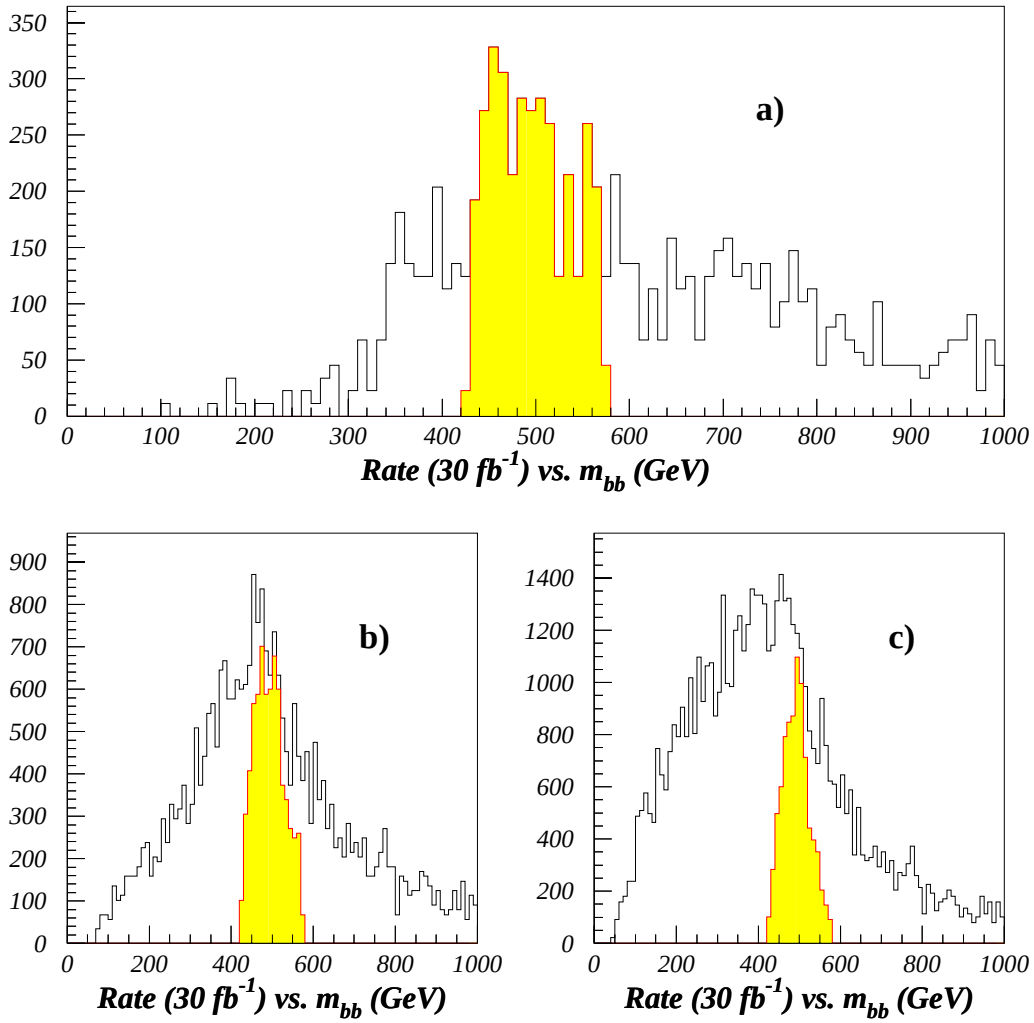

Figure 7.26: *The same as in Figure 7.25, but for* $m_H = 500\ GeV$.

7.6.3 Background contribution

Upon application of the selection criteria on the background samples the m_{bb} distributions shown in Figure 7.27 are obtained after accumulating $30\,fb^{-1}$ of luminosity. The mass distributions are obtained by utilizing the concept of weighted events as explained earlier. The weighting factor for a given event is obtained by multiplying, depending on the *id* of the jet, the b-tag/mistag efficiencies of the four b-tagged jets passing the selection criteria. For events contributing more than once to the mass window, the weight factors are summed accordingly.

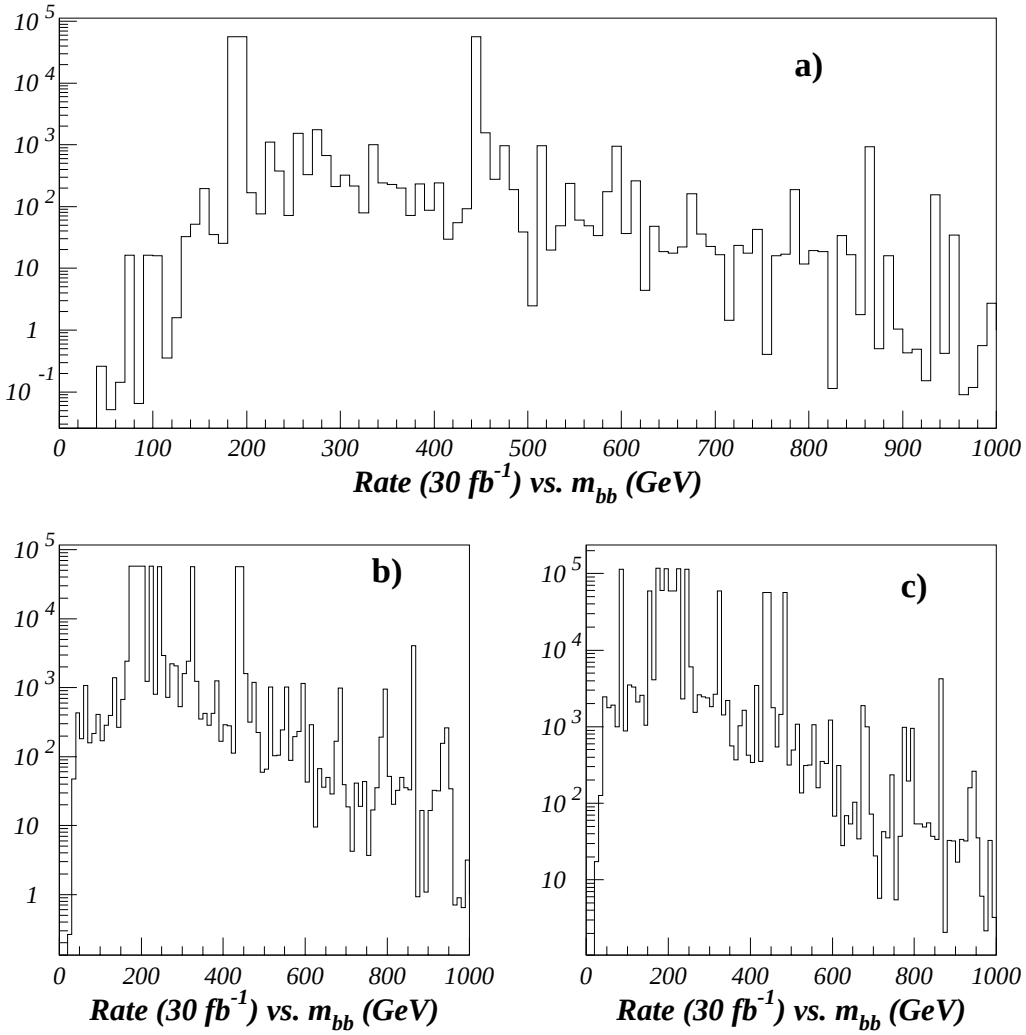

Figure 7.27: *The same as in Figure 7.25, but for the QCD background sample and with the applied selection cuts corresponding to those optimized for the $m_H = 300$ GeV case. The concept of weighted events is applied to produce these plots for the various selection criteria (see text).*

Finally, in Figure 7.28 it is illustrated that the signal does not suffer much form the applied E_T cuts (after b-tagging) and that the background rate is only reduced when the b-tagging procedure is applied. Otherwise the rate will be too large to allow any signal to be extracted. The **upper plot** is due to signal: the entries in the original (not shaded) histogram are due to events passed the b-tagging, but with no E_T cuts applied. The light-grey shaded histogram is after the application of the E_T cuts. The **lower plot** is due to background: the entries in the original (not shaded) histogram are due to events passed $|\eta| < 2.5$ cut, but with no E_T cuts and no event weighting applied. the entries in the light-grey shaded histogram is due to events passed also the E_T cuts but with no event weighting applied. And the dark-grey shaded histogram is after the application of the event weighting procedure. The rate reduction due to b-tagging procedure is evident from this figure. The dark shaded region of the histograms, in both cases indicates the applied mass window cut.

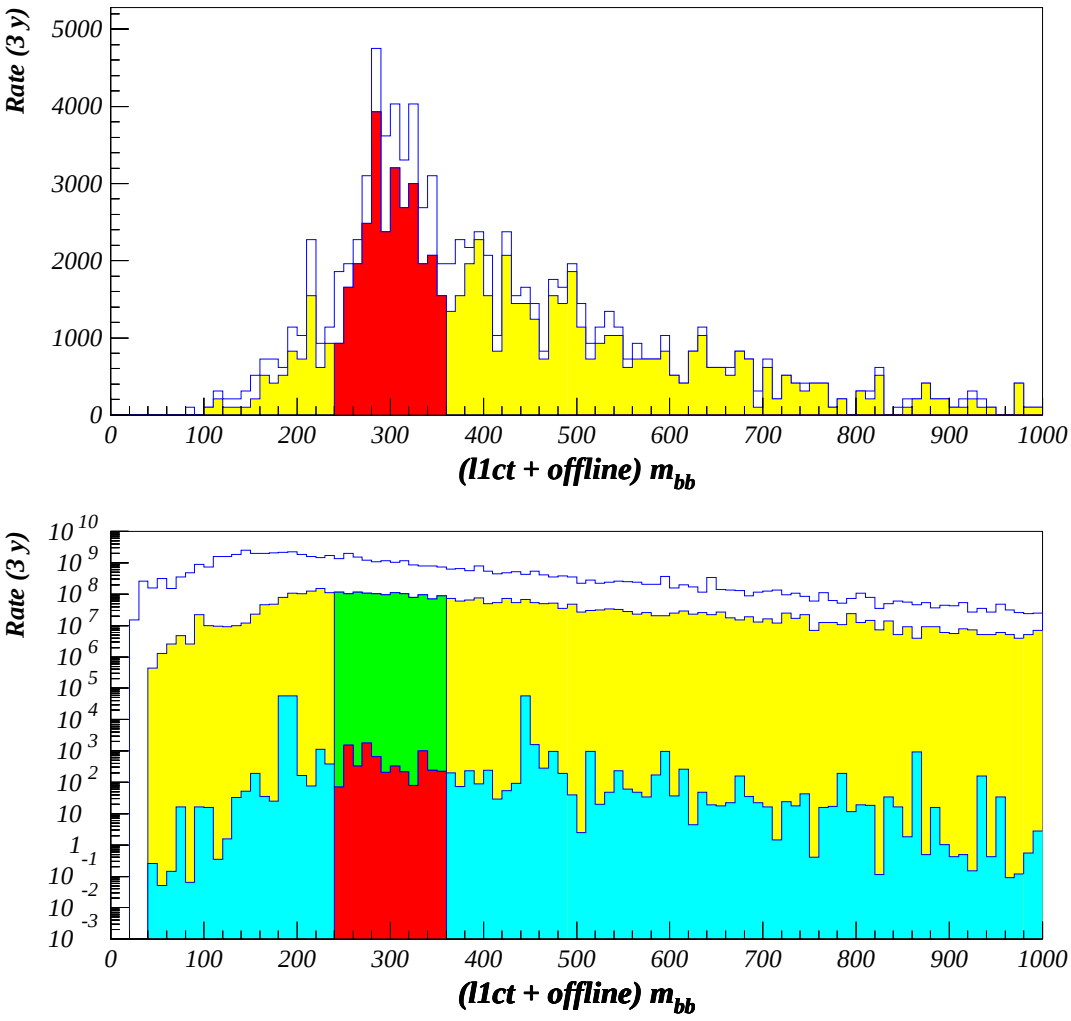

Figure 7.28: *The Signal and background m_{bb} distributions for $\tan\beta = 30$ and $m_H = 300$ GeV for an integrated luminosity of $30\, fb^{-1}$ for the tight selection algorithm after the LVL1 trigger. For details see text.*

7.6.4 Results

The signal and background rates, for an accumulated luminosity of $30\,fb^{-1}$ and of $300\,fb^{-1}$, for the three different selection cuts are compiled in tables 7.10 and 7.11 for $m_A = 300$ GeV and $m_A = 500$ GeV respectively. The observability of the signal in terms of signal (S) to background (B) ratio and the statistical significance, defined as the ratio of the signal to the square-root of the background, are also indicated in these tables for the respective selection algorithms. The effect of the LVL1 calorimeter jet trigger on the acceptance of this channel is also reproduced in the table. To be noticed is the positive effect of the LVL1 calorimeter jet trigger on the S/B and $S/\sqrt{B}$. The reason for this behaviour is the higher acceptance of the LVL1 jet triggers of the signal and its relatively higher jet rejection on the background sample than on the signal.

For the tight selection algorithm, including the effect of the LVL1 jet trigger, the 5σ discovery contour plots shown in Figure 7.29 are obtained. For comparison the 5σ discovery contours for the $b\bar{b}\,A/H \rightarrow b\bar{b}\,\tau^-\tau^+$ decay channels, at low and at high luminosities are also superimposed on the plots in Figure 7.29. It is seen that the four b-jet final states do cover a large area of the (m_A, $tan\,\beta$) plane in the large $tan\,\beta$ region. It can also be observed the $4b$ channels serve as a complementary discovery channel to the $\tau\tau$ decay mode for $m_A < 400$ GeV, whereas for A masses larger than this they will provide a better discovery chance.

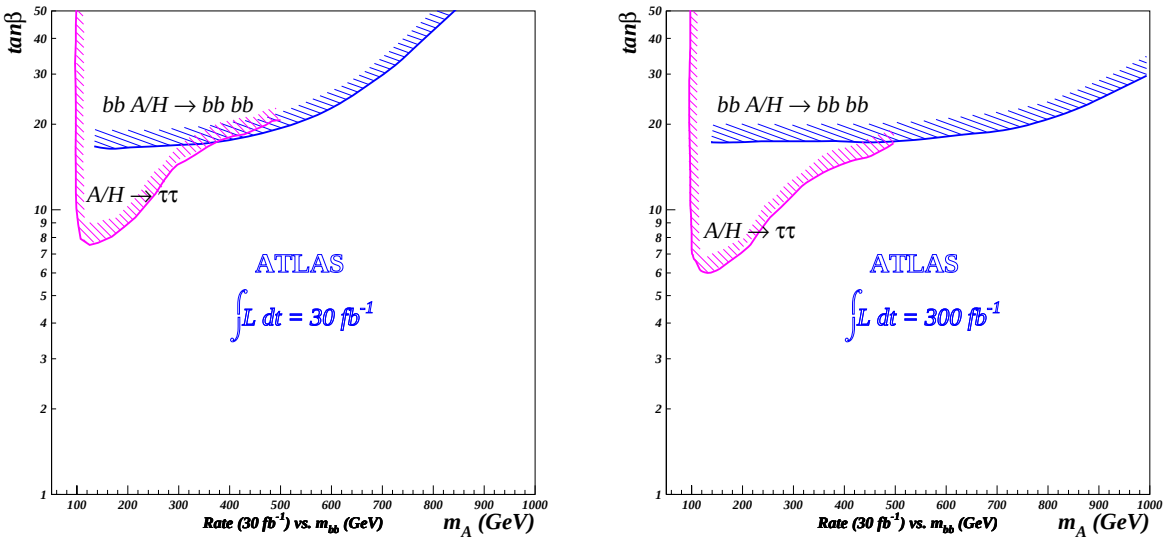

Figure 7.29: *5-σ discovery contours for low (left) and high (high) luminosities for the tight selection algorithm. For details of the selection criteria see text.*

Table 7.10: Expected number of signal and background events after having accumulated 30 fb^{-1} (low) and 100 fb^{-1} (high) luminosity. The corresponding signal (S) to background (B) ratio in percentage and significance is also given. For more details see text.

Low Luminosity						
m_H	**Offline**					
300 GeV	$tan\,\beta = 30$			$tan\,\beta = 50$		
No. of Leading b-tagged jets	**two**	**three**	**four**	**two**	**three**	**four**
S	$1.14 \cdot 10^4$	$2.58 \cdot 10^4$	$3.07 \cdot 10^4$	$2.80 \cdot 10^4$	$6.05 \cdot 10^4$	$7.75 \cdot 10^4$
B	$6.65 \cdot 10^3$	$1.28 \cdot 10^5$	$1.96 \cdot 10^5$	$6.65 \cdot 10^3$	$1.28 \cdot 10^5$	$1.96 \cdot 10^5$
S/B	1.71	0.20	0.16	4.21	0.47	0.40
$S/\sqrt{B}$	139.7	72.0	69.4	343.3	169.1	175.1
m_H	**L1CT + Offline**					
300 GeV	$tan\,\beta = 30$			$tan\,\beta = 50$		
No. of Leading b-tagged jets	**two**	**three**	**four**	**two**	**three**	**four**
S	$1.14 \cdot 10^4$	$2.58 \cdot 10^4$	$3.07 \cdot 10^4$	$2.80 \cdot 10^4$	$6.05 \cdot 10^4$	$7.72 \cdot 10^4$
B	$6.65 \cdot 10^3$	$1.28 \cdot 10^5$	$1.96 \cdot 10^5$	$6.65 \cdot 10^3$	$1.28 \cdot 10^5$	$1.96 \cdot 10^5$
S/B	1.71	0.20	0.16	4.18	0.47	0.39
$S/\sqrt{B}$	139.7	72.0	69.4	340.9	168.5	174.4

High Luminosity						
m_H	**Offline**					
300 GeV	$tan\,\beta = 30$			$tan\,\beta = 50$		
No. of Leading b-tagged jets	**two**	**three**	**four**	**two**	**three**	**four**
S	$5.64 \cdot 10^4$	$1.22 \cdot 10^5$	$1.51 \cdot 10^5$	$1.37 \cdot 10^5$	$3.13 \cdot 10^5$	$3.79 \cdot 10^5$
B	$3.06 \cdot 10^5$	$9.58 \cdot 10^5$	$1.37 \cdot 10^6$	$3.06 \cdot 10^5$	$9.58 \cdot 10^5$	$1.37 \cdot 10^6$
S/B	0.18	0.13	0.11	0.45	0.33	0.28
$S/\sqrt{B}$	101.8	124.4	129.5	248.3	319.9	324.4
m_H	**L1CT + Offline**					
300 GeV	$tan\,\beta = 30$			$tan\,\beta = 50$		
No. of Leading b-tagged jets	**two**	**three**	**four**	**two**	**three**	**four**
S	$2.59 \cdot 10^4$	$7.89 \cdot 10^4$	$1.07 \cdot 10^5$	$1.37 \cdot 10^5$	$3.13 \cdot 10^5$	$3.79 \cdot 10^5$
B	$2.75 \cdot 10^5$	$8.33 \cdot 10^5$	$1.14 \cdot 10^6$	$2.75 \cdot 10^5$	$8.33 \cdot 10^5$	$1.14 \cdot 10^6$
S/B	0.09	0.09	0.09	0.24	0.25	0.23
$S/\sqrt{B}$	49.4	86.5	100.4	124.2	228.8	246.2

Table 7.11: Expected number of signal and background events after having accumulated 30 fb^{-1} (low) and 100 fb^{-1} (high) luminosity. The corresponding signal (S) to background (B) ratio in percentage and significance is also given. For more details see text.

Low Luminosity						
m_H	**Offline**					
500 GeV	$tan\,\beta = 30$			$tan\,\beta = 50$		
No. of Leading b-tagged jets	**two**	**three**	**four**	**two**	**three**	**four**
S	$1.36 \cdot 10^3$	$2.90 \cdot 10^3$	$3.60 \cdot 10^3$	$3.41 \cdot 10^3$	$6.70 \cdot 10^3$	$8.43 \cdot 10^3$
B	$2.66 \cdot 10^3$	$2.99 \cdot 10^3$	$3.52 \cdot 10^3$	$2.66 \cdot 10^3$	$2.99 \cdot 10^3$	$3.52 \cdot 10^3$
$S/B(\%)$	0.51	0.97	1.02	1.28	2.24	2.40
$S/\sqrt{B}$	26.4	53.0	60.6	66.0	122.6	142.2
m_H	**L1CT + Offline**					
500 GeV	$tan\,\beta = 30$			$tan\,\beta = 50$		
No. of Leading b-tagged jets	**two**	**three**	**four**	**two**	**three**	**four**
S	$1.36 \cdot 10^3$	$2.90 \cdot 10^3$	$3.60 \cdot 10^3$	$3.41 \cdot 10^3$	$6.70 \cdot 10^3$	$8.43 \cdot 10^3$
B	$2.66 \cdot 10^3$	$2.99 \cdot 10^3$	$3.52 \cdot 10^3$	$2.66 \cdot 10^3$	$2.99 \cdot 10^3$	$3.52 \cdot 10^3$
$S/B(\%)$	0.51	0.97	1.02	1.28	2.24	2.40
$S/\sqrt{B}$	26.4	53.0	60.6	66.0	122.6	142.2

High Luminosity						
m_H	**Offline**					
500 GeV	$tan\,\beta = 30$			$tan\,\beta = 50$		
No. of Leading b-tagged jets	**two**	**three**	**four**	**two**	**three**	**four**
S	$6.53 \cdot 10^3$	$1.31 \cdot 10^4$	$1.70 \cdot 10^4$	$1.72 \cdot 10^4$	$3.20 \cdot 10^4$	$3.92 \cdot 10^4$
B	$2.72 \cdot 10^3$	$1.19 \cdot 10^4$	$1.72 \cdot 10^4$	$2.72 \cdot 10^3$	$1.19 \cdot 10^4$	$1.72 \cdot 10^4$
$S/B(\%)$	2.40	1.10	0.99	6.34	2.70	2.28
$S/\sqrt{B}$	125.3	119.9	130.0	330.2	293.9	299.0
m_H	**L1CT + Offline**					
500 GeV	$tan\,\beta = 30$			$tan\,\beta = 50$		
No. of Leading b-tagged jets	**two**	**three**	**four**	**two**	**three**	**four**
S	$6.37 \cdot 10^3$	$1.27 \cdot 10^4$	$1.66 \cdot 10^4$	$1.72 \cdot 10^4$	$3.20 \cdot 10^4$	$3.92 \cdot 10^4$
B	$1.49 \cdot 10^3$	$1.06 \cdot 10^4$	$1.58 \cdot 10^4$	$1.49 \cdot 10^3$	$1.06 \cdot 10^4$	$1.58 \cdot 10^4$
$S/B(\%)$	4.29	1.20	1.05	10.90	2.92	2.40
$S/\sqrt{B}$	165.3	123.7	132.2	420.1	301.2	300.9

7.7 Discussion

From the study, performed here, on the MSSM neutral Higgs decay channels with multi b-jet final state signatures, the follwing observations and conclusions can be inferred. The acceptance of the current LVL1 jet trigger, as implemented in the trigger menus, is in general high ($\sim$ 90%) at large $tan\,\beta$ ($\gtrsim$ 30) and intermediate to large m_A ($m_A \gtrsim 200\ GeV$) at both low and high luminosity runs. While at low $tan\,\beta$ ($\lesssim$ 3.0) and intermediate m_A ($200\ GeV < m_A < 350\ GeV$) the acceptance is moderate ($\sim$ 70%) at low and very low ($\sim$ few %) at high luminosity. The former has been studied via the $bb\,H \rightarrow bb\,bb$ decay channel and the latter via the $H \rightarrow h\,h \rightarrow bb\,bb$. In spite of the high rate of the signals in their respective regions in the MSSM parameter space, they suffer from the much higher rate QCD background contributions. Reducing the LVL1 jet trigger thresholds combined with the b-tag capability of the LVL2 trigger may be utilized to achieve a higher overall, i.e. LVL1 + offline, acceptance especially for the high luminosity case for the low $tan\,\beta$ channel. The special four b-jet final state topology, common for both decay modes, already rejects a large fraction of the background, but nevertheless a better signal to background ratio and statistical signal significance is desirable. Different additional kinematical cuts and requirements optimized to the properties of the signals were also applied in order to cover as large an area of the MSSM parameter space as possible.

The 5σ discovery contour for the low $tan\,\beta$ region covers a small region of the (m_A, $tan\,\beta$) parameter space as a complementary channel to the area covered by other decay channels, e.g. $H \rightarrow hh \rightarrow bb\,\gamma\gamma$ and $tt\,h \rightarrow tt\,bb$. In this case additional selection criteria like the angular distance between the two b-jets produced in the light Higgs decay could also be used to reject a fraction of the background events. But in any case the extraction of signal above background is not easy and at high luminosity an extremely difficult task if at all possible.

In the case of the high $tan\,\beta$ the situation is different. At small A masses ($m_A < 400\ GeV$) it complements the $\tau\tau\,/\,\mu\mu$ decay modes, whereas at higher m_A it covers a larger parameter space than, for instance, the $\tau\tau$ channel. Here the situation is rather different than in the low $tan\,\beta$ case above. Signal extraction, due to its hard b-jet distributions, is less difficult.

Summary and Conclusion

This work has been performed within the framework of the ATLAS experiment at LHC located in CERN. A detailed fast simulation environment, based on an existing code, has been developed containing detailed parameterization of the essential effects of the calorimeters, like response, longitudinal and transverse shower shape, and transition region effects, as obtained from the so-called full simulations. Essential details of the parameterization procedure has been described. A detailed pile-up implementation is another powerful feature of this simulation tool. An interface of the simulation package to the official ATLAS particle-level fast simulation program, ATLFAST, has also been implemented. Detailed pile-up simulations for low and high luminosities have also been performed and incorporated into the simulation code. The complete LVL1 trigger chain is also implemented in this code. This simulation package was used to obtain the results presented in this work.

The effect of the combination of the E_T^{miss} trigger with the jet trigger has also been discussed, which can be used to reject QCD background, or to lower the jet trigger thresholds applied at LVL1, for processes with genuine E_T^{miss} signatures. The jet trigger thresholds for the LVL1 jet triggers (defined in the trigger menu) were obtained and where applied on signal and background samples studied here. The LVL1 rates for the various jet triggers, and based on the thresholds, defined in the current LVL1 trigger menu has been estimated using the LVL1 jet trigger thresholds also determined here within the simulation tool. The overall LVL1 jet trigger rate is at low luminosity estimated to be about $\lesssim 2$ kHz and at high luminosity about $\lesssim 900$ Hz. It must be noted that the rate at low luminosity is higher than the official quoted value in [39] by a factor > 2. The reason for the disagreement in the obtained results, apart from being evaluated in different simulation environments, is a matter of definition. It makes, for instance, a difference if one obtains the thresholds based on the rate, or on the jet trigger efficiency, requirements. The latter method has been applied here for a 90% inclusive jet trigger efficiency.

The observability of the MSSM neutral Higgs bosons with four b-jet final state topologies at small and at large $tan\,\beta$ regions for intermediate to heavy A/H bosons was studied. Further, the acceptance of the LVL1 trigger on the signal was also investigated. The acceptance of the LVL1 jet trigger of the $bb\,A/H \rightarrow bb\,bb$ channel, having a large cross-section and a high branching ratio ($\sim$ 90%) in the parameter space considered here, the acceptance is high in spite of the high jet thresholds required in the LVL1 trigger menu. The reason for this is the fact that the A/H Higgs bosons are heavy and produce jets with high E_T , which can be triggered on effectively. For the light Higgs, on the other hand, the situation is different. The final state jets are usually not that high energetic, due to the lower mass, to allow an acceptance as efficient as in the heavy Higgses by the LVL1 jet trigger. Hence, the signal acceptance is particularly low at high luminosity. The effect of the QCD multi-

jet background processes has also been evaluated for both decay channels by applying the appropriate selection cuts. For both cases also the 5σ discovery contours, based on the statistical significances, were obtained. At small $tan\,\beta$ and intermediate m_A regions the obtained contours complement the $H \to h\,h \to bb\,\gamma\gamma$, $H \to Z\,Z^{(*)} \to 4\ell$ and $A \to Z\,h \to \ell\ell\,bb$ channels. At large $tan\,\beta$ the $4b$ final state channels studied here add to the area covered by the $\tau\tau$ / $\mu\mu$ channel at high A masses ($m_A > 500$ GeV).

Selection criteria can, in principle, still be optimized, for instance:

at small $tan\,\beta$ by applying a cut on the angle between the bb combinations to select the signal more effectively (this has actually been performed resulting in a reduction by a factor of 2 of the background and a loss of at most 5% of the signal).

at large $tan\,\beta$ by requiring only one of the multi-jet triggers in the LVL1 trigger menu – the LVL1 3-jet trigger, for example, and not the overall jet trigger. This reduces the QCD background rate by a factor of about 2–3 and results in a signal loss of about 5–10% (depending on luminosity).

The trigger requirement mentioned above could also be used in the small $tan\,\beta$ case in addition to the other selection cuts. Eventual correlation between the cuts (either between these or between these and the earlier cuts) should of course be studied.

In conclusion it must be noticed that the results obtained here are based on a simulation tool that can be considered as the most realistic fast simulation used for different analyzes so far, e.g. in the Physics TDR [46]. Another important point which should be mentioned is that the obtained significances do not contain any contribution from systematical uncertainties. Systematics due to uncertainties in the higher order corrections to the matrix elements (the K–factors) are in general known and evaluated for the signal but not for all the QCD background processes, and therefore has not been included. On the other hand the uncertainties in the parton distribution functions are are known and controllable, and have an effect of about 10–20% depending on the choice of the pdf (changing from CTEQ2L to CTEQ4L/M or CTEQ5L/M for instance). Other systematic effects, due to experimental features, like the calorimeter calibration effects and/or the jet energy scale, can not be estimated properly, to be included in the calculations of the signal significance. This should await the completion of the LHC and the ATLAS detector.

Acknowledgments

At this point I would like to express my gratitude to everyone who either morally or in any other way have supported me during the last few years.

I would like to thank my supervisor, Prof. K.Tittel, for giving me this great opportunity to work in the exciting field of high energy physics and for supporting me, and most important of all for guiding me, all through my Ph.D. years.

Many regards should go to the convener of the ATLAS Higgs Working Group, Prof. K.Jakobs at the physics institute of the MAinz University, for allowing me to participate in the group activities and meetings in many occasions. Especially, many thanks for his tolerance during our discussions on diverse topics in the experimental particle physics.

I have to thank Prof. E.E.Kluge for his moral support and concern during the whole period of my thesis. With his calm attitude toward matters one becomes relaxed and can work more efficiently.

Special thanks to Prof. K.Meier for supporting me and for giving me the chance to contribute to the development of the Pre-Processor ASIC. With his inspiring physics enthusiasm and his enormous interest in computer science it is always a pleasure to go to the weekly ATLAS meetings, specially when it comes to the "innocent question of the week".

My appreciations to Prof. J.D.Hansen, at the Niels Bohr Institute of the Copenhagen University (Denmark), for his support and concern throughout the Ph.D. period.

I would also like to thank Dr. M.Wunsch for giving the initial boost to my thesis and for making me acquainted with the various activities of different working groups, either at our institute, at CERN or at other places.

During the test beam periods at CERN, and all through my Ph.D., I have had several fruitful discussions with Dr. C.Geweniger, whom I would like to thank warmly. I have simply learned a lot from him.

To the colleagues of the Level-1 Calorimeter trigger collaboration, I would like to say that it has been quite a pleasure to be part of this great team. Many thanks to all of them.

Many thanks to the members of the Hadronic EndCap group from Munich, Mainz and Russia for a great cooperation during the test beams.

Many thanks to Elzbieta Richter-wąs for always being ready to help whenever you happen to need it. She Always answers your e-mails the second you send them away!

Many thanks should also go to Traudl Hansl-Kozanecka for her precious advices and for interesting discussions that we had at several occasions.

I would also like to thank all the members of the electronic department at our institute for answering patiently to my questions, specially during the test beam periods.

I have to thank the colleagues from the mainz ATLAS group for being so kind and helpful during my stays there.

During the past years many friends and colleagues have left our institute and it is not possible to name them all here, so I just thank them all for creating a balance between serious work and fun. Special thanks to all friends and the fellow members of the ATLAS, ALEPH, H1, ASIC and the computer science (Hardware Informatik) group at our institute. And many thanks to all the room mates that I had through the last few years.

I would also like to thank all the staff and employees of our institute for creating such a friendly atmosphere, and for making it so pleasent to be around them.

Many thanks to Masoumeh who with great patience and tolerance carried with me the burden of my Ph.D. "till the *bitter* end!".

And last but not least, many thanks to my brother for always encouraging me, and especially to my parents without whom none of these could ever be happening.

This work has been supproted financially 75% by the Danish Research Academy and 25% by the Graduiertenkolleg.

Bibliography

[1] Particle Data Group, *Europ. Phys. J.* C3 1-4 (2000)

[2] Francis Halzen, Alan D. Martin,
Quarks & Leptons: An Introductory Course in Modern Particle Physics,
John Wiley & Sons, Inc. (1984)

[3] Gordon Kane, *Modern Elementary Particle Physics*,
Addison–Wesley Publishing Company, Inc. (1987)

[4] David Griffiths, *Introduction to Elementary Particles*,
Harper & Row Publishers, Inc. (1987)

[5] Peter Schmüser, *Feynman–Graphen und Eichtheorien für Experimentalphysiker*,
Lecture Notes in Physics 295, Springer–Verlag, (1988)

[6] Otto Nachtmann, *Elementarteilchenphysik*, Vieweg (1992)

[7] Donald H. Perkins, *Introduction to High Energy Physics*, Third Edition,
Addison–Wesley Publishing Company, Inc. (1987)

[8] E. Schrödinger, *Annalen der Physik. Leipzig* **80** (1926) 437

[9] R. P. Feynman, *Phys. Rev.* **76** (1949) 749, 769

[10] C. N. Yang and R. L. Mills, *Phys. Rev.* **96** (1954) 191

[11] J. Goldstone, *Nuovo Cim.* **19** (1961) 154

[12] P. W. Higgs, *Phys. Rev. Lett.* **12** (1964) 132; *Phys. Rev. Lett.* **13** (1964) 508; *Phys. Rev.* **145** (1966) 1156

[13] S. L. Glashow, *Nucl. Phys.* **22** (1961) 579
S. Weinberg, *Phys. Rev. Lett.* **19** (1967) 1264
A. Salam, *Elementary Particle Theory*, ed. N. Swartholm (Stockholm: Almquist and Wiksell) (1968) 367

[14] G. 't Hooft, *Nucl. Phys.* **B33** (1971*a*) 173; *Nucl. Phys.* **B35** (1971*b*) 167

[15] M. Gell-Mann, *A Schematic Model of Baryons and Mesons*, Phys. Lett. **8** (1964) 214

[16] G. Zweig, *CERN–8182–TH–401; CERN–8419–TH–412* (1964)

[17] N. Cabibbo, *Phys. Rev. Lett.* **10** (1963) 531
M. Kobayashi and T. Maskawa, *Prog. Theor. Phys.* **49** (1973) 652

[18] L. Wolfenstein, *Nucl. Phys.* **B146** (1978) 477

[19] H. Fritzsh, M. Gell-Mann and H. Leutwyler, *Phys. Lett.* **47B** (1973) 365

[20] H. Georgi and S. L. Glashow, *Phys. Rev. Lett.* **32** (1974) 438
H. Georgi *et al.*, *Phys. Rev. Lett.* **33** (1974) 451

[21] J. Wess and B. Zumino, *Nucl. Phys.* **B78** (1974) 1

[22] P. D. B. Collins and A. D. Martin, *Hadron Interactions*,
(Adam Hilger, 1984)

[23] I. Y. Pomeranchuk, *Sov. Phys. JETP* **7** (1958) 499

[24] C. Quigg, *Gauge Theories of the Strong, Weak, and Electromagnetic Interactions*,
The Benjamin/Cummings Publishing Company (1983)

[25] A. Pich, *Quantum Chromodynamics*,
HEP-PH/9505231, FTUV/95-19, IFIC/95-19, May 1995

[26] G. Altarelli and G. Parisi, *Nucl. Phys.* **B126** (1977) 298

[27] J. F. Gunion, H. E. Haber, G. Kane, S. Dawson, *The Higgs Hunter's Guide*,
Addison–Wesley Publishing Company, Inc. (1990)

[28] Gordon L. Kane (editor) *Prospectives on Higgs Physics*,
Advanced Series on Directions in High Energy Physics — Vol. 13,
World Scientific, (1993)

[29] Gordon L. Kane (editor) *Prospectives on Higgs Physics II*,
Advanced Series on Directions in High Energy Physics — Vol. 17,
World Scientific, (1997)

[30] Gordon L. Kane (editor) *Prospectives on SUSY*,
Advanced Series on Directions in High Energy Physics — Vol. 18,
World Scientific, (1998)

[31] Graham G. Ross, *Grand Unified Theories*,
Frontiers in Physics, Lecture Note Series 60,
The Benjamin/Cummings Publishing Company, Inc. (1985)

[32] Vernon D. Barger, Roger J.N.Philips, *Collider Physics*, Updated Edition,
(Frontiers in Physics; Volume 71), Addison–Wesley Publishing Company, Inc. (1997)

[33] The LHC Study Group *The Large Hadron Collider,*
Conceptual Design Reort, CERN/AC/95–05 (LHCC), 20 October 1995

[34] ATLAS Collaboration, *Letter of Intent*,
CERN/LHCC/92-4, LHCC/I2, 1 October 1992

[35] ATLAS Collaboration, *Technical Proposal*,
CERN/LHCC/94-43, LHCC/P2, 15 December 1994

[36] CMS Collaboration, *The Compact Muon Solenoid, Technical Proposal*, CERN/LHCC 94-38, LHCC/P1, 15 December 1994

[37] LHCb Collaboration, *A Large Hadron Collider Beauty Experiment, Technical Proposal*, CERN/LHCC 98-4, LHCC/P4, 20 February 1998

[38] ALICE – *A Large Ion Collider Experiment at LHC, Technical Proposal*, CERN/LHCC/95-71, LHCC/P3, 15 December 1995

[39] ATLAS *Trigger Performance Status Report*, CERN/LHCC/98-15

[40] ATLAS *Inner Detector, Technical Design Reort*, CERN/LHCC 97-16/17, Volume I/II, ATLAS TDR 4/5, 30 April 1997

[41] ATLAS *Liquid Argon Calorimeter, Technical Design Reort*, CERN/LHCC 96-41, 15 December 1996

[42] ATLAS *Calorimeter Performance, Technical Design Reort*, CERN/LHCC 96-40, 17 January 1997

[43] ATLAS *First – Level Trigger, Technical Design Reort*, CERN/LHCC/98-14, ATLAS TDR 12, 30 June 1998

[44] ATLAS *Tile Calorimeter, Technical Design Reort*, CERN/LHCC 96-42, 15 December 1996

[45] ATLAS *Muon Spectrometer, Technical Design Reort*, CERN/LHCC 97-22, 5 June 1997

[46] ATLAS *Detector and Physics Performance, Technical Design Report*, Volume I/II, CERN/LHCC/99-15, ATLAS TDR 15, 25 MAY 1999

[47] S. George and T. Hansl-Kozanecka (eds.), *ATLAS Trigger Menus*, ATLAS–note DAQ–NO–121

[48] The LEP working group for Higgs boson searches, *Searches for Higgs bosons: Preliminary combined results using LEP data collected at energies up to 202 GeV* CERN-EP–2000-055, 25 April 2000

[49] B. Pietrzyk, *The global fit to electroweak data*, XXXth International Conference on High Energy Physics, July 27 – August 2, 2000, Osaka, Japan

A. Gurtu, *Precision tests of the electroweak gauge theory*, ICHEP2000, Osaka CERN-EP–2000-055, 25 April 2000

[50] Ulrich Pfeiffer, *A Compact Pre-Processor System for the ATLAS Level-1 Calorimeter Trigger*, PHD thesis, Heidelberg University, Germany proc.: *submitted to* **World Scientific** *on 22 September 2000*

[51] R. Dubitzky, *Untersuchung von Algorithmen zur Ereignisselektion im Hardware–Trigger des ATLAS–Experiments*, Diploma thesis, Mainz University, Germany, February 1999

[52] R. Dubitzky and K. Jakobs, *Study of the performance of the Level-1 P_T^{miss}-Trigger*, ATL-DAQ-99-010 (ATL-COM-DAQ-99-018)

[53] M. Wunsch, *Results of a Fast Simulation of the E_T^{miss} Trigger of ATLAS*, ATL-DAQ-97-074 (ATL-D-PN-74)

[54] R. Dubitzky *et al.*, *Level–1 Rates for Triggers using the E_T^{miss} Trigger*, ATL-DAQ-99-011 (ATL-COM-DAQ-98-011)

[55] S. George *et al.*, *RoI based event descriptions for modelling the ATLAS second level trigger*, 12 April 1999

[56] T. Sjöstrand, *PYTHIA 5.7 and JETSET 7.4, Physiscs and Manual*, CERN-TH 7112/93

[57] T. Sjöstrand, *Comp. Phys. Comm.* 82 (1994) 74

[58] A. Djouadi, J. Kalinowski and M. Spira, *HDECAY*, DESY 97–079, IFT–96–29, PM–97/04; April 1997

[59] Michael Spira, *HIGLU*, Internal Report DESY T–95–05, hep-ph/9510347; October 1995

[60] Michael Spira, Monte-Carlo programs to calculate various cross-sections and decay in the Higgs sector:

HIGLU:$g\,g \leftrightarrow H/A$,

VV2H:$WW\,/\,ZZ \rightarrow H$,

V2HV:$W^*\,/\,Z^* \rightarrow H\,W\,/\,Z/A$,

HQQ:$qq, gg \rightarrow H/A\,QQ$,

HPAIR:$qq, gg \rightarrow HH\,/\,HA\,/\,AA$,

where H represents either a SM Higgs or a CP-even MSSM Higgs.
For more information see: www.cern.ch/ mspira.

[61] H. Plothow–Besch/CERN–ETT/TT, W5051 PDFLIB, PDFLIB – User's Manual, CERN Computer Program Library, Entry W5051

[62] GEANT - Detector Description and Simulation Tool, CERN Library package, http://atlas.web.cern.ch/Atlas/GROUPS/SOFTWARE/DOCUMENTS/simulation.html

[63] DICE-95, ATLAS-SOFT/95-14c, 15 January 1996
Reconstruction interface for DICE95, ATLAS-SOFT/95-draft, 29 November 1995
http://atlasinfo.cern.ch/Atlas/GROUPS/SOFTWARE/DOCUMENTS/DICE95/DICE95.html

[64] ATRECON, the ATLAS Reconstruction program
Version 1.41 (Atlas release of 29th July 1998 on 98_2 area)
http://atlas.web.cern.ch/Atlas/GROUPS/SOFTWARE/DOCUMENTS/reconstruction.html

[65] ATlas TRIGger Simulation Package (ATRIG)
http://atlas.web.cern.ch/Atlas/GROUPS/DAQTRIG/ATRIG/atrigdoc-cvs.html

[66] CERN Library package, CERN progrm Library

[67] *ATLFAST*, E.Richter–Was et al., ATLAS–PHYS–NO–79.

[68] E. Richter-was, D. Froidevaux and F. Gianotti, L. Poggioli, D. Cavalli, S. Resconi, *Minimal Supersymmetric Standard Model Higgs rates and backgrounds in ATLAS*, ATLAS Internal Note, PHYS–No–048, 17/07/1995
ATLAS Internal Note, PHYS–No–074, 22/04/1996

[69] E. Richter-was and D. Froidevaux, *MSSM Higgs searches in multi-b-jet final states*, ATLAS Internal Note, PHYS–No–104, July 1997

[70] J. Dai, J. F. Gunion and R. Vega *LHC detection of Neutral MSSM Higgs bosons via* $gg \to b\bar{b}\,h \to b\bar{b}\,b\bar{b}$,
UCD-94–7, SMU-HEP–94/4, UCSD/PTH-94–2, HEP-PH/9403362, March 1994

J. Dai, J. F. Gunion and R. Vega *Searching for Higgs bosons ON LHC using b-tagging*, HEP-PH/9503449, 28 March 1995

J. Dai, J. F. Gunion and R. Vega *Detection of the Minimal Supersymmetric Model Higgs Boson* H^0 *in its* $h^0h^0 \to 4b$ *and* $A^0A^0 \to 4b$ *Decay Channels*,
UCD-95–25, UCSD/PTH-95–16, HEP-PH/9511319, October 1995

J. Dai, J. F. Gunion and R. Vega *Detection of Neutral MSSM Higgs Bosons in Four-b Final State at the Tevatron and the LHC: An Update*, UCD-96–12, July 1996

[71] Dirk Graudenz, *The Physics of the Standard Model Higgs Boson at the LHC*, CERN–TH/95-77, March 1995

[72] Karl Jakobs, *The Physics Potential of the ATLAS Experiment at the LHC*, ATL–CONF–2000–004, 01/07/2000

[73] Fabiola Gianotti, *Collider Physics: LHC*, ATL–CONF–2000–001, 26/04/2000